Indigo Mono- and Diimine Ligands as Proton and Electron Reservoirs

by

Dillon T. Hofsommer
B.Sc., North Dakota State University, 2012

A Dissertation Submitted in Partial Fulfillment of the
Requirements for the Degree of

DOCTOR OF PHILOSOPHY

in the Department of Chemistry

University of Victoria

Supervisory Committee

Indigo Mono- and Diimine Ligands as Proton and Electron Reservoirs

by

Dillon T. Hofsommer
B.Sc., North Dakota State University, 2012

Supervisory Committee

Dr. Robin G. Hicks, Department of Chemistry
Supervisor

Dr. Neil Burford, Department of Chemistry
Departmental Member

Dr. J. Scott McIndoe, Department of Chemistry
Departmental Member

Dr. Dean Karlen, Department of Physics
Outside Member

Abstract

Supervisory Committee
Dr. Robin G. Hicks, Department of Chemistry
Supervisor
Dr. Neil Burford, Department of Chemistry
Departmental Member
Dr. J. Scott McIndoe, Department of Chemistry
Departmental Member
Dr. Dean Karlen, Department of Physics
Outside Member

Indigo *N,N'*-diarylimine (Nindigo) and indigo *N*-arylimine (Mindigo) are redox-active ligands which exhibit near-infrared absorption and can accommodate up to five ligand charge states. This dissertation explores the coordination chemistry of these ligands to further understand the role that metal-ligand combinations play on ligand-centered properties, which include electrochemical potentials, UV-Vis-NIR absorption, pK_a values, hydricities, and NH bond strengths at different ligand charge states.

A series of *cis*-Nindigo palladium complexes containing acetylacetonate (acac) and hexafluoroacetylacetonate (hfac) ligands were synthesized. The acac complexes were easier to oxidize by 0.11 to 0.16 V and absorbed at lower wavelengths compared to their hfac analogues. Complexes using indigo bis(4-methylphenylimine) were more easily reduced than complexes of indigo bis(2,6-dimethylphenylimine).

Cis- and *trans*-Mindigo complexes of palladium acac and hfac were synthesized as the first coordination complexes of Mindigo. *Trans*-Mindigo complexes were more difficult to reduce by 0.33 to 0.37 V and absorbed at lower wavelengths than their *cis*-Mindigo counterparts. *Cis*-Mindigo complexes were easier to reduce and harder to oxidize than the corresponding *cis*-Nindigo complexes.

The NH bond strengths of *cis*-Nindigo complexes containing Pd(acac) and $Ru(bipy)_2$ (bipy = 2,2'-bipyridyl) fragments were determined through a potential-pK_a

diagram in tetrahydrofuran and acetonitrile, respectively. The NH bond strength and hydricity values of the Pd(acac) complex were comparable to the values of diaryl amines. The NH bond strength and hydricity of the $Ru(bipy)_2$ complex were substantially smaller due to the lower oxidation potentials of this complex. In both cases, the ligand's NH bond strengths were not affected greatly by the ligand's charge state.

$Ru(acac)_2$ complexes of neutral, aprotic *cis*-Nindigo and *cis*-Mindigo ligands were synthesized. The Nindigo/Mindigo ligand could be protonated, and the resulting complexes demonstrated substantial temperature dependence of some of their ^1H NMR chemical shifts. The NH bond strengths and hydricities of the $Ru(acac)_2$ complexes were determined using cyclic voltammetry and pK_a measurements. The NH bond strengths and hydricities of these complexes are substantially smaller than the Pd(acac) and $Ru(bipy)_2$ complexes. Collectively, these results show that Nindigo and Mindigo can act as both a proton and electron reservoirs, and the thermodynamics of proton and electron transfer can be tuned through the choice of metal and ligand combinations.

Table of Contents

List of Figures

List of Schemes

List of Tables

List of Numbered Compounds

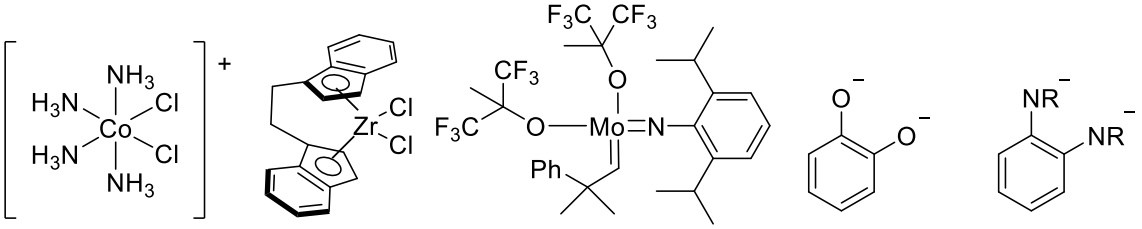

1.1 **1.2** **1.3** **1.4** **1.5**

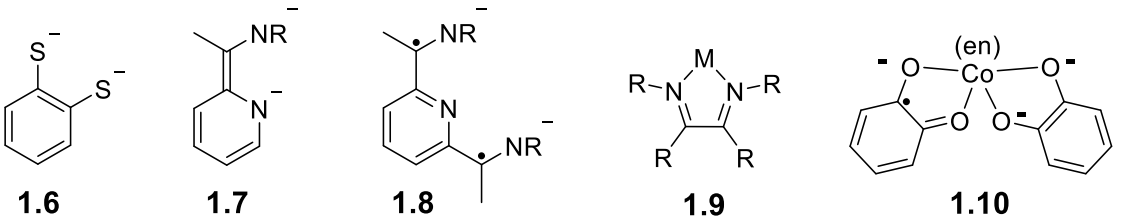

1.6 **1.7** **1.8** **1.9** **1.10**

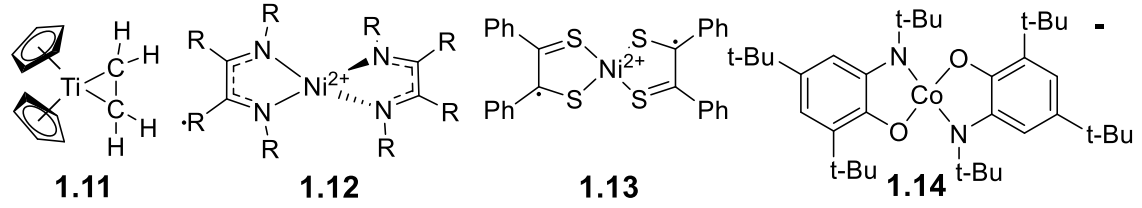

1.11 **1.12** **1.13** **1.14**

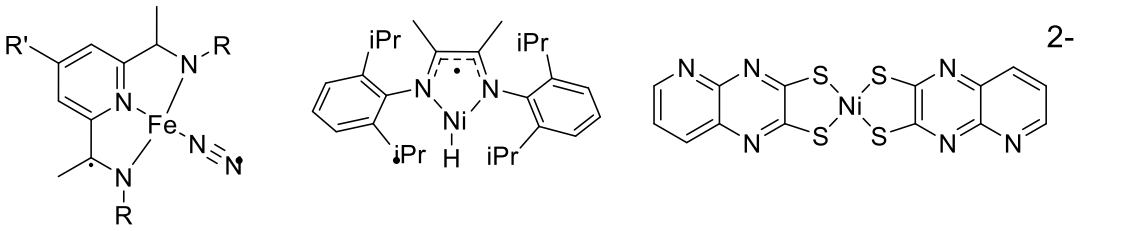

1.15 **1.16** **1.17**

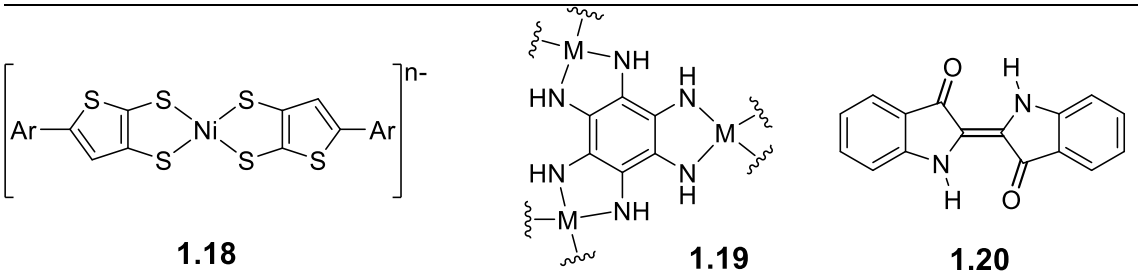

1.18 **1.19** **1.20**

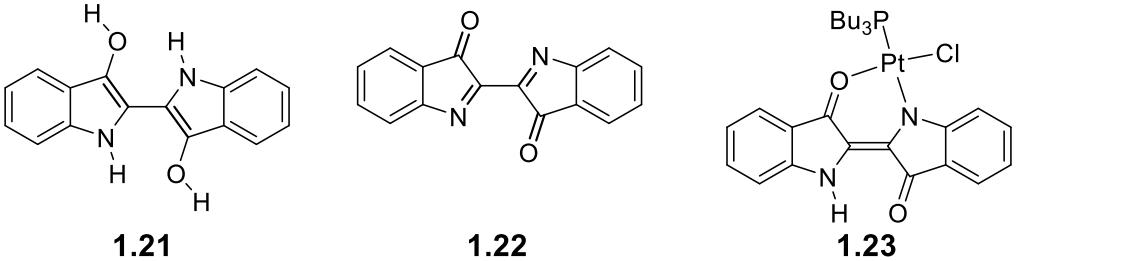

1.21 **1.22** **1.23**

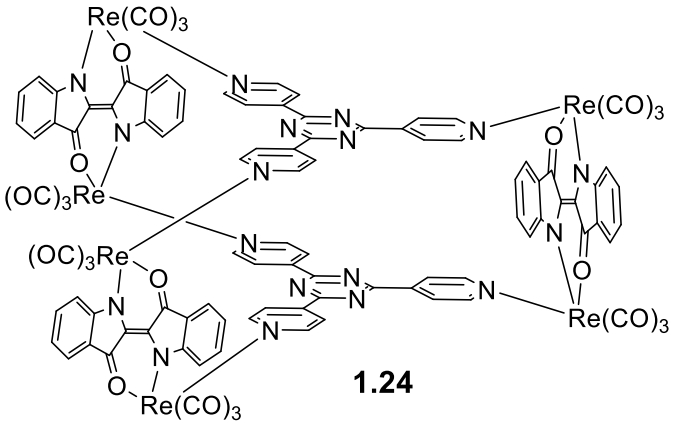

1.24

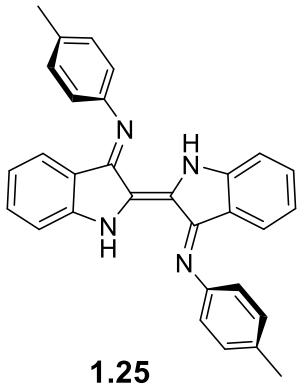

1.25

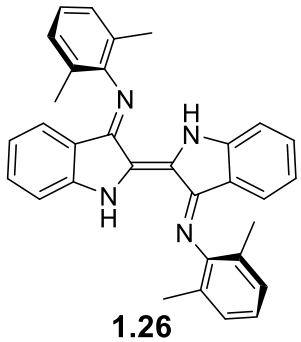

1.26

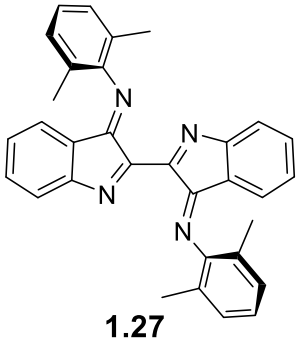

1.27

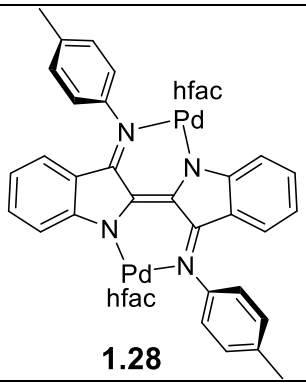

1.28

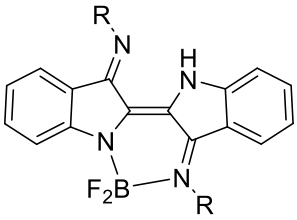

1.29

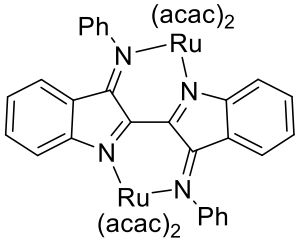

1.30

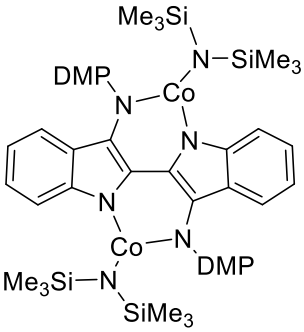

2-

1.31

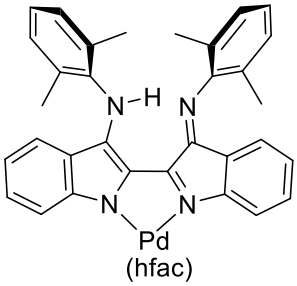

1.32

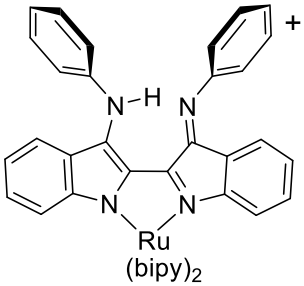

+

1.33

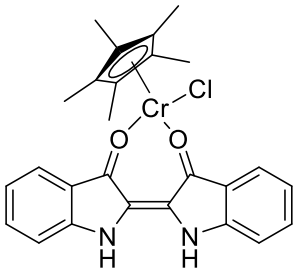

1.34

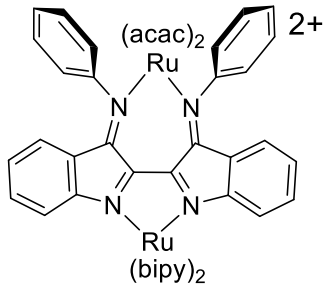

1.35

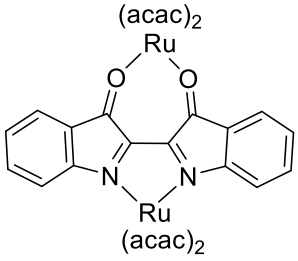

1.36

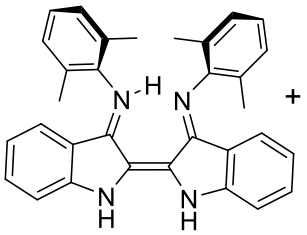

1.37

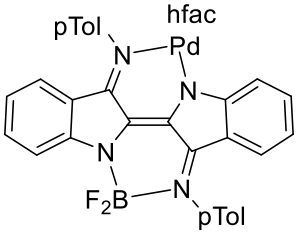

2.1a

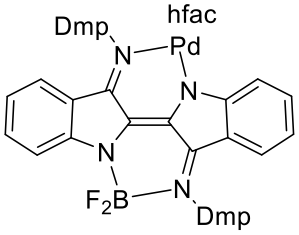

2.1b

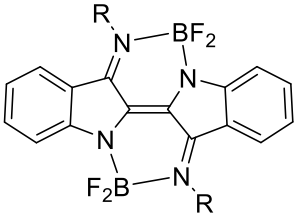

2.2

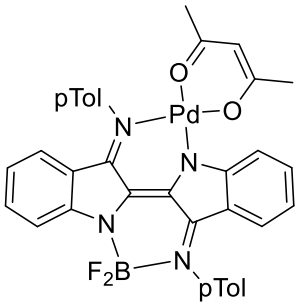

2.3a

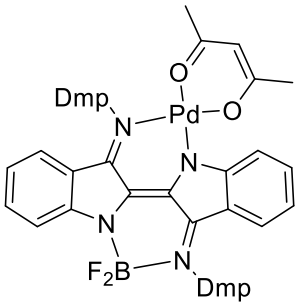

2.3b

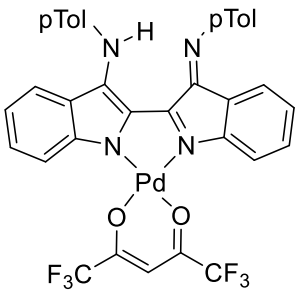

2.4a

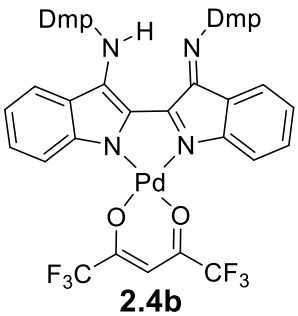

2.4b

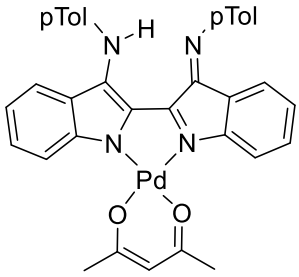

2.5a

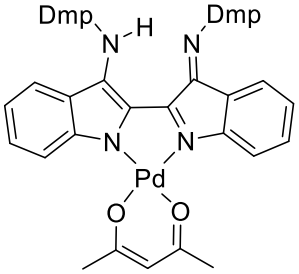

2.5b

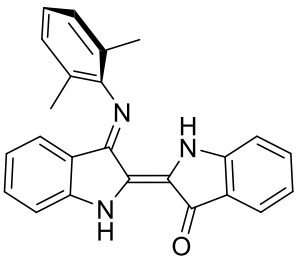

3.1

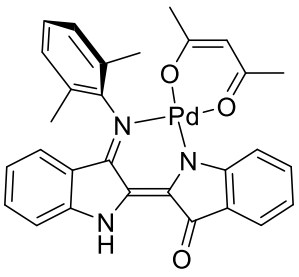

3.2

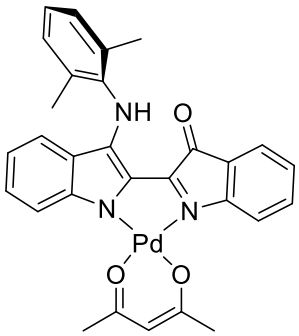

3.3

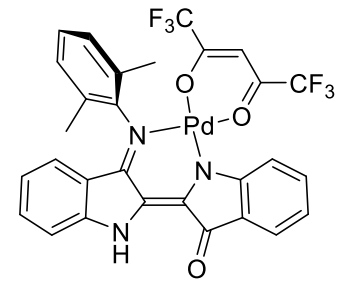

3.4

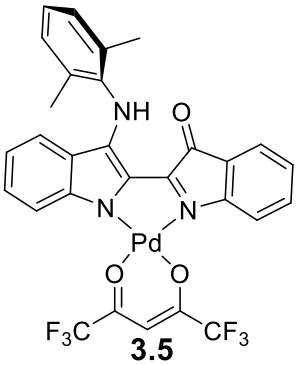

3.5

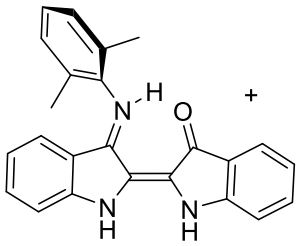

3.6

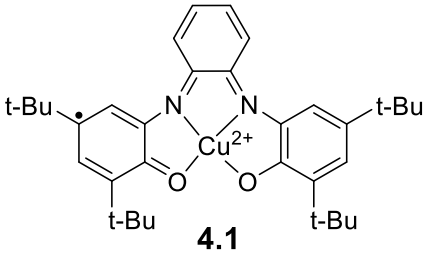

4.1

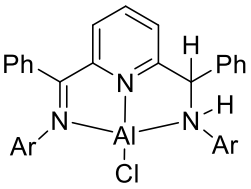

4.2

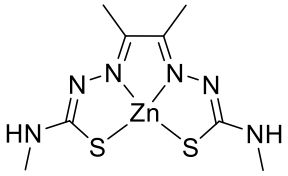

4.3

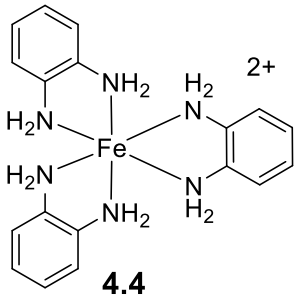

4.4

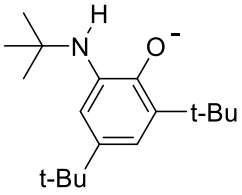

4.5

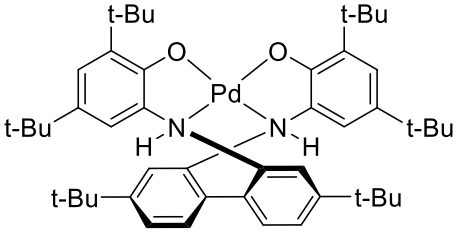

4.6a

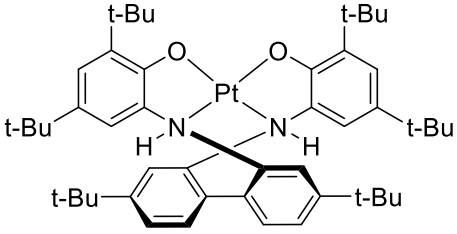

4.6b

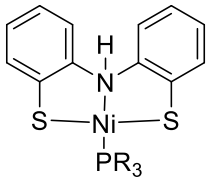

4.7

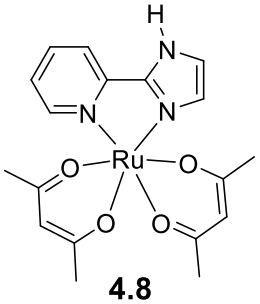

4.8

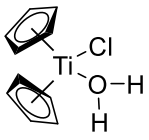

4.9

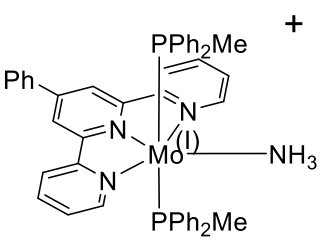

4.10

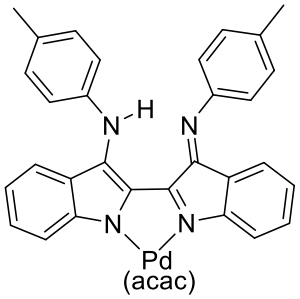

H4.11

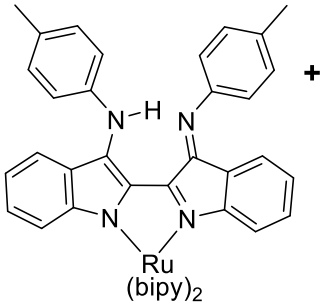

H4.12^{+}

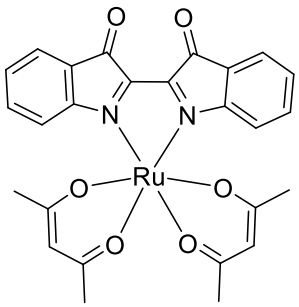

5.1

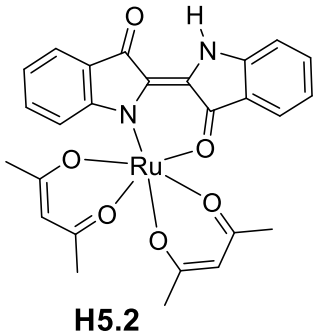

H5.2

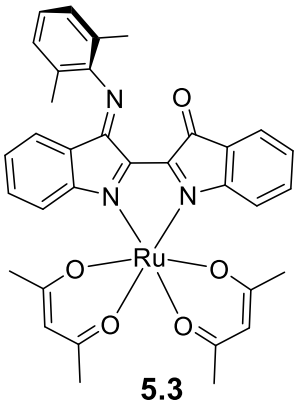

5.3

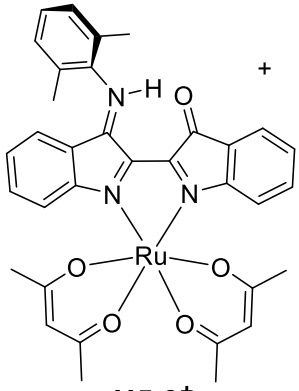

H5.3^{+}

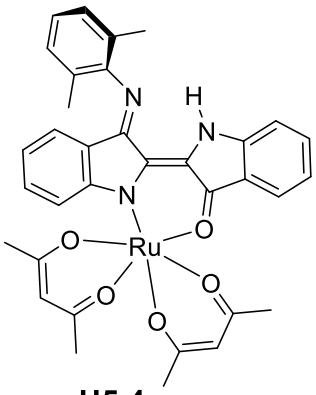

H5.4

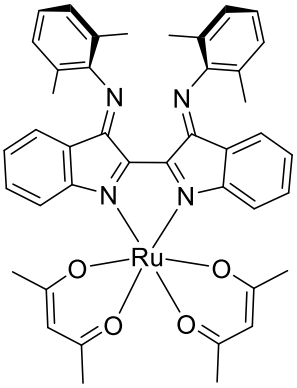

5.5

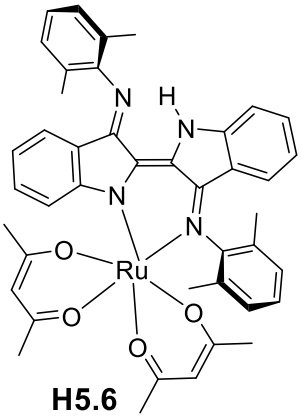

H5.6

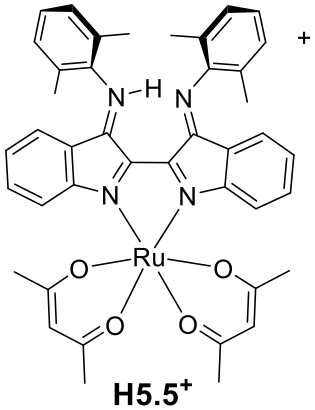

H5.5^{+}

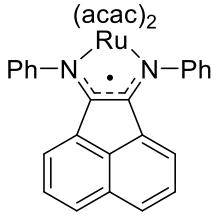

5.7

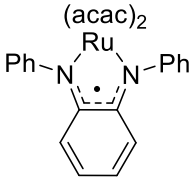

5.8

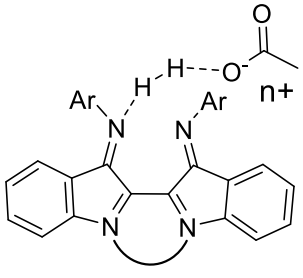

6.1

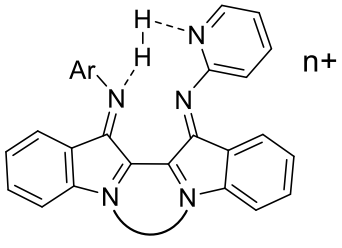

6.2

List of Abbreviations

A	absorbance
Å	angstroms
acac	acetylacetonate
Ar	aromatic ring
br	broad
bipy	2,2'-bipyridyl
^{o}C	degrees Celsius
ca.	circa/approximately
CV	cyclic voltammetry
Cp	cyclopentadienyl
DABCO	1,4-diazabisbicyclo[2.2.2]octane]
dcm	dichloromethane
DMP	2,6-dimethylphenyl
d	doublet
δ	chemical shift (ppm)
Δ	reflux
E_{cell}	electrode potential
$E_{1/2}$	half wave potential
EPR	electron paramagnetic resonance
ESI	electrospray ionization
Et	ethyl
e^{-}	electron
ε	molar extinction coefficient
Fc	ferrocene
Fc^{+}	ferrocenium
hfac	1,1,1,5,5,5-hexafluoroacetylacetonate
HOMO	highest occupied molecular orbital
HRMS	high resolution mass spectrometry
Hz	hertz
IUPAC	International Union of Pure and Applied Chemistry
FT-IR	Fourier transformed infrared spectroscopy
J	coupling constant (Hz)
K	Kelvin
L	ligand
LUMO	lowest unoccupied molecular orbital
λ	wavelength
λ_{max}	wavelength of maximum absorbance
m	multiplet
M	molar
Me	methyl
MeCN	acetonitrile
MHz	megahertz
Mindigo	indigo monoimine
mol	mole
mp	melting point

MS	mass spectrometry
mV	millivolt
m/z	mass per charge unit
μA	microamps
NH	nitrogen-hydrogen bond
NacNac	diketimine
NEt_3	triethylamine
Nindigo	indigo diimine
NIR	near-infrared
nm	nanometer
NMR	nuclear magnetic resonance
Ph	phenyl
ppm	parts per million
pTol	4-methylphenyl
q	quartet
RAL	redox-active ligand
s	singlet
t	triplet
T	temperature
THF	tetrahydrofuran
UV-Vis-NIR	ultraviolet-visible-near infrared spectroscopy
V	volt
vs.	versus
XAS	x-ray absorption spectroscopy

Acknowledgments

I would first like to thank Dr. Robin G. Hicks for being a wonderful supervisor and mentor. He gave me substantial intellectual independence while regularly being there to encourage and instruct me during my path towards becoming a physical inorganic chemist. I would also like to graciously thank the wonderful teaching staff. In particular, Dave Berry and Kelli Fawkes have been the best teaching supervisors I could ever ask for.

I would like to thank the many Hicks group members – past, present, and future. In particular, Simon Oakley, Graeme Nawn, and Emma Davy for laying the groundwork for all of the work in this dissertation; Emma, Genny Boice, and Corey Sanz for their patience when I was incompetent, and for being great friends and colleagues; Nicholas Richard for the many wing nights and Kickstart™ breaks which kept me sane; honorary member Aiko Kurimoto for being my little Japanese big sister; Hye Jin (Erica) Hong who has been with me in the Hicks group since the beginning; Shaun MacLean for the many insightful conversations about computational chemistry, coördination chemistry, and for teaching me enough Maple to fit my data in Chapter 5; Tianyi Wang for being a great labmate and friend; Koichi Yatsuzuka for giving me someone to finally talk to about Nindigo coordination chemistry; the 2.5 cm diameter column for purifying nearly every compound that I've made; all of the many competent undergraduate students that I was able to supervise – especially Maria Walker who contributed to Chapter 3; and whomever gains a passion for Mindigo and Nindigo.

I would like to acknowledge all of the staff in the chemistry department. I'd especially like to thank Chris Barr for keeping the NMR facility running well, being tolerant of me when I spill my dyes and break the machines, and for talking me through

much of the NMR interpretation of chapter 5. I would like to thank the chemistry secretaries past and present for faithfully reminding me to sign up for classes, renew my student visa, apply for funding, etc. I would not have made it without them. I would also like to thank professors Dave Berg, Neil Burford, Natia Frank, Scott McIndoe, and Lisa Rosenburg for their valuable instruction and feedback about research and department function.

I would also like to acknowledge the members of UBC who contributed to this dissertation. Firstly, Dr. Pierre Kennepohl and his graduate student Weiying He recorded the EPR spectra in chapter 4. Dr. Brian O. Patrick collected the data for every crystal structure in this dissertation, and was responsive when I had troubles solving any structures.

Lastly, I have to thank my family and friends for supporting me the last six years. I cannot thank enough the lifelong friends I've gained in Victoria, especially my church family at Victoria (Pacific Rim) Alliance Church. You are my anchor in the storm. And finally, my parents and siblings have always supported me despite the physical and emotional distance. I can't thank you enough.

Chapter 1 Introduction and Background

1.1 Redox-Active Ligands

The field of coordination chemistry requires an understanding of the metal's coordination sphere: the ligands, counterions, and possible interactions of the complex with other molecules. Early coordination complexes like the classical "Werner compounds" (**1.1** for instance)[1] clearly demonstrate that a metal's oxidation state, ligand connectivity, and symmetry play a large role in the properties of the given compound. These fundamental properties have been explored extensively, and the pursuit of these compounds has led to several applications of coordination chemistry. While very simple salts like **1.1** are at times usefully reactive, designing the coordination sphere of these systems has led to improvements and novel reactions from high-tech catalysts. For instance, although propylene can be polymerized with early transition metal-chloro complexes, the properties of the resultant plastics are improved and controlled through ligand design such as in complex **1.2**. Furthermore, many reactions such as alkene metathesis are drastically improved with intricately designed catalysts such as **1.3**.[2]

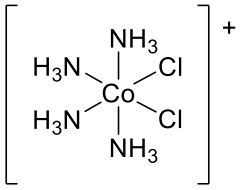

1.1

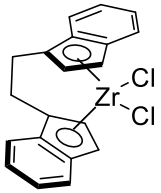

1.2

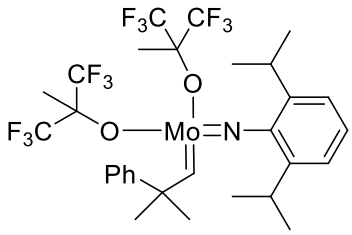

1.3

Ligands in coordination chemistry are generally thought of as having a supporting role while the metal has the interesting properties. From a simplistic point of view, the role of ancillary ligands is to modify metal-centered properties: Lewis acidity, redox potentials,

color, magnetism, and the structure itself.[3] For many systems, this simplification is useful. However, modern coordination chemistry has increasingly looked to multifunctional ligands that are responsive to protons, electrons, or other atoms and molecules.[4]

One important property of transition metal complexes is the metal center's ability to be oxidized and reduced by one or more electron. Indeed, knowledge of the metal's oxidation state is a critical part of the understanding of a coordination complex's properties. Oxidation state is a model for counting electrons and accounting for charge in a given system. According to IUPAC, a metal's oxidation state is "the charge of [an] atom after ionic approximation of its heteronuclear bonds".[5] Changes in oxidation state can lead to changes in a multitude of properties without changes in connectivity. Electronic spectra, magnetism, and reactivity are a few of many observable properties which are affected by a metal's oxidation state.[3]

Redox-active ligands (RAL) are a subclass of ligands that, when coordinated to a metal, can be isolated with different ligand-centered charge states without changes in atom connectivity. In this thesis, the term *charge state* represents the ionic approximation for a ligand (i.e. its charge after removal of the metal). An oxidation state is atomic[3] while charge state refers to part or whole of a moiety. **Figure 1.1** shows some well-studied RALs in their fully reduced state. Each ligand contains two or three donor atoms with two sp^2-carbons between them that form a 5-membered ring chelate upon coordination to a metal. In the states shown, they are dianionic. Each ligand can be oxidized by one electron, leading to stable, open-shell state ligands. Oxidation by two electrons leads to neutral ligands with two carbon-heteroatom double bonds.

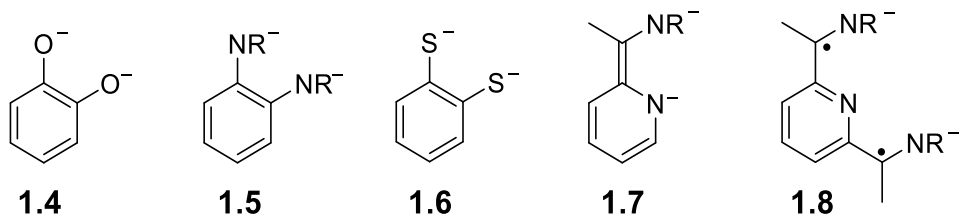

Figure 1.1 Some common redox-active ligands in their fully reduced charge state.

Because of the potential for different charge states and tendency of these ligands to form stable radicals, determination of the oxidation state of a central metal in complexes of redox-active ligands is often not trivial.[6] In order to use IUPAC's ionic approximation method to determine oxidation state (or conversely, a ligand's charge state), the ligand's charge state (or metal's oxidation state) must be determined experimentally.

The ambiguity of oxidation and charge states in complexes of RALs leads to RALs often being called (redox) "non-innocent". As originally defined by Jørgensen,[7] a ligand is *innocent* when it allows the oxidation state of a central atom to be defined. A *suspect* or non-innocent ligand is a ligand that prevents the unambiguous determination of the oxidation state of a central atom. Consider the species in **Figure 1.2** that demonstrates the series of possible charge states of an alpha-diimine ligand.[8] **1.9** shows two localized carbon-nitrogen double bonds. **1.9''** conversely contains a localized carbon-carbon double bond. The radical state **1.9'** is a delocalized structure with partial single and double bond character within the chelate. [9] **1.9, 1.9'**, and **1.9''** only differ in where the electrons reside: ligand or metal. It is often not obvious which electronic structure is possible or dominant *in reality*. Therefore, the oxidation state is ambiguous on paper.

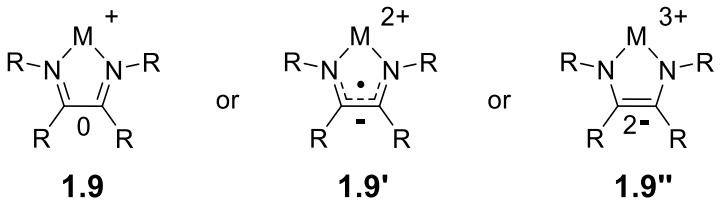

1.9 **1.9'** **1.9"**

Figure 1.2 Potential charge states of α-diimine ligands.

When considering the oxidation and charge states of complexes, there are four different levels of ambiguity. Firstly, in the case that the metal is redox innocent, only one "resonance form" is realistic, which is most commonly the case with alkali, alkaline earth, main group atoms, zinc(II), or those metals that are in their group oxidation state that require the use of core electrons to change in oxidation state. In this case, the ligand's charge state is unambiguous.

A second case exists where a change in the metal oxidation state is accessible but is clearly distinct from a change in ligand oxidation states. The oxidation state is ambiguous by simple electron counting such as Lewis structures, but can be determined, in principle, through the physical methods mentioned below. Such is the case for **1.12**, **1.13** (see below), and all of the compounds investigated in Chapters 2 and 3. In this case, the ligand is not considered "redox non-innocent" since the oxidation state of the metal can be readily defined.

In some complexes, multiple oxidation and charge state combinations are possible. In some instances, these combinations may be able to interconvert between one another reversibly. The most notable class of compounds that demonstrates this property is based upon cobalt bis(dioxolene) complexes such as the one shown in **Figure 1.3**. The catecholate ligand in **1.10** reversibly reduces the metal to form **1.10'**. The change in oxidation state, in turn, leads to a change from low spin to high spin. This change in

oxidation/charge state is a reversible, temperature-dependent equilibrium termed valence tautomerism.[10]

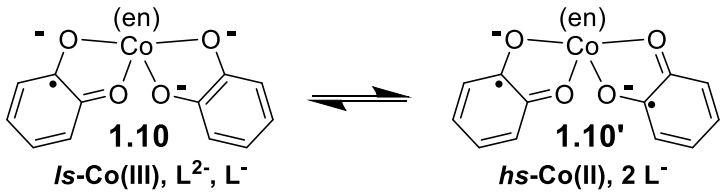

Figure 1.3 Valence tautomerism of a cobalt dioxolene complex.

Finally, cases exist where the oxidation state is truly ambiguous. Such is the case of **1.11** in **Figure 1.4**: the C_2H_4 ligand is somewhere in the continuum between alkene and metallocyclopropane.[11-12] The ligand is truly "non-innocent" as the oxidation state is ambiguous. In this particular case, however, the alkene is not a redox-active ligand since it cannot be isolated with different ligand charge states. Instead, the bonding situation leads to the ambiguity in oxidation state.

Figure 1.4 Ambiguity of the oxidation state of titanium in compound **1.11**.

Through a battery of physical techniques, attributes of a ligand's charge state and a metal's oxidation state can be pieced together to form a picture of the electronic structure of the complex. Although individual experiments may provide evidence that appears to support an assignment of oxidation and charge state, generally, many techniques must be used to create a complete picture. Techniques to assess the electronic structure of complexes include:

- Electron paramagnetic resonance (EPR)
- Electronic spectroscopy (UV-Vis-NIR)
- In silico modeling
- Infrared spectroscopy (IR)
- Magnetic susceptibility
- Mössbauer spectroscopy
- Nuclear magnetic resonance spectroscopy (NMR)
- Spectroelectrochemistry
- X-ray absorption spectroscopy (XAS)

X-ray crystallography is particularly useful in giving a picture of the coordination sphere as a whole. Complexes of RALs can often be compared directly to model compounds in which the metal has no RAL's bonded or which a RAL's charge state can be unambiguously assigned. By changing the population of bonding or antibonding orbitals, the metal-ligand bonds or ligand π-bonds can change in bond order. Unambiguous assignment of charge states can arise from the presence or lack of double bond character as measured by bond lengths. For instance, in **Figure 1.2**, **1.9** contains short, C-N double bonds and a longer C-C single bond. The reduced radical form **1.9'** contains a delocalized partial double bond. **1.9''** contains long C-N single bonds and a shorter C-C double bond. Thus the bond lengths in this series can provide evidence toward a specific charge state.

Predicting oxidation and charge states when complexes of redox-active ligands undergo chemical transformations is likewise not trivial. For instance, complexes of RALs can undergo "redox-induced charge transfer", whereby a redox reaction of a complex leads to the metal or ligand providing the extra oxidizing or reducing equivalent.[13] **Scheme 1.1**

shows the oxidation of a nickel complex that leads to the net reduction of the metal.[14] Oxidation of one radical alpha-diimine ligand in **1.12** (an example of **1.9'**) leads to an oxidation of the other ligand by the nickel (II) in **1.12**$^{+}$.

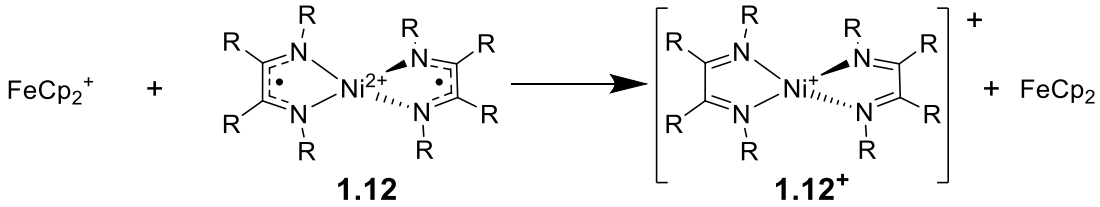

Scheme 1.1 Oxidation induced charge transfer in a nickel alpha-diimine complex.

Competing effects can render two oxidation state assignments equally likely, as demonstrated in **Figure 1.5**. This figure shows one example of a very early series of RAL complexes containing dithiolene ligands. The ligands became known for their delocalized electronic structure, and assignment of ligand charge states in this class of compounds was controversial.[15] **1.13** is a diamagnetic, square planar structure. Resonance form **1.13''**, that contains one fully oxidized ligand and one fully reduced ligand, was eliminated due to the ligands appearing totally symmetric by X-ray crystallography. Structures **1.13** (d^6) and **1.13'''** (d^{10}) initially appear reasonable since they do not contain radical ligands and would be expected to be diamagnetic. However, after a number of experiments including crystallography, EPR, XAS, magnetic susceptibility, and analysis of different redox states, resonance structure **1.13'**, that contains two delocalized, strongly antiferromagnetically coupled radical ligands, was eventually the electronic structure assignment that was agreed upon.[16]

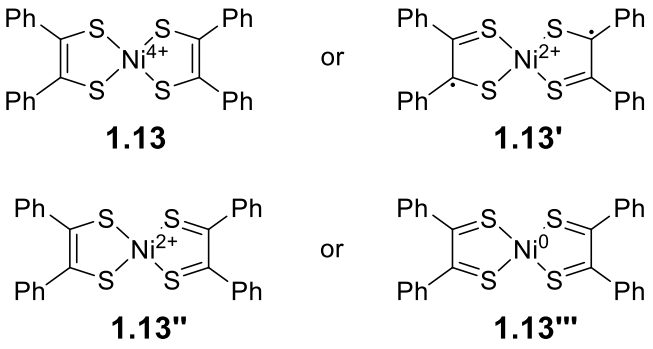

Figure 1.5 Potential oxidation and charge states of a neutral nickel dithiolene complex.

While esoteric debates of electronic structures of complexes are interesting in their own right, the study of the redox-active ligand complexes has the potential to play real and impactful roles in everyday life. The interesting electronic structure of the complexes of RALs can lead to novel and useful reactivity. RALs may act as electron reservoirs[17-18] by giving and/or receiving electrons. Furthermore, if a metal and ligand can be oxidized or reduced by one electron each, the potential for net two-electron chemistry can be realized.

The reactivity of the complexes of RALs is highlighted in some biological systems.[19] For instance, galactose oxidase contains a phenoxyl type radical (further described in Chapter 4.1). Another notable, intensely studied example from biology is the so-called "Compound I", an intermediate in the aerobic alkane oxidation reaction carried out by cytochrome P450.[20] As shown in **Scheme 1.2**, oxidation of both the iron center and the porphyrin/thiolate ligands occurs through dioxygen activation by this protein.[21-22] In this case, the electron-rich ligand gives up its electron to form a potent oxidant. The resultant iron (IV) oxo species is able to abstract hydrogen atoms of isolated hydrocarbons such as fatty acids. The net reaction is an oxidation of a C-H to a C-OH which is a net two-electron oxidation; one electron goes to the metal and one to the ligand.

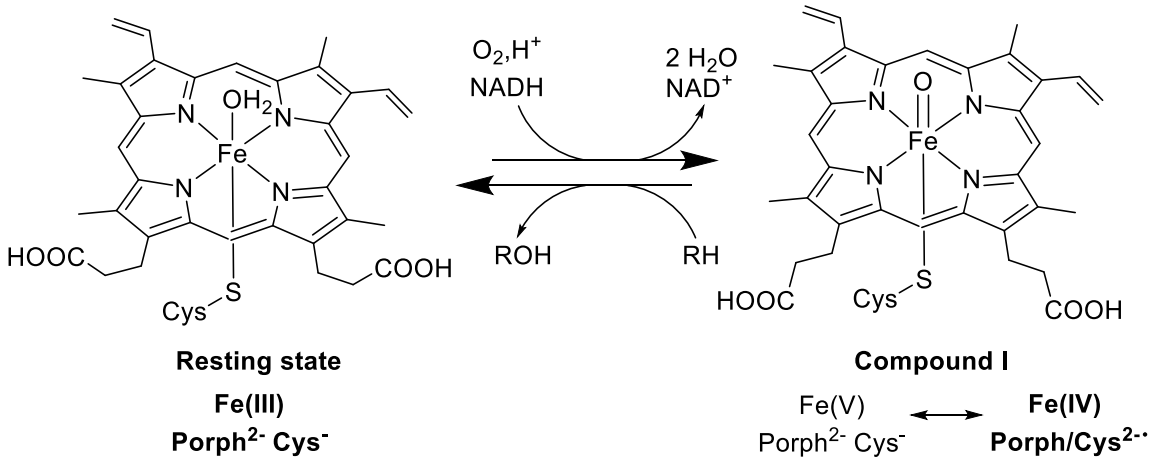

Scheme 1.2 Truncated cycle for the oxidation of alkanes with a Cytochrome P450 active site.

In the past 10 years, much effort has been put forth toward replacing catalysts using expensive, toxic coinage metals.[23] One possible route combines redox-active ligands with base metals. The single electron transfer reactivity prevalent in complexes of these transition metals is combined with electron reservoir ligands to "confer nobility" on base metals.[24] For example, the elementary steps to cross-coupling using the redox activity of the ligand have been demonstrated: (pseudo-)oxidative addition with a zirconium (IV) center,[25] reductive elimination of biphenyl[26] and aryl diazenes,[27-28] and even a full Negishi reaction using complex **1.14**.[29-30] Unfortunately, these exciting proofs-of-principle are not yet practical due to low turn-over number. In other examples, hydrogenation[31] and hydrosilation[32] of alkenes was accomplished using pyridine diimine complexes such as **1.15**. Radical α-diimine ligands such as **1.16** have been invoked in the catalytic cycle of hydrosilylation[33] and the hydroboration of alkenes[34] to commercially relevant products. Several homogeneous catalysts designed by the Sakai group such as **1.17** have shown proton-coupled reduction of the ligand leads to efficient electrocatalytic hydrogen evolution in water.[35-37] These examples are only a few of many that clearly demonstrate

that there are several useful systems emerging for the production of consumer products using RALs.

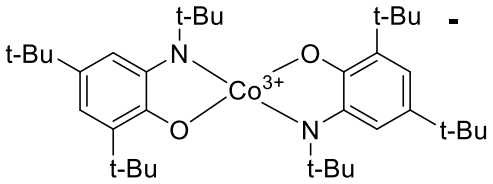

1.14

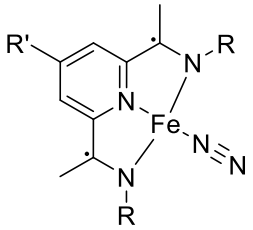

1.15

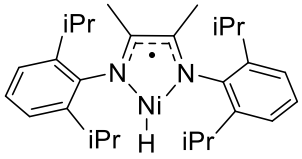

1.16

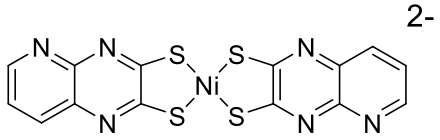

1.17

RALs also have the potential to impact materials applications. Complexes of dithiolene ligands such as **1.18** have recently been investigated for use as NIR dyes, solar energy converters,[38] and for semiconductor applications.[39-40] Several examples also use radical ligands for their single-molecule magnetic possibilities.[41] Use of a bridging RALs such as hexa-aminobenzene or chloranilic acid has led to metal organic frameworks such as **1.19** that exhibit metallic[42] and semimetallic[43] conductivity and ferromagnetism.[44-45] RALs have also been shown to enable metal organic frameworks to withstand oxidation reactions without loss of structure.[46]

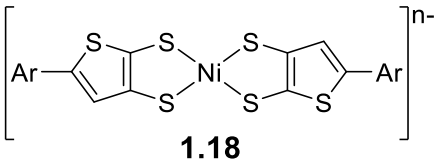

1.18

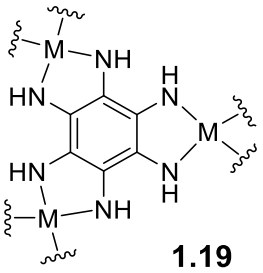

1.19

1.2 Coordination Chemistry of Indigo and Nindigo

Indigo **1.20** is a well-known blue dye which has been used as a colorant since antiquity. Although initially derived from several plants (especially *indigofera tinctoria*[47]), indigo is now produced synthetically. Kilotons of indigo are synthesized each year. Most notably, the colorant is used in blue jeans which is expected to be a $143 billion USD industry in 2019.[48] The source of the extraordinary color of indigo has been a long-term interest since the original synthesis by Adolf von Baeyer in 1882.[49-50] Indigo absorbs at relatively low energy for its small molecular weight and small number of conjugated units. The blue color of indigo is caused by the cross conjugation of donor NH and acceptor C=O in the indigo core, termed the "H-Chromophore".[51] When processing indigo for use in dyeing, the molecule is chemically reduced to a colorless "leuco" form, **1.21**.[52] While indigo is completely insoluble in almost every solvent, reduction to the leuco form makes indigo water soluble. The color is then regenerated by aerobic oxidation back to indigo. Indigo can also be oxidized by two electrons and two protons to form the red "dehydro" form, **1.22**.[53] **Scheme 1.3** highlights the structural changes associated with reduction and oxidation of indigo.

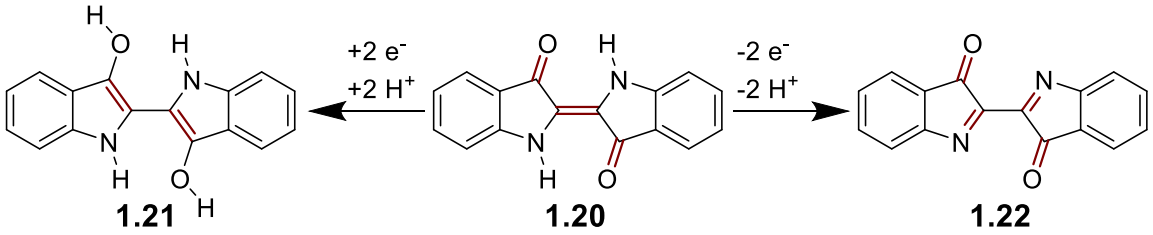

Scheme 1.3 Reduction and oxidation of indigo **1.20**.

Up until very recently the coordination chemistry of indigo remained poorly explored. Early in the twentieth century, indigo was claimed to form metal complexes with

zinc,[54] copper,[55] and iron,[56] but the resultant structures remained poorly defined. More recently, complexes of gold,[57] palladium, platinum (**1.23**),[58-60] zinc, copper,[61] and rhenium (**1.24**)[62] showed the capacity of indigo derivatives to form mononuclear and bridged binuclear chelates, most of which absorbed strongly into the near-infrared. Despite these results, there were no indications that indigo could act as a redox-active ligand.

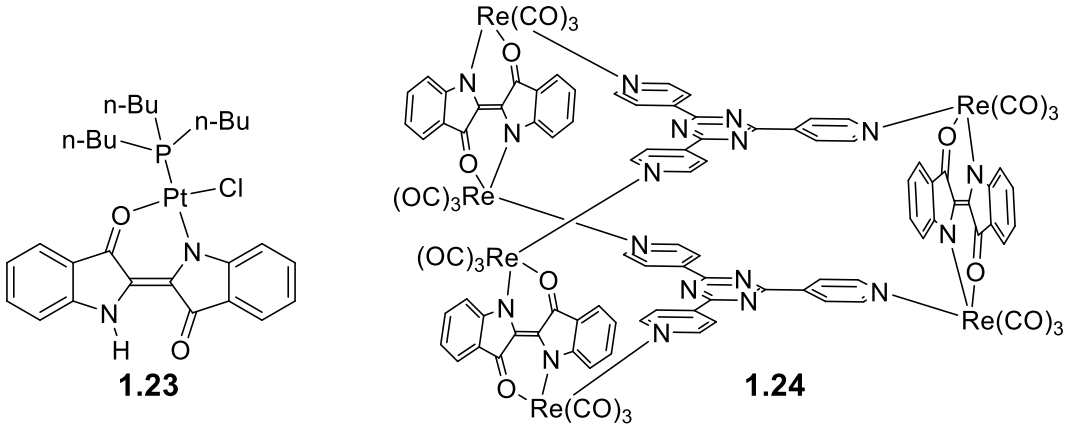

In 2010, the Hicks group modified the indigo core by replacing the carbonyl groups with arylimines as in **Scheme 1.4**.[63] These "Nindigos" such as the 4-methylphenyl (pTol) substituted **1.25**, 2,6-dimethylphenyl substituted (DMP) **1.26,** and many others, retained the intense color of indigo (purple or blue), but became significantly more soluble in organic solvents. Like indigo, Nindigo can be oxidized by two protons and electrons to form a "dehydro" structure **1.27** (**Scheme 1.5**).

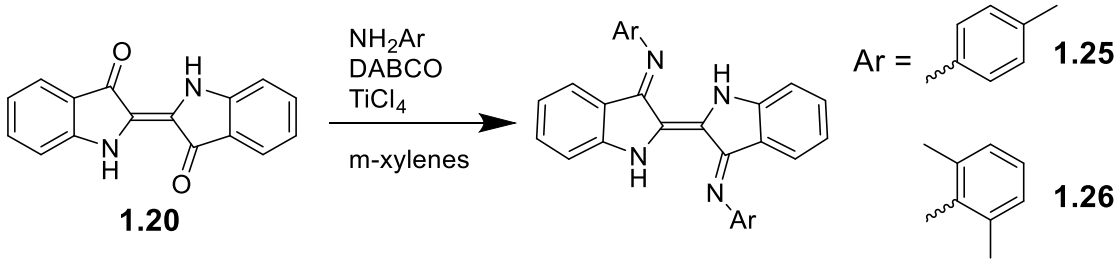

Scheme 1.4 Synthesis of Nindigo.

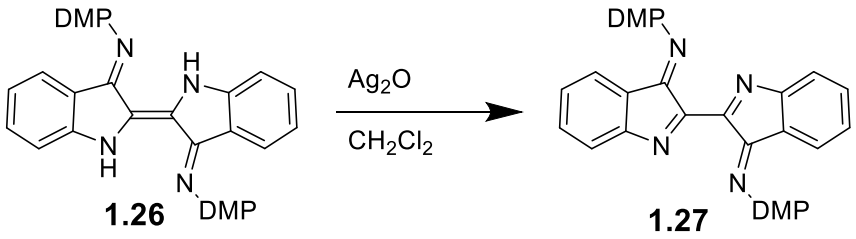

Scheme 1.5 Oxidation of Nindigo **1.26**.

Initially, complexes of palladium including **1.28** were synthesized by the Hicks group.[64] These complexes are near-infrared dyes and show many reversible redox events by cyclic voltammetry as demonstrated in **Figure 1.6**. Up to five ligand charge states (from neutral to tetraanionic) could be assigned.

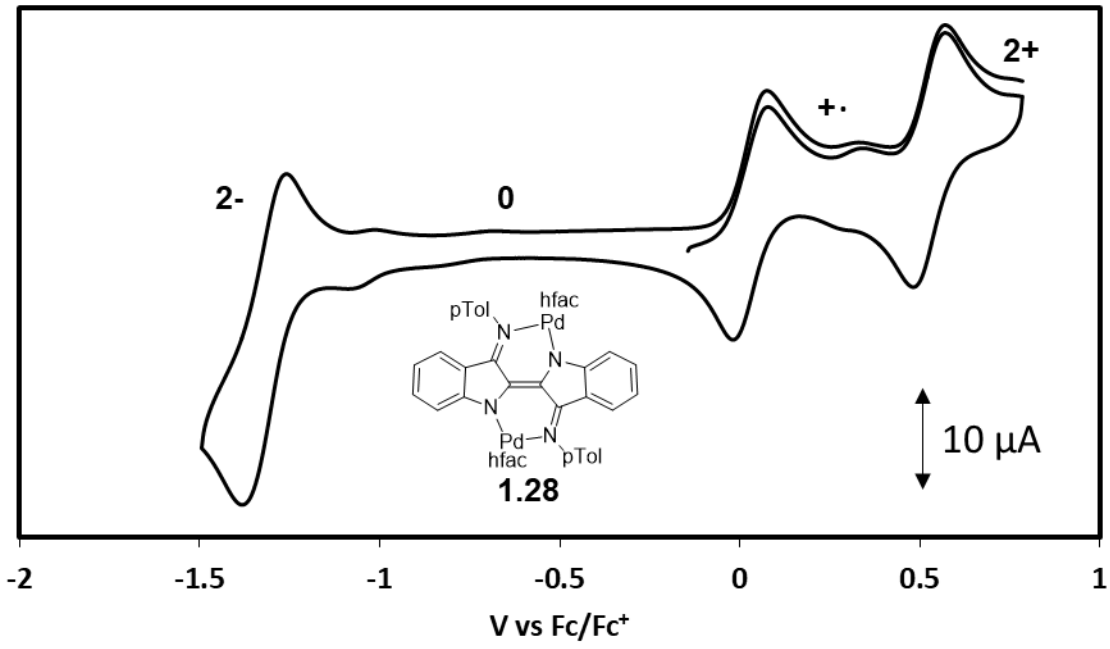

Figure 1.6 Cyclic voltammogram of **1.28** in dichloromethane.

Following this report, boron difluoride compounds were synthesized.[65] Using the mono-BF_2 chelate compound **1.29** that retains an open chelation site, palladium complexes[66] were synthesized and found to be similarly redox-active, near-infrared dyes.

The redox activity of bis-ruthenium complex **1.30**, which is isolated with a fully oxidized "dehydro"-Nindigo ligand, was explored via spectroelectrochemistry.[67-68] Three-coordinate cobalt complex **1.31** was synthesized, and several related complexes were isolated with Nindigo in its monoanionic (radical), dianionic, trianionic (radical), and tetraanionic ligand charge states.[69-70] These cobalt complexes showed that the five ligand charge states of Nindigo, including those that are organic radicals, are stable and isolable. In those examples where Nindigo is in its native charge state (dianionic), the complexes are also strong near-infrared dyes just as the indigo complexes were.

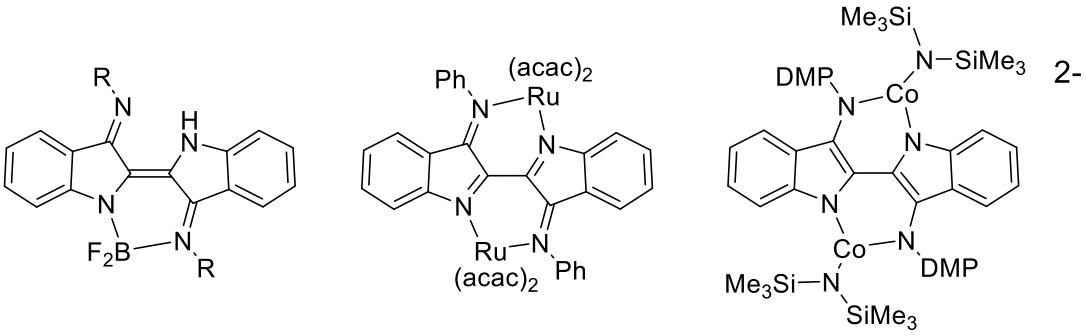

1.29 **1.30** **1.31**

Since the initial reports of Nindigo coordination chemistry, a resurgence of interest in the coordination chemistry of indigo has taken place. The hexa-rhenium carbonyl metalloprism **1.24**, which was published before the exploration of the coordination chemistry of Nindigo, was reinvestigated[71] to show that indigo is also a redox-active ligand. Mono- and binuclear ruthenium complexes with phenylazopyridine,[72] 2,2'-bipyridyl,[73] and acetylacetonate[74-75] ligands were synthesized. Comparison of the spectroelectrochemical results of these ruthenium complexes to computational results showed that each complex allows for multiple ligand charge states. Complexes of *trans*-indigo with two (bis-pentamethylcyclopentadienyl)lanthanide units[76] were isolated with 2-, 3-, and 4- ligand charge states, and their single molecule magnet behavior was investigated.

Occasionally, when forming a complex of indigo or Nindigo, *trans*- to *cis*-isomerization is observed upon coordination. These complexes are formed in acidic media (with free hexafluoroacetylacetone for **1.32**), basic media (with triethylamine for **1.33**), and reducing media (with decamethyl chromocene for **1.34**). Further development into the chemistry of these *cis*-Nindigo or indigo structures is difficult as the cause of isomerism is not explicitly known. As a result, whether a *cis*- or *trans*- structure will be isolated is not easy to predict. Like the *trans*-Nindigo complexes, these *cis*-Nindigo complexes absorb well into the near-infrared. The structures also show the presence of many ligand-centered redox events by cyclic voltammetry which will be discussed in subsequent chapters.

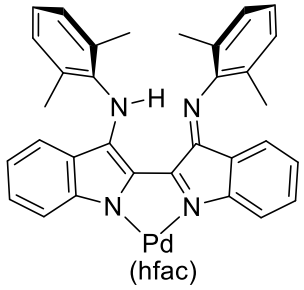

1.32

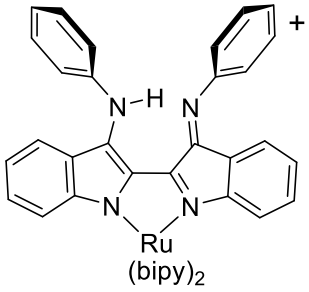

1.33

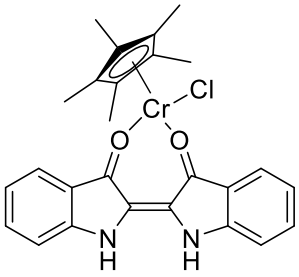

1.34

The formation of *cis*-Nindigo complexes creates an unusual γ-diimine(ate). Conjugated chelates that form 7-membered rings are incredibly rare. Although this sort of chelate is nearly unprecedented, one complex with *cis*-Nindigo (**1.35**) and two complexes with *cis*-indigo (**1.34** and **1.36)** have been obtained.[77-78] Furthermore, the potential formation of complexes by a γ-diimine moiety have been proposed as an avenue of exploration into redox-active ligands.[8] With tunable steric bulk from the arylimine moiety, these complexes could provide a good scaffold for low-coordinate complexes similar to the well-known β-diketiminate "NacNac" ligands.[79] Although the use of *cis*-Nindigo as a

γ-diimine ligand has yet to be realized except in one case, the goal of studying this unusual chelate led to the research presented in the following chapters.

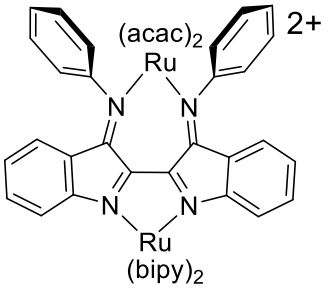

1.35

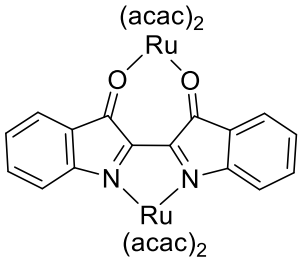

1.36

This *trans*- to *cis*- isomerism is further manifested in the reactions of Nindigo with Brønsted acids, as in **Scheme 1.6**. Protonation leads to a *trans*-to-*cis* isomerization of the central double bond to **1.37**, termed protoisomerization.[80-81] This isomerization is reversed upon reaction with a base.

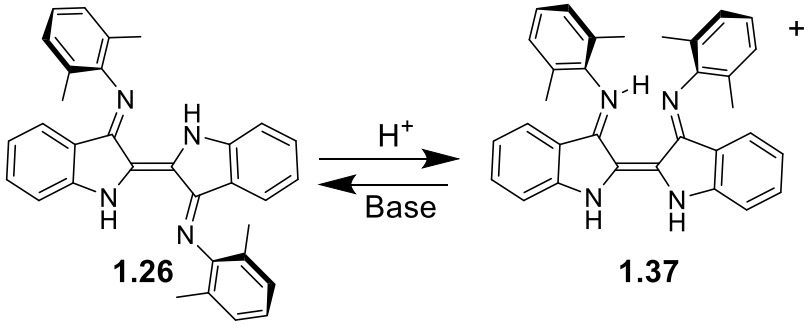

1.26 **1.37**

Scheme 1.6 Protoisomerization of Nindigo.

1.3 Thesis Objectives

As the topic of redox-active ligands continues to be explored, it will be increasingly important to fully understand the interplay of metal and ligand reactivity. The number of redox-active ligands that are studied in any depth is still small, and most studies are tweaks of a few "privileged" ligands displayed in **Figure 1.1**. In order to broaden the field, it is necessary to explore new ligands. The understanding of the coordination chemistry of

ligands based upon the indigo framework is still limited. Exploration of the coordination chemistry of Nindigo and indigo-monoimine will provide the groundwork for design of systems containing these ligands for use as dyes, catalysts, and materials. Furthermore, the systems targeted, summarized in **Figure 1.7**, serve to grow the understanding of redox-active ligands as a whole.

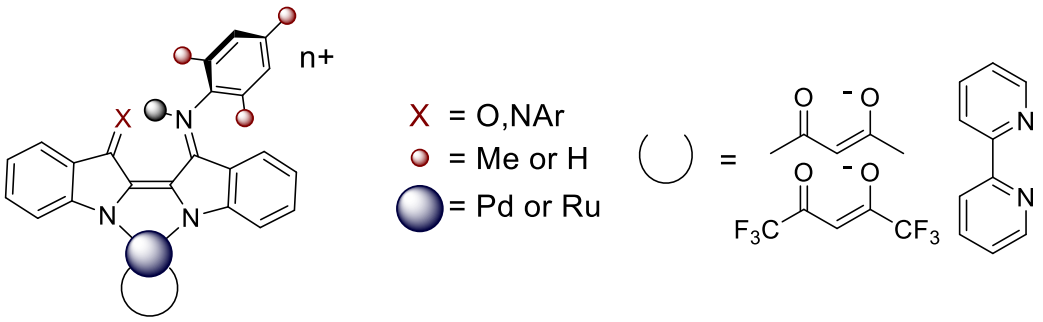

Figure 1.7 Complexes explored in this dissertation.

Two major concepts are targeted in this thesis. In chapters two and three, the role of ancillary ligands on the electronic properties of the redox-active ligands are described. In Chapter 2, palladium complexes are synthesized to test the role of electron deficient vs. electron rich ancillary ligands. The role of the choice of arylimine substitution in determining electronic and electrochemical properties is also demonstrated.

Chapter 3 presents the first complexes of indigo monoimine. In addition to developing the coordination chemistry of this ligand, the properties of *cis*- and *trans*-indigo monoimine complexes are compared to their indigo and Nindigo counterparts. Additionally, the role played by the ligand ancillary to the redox active ligand to ligand-centered absorptions and redox properties is reinforced.

The second half of this thesis presents some of the first systematic studies of redox-active ligand centered proton-coupled electron transfer. Chapter 4 begins the investigations

of *cis*-Nindigo complexes as electron and proton reservoirs. The complexes studied are subjected to a battery of electrochemical experiments in order to construct potential-pK_a (Pourbaix) diagrams which give estimations of the N-H bond strengths. The first complexes of *cis*-Nindigo in different charge states are also isolated. Chapter 5 presents the synthesis of ruthenium bisacetylacetonate complexes of *cis*-indigo mono and diimines. The properties of the complexes with protonated and deprotonated ligands are described. The electrochemistry of both states of protonation are used to determine the NH bond strengths of many different charge/oxidation states of the complexes.

Chapter 2 Electronic Effects of Ancillary Ligands in Nindigo Complexes with Palladium Diketonates

2.1 Introduction

The electronic structures of redox-active ligand complexes depend primarily on the metal-RAL pair. In a series of related complexes, this electronic structure can be perturbed through changes of the ligand's functional groups[82-83] or by changing which metal is coordinated.[6,84] In many cases, the metal has other, redox-inactive "spectator" ligands. While these ancillary ligands are known to play large roles in modifying metal-centered properties, it is not as well understood how these ancillary ligands can affect the properties of the redox-active ligand.

The Hicks group previously reported a series of Nindigo complexes containing boron difluoride and palladium hexafluoroacetylacetonate (hfac) chelates **1.28**,[64] **2.1**,[66] and **2.2**.[65] The redox activity and near infrared absorption of all of these complexes are nominally ligand centered. Replacement of Pd(hfac) substituents with one (**2.1**) and two (**2.2**) difluoroboron substituents made oxidations more difficult by around 400 mV per metal and makes reductions easier by around 200 mV per metal.

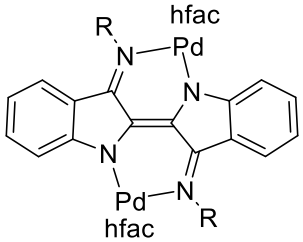

1.28

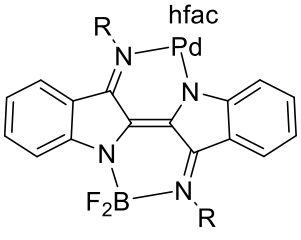

2.1

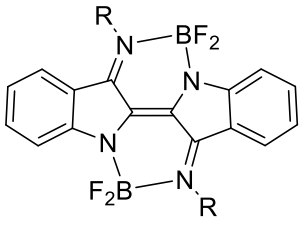

2.2

Palladium complexes of redox-active ligands are being researched as redox/radical substrate activators by acting as electron reservoirs.[85-89] This recent interest has prompted research to further the understanding of the role ancillary ligands can play in the spectral

and electrochemical properties of RAL-coordinated palladium complexes. In this chapter, the role of ancillary ligands, hexafluoroacetylacetonate (hfac) and acetylacetonate (acac), in influencing the physicochemical properties of palladium complexes of *trans*-NindigoBF_2 and *cis*-Nindigo are investigated.

2.2 Results and Discussion

Complexes with palladium (II) hexafluoroacetylacetonate (hfac) fragments **2.4b**,[66] **2.1a**, and **2.1b**[64] were previously reported. These complexes were formed by reaction of $Pd(hfac)_2$ with a Nindigo derivative (**1.25**) or BF_2-Nindigo adduct (**1.29**) in dichloromethane. We imagined an analogous reaction with palladium (II) acetylacetonate (acac) to make corresponding Nindigo Pd acac complexes. $Pd(acac)_2$ is less reactive to ligand displacement, so the reactions were carried out at elevated temperatures. **2.3a** and **2.3b** were synthesized by reaction of **1.29** with $Pd(acac)_2$ in refluxing toluene. The use of ethyl diisopropyl amine in the synthesis of **2.3b** led to an increase of yield from 16% to 67% while the corresponding attempt to prepare **2.3a** led to deposition of metallic palladium. Similarly, we attempted to synthesize (bis-palladium) complexes by reaction of Nindigo **1.25** and **1.26** with $Pd(acac)_2$. These reactions, even with excess palladium reagent, yielded primarily *cis*-mononuclear complexes **2.5** rather than their binuclear counterparts irrespective of the chosen Nindigo, **1.25** or **1.26**.

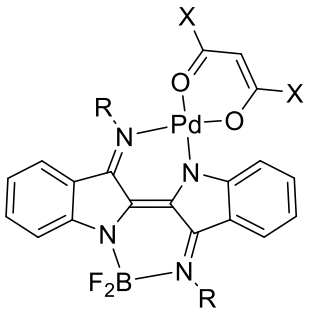

2.1 (X=CF_3)
2.3 (X=CH_3)

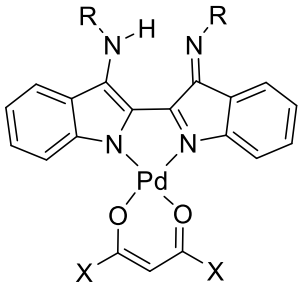

2.4 (X=CF_3)
2.5 (X=CH_3)

a. R=4-MePh (pTol)
b. R=2,6-Me_2Ph (DMP)

The isolation of **2.5a** indicated that *cis*-Nindigo complexes may be more prevalent than originally thought. Previous syntheses of palladium complexes yielded *cis*-mononuclear structures only when R contained bulky arylimine groups (i.e. **2.4b**), and yielded binuclear structures with all other Nindigos (i.e. **1.28**). **2.4a** was synthesized by slow addition of $Pd(hfac)_2$ to Nindigo **1.25** in an open flask. In this case, addition of a second equivalent gave no further reaction. If $Pd(hfac)_2$ is added quickly, bimetallic complex **1.28** was obtained. If the flask was stoppered and only briefly stirred before evaporation of solvent, the ^1H NMR of the crude reaction mixture indicates a mixture of bis-palladium complex **1.28** and protonated *cis*-Nindigo. We suspect the protoisomerization of Nindigo[80] may play a role in the formation of these *cis*-Nindigo structures by forming protonated Nindigo salts with the acidic hexafluoroacetylacetone by-product as shown in **Scheme 2.1**. However, this observation does not necessarily explain the reactivity of $Pd(acac)_2$, as acetylacetone does not protonate Nindigo appreciably at room temperature. Despite the absence of observed protoisomerism, no *trans*-complexes can be isolated which contain Pd(acac) fragments. Regardless, reaction in acidic media seems to encourage the formation of these *cis*-complexes, and the control of formation of *cis*- or *trans*- isomers is clearly possible.

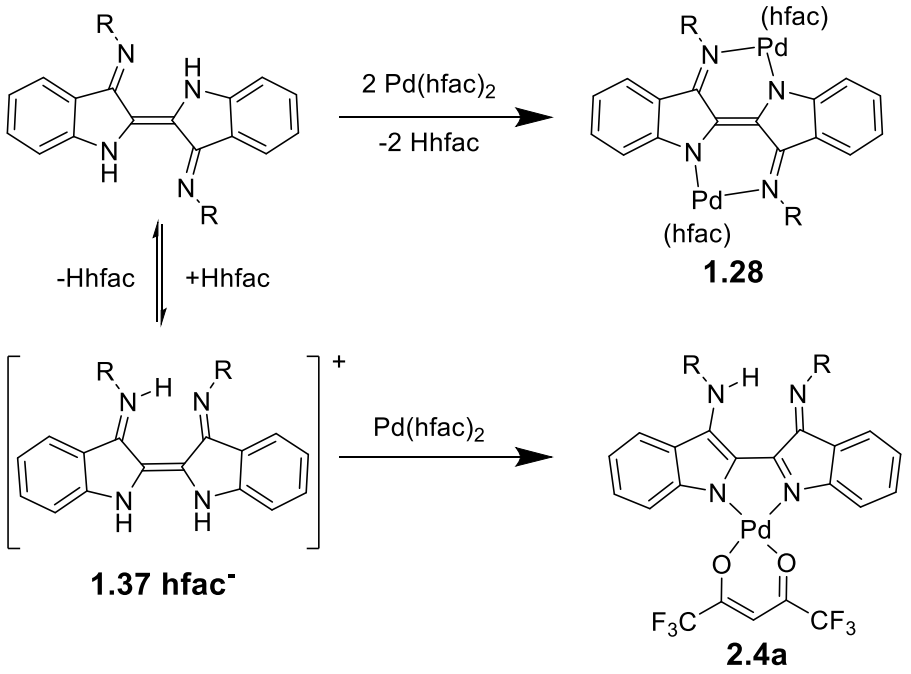

Scheme 2.1 Synthesis of **2.4a** (R=*para*-Toluyl).

The redox properties of these new complexes were probed by cyclic voltammetry and are summarized along with data for related species in **Table 2.1**. Within the subset of compounds in which the Nindigo ligand is bound to Pd and B, compounds **2.1a**, **2.1b**, **2.3a**, and **2.3b** have two reversible oxidations. Hfac complexes **2.1a** and **2.1b** have one reversible reduction, while acac complexes **2.3a** and **2.3b** have two reversible reductions. All redox processes of acac complexes **2.3a** and **2.3b** were found at more negative potentials than the corresponding hfac complexes **2.1a** and **2.1b**. All of the redox potentials of acac complexes **2.3a** and **2.3b** shift to less positive voltages than hfac complexes **2.1a** and **2.1b** by 120 mV in each reduction and by 160-170 mV in oxidations. Changing the arylimine substituent from *para*-toluyl in **2.3a** to 2,6-dimethylphenyl in **2.3b** shows little change in potential to the reversible redox events.

Table 2.1 Electrochemical potentials for compounds compared in this chapter vs Fc/Fc^+ in dichloromethane

Compound	$E_{1/2,\ red}$	$E_{1/2,\ ox}$	E_{cell}[a]
2.1a[b]	-1.02, -1.26[d]	+0.44, +0.94	1.46
2.1b[b]	-1.02, -1.64[d]	+0.48, +0.93	1.53
2.3a	-1.15, -1.43	+0.28, +0.82	1.43
2.3b	-1.18, -1.80	+0.31, +0.86	1.49
2.4a	-1.10[d]	+0.17, +0.65	1.27
2.4b[c]	-1.36	+0.17, +0.65	1.53
2.5a	-1.16, -1.59[d]	+0.01, +0.50	1.17
2.5b	-1.37	+0.06, +0.65	1.43

[a]The difference of first oxidation and first reduction potentials. [b]From reference[66] [c]From reference[64] [d]Irreversible process; cathodic potential given.

For the *cis*-Nindigo-Pd complexes, compounds **2.4a**, **2.4b**, **2.5a**, and **2.5b** have two reversible or quasi-reversible oxidations and at least one quasi-reversible reduction. The oxidation potentials in these *cis*-Nindigo complexes appear to be more sensitive to a change in ancillary ligand. Compounds **2.5a** and **2.5b** shift to less positive potentials than **2.4a** and **2.4b** by over 100 mV compared to reduction potentials that only shift by 10 or 50 mV. On the other hand, the first reduction potentials appear to be sensitive to arylimine choice for **2.4** and **2.5**. Reduction potentials are lower by 210 mV from **2.5a** to **2.5b** and by 260 mV from **2.4a** to **2.4b**. Thus, both oxidation and reduction potentials can be modulated nearly independently. These modulations lead to large changes in E_{cell}, where hfac complexes have larger E_{cell} than acac complexes, and 2,6-dimethylphenyl-Nindigo complexes have larger E_{cell} than *para*-toluyl-Nindigo complexes.

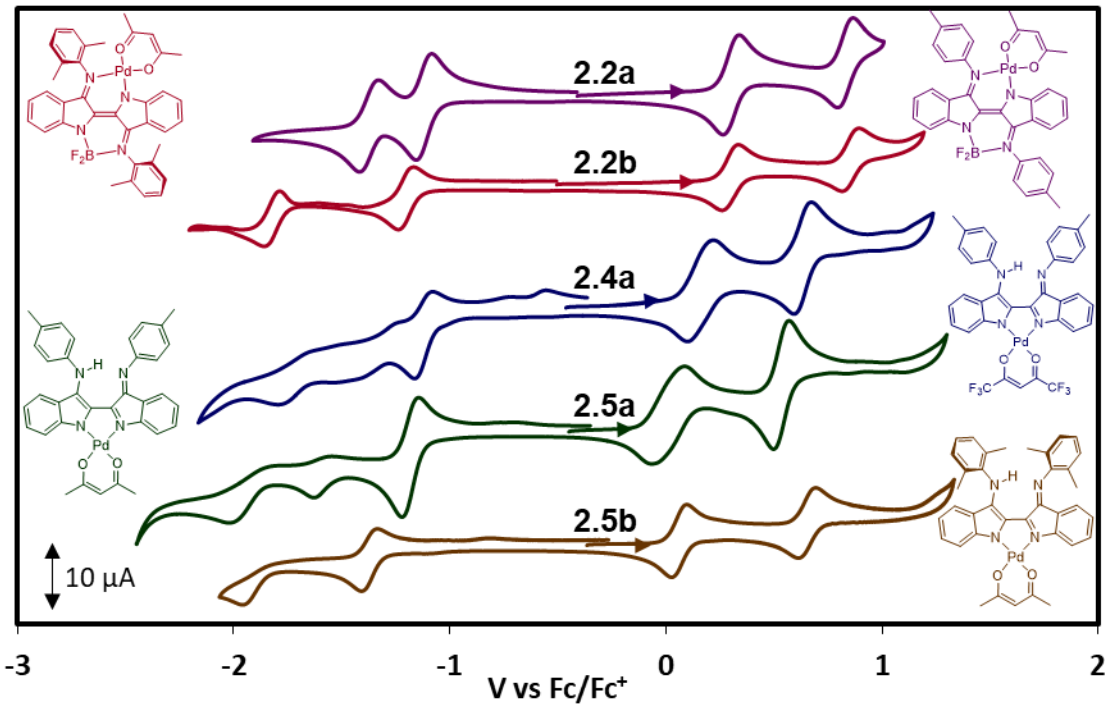

Figure 2.1 Cyclic voltammetry (dichloromethane) of **2.2a**, **2.2b**, **2.4a**, **2.5a**, and **2.5b** at 100 mV/s scan rate, 0.1 M NBu_4BF_4 electrolyte, 1 mM analyte.

The trends seen in E_{cell} values, which are estimates of the HOMO-LUMO gap, are mirrored in the electronic spectra as shown in **Figure 2.2** and tabulated in **Table 2.2**. The absorption maxima for acac complexes **2.3a** and **2.3b** are bathochromically shifted by 200 cm^{-1} from hfac complexes **2.1a** and **2.1b**. Likewise, acac complexes of *cis*-Nindigo **2.5a** and **2.5b** are bathochromically shifted by 600 and 400 cm^{-1} from **2.4a** and **2.4b** respectively.

In the *trans*-Nindigo-BF_2 Pd complexes, absorption maxima did not change with different arylimine substituents. Complexes of *cis*-Nindigo containing *para*-toluyl substituents **2.4a** and **2.5a** are bathochromically shifted from their corresponding 2,6-dimethylphenyl derivatives by 400 cm^{-1} for **2.4b** and 600 cm^{-1} **2.5b** respectively. In this series of complexes, absorption varies by 72 nm (990 cm^{-1}). These observations reinforce

that aryl imines play almost no role in the electronic structure of *trans*-Nindigo complexes, but play a larger role in complexes of *cis*-Nindigo.

Table 2.2 Electronic spectra, ca. 10^{-5} M in dichloromethane.

Compound	λ_{max} (nm)	$1/\lambda_{max}$ (cm^{-1})	$\varepsilon \times 10^3$ (M^{-1} cm^{-1})
2.1a[a]	820	12,200	19.9
2.1b[a]	819	12,200	17.5
2.3a	833	12,000	18.5
2.3b	833	12,000	16.0
2.4a	849	11,800	14.0
2.4b[b]	818	12,200	15.2
2.5a	890	11,200	13.0
2.5b	848	11,800	16.0

[a]*From reference*[64] [b]*From reference*[65]

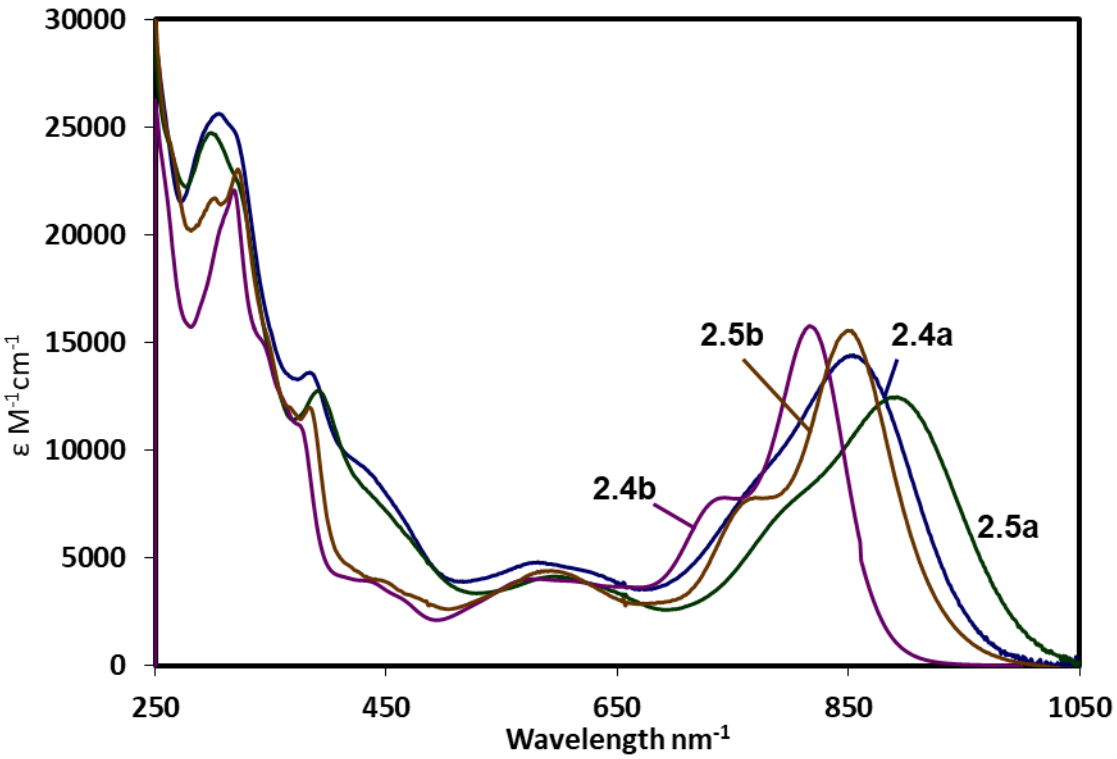

Figure 2.2 Electronic spectra of **2.4a**, **2.4b**, **2.5a** and **2.5b**, ca. 10^{-5} M in dichloromethane at 20 ^{o}C.

X-ray crystal structures were obtained for **2.3b**, **2.5a**, and **2.5b**. The structures obtained are nearly identical to the structures obtained in previous studies; all bond lengths are statistically identical to previously reported structures except for those listed in **Table 2.3**. In general, complexes containing the more electron rich acac ligands have shorter Pd-O bonds and longer Pd-N bonds than the corresponding complexes of hfac. **2.3b** has slightly shorter Pd-O bonds and a longer Pd-N4 bond than **2.1b**. Similarly, **2.3a** has longer Pd-N bonds and shorter Pd-O bonds than its hfac analogue **2.4b**.

Table 2.3 Selected bond lengths for Pd-Nindigo complexes.

Bond	**2.1b**[a]	**2.3b**	**2.4b**[b]	**2.5a**	**2.5b**
Pd1-N1	1.998 (3)	1.996 (1)	1.982 (2)	2.002 (3)	2.011 (2)
Pd1-N2	-	-	1.991 (2)	2.004 (3)	2.007 (1)
Pd1-N4	2.025 (2)	2.051 (1)	-	-	-
Pd1-O1	2.018 (2)	1.995 (1)	2.018 (2)	1.997 (2)	1.993 (1)
Pd1-O2	2.013 (2)	1.993 (1)	2.027 (2)	1.990 (2)	2.001 (1)

[a]Reproduced from reference[66]. [b]Reproduced from reference[64]

In comparing the structures of the less sterically encumbered *para*-toluyl containing molecule **2.5a** with the bulkier 2,6-dimethylphenyl based molecules **2.5b** in **Figure 2.3**, a noticeable difference arises in the dihedral angle between the imine and phenyl groups. The torsion angles of *para*-toluyl complex **2.5a** defined by C2-N3-C22-C23 and C10-N4-C29-C30 are 32^{o} and 40^{o} respectively. Analogous dimethylphenyl rings are rotated substantially, containing analogous dihedral angles of 71^{o} and 76^{o} for **2.4b** and 82^{o} and 69^{o} for **2.5b**. These measurements show that *para*-toluyl substituents are able to be closer to coplanarity with the Nindigo chromophore while the bulky 2,6-dimethylphenyl substituents are forced to be closer to perpendicular in these *cis*-Nindigo complexes. This coplanarity likely allows the phenyl ring to contribute to frontier molecular orbitals, and

are likely the cause of the noticeably less negative reduction potentials seen in **2.4a** and **2.5a**. The aryl unit in solution is likely able to more freely rotate and contribute to conjugation in the molecule. This greater rotational freedom could also lead to the broader absorption spectra of **2.4a** and **2.5a** due to the existence of multiple rotational configurations in solution. In *trans*-binuclear species, these aryl rings are forced closer to the Nindigo backbone, as demonstrated by the smaller dihedral angle defined by C10-N4-C(ring) (118^{o} for **2.3b**, 129^{o} for **2.5a**, and 126^{o} for **2.5b**).

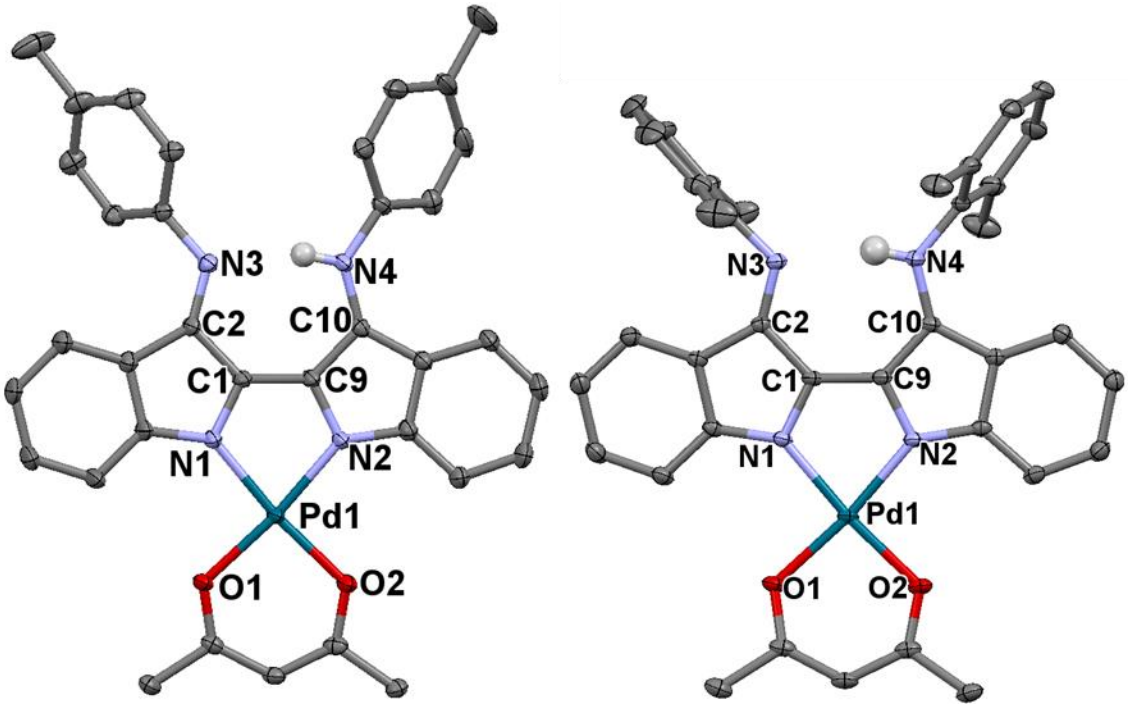

Figure 2.3 X-ray structures of molecule A of **2.5a** (left) and **2.5b** (right). Hydrogen atoms bonded to carbons and lattice trapped solvent are omitted for clarity. Thermal ellipsoids are drawn at the 50% probability level.

2.3 Conclusions

In conclusion, the electronic spectra, oxidation potentials, and reduction potentials of *cis*-Nindigo complexes can be tuned by changing ancillary ligands and arylimine substituents. Unlike *trans*-Nindigo complexes, the reduction potentials of *cis*-Nindigo

complexes appear to be sensitive to the choice of aryl diimine due to the possibility of conjugation in the arylimine subunit. These *cis*-Nindigo complexes appear more accessible and more prevalent than originally thought, and they provide a tunable scaffold for the study of their ligand-centered proton and electron transfer reactivity which are further discussed in Chapter 4 and 5.

Complexes of the electron poor hfac were more difficult to oxidize than the electron rich acac complexes. This result shows that the change of ancillary ligands provides an extra aspect of consideration when designing systems containing redox-active ligands. Although the effects of ancillary ligands on RALs are not as drastic as their effects on the metal itself, these ancillary ligands are not merely "spectators". The effect these ligands have on the properties of RALs must be taken into account.

2.4 Experimental Methods

All reactions and manipulations were carried out in air unless otherwise stated. Nindigos **1.25** and **1.26** and BF_2Nindigos **1.29a**, and **1.29b** were prepared according to literature methods.[63,65] $Pd(hfac)_2$ was sublimed prior to use. All other reagents and solvents were purchased from Sigma-Aldrich and used as received. NMR spectra were recorded at room temperature on either Bruker AV300 or AV500 instruments and are referenced to residual solvent. FT-IR were recorded on a Perkin-Elmer Spectrum One FT-IR spectrometer on sodium chloride plates by allowing a dilute solution in dichloromethane solution to dry on the plate. Electronic spectra were recorded on an Agilent 8453 spectrometer over a range of concentrations in CH_2Cl_2. As previously reported, these palladium complexes routinely show low carbon from elemental analysis due to incomplete combustion; in lieu of elemental analysis, high resolution mass spectrometry and isotope

matching are provided. Accurate mass determination and isotope matching was performed on a Thermo Ultimate 3000 Orbitrap with electrospray ionization in the positive mode. Cyclic voltammetry experiments were performed with a Bioanalytical Systems E2 Epsilon Electrochemical Analyzer with a cell consisting of a glassy carbon working electrode, platinum wire counter electrode, and a silver wire quasireference electrode. Experiments were performed in dichloromethane (distilled from calcium hydride prior to use) that was degassed by sparging with argon. Tetrabutylammonium tetrafluoroborate (0.1 M) was added to the solution as electrolyte, and ferrocene or decamethylferrocene (-0.48 V vs. Fc/Fc^+ in dichloromethane) was added as internal standard after several runs to correct potentials. Melting points were determined using a Gallenkamp melting point apparatus.

(μ-Indigo-bis(4-methylphenylimine) (acetylacetonatopalladium(II))(difluoroboron) (2.3a): [Indigo bis(4-methylphenylimine)]difluoroboron (41.5 mg, 85 μmol) and $Pd(acac)_2$ (26.3 mg, 86 μmol), were dissolved in 8 mL toluene. The mixture was heated to reflux for 1.5 hours. The mixture was cooled to room temperature, layered with 10 mL acetone, cooled to -20°C, and filtered to obtain a fine black precipitate. The precipitate was dissolved in excess chloroform, filtered through Celite, and evaporated to obtain 15.6 mg black solid (27% yield). mp >300 °C. UV-Vis-NIR λ_{max} (CH_2Cl_2)/nm: 374 ($\varepsilon/M^{-1}cm^{-1}$ 8,700), 558 (3,100), 833 (17,800). FT-IR (Thin film, NaCl) $\tilde{\nu}_{max}/cm^{-1}$: 1601w, 1567w, 1532s, 1509sh, 1474m, 1461m, 1437m, 1370m, 1341m, 1315m, 1294m, 1284m, 1226s, 1217s, 1134s, 1062m, 969m, 851w, 818w, 802w, 767m, 747s cm^{-1}. ^1H NMR (300 MHz, $CDCl_3$): δ 7.73 (d, 1H, 8.6 Hz), 7.36 (d, 1H, 8.1 Hz), 7.26-7.16 (m, 10H), 7.07 (dt, 1H, 1.3 Hz, 7.1 Hz), 7.01 (d, 2H, 8.2Hz), 6.47 (dt, 1H, 1.0 Hz, 7.3 Hz), 6.36 (dt, 1H, 1.0, 7.2 Hz), 6.12 (d, 1H, 7.9 Hz), 5.84 (d, 1H, 7.9 Hz), 5.31 (s, 1H), 2.40 (s, 3H), 2.36 (s, 3H), 1.98 (s,

3H), 1.46 (s, 3H) ppm. ^{13}C NMR (125.8 MHz, $CDCl_3$): δ 186.2, 185.1, 159.6, 144.2, 136.6, 134.1, 133.7, 130.1, 129.3, 126.4, 126.3, 12.1, 124.6, 120.5, 118.4, 117.2, 100.8, 24.84, 24.81, 21.30, 21.28 ppm. ^{19}F NMR (282.5 MHz, CD_2Cl_2) δ -130.6 (1:1:1:1 q, 29.5 Hz). ESI-HRMS: [M^+] Calcd for $C_{35}H_{29}BF_2N_4O_2Pd$ 692.13810; Found 692.13655.

μ-Indigo-bis(2,6-dimethylphenylamine)(acetylacetonatopalladium)(difluoroboron) (2.3b): [Indigo-bis(2,6-dimethylphenylimine)]difluoroboron (85.8 mg, 166 μmol), $Pd(acac)_2$ (50.9 mg, 167 μmol), and Hünig's base (5 drops) were dissolved in 10 mL toluene. The mixture was heated to reflux for 4 hours. The volatiles were removed via rotary evaporator. The resulting solution was recrystallized by dissolving the solid in hot toluene, filtering through Celite, layering the solution with hexanes and cooling to -20^{o}C to receive 79.7 mg shiny black x-ray quality crystals (67% yield). mp 280-281 ^{o}C (from toluene/hexanes). UV-Vis-NIR (CH_2Cl_2) λ_{max}/nm (ε/$M^{-1}cm^{-1}$): 374 (6,900), 559 (2,900), 833 (15,400). FT-IR (Thin film, NaCl) *ṽ/cm-1*: 1600m, 1577m, 1527s, 1476m, 1459w, 1438m, 1375w, 1339s, 1312w, 1296m, 1219s, 1134s, 1063w, 964s, 917w, 906w, 836w, 766w, 750w cm^{-1}. ^{1}H NMR (300 MHz, $CDCl_3$): δ 7.85 (d, 8 Hz, 1H), 7.37 (d, 8 Hz, 1H), 7.05-7.28 (m, H), 6.48 (tod, 8 and 1 Hz, 1H), 6.34 (tod, 8 Hz, 1 Hz, 1H), 5.79 (d, 8 Hz, 2H), 5.32 (s, 1H), 2.29 (s, 3H), 2.20 (s, 6H), 2.19 (s, 6H), 2.02 (s, 3H). ^{19}F NMR (282.5 MHz, CD_2Cl_2) δ -129.9 (1:1:1:1 q, *J*=30.3 Hz). ^{13}C NMR (75.5 MHz, CD_2Cl_2): δ 187.1, 185.9, 160.3, 144.8, 139.2, 135.6, 134.9, 134.3, 132.4, 129.3, 128.6, 127.3, 125.6, 125.2, 121.5, 120.0, 119.3, 117.6, 115.3, 101.1, 25.0, 24.6, 18.6, 18.3 ppm. ESI-HRMS: [M^+] Calcd for $C_{37}H_{33}BF_2N_4O_2Pd$ 720.1694; Found 720.1691.

Hexafluoroacetylacetonate[*cis*-1*H*-indigo-bis(4-methylphenylimine)]palladium 2.4a: To a solution of indigo bis(*p*-toluylimine) (126 mg, 286 μmol) in 17 mL dichloromethane

and 6 mL acetonitrile was added $Pd(hfac)_2$ (148 mg, 284 µmol) in 8 mL dichloromethane over 30 minutes and stirred in air for an additional 18 hours. The mixture was concentrated to half, layered with acetonitrile, and cooled to -20°C. The green, papery precipitate was vacuum filtered and washed with acetonitrile and hexanes, gaining 117.3 mg (55% yield). mp 249-251 °C (from dichloromethane/acetonitrile). UV-Vis-NIR (CH_2Cl_2) λ_{max}/nm (ε/$M^{-1}cm^{-1}$): 306 (25,700), 617 (4,310), 853 (14,100). FT-IR (Thin film, NaCl) $\tilde{\nu}$/cm^{-1} 3369m, br, 2980w, 2850w, 1628m, 1597m, 1568w, 1552w, 1510w, 1472m, 1444m, 1368s, 1303s, 1260s, 1203s, 1148s, 1120w, 1067w, 1025w, 885w, 817w. ^{1}H NMR (500 MHz, CD_2Cl_2): δ 12.59 (s, 1H), 7.56 (d, 8.4 Hz, 2H), 7.21-7.16(m, 6H), 7.08 (d, 8.2 Hz, 4H), 7.05 (d, 8.1 Hz, 2H), 6.60 (d, 7.4 Hz, 2H), 6.25 (s, 1H), 2.39 (s, 6H) ppm. ^{13}C NMR (125.8 MHz, $CDCl_3$): δ 174.1 (q, 36 Hz), 155.7, 150.6, 145.2, 141.2, 135.5, 132.4, 129.8, 125.3, 121.8, 118.8, 118.2, 114.4, 92.2, 21.1 ppm. ^{19}F NMR (282.5 MHz, $CDCl_3$) -73.84 (s). ESI-HRMS: [M^+] Calcd for $C_{35}H_{23}F_6N_4O_2Pd$ 752.08328; Found 752.08295.

Acetylaceonato[*cis*-1*H*-indigo-bis(4-methylphenylimine)]palladium 2.5a: Indigo bis(*p*-Toluylimine) (28.7 mg, 65 µmol) and $Pd(acac)_2$ (19.8 mg, 65 µmol) were dissolved in 4 mL toluene and the solution was heated to reflux for 3 hours. The mixture was concentrated to half, layered with hexanes, and cooled to -20°C. The black precipitate was vacuum filtered and washed with hexanes, gaining 29.0 mg (69% yield). Single crystals were grown by slow evaporation of a concentrated dichloromethane solution. mp 288-289 °C (from toluene/hexanes). UV-Vis-NIR (CH_2Cl_2) λ_{max}/nm (ε/$M^{-1}cm^{-1}$): 390 (12,800), 595 (4,100), 890 (12,400). FT-IR (Thin film, NaCl) $\tilde{\nu}$/cm^{-1} 3436s,br, 2091w,br, 1634s, 1898s, 1580s, 1519m, 1443m, 1373s, 1299s, 1196s, 1117s, 1016w, 942w, 883w, 818w, 739m cm^{-1}. ^{1}H NMR (300 MHz, CD_2Cl_2): δ 12.32 (s, 1H, br), 7.88 (d, 2H, 8.3 Hz), 7.20 (m, 10 H),

7.08 (d, 2H, 8.0 Hz), 6.62 (t, 2H, 7.5 Hz), 5.57 (s, 1H), 2.42 (s, 6H), 2.15 (s, 6H) ppm. ^{13}C NMR (300 MHz, CD_2Cl_2): δ 186.2, 156.5, 150.6, 146.3, 135.5, 132.0, 130.2, 125.4, 121.7, 118.9, 115.6, 101.1, 25.8, 21.1 ppm. ESI-HRMS: [M^+] Calcd for $C_{35}H_{30}N_4O_2Pd$ 644.13981; found 644.13935.

Acetylacetonate[*cis*-1*H*-indigo-bis(2,6-dimethylphenylimine)]palladium 2.5b: Indigo bis-(2,6-dimethylphenylimine) (90.2 mg, .19 mmol) and Pd(acac)$_2$ (59.7 mg, .19 mmol) were dissolved in seven mL of toluene and the mixture was heated to reflux for 4 hours. The mixture was filtered through Celite and evaporated. The residue was recrystallized by layering a saturated dichloromethane solution with two times by volume acetonitrile and cooling to -20 ^{o}C. The shiny black precipitate was vacuum filtered and washed with acetonitrile and hexanes to obtain 74.0 mg (56%) yield. Single crystals suitable for x-ray diffraction were grown by the same method. mp 255^{o}C (from dichloromethane/acetonitrile). UV-Vis-NIR (CH_2Cl_2) λ_{max}/nm (ε/$M^{-1}cm^{-1}$): 383 (11,900), 594(4,400), 848 (15,500). FT-IR (Thin film, NaCl) $\tilde{\nu}$/cm^{-1}: 3435s,br, 3054s, 2987m, 2306m, 1638s, 1521w, 1422s, 1367w, 1265s, 1197w, 1120w, 896m, 738s, 705s. ^{1}H NMR (300 MHz, CD_2Cl_2): δ 12.22 (s, 1H), 7.84 (d, 2H, 8.4 Hz), 7.22 (m, 8H), 6.52 (td, 2H, 7.3 Hz, 0.7 Hz), 6.28 (d, 2H, 8.0 Hz), 5.62 (s, 1H), 2.19 (s, 6H), 2.17 (s, 12H) ppm. ^{13}C NMR (75.5 MHz, CD_2Cl_2): δ 186.4, 156.7, 153.7, 144.6, 142.8, 132.7, 131.6, 128.8, 126.5, 124.4, 119.6, 119.1, 115.1, 101.1, 25.8, 18.3 ppm. ESI-HRMS: [M^+] Calcd for $C_{37}H_{34}N_4O_2Pd$ 672.17111; Found 672.17082.

Chapter 3 Palladium (II) Complexes of the Redox-Active Ligand *cis*- and *trans*-Indigomonoimine "Mindigo"

3.1 Introduction

The coordination chemistry of indigo **1.20** and Nindigo has been established. Nindigo relates to indigo by its exchange of two ketones for two arylimines. The hybrid ligand between indigo and Nindigo has been synthesized by the Hicks group: indigo mono(2,6-dimethylphenylimine) **3.1**,[80] which we colloquially call "Mindigo". Mindigo is a beautiful purple dye (λ_{max} of 592 nm in CH_2Cl_2) which absorbs strongly at wavelengths between indigo (λ_{max}=604 nm in $CHCl_3$) and the related Nindigo analogue **1.26** (R=2,6-dimethylphenyl, λ_{max}=586 in CH_2Cl_2). Like Nindigo, Mindigo is substantially more soluble than indigo in most common organic solvents due to its arylimine functionality.

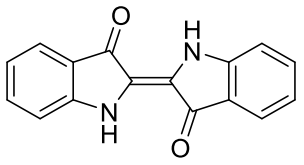

1.20

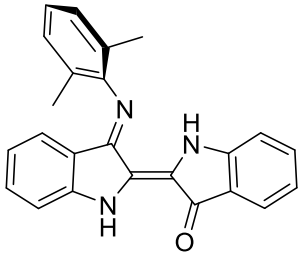

3.1

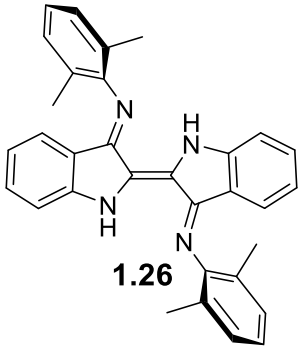

1.26

The coordination chemistry of Mindigo remains completely unexplored. Mindigo differs from indigo and Nindigo by its lower C_s symmetry. The lower symmetry of Mindigo creates a greater diversity of coordination modes than indigo or Nindigo. As shown in **Figure 3.1**, Mindigo complexes may exist as *trans*-Mindigo or *cis*-Mindigo. As a result, six and seven membered N^O chelates can be formed (e.g. **A** and **D** in **Figure 3.1**), or six and five membered N^N chelate can be formed (e.g. **B** and **C** in **Figure 3.1**). It was a primary goal of this research to explore the coordination chemistry of Mindigo, and to

compare the properties of the formed complexes to Mindigo's sibling ligands, indigo and Nindigo. Herein, we present the first examples of coordination complexes of Mindigo, and explore the structural, spectral and electrochemical properties of these palladium (II) diketonate complexes.

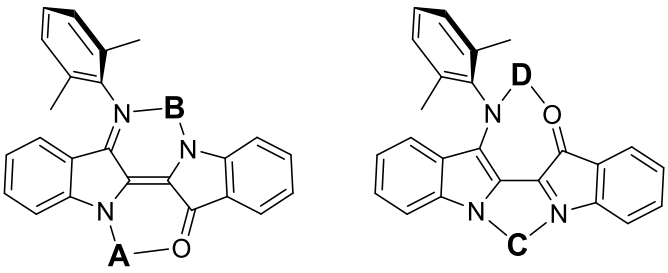

Figure 3.1 The possible chelating coordination modes of Mindigo.

3.2 Results and Discussion

As has been recently reported,[80] the synthesis of Mindigo (R=2,6-dimethylphenyl) is accomplished via a titanium (IV) chloride mediated process similar to the synthesis of Nindigo. Use of the lower boiling point solvent tetrahydrofuran allows for selective installation of a single arylimine functionality in up to 90% yields. Bulky 2,6-disubstituted anilines are required for this synthesis. Under these milder conditions, attempts to use *para*-substituted anilines under the same reaction conditions resulted in low yields of the diimine Nindigo and no monoimine.

Several palladium (II) complexes of Mindigo **3.2**-**3.5** were synthesized as described in **Scheme 3.1**. All complexes were synthesized by reaction of Mindigo with their corresponding palladium bis-diketonate. Complexes **3.2** and **3.4** contain *trans*-N^N chelates. **3.3** and **3.5** contain a ligand that has *trans*-to-*cis* isomerized about the central double bond. In both cases, the ligands are formally anionic and contain one NH unit.

Under the conditions surveyed, no chelates that form from coordination to the oxygen of Mindigo were isolated or detected.

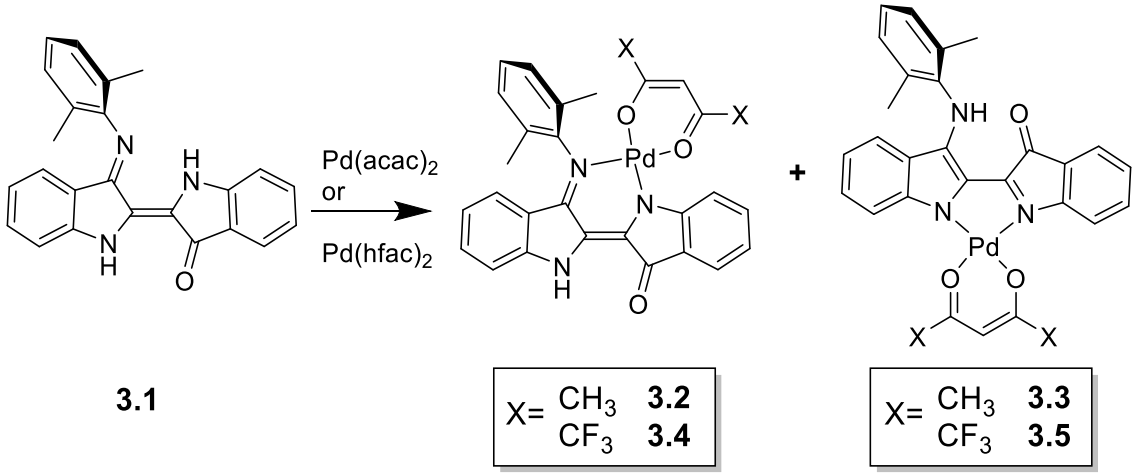

Scheme 3.1 Synthesis of the complexes studied in Chapter 3.

Acetylacetonate (acac) complexes **3.2** and **3.3** were synthesized by reaction of Mindigo with one equivalent of $Pd(acac)_2$ in refluxing toluene. *Cis*-Mindigo complex **3.3** (46% yield) was favored over the *trans*-Mindigo complex **3.2** (27% yield) under these conditions. Attempts at the optimization of reaction conditions using different solvent and conditions gave similar relative yields of both complexes but lower overall conversion based on the amount of isolated free Mindigo. Reactions with two equivalents of palladium likewise afforded **3.2** and **3.3**.

It was possible to favor the formation of one isomer over another with hexafluoroacetylacetonate (hfac) compounds **3.4** and **3.5**. Slow addition of $Pd(hfac)_2$ to ligand **3.1**, both dissolved in acetone, gave 74% *trans*-Mindigo complex **3.4** after recrystallization. Alternatively, dissolving solid **3.1** and $Pd(hfac)_2$ in dichloromethane together simultaneously and evaporating after 4 hours gave 50-55% yield of *cis*-complex **3.5** after recrystallization and **3.4** as a 15% byproduct.

Although the cause of *trans*-to-*cis* isomerization of Mindigo during coordination is not known, proton transfer is thought to play a role in whether *trans*- or *cis*- isomers are isolated as was described in Chapter 2 (**Scheme 2.1**). Like Nindigo, Mindigo **3.1** is known to "protoisomerize" as seen in **Scheme 3.2**: a *trans*-to-*cis* isomerization occurs about the central double bond upon protonation. During the course of the reaction between **3.1** and $Pd(hfac)_2$, ^1H NMR resonances closely resembling protonated Mindigo **3.6**[80] are detected. The same pattern is obtained by reacting Mindigo with one equivalent of hexafluoroacetylacetone. Keeping the solid obtained from protonation by hexafluoroacetylacetone under reduced pressure for prolonged periods allows complete recovery of Mindigo **3.1**. Protonation with the hexafluoroacetylacetone byproduct therefore appears reversible. Therefore, protonated Mindigo is likely an intermediate in the synthesis of *cis*-Mindigo complex **3.5**.

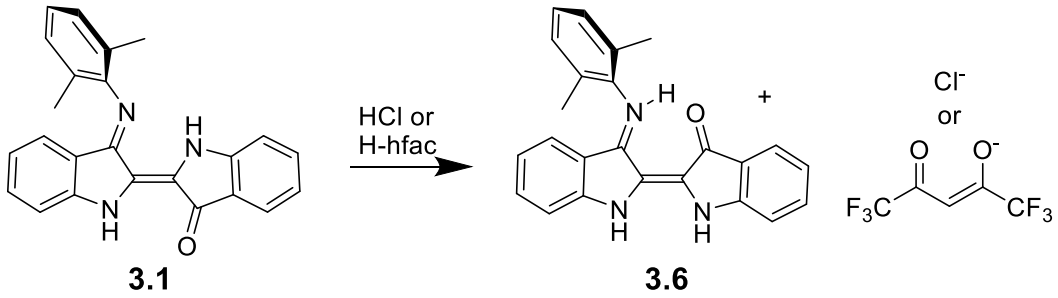

Scheme 3.2 Protoisomerization of Mindigo.

The NMR spectra of **3.2-3.5** are diagnostic despite both pairs of isomers exhibiting C_s symmetry. All compounds contain a sharp N-H peak with chemical shifts indicative of each isomer: ca. 9.5 ppm for indole NH in *trans*-Mindigo complexes, or ca. 11.3 ppm for the amine NH in the *cis*- isomers. Compounds **3.4** and **3.5**, in addition to crystallographic data, were assigned based on ^1H-^{13}C NMR correlation experiments (i.e. HMBC). The 3j ^1H-^{13}C correlations to the NH are most useful: for an N^O chelate, one would expect a

correlation between the NH and C=O. In **3.4**, the NH singlet at 9.5 ppm shows correlations to four carbons (including the imine carbon at 152 ppm), indicating coordination to N2 and N3. The NH in **3.5** at 11.4 ppm only correlates to 2 aromatic carbons. These structural assignments are further confirmed *via* x-ray crystallography which is shown in **Figure 3.2**.

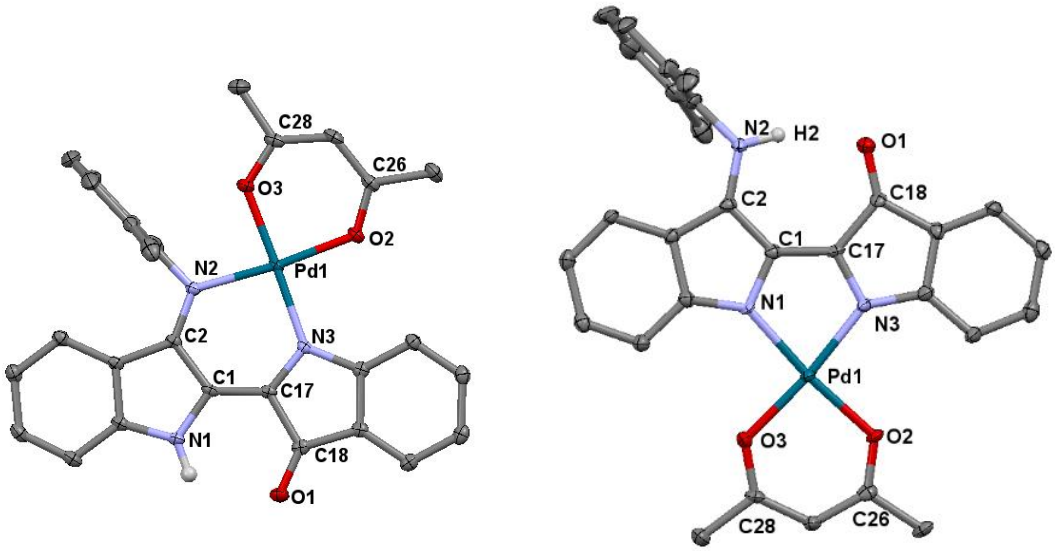

Figure 3.2 X-ray crystal structures of **3.2** (left) and **3.3** (right) displayed at 50% probability ellipsoids. Hydrogen atoms other than those bonded to nitrogen are omitted for clarity.

The bond lengths supplied in **Table 3.1** indicate that complexes **3.2-3.5** are all structurally quite similar. Structures **3.3** and **3.5** confirm the isomerization about the central double bond to form *cis*-monoimine structures. Despite different *cis*/*trans*- orientations, the ligand core bond lengths of all four compounds remain statistically similar. In *trans*-Mindigo complexes, the imine bond C2-N2 lengthens slightly (0.02 Å) compared to free ligand **3.1,** indicative of the greater single bond character expected with β-diketiminate structures. In *cis*-Mindigo complexes **3.3** and **3.5**, C2-N2 is much longer than the *trans*-complexes and even longer than protonated ligand **3.6** due to the significant single bond character of C2-N2.

Table 3.1 Selected bond lengths of *trans*-|*cis*- compounds studied.

	3.1[80]	**3.2**	**3.4**	**3.6**[80]	**3.3**	**3.5**
Pd-O2	-	2.011 (1)	2.041 (2)	-	2.021 (5)	2.027 (3)
Pd-O3	-	2.006 (1)	2.037 (2)	-	2.021 (5)	2.011 (3)
Pd-N3	-	2.033 (2)	2.019 (3)	-	2.010 (4)	2.010 (3)
Pd-N1/2	-	2.028 (2)	2.010 (2)	-	2.021 (5)	1.999 (3)
N1-C1	1.375 (2)	1.393 (2)	1.390 (4)	1.378 (3)	1.387 (7)	1.373 (4)
C1-C2	1.476 (2)	1.442 (2)	1.439 (4)	1.454 (3)	1.433 (8)	1.453 (5)
C2-N2	1.291 (2)	1.324 (2)	1.319 (4)	1.342 (3)	1.356 (7)	1.348 (5)
N3-C17	1.380 (2)	1.367 (2)	1.363 (4)	1.366 (3)	1.360 (7)	1.355 (4)
C17-C18	1.479 (2)	1.490 (2)	1.504 (4)	1.501 (3)	1.505 (7)	1.480 (5)
C18-O1	1.239 (2)	1.237 (2)	1.231 (4)	1.231 (3)	1.235 (7)	1.238 (4)
C1-C17	1.354 (2)	1.377 (2)	1.372 (4)	1.377 (2)	1.394 (7)	1.387 (5)

The electrochemical properties of **3.1**, **3.6** and complexes **3.2**-**3.5** were analyzed by cyclic voltammetry measurements in dichloromethane solution. As seen in **Figure 3.3**, compounds **3.1** and **3.6** only show one oxidation and one reduction, both of which are electrochemically irreversible, multielectron redox events. Similarly irreversible oxidations and reductions have been observed for Nindigo, and the irreversibility likely arises from proton transfer.[64] Mindigo **3.1** is easier to reduce and harder to oxidize than Nindigo **1.26** by about 100 mV.

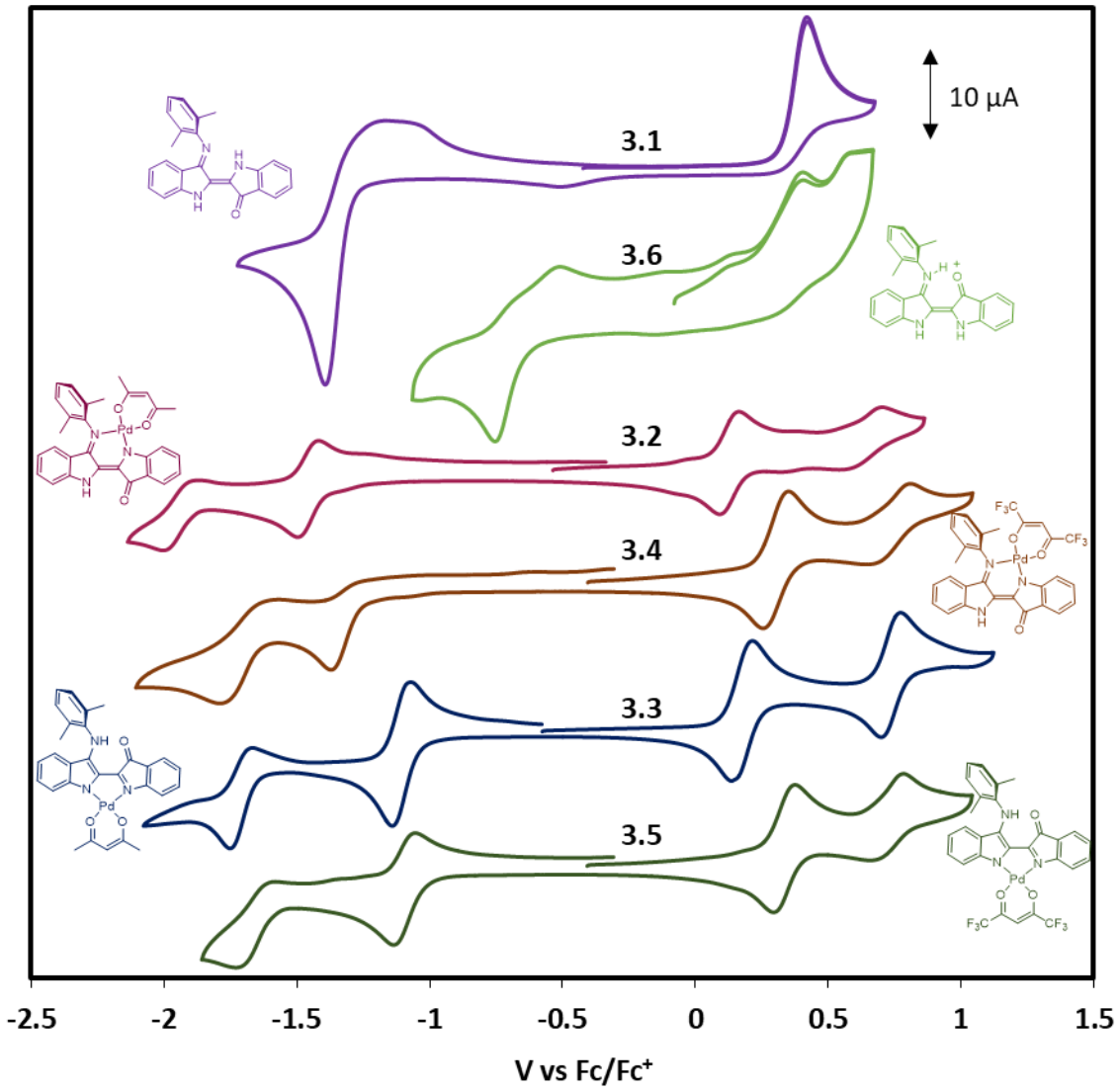

Figure 3.3 Cyclic voltammetry of **3.1**, **3.6**, **3.2**, **3.3**, **3.4**, and **3.5** (CH_2Cl_2 solution, 1 mM analyte, 0.1 M NBu_4BF_4 electrolyte, 100 mV s^{-1} scan rate).

As with complexes of indigo and Nindigo, **3.2-3.5** have four one-electron redox events that are presumed to be changes in the ligand's charge states. Compared to analogous complexes of *cis*-Nindigo **2.4b** and **2.5b** with the same ancillary ligand and metal, all redox events of **3.2-3.5** are shifted to more positive potentials. Reduction potentials are shifted to a greater degree which causes the E_{cell} (the difference in oxidation

vs. reduction potentials) of the Mindigo complexes in this chapter to be smaller than the analogous complexes of Nindigo.

As demonstrated in Chapter 2, the nature of other ligands (i.e. acac or hfac) ancillary to the redox active ligand Nindigo can have noticeable consequences for the ligand-centered spectral and electrochemical properties. Similarly, Mindigo complexes of the electron rich ligand acac **3.2** and **3.3** are, in general, easier to oxidize than the analogous complexes with electron-poor ligands hfac **3.4** and **3.5** by around 150 mV and 90 mV for the first and second oxidation respectively. Like the complexes of Nindigo seen in Chapter 2, the reduction potentials of all four complexes appear insensitive to ancillary ligands. The combined effects of oxidation and reduction potentials together lead to a larger E_{cell} with complexes of hfac than acac.

Table 3.2 Cyclic voltammetry potentials vs. Fc/Fc^+ for M-Pd complexes.

Compound	Reduction	Oxidation	E_{cell}
3.1	-1.39[b]	+0.42[b]	1.81
3.6	-0.76[a]	+0.40[b]	1.16
3.2	-1.45, -1.93[b]	+0.13, +0.65[b]	1.58
3.3	-1.12[b], -1.74[b]	+0.15, +0.64[b]	1.28
3.4	-1.47[a], -1.88[b]	+0.32, +0.73[b]	1.56
3.5	-1.10, -1.70[a]	+0.33, +0.73[b]	1.42
2.4b	-1.36	+0.17, +0.65	1.53
2.5b	-1.37	+0.06, +0.65	1.43

[a]Quasi-reversible process. [b]Irreversible process: only peak potential given.

The reduction potentials in *trans*-Mindigo complexes **3.2** and **3.4** are more negative than *cis*-Mindigo complexes **3.3** and **3.5** by 0.33-0.37 V. Surprisingly, the oxidation potentials are insensitive to the coordination mode of the Mindigo. Thus, E_{cell} is larger for *trans*- complexes **3.2** and **3.4** than *cis*-complexes **3.3** and **3.5**

All Mindigo palladium complexes absorb strongly in the near-infrared, as summarized in **Table 3.3**. In general, the relative absorption maximum values follow the trend seen in E_{cell}. The *trans*-Mindigo complexes **3.2** and **3.4** absorb at 775 and 762 nm respectively. These complexes absorb in a similar range to *trans*-mononuclear indigo complexes of Pd[60], Ru[90], and Au[57], which absorb intensely at 748 to 796 nm. The near-infrared absorption maximum of complexes of *trans*-Mindigo **3.2** and **3.4** only differ by 200 cm^{-1} meaning the ancillary ligand did not have a substantial effect on absorption maxima. Complexes of *cis*-Mindigo **3.3** and **3.5** are bathochromically shifted from *trans*-isomers with absorption maxima from 860-895 nm. Absorptions of **3.3** and **3.5** differ by 400 cm^{-1}, so are somewhat sensitive to changes of the ancillary ligands that are present. Complexes *cis*-Mindigo **3.3** and **3.5** are bathochromically shifted from their *cis*-Nindigo analogues **2.5b** and **2.4b** respectively by 600 cm^{-1}. This shift in absorption maxima matches the trends in E_{cell} mentioned above. Replacement of imines with ketones therefore leads to a bathochromic shift due to a greater stabilization of the LUMO than the HOMO.

Table 3.3 Absorption maxima of lowest energy absorptions.

Compound	λ_{max} (nm)	$1/\lambda_{max}$ (cm^{-1})	ε ($M^{-1}\,cm^{-1}$)
2.4b	818	12,200	15,200
2.5b	848	11,800	16,000
3.2	775	12,900	17,500
3.3	895	11,200	16,900
3.4	762	13,100	13,400
3.5	860	11,600	17,200

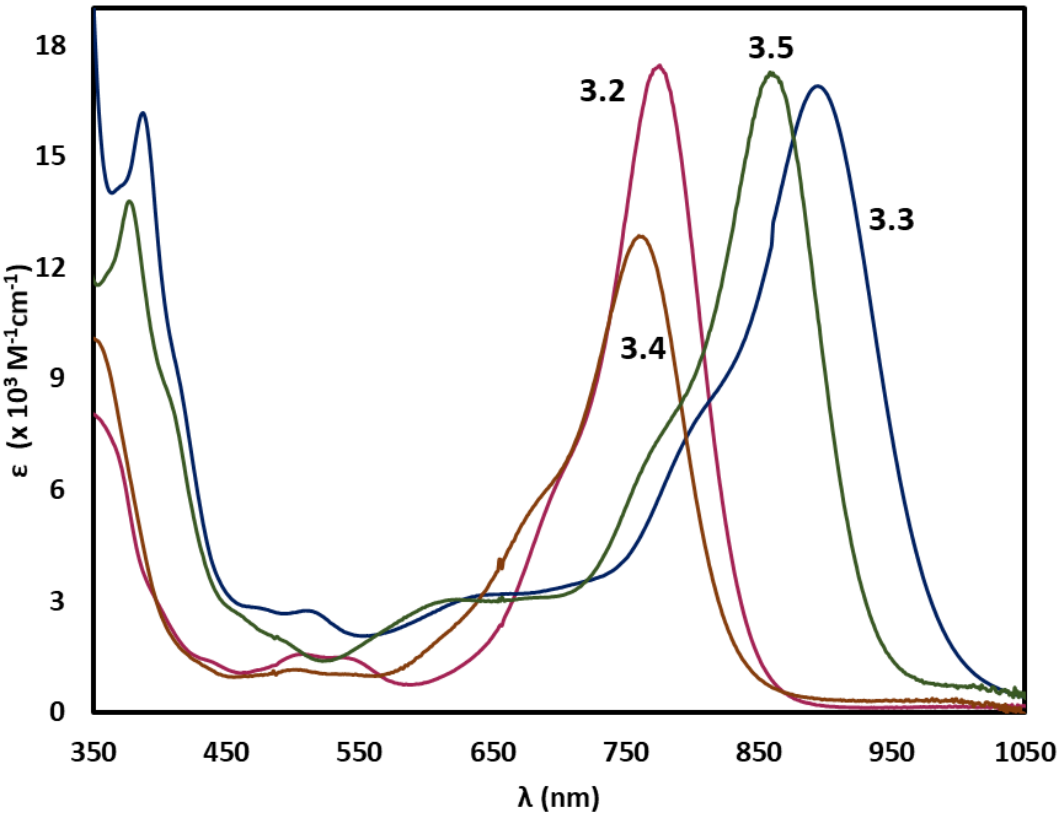

Figure 3.4 Electronic spectra of **3.2**, **3.3**, **3.4**, and **3.5** at 300 K (ca. 10^{-5} M in DCM).

3.3 Conclusions

Mindigo retains the redox activity and near-infrared absorption of indigo and Nindigo. The spectral and redox properties of Mindigo complexes fall between those of indigo and Nindigo. The replacement of ketones with imines makes the ligands more

electron rich as seen by the negative shift in electrochemical potentials going from Mindigo to Nindigo complexes. The replacement of ketone to imine has a larger effect on reduction potentials (and therefore the LUMO) than oxidation potentials, so Mindigo complexes are bathochromically shifted from analogous Nindigo complexes.

Mindigo is distinct from indigo and Nindigo by its many accessible coordination modes. No *trans*-Nindigo species with one metal have been isolated to date. Conversely, complexes of *cis*-indigo ligands are rare and only are known where the ligand is oxidized or reduced. For Mindigo, reaction conditions could be optimized to get *trans*- or *cis*-mononuclear complexes. These *trans*-Mindigo complexes have distinct properties from *cis*- isomers, and have an open N^O chelate that may be used in extended, multimetallic systems. In conclusion, these complexes show indigo monoimine has further potential as a scaffold for mononuclear and binuclear complexes with an abundance of useful ligand centered properties.

3.4 Experimental Methods

See chapter two for general considerations. Mindigo **3.1**[91] and Mindigo·HCl **3.6**[80] were prepared according to literature methods. Peak positions in the ^{13}C NMR of fluorine-coupled quaternary carbons in **3.4** and **3.5** are estimated based on HMBC ^{1}H-^{13}C correlations.

Acetylacetonato[*trans*-indigo-mono(2,6-dimethylphenylimine)κ^2-*N,N'*]palladium (**3.2**) and **Acetylacetonato[*cis*-1*H*-indigo-mono(2,6-dimethylphenylimine)κ^2-*N,N'*] palladium** (**3.3**): Mindigo **3.1** (105 mg, 0.287 mmol) and $Pd(acac)_2$ (88 mg, 0.29 mmol) and 10 mL toluene were magnetically stirred and gently boiled in a large glass vial for 3 hours. The mixture was layered with hexanes, precipitating out 75 mg green solid **3.3** (46%

yield). The remaining residue was evaporated and chromatographed on silica gel using 1:3 hexanes/dichloromethane eluent. Once residual **3.3** was eluted, the column was eluted with dichloromethane and the residue evaporated to dryness to obtain 44 mg magenta solid (27% yield) **3.2**. Single crystals of each were obtained by slow evaporation of a concentrated dichloromethane/hexanes solution.

3.2: mp > 340 ^{o}C. Anal. Calc. for $C_{29}H_{25}N_3O_3Pd \cdot 1/2\ CH_2Cl_2$: C 57.86; H 4.28; N 6.86. Found: C 57.88; H 4.24; N 6.48. UV-Vis-NIR (CH_2Cl_2): λ_{max}/nm (ε/M^{-1} cm^{-1}) 268 (33,800), 300 (34,900), 507 (1,950), 774 (17,500). FT-IR (KBr pellet): 3383 br, 1664 w, 1608 s, 1580 s, 1519 vs, 1473 m, 1448 m, 1373 m, 1325 w, 1289 m, 1185 m, 1148 w, 1113 vs, 746 w, 688 w cm^{-1}. ^{1}H NMR (CD_2Cl_2, 300 MHz): 9.60 (1H, s, br), 7.78 (1H d, 8 Hz), 7.56 (1H dd, 7.6, 1.2 Hz), 7.30 (1H dt, 8.6 Hz, 1.3 Hz), 7.27 (1H dt), 7.21 (1H t), 7.11 (2H d, 7.8 Hz), 7.03 (1H d, 8.9 Hz), 6.80 (1H dt, 7.3, 1Hz) 6.50 (1H dt 7.3, 1 Hz), 5.87 (1H d, 9 Hz), 2.20 (s, 6H), 2.03 (s, 3H), 1.46 (s, 3H). ^{13}C NMR (CD_2Cl_2, 75 MHz): 187.0, 186.4, 160.0, 159.2, 149.2, 137.2, 136.8, 136.6, 136.2, 133.6, 129.1, 128.7, 124.7, 124.5, 123.4, 121.2, 117.9, 117.5, 116.0, 115.2, 101.1, 25.8, 18.4. ESI-HRMS: [M^{+}] Calcd for $C_{29}N_3O_3H_{25}Pd$ 569.1; Found 569.2.

3.3: mp > 340 ^{o}C. Anal. Calc. for $C_{29}H_{25}N_3O_3Pd$: C 61.11; H 4.42; N 7.37. Found: C 60.82, H 4.48, N 7.27. UV-Vis-NIR (CH_2Cl_2): λ_{max} nm (ε, M^{-1} cm^{-1}) 327 (96,700), 387 (16,200) 815 (8,490 sh), 895 (16,900). FT-IR (KBr Pellet): 3466 br, 2922 w, 1641 m, 1597 s, 1568 vs, 1518 s, 1491 w, 1473 m, 1440 m, 1368 s, 1296 s, 1189 s, 1139 w, 1112 s, 1081 m, 922 w, 867 w, 744 s, 596 w, 426 w cm^{-1}. ^{1}H NMR (CD_2Cl_2, 500 MHz): 11.38 (1H, s), 7.69 (1H, d, 8 Hz), 7.60 (1H, d, 9 Hz), 7.57 (1H, d, 7 Hz), 7.41 (1H, dt, 8, 1Hz), 7.32-7.22 (3H, m), 7.11 (1H, dt, 7 Hz, 1 Hz), 6.92 (1H, t, 7 Hz), 6.36 (1H, t, 8 Hz), 6.19 (1H, d, 8 Hz),

5.55 (1H, s), 2.24 (6H, s), 2.14 (3H, s), 2.13 (3H, s). ^{13}C NMR (CD_2Cl_2, 75 MHz): 186.9 (Q), 186.3 (Q), 160.0 (Q), 159.1 (Q), 149.5 (Q), 149.2 (Q), 137.2 (Q), 136.8 (Q), 136.5, 136.2(Q), 133.2, 129.1, 128.7, 124.6, 124.4, 123.4 (Q), 121.2, 117.9, 117.5 (Q), 116.0, 115.2, 101.8, 25.7, 18.4. ESI-MS: [M^+] Calcd for $C_{29}N_3O_3H_{25}Pd$ 569.1; found 569.2.

Hexafluoroacetylacetonato[*trans*-indigo-mono(2,6-dimethylphenylimine)κ^2-*N,N'*] palladium 3.4: To a solution of **3.1** (32 mg, 8.7 µmol) in 15 mL acetone was added a solution of Pd(hfac)$_2$ (30 mg, 5.8 µmol) dissolved in 5 mL acetone over 10 minutes with rapid stirring. The mixture was stirred for 8 hours and the solvent evaporated. The mixture was recrystallized from layering a dichloromethane solution with acetonitrile at -10 ^{o}C giving **3.4** (29 mg, 4.3 µmol, 74% yield) as a blue-green precipitate. Mp > 340 ^{o}C. Anal. Calc. for $C_{29}H_{19}F_6N_3O_3Pd$: C 51.38; H 2.83; N 6.20. Found: C 51.17, H 2.57, N 6.11. UV-Vis-NIR (CH_2Cl_2): λ_{max} (nm) (ε, M^{-1} cm^{-1}) 297 (54,244) 762 (17,000). FT-IR (KBr pellet): 3436 (s, br), 2099 w, br, 1623 s, 1598 s, 1571 m, 1497 m, 1473 m, 1442 m, 1358 m, 1299 s, 1256 s, 1213 s, 1150 s, 1103 m, 1083 m, 926 w, 870 w, 799 w, 767 w, 746 s, 689 w, 598 w, 572 w, 426 w cm^{-1}. ^{1}H NMR (300 MHz, CD_2Cl_2): δ 9.46 (1H, s, br), 7.53 (dd, 1H, 7 Hz, 1 Hz), 7.40 (d, 1H, 8 Hz), 7.27-7.37 (m, 3H), 7.15 (d, 2H, 8 Hz), 7.10 (d, 1H, 8 Hz), 6.89 (dt, 1H, 7 Hz, 1 Hz), 6.53 (dt, 1H, 1Hz, 6 Hz), 6.20 (s, 1H), 5.83 (d, 1H, 8 Hz), 2.21 (s, 6H) ppm. ^{13}C NMR (75 MHz, CD_2Cl_2): δ 189.6, 175.2 (q, 37 Hz), 174.2 (q, 35 Hz), 159.4, 152.3, 147.8, 143.4, 135.6, 133.5, 132.8, 130.0, 128.6, 127.2, 125.3, 124.5, 124.5, 123.7, 120.9, 119.6, 117.6 (q, 114 Hz), 117.2, 117.1, 115.3 (q, 122 Hz), 111.9, 92.2, 18.1 ppm. ^{19}F NMR (282.5 MHz) -74.12 (s), -75.48 (s).

Hexafluoroacetylacetonato[*cis*-1*H*-indigo-mono(2,6-dimethylphenylimine)κ^2-*N,N'*] palladium 3.5: Pd(hfac)$_2$ (78 mg, 0.15 mmol) in 4 mL dichloromethane was added to a

solution of **3.1** (55 mg, 0.15 mmol) dissolved in 4 mL dichloromethane. The mixture was stirred magnetically for 4 hours. The mixture was evaporated, and the crude mixture was purified by silica gel column chromatography. After evaporation of eluent, 47 mg (47% yield) of green **3.5** followed by 19 mg (19% yield) of green **3.4** was obtained by eluting with 3:1 Hexanes/dichloromethane. Single crystals of each were grown by slow evaporation of a concentrated dichloromethane/hexanes solution. Mp > 340 ^{o}C. Anal. Calc. for $C_{29}H_{19}F_6N_3O_3Pd$: C 51.38; H 2.83; N 6.20. Found: C 51.78, H 2.96, N 6.03. UV-Vis-NIR (CH_2Cl_2): λ_{max} (nm) (ε, M^{-1} cm^{-1}) 323 (27,600), 377 (13,300), 860 (17,200). FT-IR (KBr pellet): 3369 m, 2921 w, 1679 w, 1623 vs, 1516 s, 1489 m, 1473 s, 1448 m, 1401 m, 1374 w, 1327 s, 1301 s, 1247 m, 1215 vs, 1188 vs, 1160 s, 974 w, 800 m, 743 s, 688 m, 595 w, 577 w, 501 m, 430 w cm^{-1}. ^{1}H NMR (500 MHz, CD_2Cl_2): δ 11.41 (1H, s), 7.58 (d, 7.5 Hz, 1H), 7.42-7.43 (m, 2 H), 7.37 (d, 8.5 Hz, 1H), 7.30 (t, 7.6 Hz, 1H), 7.23 (d, 7.5 Hz, 2H), 7.17 (t, 7.4 Hz, 1H), 6.93-6.96 (m, 1H), 6.42 (t, 7.8 Hz, 1H), 6.33 (s, 1H), 6.20 (d, 8.2 Hz), 2.25 (s, 6H) ppm. ^{13}C NMR (75 MHz, CD_2Cl_2): δ 186.5, 174.6 (q, 36 Hz), 158.8 (q, 5.7 Hz), 149.9, 137.0, 136.0, 135.8, 134.5, 128.8, 124.8, 123.0, 121.6, 118.6, 117.1, 117.0 (q, 283 Hz), 115.1, 114.3, 92.5, 18.4 ppm. ^{19}F NMR (282.5 MHz) -74.13 (s), -74.20 (s). ESI-MS: [M^{+}] Calcd for $C_{29}H_{19}F_6N_3O_3Pd$ 677.0; found 677.2.

Chapter 4 Investigations of *cis*-Nindigo Palladium and Ruthenium Complexes as Proton and Electron Reservoirs

4.1 Introduction to Chapters 4 and 5

Many redox-active ligands are based on protic donor groups, e.g. phenols, amines, or thiols. The basicity endemic to these groups in principle permit some redox-active ligands to deliver or receive electrons *and* protons, i.e. proton-coupled electron transfer. These so called "hydrogen atom non-innocent" ligands[92] are a subset of redox-active ligand chemistry which provide a second dimension of reactivity beyond the well-established electron transfer reactivity. In addition to changes in ligand charge states, chapters 4 and 5 explore the change in the *protonation state* of the ligand in RAL complexes. For these chapters, where a series of compounds **4.X** differ by protons and electrons, the number of protons **m** and the overall charge **n** will be defined by $\mathbf{H_m4.X^n}$.

The hydrogen atom non-innocence of RAL complexes is demonstrated in the enzyme galactose oxidase. Galactose oxidase is a well-studied[93] fungal enzyme that uses a copper bound tyrosyl radical[94-95] to oxidize substrates (**Scheme 4.1**). After oxidation, the active site is regenerated with dioxygen.[96] The active site uses the redox-active tyrosine-based ligand as a proton and electron reservoir. The ligand and metal work together to dehydrogenate the substrate.[97]

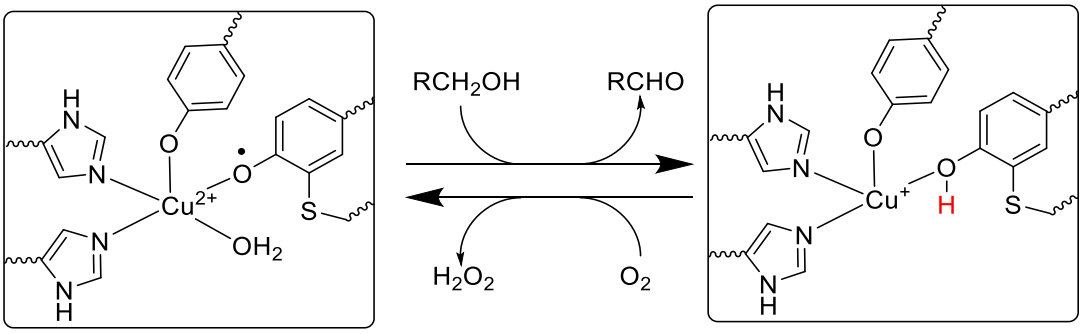

Scheme 4.1 The oxidized and reduced states of the galactose oxidase active site. Wavy lines represent connectivity to the rest of the protein.

Galactose oxidase has inspired many synthetic analogues.[98-100] One such biomimetic system, shown in **Scheme 4.2**, can also dehydrogenate alcohols. Complex **4.1** differs from galactose oxidase in that there is no change in the oxidation state of copper through the reaction.[101] The examples of galactose oxidase mimics succeed in translating the role of hydrogen-atom noninnocent ligands to a non-biological system and highlight that these ligands can work in concert with a metal center for novel reactivity.

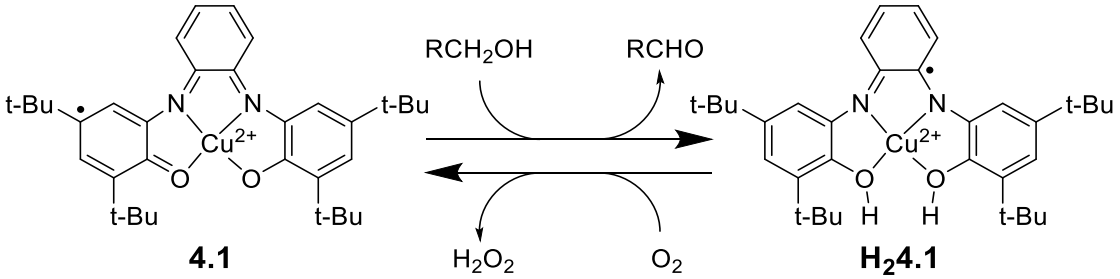

Scheme 4.2 Oxidation of primary alcohols by a synthetic analogue to galactose oxidase.

Several recent examples[102] have begun to develop a repertoire of ligands that exhibit hydrogen atom non-innocence. A number of these examples have shown that redox-active ligands can facilitate the electro-catalytic hydrogen evolution reaction such as the nickel dithiolene complex **1.17**.[103-105] In some cases, RALs have been shown to enable the electrocatalytic hydrogen evolution reaction with redox-inert metals such as aluminum

(**4.2**)[102,106-107] and zinc (**4.3**).[108] One example, **4.4**, showed that hydrogen evolution could be achieved photochemically where the ortho-phenylene diamine ligand served as both the electron and proton source.[109] Other examples of metal complexes that feature hydrogen atom non-innocence have been shown to facilitate nitrite reduction,[110] dioxygen activation,[111-114] oxidation of hydrocarbons,[115] phenols and amines,[106] and dinitrogen activation[116] have been reported in the past four years alone. These examples provide greater breadth of reactivity and serve to highlight some specific, potentially important intermediates, but don't provide as much insight into how or why these reactive intermediates exist. In order to enable the rational design of these types of systems, the fundamental interplay of metal and protons in proton-responsive redox-active ligand based systems must be explored.

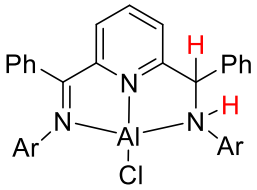

4.2

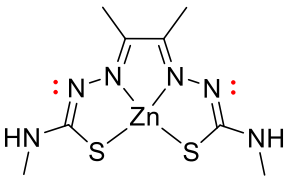

4.3

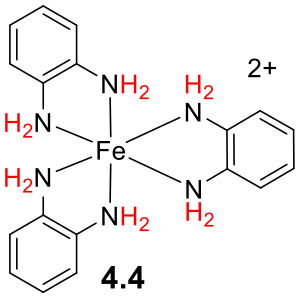

4.4

An important first step toward understanding systems containing hydrogen atom non-innocent ligands is in the analysis of trends of the homolytic XH bond strength of these compounds. In 2018, Brown et al looked at complexes **4.6a** and **4.6b**.[117] Compared to a related free ligand, N-(*tert*-butyl)aminophenolate, the NH bond weakened substantially from 86 kcal mol^{-1} in **4.5**[118] to 63 kcal mol^{-1} in **4.6a** and 55 kcal mol^{-1} in **4.6b**. Also in 2018, Heyduk et al showed proton, electron, and hydrogen atom transfers in complex **4.7**.[92] The bond strength of **4.7** was determined to be 63-64 kcal mol^{-1} in acetonitrile which is

substantially weaker than the model species diphenylamine (BDFE = 87.5 kcal mol^{-1}).[119] **4.7** is also weaker than the hydrogen atom donor 2,2,6,6-tetramethylpiperidin-N-ol (TEMPOH), which has a BDFE = 66.5 kcal mol^{-1}. In both **4.6** and **4.7**, the d^8 metal did not change oxidation states upon proton-coupled oxidation.

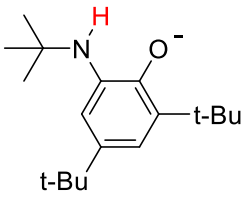

4.5

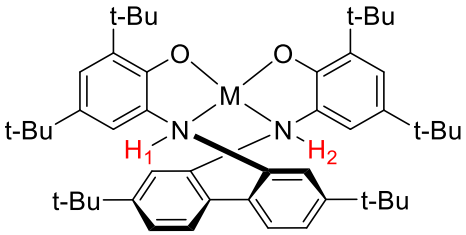

4.6 **a**: M=Pd
b: M=Pt

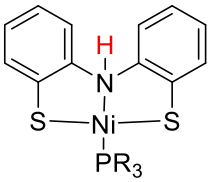

4.7

Coordination of redox-active ligands tends to stabilize the anionic forms, making oxidation of the ligand more difficult relative to the free anion. For traditional redox-active ligands, the interplay between redox activity and acidity has not been thoroughly investigated, and the control of each property affects both the thermodynamics (ΔG_{BDFE}; the bond dissociation free energy) and the mechanism (stepwise or concerted) of hydrogen atom transfer.[120]

The thermodynamics of proton-coupled electron transfer can be understood as a sum of the acidity and redox activity contributions based upon Hess's law.[121] The free energy for the homolytic atom-hydrogen bond cleavage (ΔG_{BDFE}) can be estimated by the Bordwell equation (**Equation 4.1**) where, in this case, C_g is the value for proton reduction for the given solvent (e.g. 54.9 kcal mol^{-1} for acetonitrile[119,122] and 66 kcal mol^{-1} for tetrahydrofuran[123]), the potential is referenced to ferrocene, and the values are given in kcal mol^{-1}.[119]

$$\Delta G_{BDFE} = 23.06\, E^o + 1.37\, pK_a + C_g \qquad \textbf{(4.1)}$$

As a consequence of the above expression, a decrease in the pK_a and/or the reduction potential will lead to a weaker hydrogen bond. Coordination to a Lewis acid is well known to increase the Brønsted acidity of protic substrates. **Equation 4.1** indicates that a change in a pK_a value leads to a change of 1.37 kcal mol^{-1} pK_a^{-1}. For instance, the $pK_{a,MeCN}$ of **4.7** drops from 37.5 (for a model compound, diphenylamine)[119] to 17 for **4.7**, a 28 kcal mol^{-1} difference. In **4.6** and **4.7**, the proton is adjacent to the metal (i.e. two bonds away), which makes the difference in pK_a substantial.

Metals have also been used as electron reservoirs to weaken bonds. As predicted by equation **4.1**, a difference in oxidation potentials will weaken an NH or OH bond by 23.06 kcal mol^{-1} V^{-1}. In the case where the metal is an electron reservoir and the ligand is protic, the oxidation state of the metal changes while the protonation state of the ligand changes, a pseudo-homolytic ligand-hydrogen bond cleavage. Several cases, including **4.8**, have shown that the redox-activity of the metal can take part in a pseudo-homolytic bond cleavage of hydrogen atoms in a concerted manner.[124-127] Furthermore, a growing body of work has shown metals can act as both electron reservoirs and as pK_a-lowering Lewis acids. This bond weakening upon coordination is able to substantially lower very large bond strengths.[128-129] For instance, the coordination of water to titanocene chloride in **4.9** weakens the OH bond strength of 111 kcal mol^{-1} to 49 kcal mol^{-1}.[128] Additionally, upon coordination of ammonia to a molybdenum (I) source as in **4.10**, the NH bond strength was cut in half from 99.5 to 45.1 kcal mol^{-1} which resulted in spontaneous dihydrogen evolution from NH bond cleavage.[130] Coordination of a substrate to an easily oxidized metal therefore makes the H-bond substantially weaker.

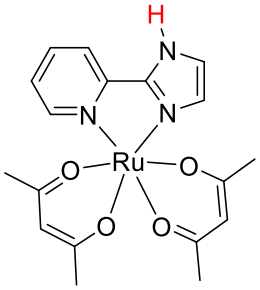

4.8

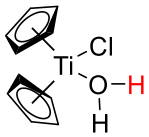

4.9

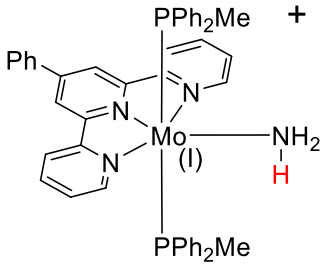

4.10

Complexes of *cis*-Nindigo present an opportunity to investigate the role of metals that are further removed from the protons in question. The redox chemistry of a number of different *cis*-Nindigo complexes are investigated in Chapters 4 and 5 to determine the role that the metal has in NH bond weakening without a significant contribution from coordination induced acidity.

The redox chemistry of complex **2.5a**, here renumbered as **H4.11**, is surveyed as a case where the metal is nominally redox innocent. The redox chemistry of **H4.12**$^{+}$ is also investigated because it is known to have metal-centered contributions to nominally ligand-centered oxidation products. Investigations into the thermochemistry of single electron, two electron, and proton coupled electron transfer processes are here reported.

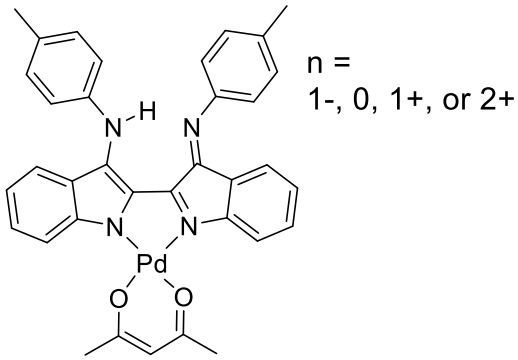

H4.11^{n}

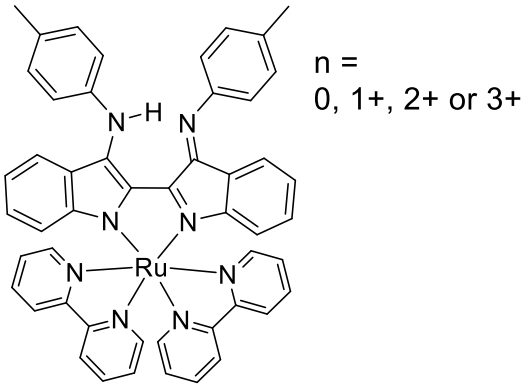

H4.12^{n}

4.2 Synthesis and Physical Properties of Complexes

The simplest method for estimating the N-H bond strengths of complexes in solution is by measuring the corresponding redox potentials and pK_a values and applying the values obtained to **Equation 4.1**. Thus far, no *cis*-Nindigo complexes had been isolated with a vacant, non-protonated γ-diketiminate. Initial efforts were focused on deprotonating and determining the bond strength of the complexes studied. Attempts to deprotonate **H4.11^{0}** and **H4.12^{+}** with strong bases led to intractable mixtures. The reaction of **H4.11^{0}** and **H4.12^{+}** with sodium hydride and **H4.12^{+}** with benzyl potassium in dry, degassed tetrahydrofuran led to uninterpretable, broad ^{1}H NMR spectra. As a result, the deprotonated complexes were not pursued, and the deprotonation of the more acidic oxidized complexes were sought.

For **H4.11^{0}**, cyclic voltammetry showed a one electron oxidation at +0.04 V versus ferrocene in dichloromethane. Chemical oxidation of **H4.11^{0}** was accomplished by treating the compound with silver (I) triflate in dichloromethane to obtain paramagnetic, air stable red-brown **H4.11^{+}**. The x-ray structure of **H4.11^{+}** (**Figure 4.1**) confirms that the atom connectivity remained unchanged upon oxidation and supports a delocalized ligand radical

as evidenced by the changes in bond lengths (**Table 4.1**). Upon oxidation, the Pd-N bonds slightly elongate while the Pd-O bonds shorten. The C-N and C-C bond lengths on one half of the indigoid backbone (C1-C8) are the same for **4.11** and **4.11**$^{+}$ while the bond lengths of C9-C16 lengthen or shorten such that the bond lengths of each half of the molecule are within error of one another. Thus, other than the presence of the NH bond, the complex demonstrates C_{2v} symmetry within experimental error. These changes in bond lengths are indicative of a highly delocalized ligand radical.

Table 4.1 Bond length comparison of neutral and oxidized complexes **H4.11** and **H4.11**$^{+}$

	Pd-N1	Pd-N2	Pd-O1	Pd-O2	N1-C1	N2-C9	C1-C9
H4.11	2.002 (2)	2.005 (2)	1.989 (2)	1.997 (2)	1.350 (3)	1.383 (3)	1.396 (4)
H4.11^{+}	2.019 (4)	2.021 (4)	1.983 (3)	1.979 (4)	1.351 (6)	1.355 (7)	1.417 (8)

	C1-C2	C9-C10	N3-C2	N4-C10	N1-C8	N2-C16
H4.11	1.474 (4)	1.428 (4)	1.301 (3)	1.350 (4)	1.396 (3)	1.366 (3)
H4.11^{+}	1.463 (4)	1.484 (7)	1.304 (6)	1.308 (8)	1.403 (7)	1.390 (7)

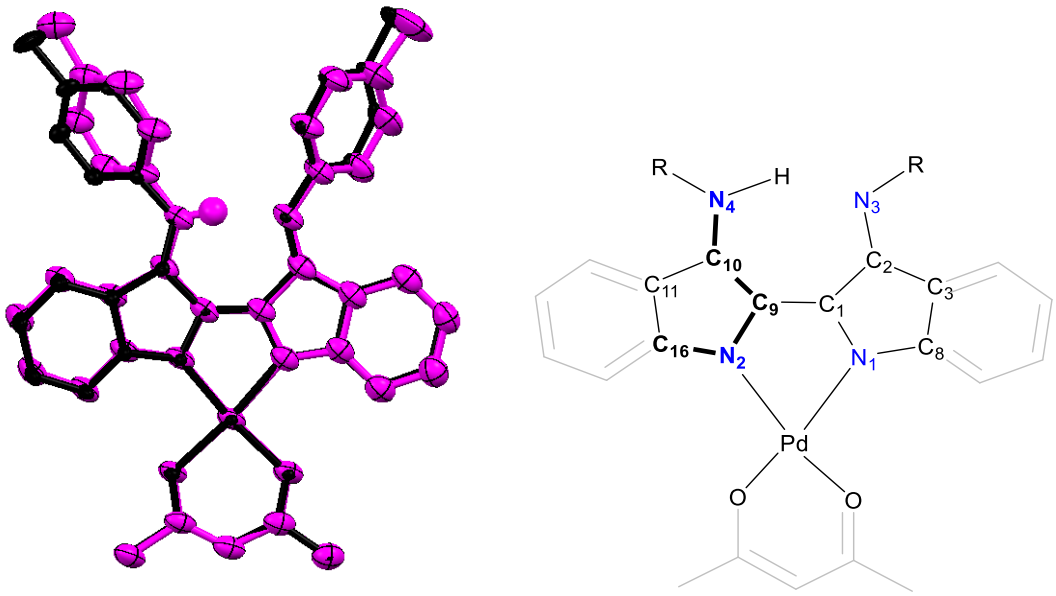

Figure 4.1 Structural comparison of **H4.11** (black) and **H4.11**$^{+}$ (pink) (Left); partial atom labelling scheme for **H4.11** and **H4.11**$^{+}$ (Right).

In 2014, Lahiri and Kaim investigated complex **H1.32**$^{+}$ (**H4.12**$^{+}$ with phenyl instead of *para*-tolyl groups) using spectroelectrochemistry.[68] They presented a scheme that a proton was lost in the oxidation of **H1.32**$^{+}$ in acetonitrile, but did not comment about or explain this assignment in the main text. The oxidation products of **H1.32**$^{+}$ were not isolated, the issue of the protonation state of the oxidized form seems unresolved.

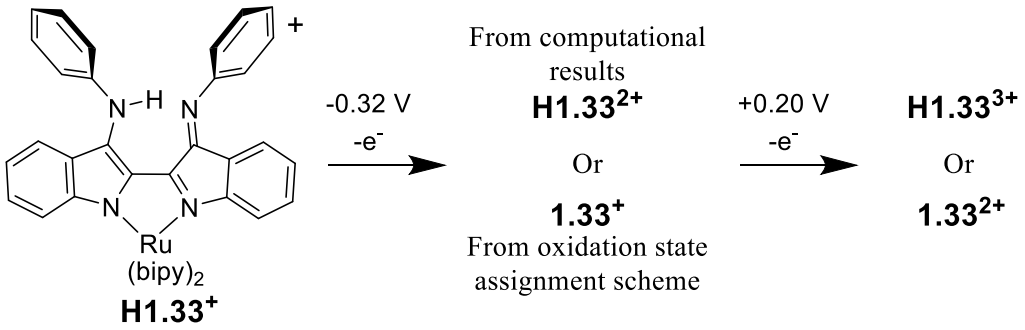

Scheme 4.3 The oxidation of **H1.33**$^{+}$ as depicted in reference 68.

H4.12^{+} was synthesized by the procedure of Lahiri and Kaim using *para*-toluyl substituted Nindigo **1.25** instead. The NMR, redox potentials, UV-Vis, and crystal structure mirror those of **1.25** except for the presence of the *para*-methyl group. Cyclic voltammetry measurements showed that **H4.12**$^{+}$ could be oxidized by one electron at -0.32 V versus ferrocene in acetonitrile. Orange-brown **H4.12**$^{+}$ was oxidized to bright green **H4.12**$^{2+}$ with either ferrocenium or silver (I) tetrafluoroborate. **H4.12**$^{2+}$ has the same cyclic voltammogram as **H4.12**$^{+}$ except for a shift in the open circuit potential (where no faradaic processes occur), indicating the compounds differ by a single electron. **H4.12**$^{2+}$ displays multiple strong absorbance peaks from 300 to 1500 nm which are nearly identical to those observed in the spectroelectrochemical oxidation of **1.32**.[68] Therefore it seems likely that deprotonation does not accompany a single electron oxidation of **H4.11**$^{+}$.

The EPR spectra of **H4.11**$^{+}$ and **H4.12**$^{2+}$ are isotropic in solution while their NMR spectra showed only a few, broad peaks, consistent with their paramagnetic nature. As shown in **Figure 4.2**, the EPR spectrum of **H4.11**$^{+}$ as a crystalline material broadens and the g value shifts slightly compared to the compound dissolved in dichloromethane. Although the radical is presumed to be ligand centered, the spectra lack ^{14}N hyperfine structure. This may be due to the presence of many, small and different coupling constants which are unresolvable. The spectra resemble those of a ligand based radical with g values close to the value of a free electron. Therefore, the EPR spectra suggest that oxidation has taken place on the ligand.

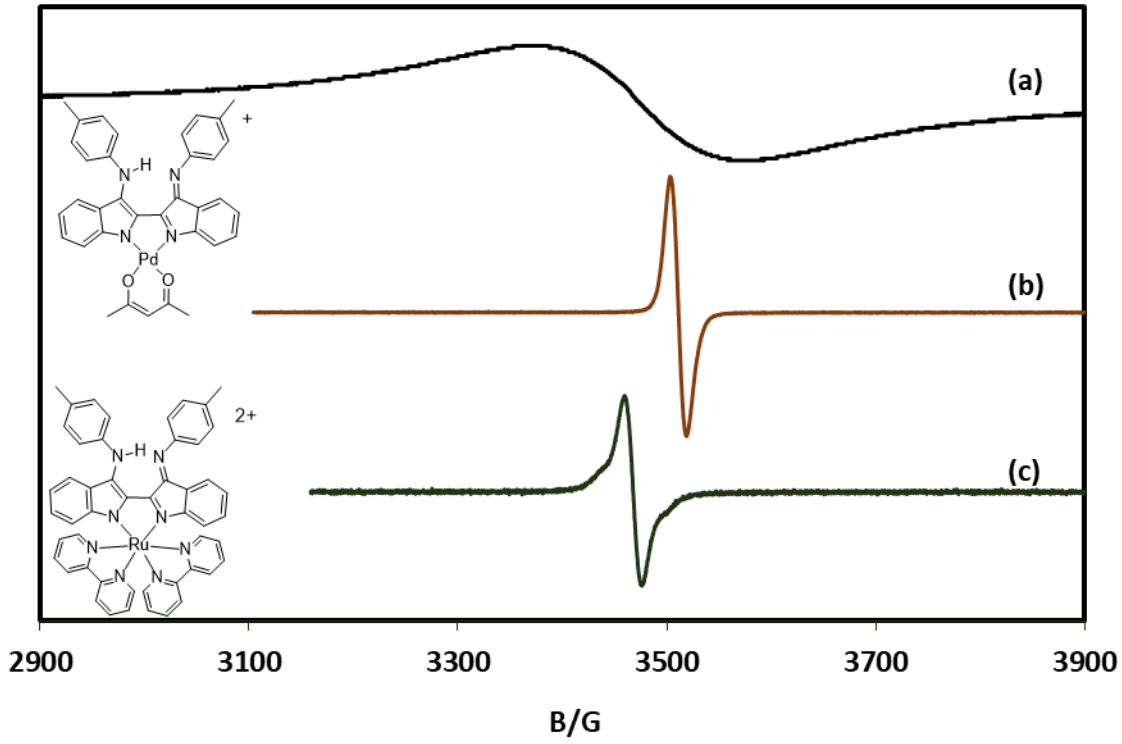

Figure 4.2 EPR of (a) **H4.11**$^{+}$**OTf** in the solid state at room temperature, g=2.0484; (b) **H4.11**$^{+}$**OTf** in dilute dichloromethane, g=2.0059; (c) **H4.12**$^{2+}$**BF**$_4$ in dilute dichloromethane, g=2.0310.

Two-electron oxidized products proved to be difficult to isolate. The second oxidation observed by cyclic voltammograms of **H4.11** and **H4.12**$^{+}$ are quasi-reversible indicating the desired compounds may be reactive. Attempts to generate **H4.11**$^{2+}$ gave an intractable mixture. Attempts to generate **H4.12**$^{3+}$ by oxidation of **H4.12**$^{+}$ with silver (I) tetrafluoroborate led to a red, NMR silent substance. Treatment of that solution with base to generate **4.12**$^{2+}$ gives a mixture that absorbs at 600 nm and resembled the spectra generated by Lahiri and Kaim through spectroelectrochemistry.[68] Aqueous workup, however, led to hydrolysis to the dicationic *cis*-indigo ruthenium-bis(bipyridyl) complex. Due to the apparent instability of two electron oxidized products, bond strength measurements and reactivity tests were therefore attempted without their isolation.

4.3 Determination of NH Bond Strengths

Attempts to determine the pK_a values for **H4.11** and **H4.12**$^{+}$ were hampered by the extremely low acidity of each compound and low stability of the deprotonation products. Weaker bases such as 1,8-diazabicyclo[5.4.0]undec-7-ene (DBU) did not react, as determined by UV-Vis or NMR spectroscopy. Attempts to generate fully deprotonated or equilibrium mixtures with strong bases such as NaH or benzyl potassium led to intractable mixtures. No reaction occurred, when **H4.11**, **H4.11**$^{+}$, **H4.12**$^{+}$, and **H4.12**$^{2+}$ were mixed with the weak hydrogen-atom abstractor TEMPO. This experiment indicates that the NH bond strengths for the four complexes are greater than 67 kcal mol^{-1}.

The pK_a of single electron oxidized complexes **H4.11**$^{+}$ and **H4.12**$^{2+}$ were instead sought. Treatment of **H4.11**$^{+}$ with sufficiently strong bases led to intractable mixtures. **H4.12**$^{2+}$ was titrated with a suitable base and the reaction was monitored by UV-Vis. In both cases, spectra were obtained that appeared to contain impure, reduced complexes. As

shown in **Figure 4.3**, treating **H4.12**$^{2+}$ with NEt_3 resulted in the appearance of spectral features resembling **H4.12**$^{+}$ and a band at 614 nm. The position of this band closely matches the band observed in the spectroelectrochemistry experiment carried out by Lahiri and Kaim for the second oxidation of **1.25**, i.e. "**4.12**$^{2+}$".[68] The authors assigned that spectrum to the one proton and two electron oxidized complex, i.e. **4.12**$^{2+}$, based on computational data. Although the fate of the proton in those spectroelectrochemical experiments is unclear, these experiments appear to validate the loss of a proton in their experiment.

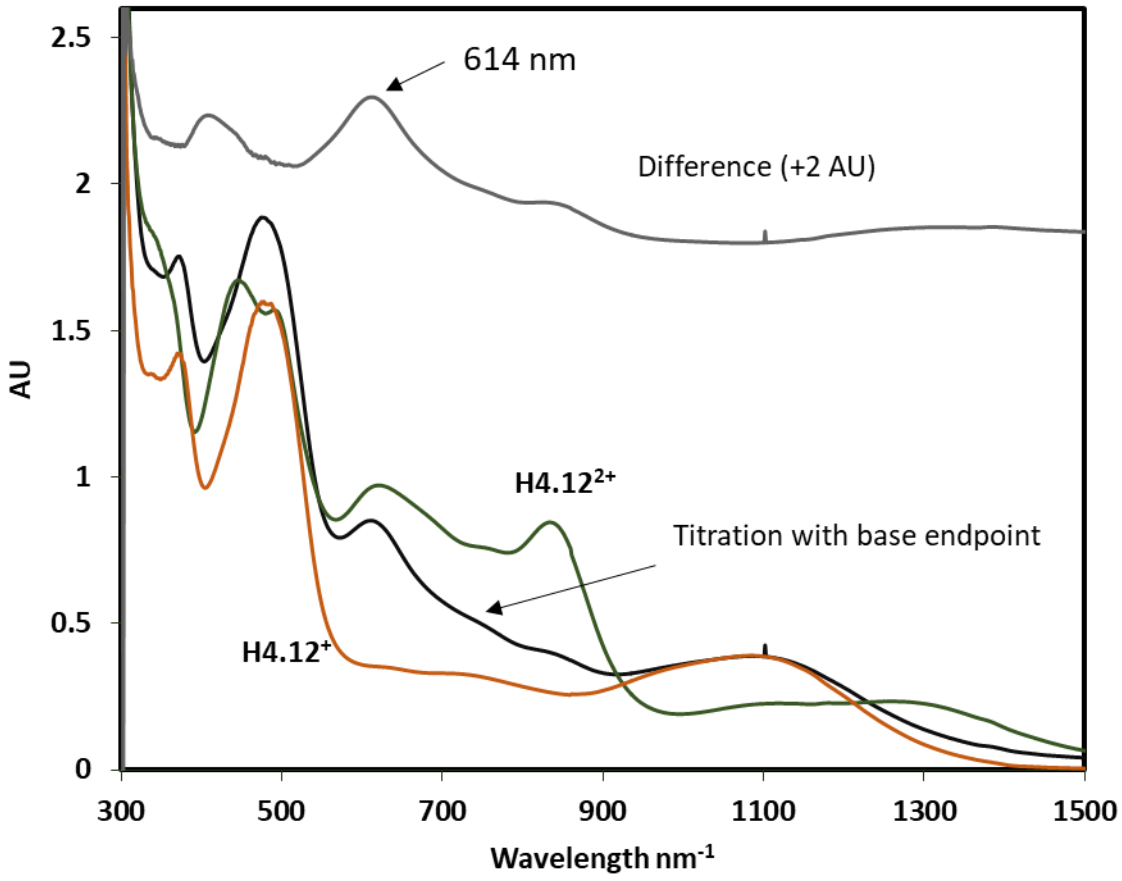

Figure 4.3 UV-Vis-NIR in acetonitrile of: **H4.12**$^{2+}$ (green); titration end-point of **H4.12**$^{2+}$ with NEt_3 (black); **H4.12**$^{+}$ normalized to equivalence at 1100 nm (orange); and difference spectra + 2 AU (grey).

The presence of **H4.12**$^{+}$ and **4.12**$^{2+}$ indicate that deprotonation induces electron transfer from **4.12**$^{+}$ to **H4.12**$^{2+}$. As depicted in **Scheme 4.4**, the deprotonated complex **4.12**$^{+}$ is as easily oxidized as **H4.12**$^{+}$, so the protonated complex **H4.12**$^{2+}$ oxidizes the deprotonated complex **4.12**$^{+}$ when there is a mixture of each. Because the equilibrium observed contains four products, no clean isosbestic points or pK_a value can be obtained.

$$NEt_3 + \mathbf{H4.12^{2+}} \rightleftharpoons \mathbf{4.12^{+}} + HNEt_3^{+}$$

$$\mathbf{H4.12^{2+}} + \mathbf{4.12^{+}} \rightleftharpoons \mathbf{H4.12^{+}} + \mathbf{4.12^{2+}}$$

Scheme 4.4 Proton induced disproportionation of **H4.12**$^{2+}$ and **4.12**$^{+}$.

Proton transfer induced internal redox reactions have been observed with other redox active ligands,[131] and may be a common attribute of these proton responsive RALs; the rich redox reactivity of RALs in general may hamper attempts at a direct determination of pK_a values.

Another method of analyzing the thermodynamics of proton and electron transfer is through the analysis of the electrochemistry of "buffered" proton donors or acceptors. This allows for the construction of potential-pH (Pourbaix) diagrams. In aqueous media, these are constructed by analyzing the electrochemistry of a given metal or substrate in water that is buffered at a given pH and plotting pH versus potential. These diagrams were initially very useful in studying the stability of metals and their salts in different conditions, and continue to be used to describe corrosion processes.[132] More recently these diagrams have been used to study the proton coupled electron transfer of molecules, clusters, and the hydrogen evolution reaction.[35,133]

Non-aqueous Pourbaix diagrams are rare due to the difficulty of the determination of pH in non-aqueous systems. The value of pH is defined as the negative logarithm of the

activity of protons.[134] Outside of protic solvents, these activities are difficult to determine because of the lack of solvated protons. However, self-consistent measures of pK_a values in several polar and non-polar solvents have been made including acetonitrile[135-136] and tetrahydrofuran (THF).[137] These pK_a scales provide the thermodynamic information about the transfer of a proton from an acid to a base in these solvents. In addition to accessing data for hydrophobic compounds, stronger bases and acids can be used without levelling in the solvent because of the wider range of pK_a units in non-aqueous solvents.

Several recent examples exist where pK_a-potential diagrams were constructed in acetonitrile[138-139] or tetrahydrofuran.[140] The addition of a base, acid, or a base with its conjugate acid ("buffered") of known pK_a in the given solvent leads to pK_a dependent shifts in electrochemical measurements. For oxidation of a protic substrate "HB" in the presence of a base, redox potentials are expected to follow the equation:

$$E^{o\prime} = E_{1/2}(HM) + 2.303\frac{mRT}{nF}\Delta pK_a - 2.303\frac{mRT}{nF}\log\left(\frac{[HM][Base]}{[M][HBase^+]}\right) \qquad \textbf{(2)}$$

where m is the number of protons and n is the number of electrons.[138] At $E_{1/2}$, [HM] = [M], and at sufficiently high concentrations of a 1:1 buffer, [Base]/[HBase] = 1, so the third term becomes zero. Therefore, the data for these potential-pK_a diagrams is collected in 1:1 buffers. **Equation 4.2** also shows that at 298 K, the oxidation potentials of a substrate should change with a slope of 59 mV for a one electron one proton process or 29 mV for a two electron one proton process. This line intersects with the unbuffered redox potential at the point where the compound and buffer are the same pK_a, so the pK_a of HM can be determined directly from this graph.

Figure 4.4 shows representative cyclic voltammograms of **H4.11** in buffered and unbuffered solutions. **H4.11** in unbuffered tetrahydrofuran exhibits one reversible

oxidation and a second, quasireversible oxidation. Addition of sufficiently weak bases shifts the second oxidation potential. There are a limited number of bases with known pK_a values that do not react directly with **H4.11** (e.g. PPh_3) or are not susceptible to oxidation at the required potentials (eg. substituted anilines). As a result, only one data point was successfully gathered at a sufficiently low pK_a to see a shift in the second oxidation potential. Voltammograms containing bases with pK_a values greater than 9.5 showed no second oxidation wave, but contained one oxidation that was double in current from the unbuffered voltammogram. Using 2,6-lutidine as the base, this oxidation was reversible. With higher pK_a buffers, the oxidation gradually became less reversible. As the pK_a of the conjugate acid/base mixture was increased, the oxidation potential shifted by 28 mV per pK_a unit, close to the theoretical value of 29 mV / pK_a unit for a one proton, two electron oxidation, i.e. hydride loss. It is likely that the bases are reactive to the electro-generated **4.11**$^+$ due to coordination, hydrogen atom transfer, or hydride transfer (*vide infra*).

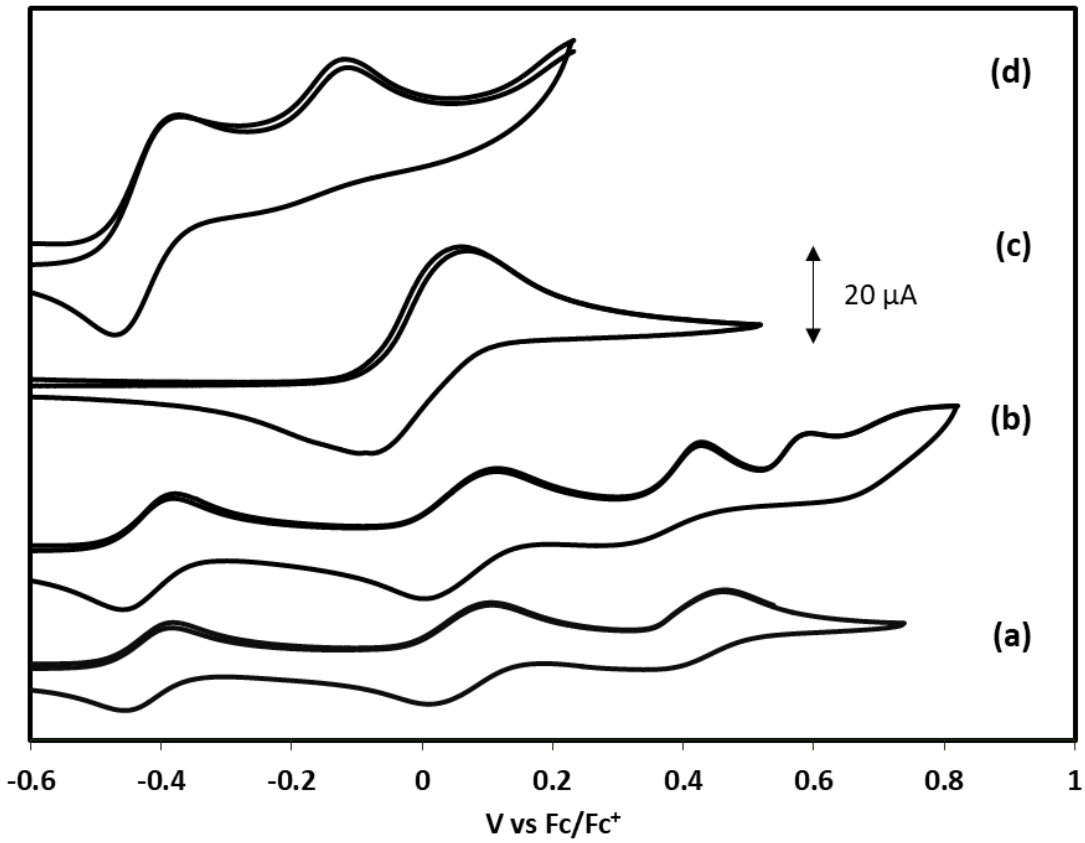

Figure 4.4 Cyclic voltammograms of **H4.11** at 100 mV/s in 0.1 M NBu_4PF_6 tetrahydrofuran and **(a)** no buffer; containing 15 mM $MeSO_3H$ and 15 mM **(b)** 4-bromoaniline ($pK_{a,THF}$=6.2); **(c)** 2,6-lutidine ($pK_{a,THF}$=9.5); **(d)** 1,8-diazabicyclo[5.4.0]undec-7-ene ($pK_{a,THF}$=19.1). The reversible wave at -0.48 V vs. ferrocene is the internal standard, decamethylferrocene.

From these measurements, a potential-pK_a diagram for **H4.11** was constructed and is shown in **Figure 4.5**. It must be noted that information about the potentials of this diagram cannot be directly translated into ΔG values of the observed proton coupled electron transfers since it is *oxidation potentials* that are reported, not $E_{1/2}$ values. However, the slope and intersection points allow for the calculation of the pK_a value of **H4.11**$^+$, which allows for the determination of the NH bond strengths at different ligand charge states as is further described in section **4.4**.

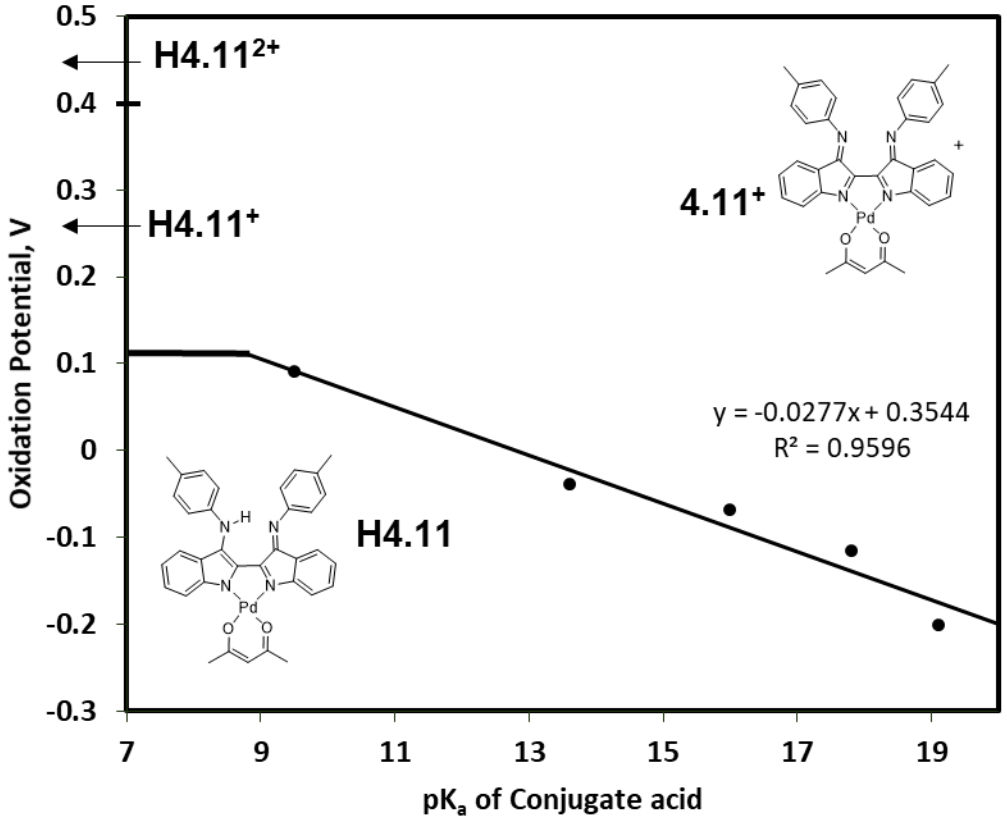

Figure 4.5 Potential-pK_a diagram for the oxidation of **H4.11**. Bold lines on the left side indicate oxidation potentials in the absence of buffers.

A potential-pK_a diagram for **H4.12**$^+$ was constructed similarly in acetonitrile. A wider pK_a range was possible due to the greater number of bases with known pK_a values that were accessible. Several representative voltammograms are displayed in **Figure 4.6**.

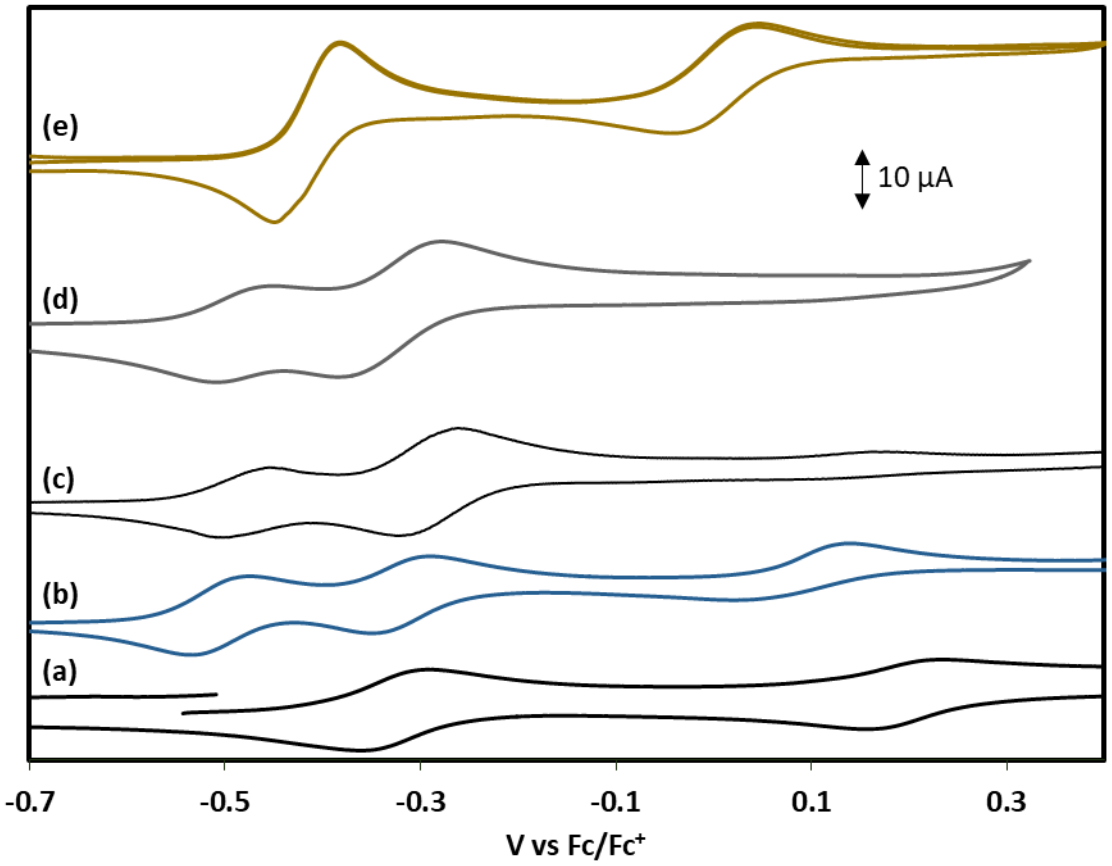

Figure 4.6 Representative cyclic voltammograms of 1 mM **H4.12**$^+$ in acetonitrile with 0.1 M NBu_4PF_6 and **(a)** no buffer; **(b)** 15 mM $MeSO_3H$ and 30 mM pyridine ($pK_{a,MeCN}$=12.53); **(c)** 2 mM benzylamine ($pK_{a,MeCN}$=16.91); **(d)** 15 mM $MeSO_3H$ and 30 mM triethylamine ($pK_{a,MeCN}$=18.82); **(e)** 15 mM $MeSO_3H$ and 30 mM tetramethylguanidine ($pK_{a,MeCN}$=23.3).

Voltammograms of **H4.12**$^+$ contain a reversible oxidation followed by a quasi-reversible oxidation. On addition of a weak base, the second oxidation peak shifts to less positive potentials. Data for the second oxidation potential are obtained from square-wave voltammetry due to the difficulty in determining return peak potentials. Addition of stoichiometric or slight excesses of intermediate strength bases such as benzyl amine (pK_a = 16.91) leads to a decrease in current of the second oxidation while the current of the first oxidation increases. At higher concentrations of base (such as was used for generation of the potential-pK_a diagram), the second oxidation disappears entirely. Voltammograms

containing buffers of bases with pK_a values between 16 and 18 led to a disappearance of a second oxidation wave without a shift in $E_{1/2}$. As the pK_a values of the base were further increased, the $E_{1/2}$ values became more negative. The combined, double current oxidation shifted by 23 mV / pK_a. This data allowed for the construction of the Pourbaix diagram shown in **Figure 4.7**.

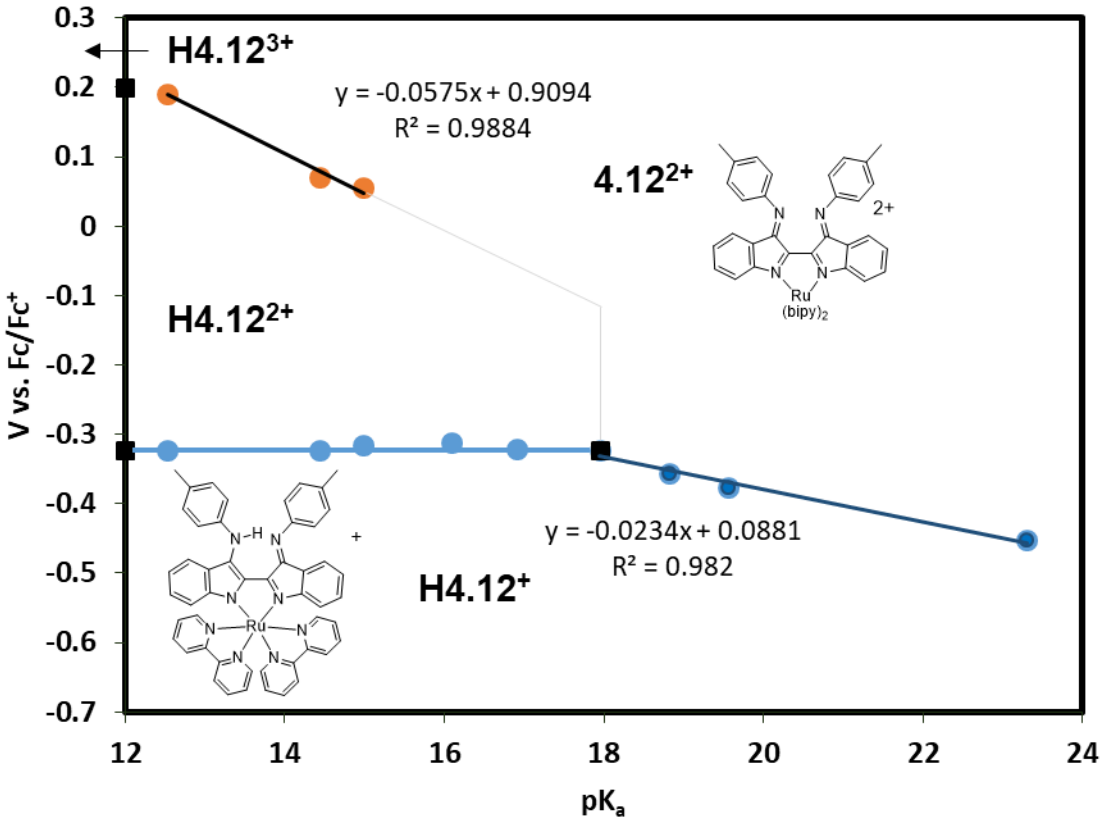

Figure 4.7 Potential-pK_a diagram for the oxidation of **H4.12**$^+$. The grey line represents the predicted but unobserved trend for the second oxidation.

The use of buffers containing anionic bases benzoate (pK_a = 21.51) and 2,4,6-tribomophenolate (pK_a = 20.35) were also attempted for the construction of **Figure 4.7**. These bases should be sufficiently strong to shift the oxidation potential, but do not. A fully reversible, two electron oxidation occurred at -0.32 V versus ferrocene, identical to what is seen in unbuffered voltammograms. It is possible that ion pairing of the cationic substrate

with the anionic base may change the pK_a of the base. Hydrogen bonds formed with the conjugate acids are also known to change the pK_a values of acids and bases.[141] Due to this complication, anionic bases are not used for the construction of **Figure 4.7**.

Cyclic voltammograms with bases with pK_a values above 24 contained irreversible oxidations so are not plotted. Two possibilities are envisioned for the observed irreversibility. Firstly, the oxidation potential expected in those buffer solutions may be lower than the reduction potential of **4.12**$^{2+}$. Secondly, such electron rich bases may be susceptible to hydrogen atom and hydride transfer (or other reactions) with the electrogenerated complex.

4.4 Discussion

pK_a, bond dissociation free energy (BDFE), and hydricity or hydride affinity (the capacity to undergo the net transfer of one proton and two electrons) values can be extracted from the experiments used to generate potential-pK_a diagrams (**Figures 4.5** and **4.7**). Because oxidation potentials (not $E_{1/2}$ values) are used in **Figure 4.5** for palladium complex **4.11**, BDFE and hydricity values cannot be specifically extracted. In potential-pK_a diagrams, the intercept of diagonal lines with horizontal lines is the pK_a of the generated compound. Thus, the pK_a value of **H4.11**$^{+}$ can be estimated to be 9 in THF. Using the pK_a and the $E_{1/2}$ from the unbuffered experiment, **Equation 4.1** gives a BDFE of 80 kcal mol^{-1} for **H4.11**.

Although the sloped line obtained from the raw data cannot be used explicitly, the *intersection point* (which is the beginning for the one proton, two electron oxidation event) can be used to determine hydricity values. The intersection point is at the pK_a of 9 and the zero-slope line formed at the values of $E_{1/2}$ in low pK_a buffers and unbuffered

voltammograms (+0.06 V). The hydricity in this case can be calculated by use of **Equation 4.3** where $E_1^o = E_2^o = +0.06$ V:

$$\Delta G_{Hydride} = 23.06\ (E_1^o + E_2^o) + 1.37\ pK_a + C_{g,H^-} \quad \textbf{(4.3)}$$

In **Equation 4.3**, the constant $C_{g,H-}$ represents the two electron reduction of free protons in a given solvent versus the ferrocene/ferrocenium redox couple. For acetonitrile, $C_{g,H-}$ is reported as 79.6.[142] For tetrahydrofuran, this number can be estimated by a thermochemical cycle shown in **Scheme 4.5**. This thermochemical cycle compares the estimates of heterolytic cleavage of dihydrogen with reported H-H bond strength. The pK_a of H_2 has been estimated in tetrahydrofuran as close to but greater than 49,[143] and the free energy of proton reduction versus ferrocene (C_g) is 66 kcal mol^{-1}.[123] The homolytic bond strength of dihydrogen in tetrahydrofuran can be determined by addition of the free energy of solvation for hydrogen in (4.87 kcal mol^{-1})[144] to the gas phase bond strength (97.2 kcal mol^{-1}).[119] The constant $C_{g,H-}$ is therefore estimated as 97 kcal mol^{-1}.

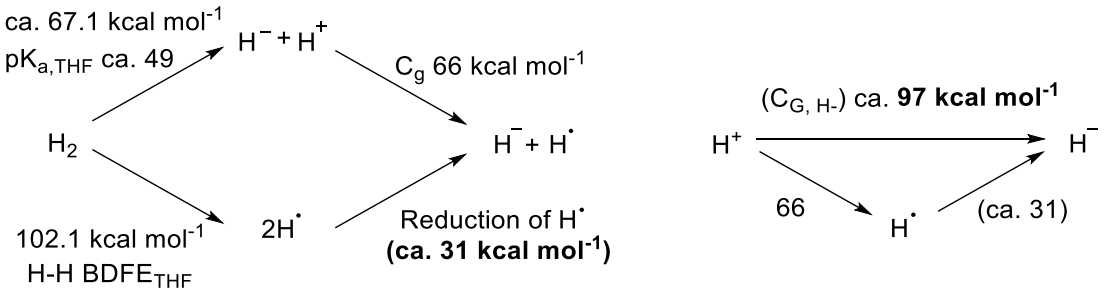

Scheme 4.5 Thermochemical cycle for the estimation of the reduction potential of protons to hydrides in THF.

Because the free energy of a net proton and electron transfer reaction is not path-dependent, **Equations 4.1** and **4.3** can be reorganized to determine the remaining pK_a, BDFE, and hydricity values. These values are summarized in a square scheme, shown in **Scheme 4.6**.

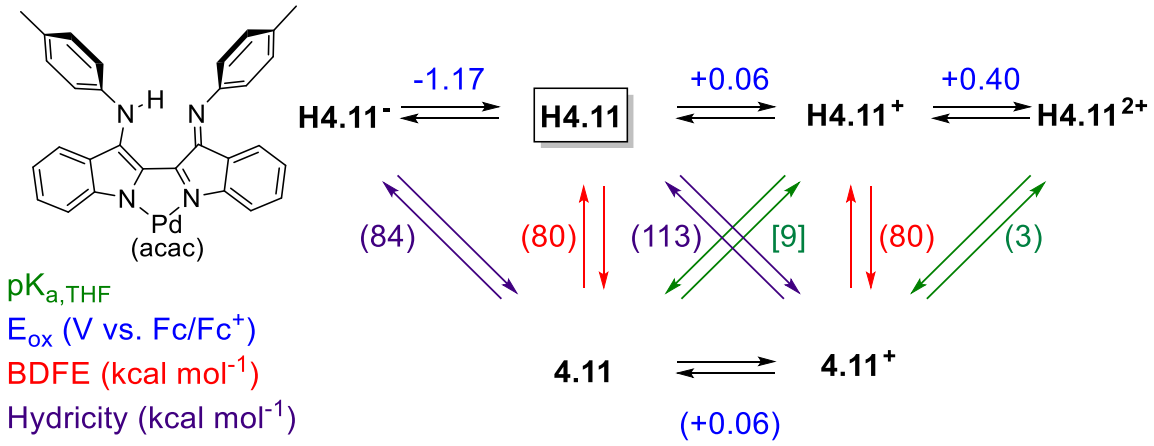

Scheme 4.6 Square scheme for **H4.11** in 0.1 M NBu_4PF_6 in tetrahydrofuran. Bracketed numbers are obtained directly from **Figure 4.6**. Numbers in parentheses are generated through **Equation 4.1** and **4.3**.

The N-H bond dissociation free energies (BDFE) of **H4.11** and **H4.11**$^+$ are quite high and lie within the ranges of other conjugated amines such as bis(4-methylphenyl)amine (NH BDFE = 82.9 kcal mol^{-1}).[119] Coordination to palladium (II) did not substantially weaken the NH bond. This contrasts with the results of Heyduk[92] and Brown[117] who reported substantial bond weakening upon coordination, estimated at ca. 10-30 kcal mol^{-1} based on a loose comparison to the NH bond strengths of diphenylamine and amidophenolate. The difference likely lies in the invariance in acidity of **H4.11** because the NH is relatively far removed from the metal. The pK_a value of **H4.11**, a hydrogen bonded secondary amine, should be very high (>30). The deprotonation of **H4.11** is indeed inaccessible except by very strong bases. For complex **4.7** where the amine is directly coordinated, the NH is substantially more acidic (pK_a=16-17). Coordination to palladium (acac) therefore did not weaken the bonds significantly, but did modulate the oxidation potentials and stabilized the radical forms of the ligand such that they are isolable.

The hydricity energy of **H4.11** is exceptionally high at 113 kcal mol^{-1}. The hydricity of **H4.11**$^{-}$ is comparatively low at 84 kcal mol^{-1} due to the negative charge. Both compounds are very poor hydride donors. Conversely, **4.11** and **4.11**$^{+}$ are anticipated to be exceptionally strong hydride abstractors. A very high hydricity value is generally expected for electronegative atoms such as nitrogen. The NH hydricity of several heterocycles in acetonitrile are known and range from 84-112 kcal mol^{-1}.[145] Thus **H4.11** and **H4.11**$^{-}$ lie well within normal ranges for NH hydricities.

The pK_a values, bond strengths, and hydricity values of the ruthenium complex, **4.12**$^{+}$, are determined in the same manner as their palladium based congeners and are summarized in **Scheme 4.7**. For the potential-pK_a diagram **Figure 4.7**, the reported values are $E_{1/2}$ values for the first oxidations, the data is extracted directly from the diagram.

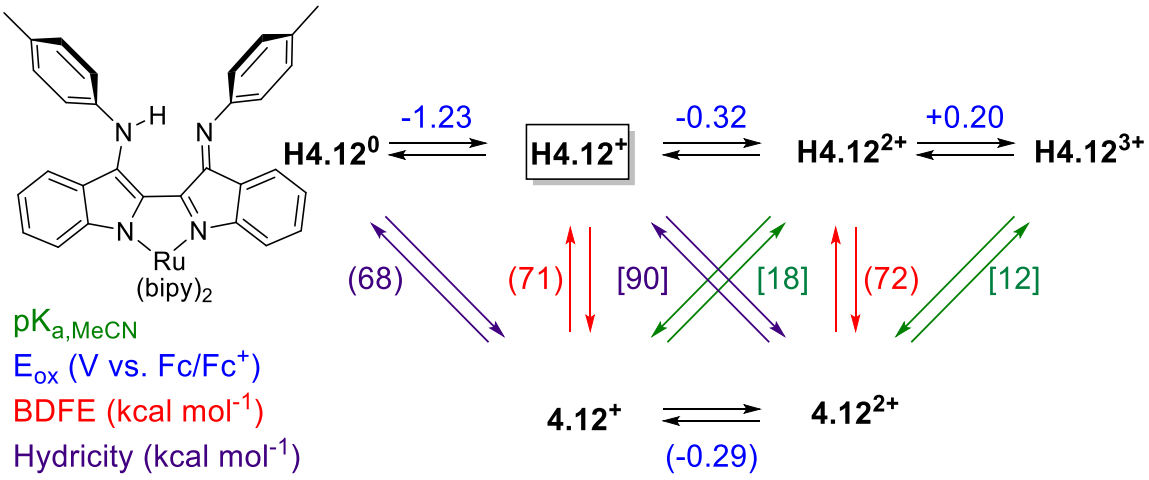

Scheme 4.7 Square scheme for **H4.12**$^{+}$ in 0.1 M NBu_4PF_6 in acetonitrile. Bracketed numbers are obtained directly from potential pK_a diagram **Figure 4.7**. Numbers in parentheses are generated through **Equation 4.1** and **4.3**.

Like **H4.11**, coordination does not appear to increase the acidity of **H4.12**$^{+}$ or its oxidation products. Despite its high cationic charge **H4.12**$^{2+}$ is weakly acidic. Its pK_a of 18

is close to the value for 4-(dimethylamino)pyridinium (pK_a= 17.95). Complex **H4.12^{3+}** is approximately as acidic as pyridinium despite being tricationic. The NH bond strengths of ruthenium complexes **H4.12^{+}** and **H4.12^{2+}** of 71 and 72 kcal are relatively weak, lying between the bond strengths of TEMPOH (66 kcal mol^{-1}) and 2,4,6-tri-*tert*-butyl phenol (77 kcal mol^{-1}).[119]

H4.12 is considered a moderate hydride donor at 69 kcal mol^{-1}. For reference, **H4.12** is only a slightly weaker hydride donor than $HB(C_6F_5)_3^-$ which has a hydricity of 65 kcal mol^{-1}.[145] **H4.12^{+}** is a weak hydride donor at 90 kcal mol^{-1}, although this value is quite low considering it is a cation.

The cause of the proton transfer induced disproportionation observed for **H4.12^{2+}** is clearly demonstrated in **Scheme 4.7**. Complex **4.12^{+}** is oxidized at a potential 0.02 V more positive than the reduction of **H4.12^{+}**, making the comproportionation constant very close to zero. The pK_a of **H4.12^{2+}** of 18 is close to the pK_a of the triethylamine titrant, so an equilibrium mixture of all four (conjugate) acids and bases occurs. The small difference in potentials also bears out in the cyclic voltammograms buffered at pK_a values between 15 and 18. These voltammograms show a two-electron oxidation at -0.32 V that likely follows an electron-proton-electron transfer (ECE) or disproportionation type path.

The pK_a values reported in **Schemes 4.6** and **4.7** show clear parallels with one another. **H4.11** and **H4.12^{+}** are very weak acids that cannot be deprotonated by the strongest base used, DBU, giving them a pK_a higher than 19.1 in tetrahydrofuran and higher than 24.34 in acetonitrile. The pK_a values of oxidized forms **H4.11^{+}** and **H4.12^{2+}** are substantially smaller, making the compounds susceptible to deprotonation by pyridine type bases. The acetonitrile based pK_a values of compounds can be estimated from their

measured pK_a in tetrahydrofuran by the method of Morris in **Equations 4.4** and **4.5.**[141] Using **Equation 4.5**, the pK_a of **H4.11**$^+$ is 14. Despite its additional cationic charge, ruthenium complex **H4.12**$^{2+}$ (pK_a=12) is not significantly more acidic than palladium complex **H4.11**$^+$.

$$pK_a^{MeCN} = 0.81\, pK_a^{THF} + 1.0 \text{ for neutral acids} \quad \textbf{(4)}$$

$$pK_a^{MeCN} = 1.13\, pK_a^{THF} + 3.7 \text{ for cationic acids} \quad \textbf{(5)}$$

The NH bond strengths differ more dramatically than pK_a values. A qualitative direct comparison here can be used because there is no change in charge when removing a hydrogen atom, the NH is sterically shielded, and the two complexes are roughly the same size. Thus solvation changes are not expected to drastically affect the bond strength values. The NH bond in palladium complexes **H4.11**$^{n+}$ are 8 to 9 kcal mol^{-1} stronger than ruthenium complexes **H4.12**$^{n+}$.

The difference in bond strengths arise from the role the metal plays in the redox activity of the complex. Although the metal does not change oxidation state in both cases per se, computational studies from Lahiri and Kaim on the near-identical ruthenium complex **H1.32**$^{2+}$ indicate there is 25% spin density on the ruthenium. The contribution of the ruthenium to the π-system seems to stabilize the oxidized forms of the ligand which in turn weakens the NH bond. This stabilization is not seen to the same extent in the palladium complexes. Coordination seems to have stabilized the radical states in both complexes, however. The NH bond strength of **H4.11** and **H4.12**$^+$ do not differ significantly from their one electron oxidized analogues **H4.11**$^+$ and **H4.12**$^{2+}$ despite the latter two being nominally organic centered radicals.

4.5 Conclusions

Cis-Nindigo complexes are able to act as proton and electron reservoirs. The NH bond strengths and hydricity values determined for **4.11**$^{n+}$ and **4.12**$^{n+}$ in this chapter are quite high. In other words, **4.11**$^{n+}$ and **4.12**$^{n+}$ have high hydrogen atom and hydride *affinities*. The elementary steps of proton coupled oxidation of these complexes are easily accessible indicating this class of compounds may be potent hydrogen atom and hydride abstractors which are easily regenerated. The potential for net two-electron chemistry is born out in the net hydride transfer events observed in buffered solutions. Furthermore, this study shows the role metal choice plays in the homolytic and heterolytic bond strength of these complexes. Even in these remote protonation sites, the change in metal induced a 9 kcal mol^{-1} NH bond weakening.

4.6 Experimental Methods

The Pourbaix diagram was constructed from cyclic voltammetry. A "blank" voltammogram of the solvent with electrolyte (0.1 M NBu_4PF_6) in dry acetonitrile that was sparged with argon was collected. The analyte (1 mM) was then dissolved and the voltammogram collected to ensure consistency. Base (1 mole equivalent) and internal standard (Ferrocene for bases with pK_a greater than 20, otherwise decamethylferrocene $E_{1/2}$= -0.505 versus ferrocene) was then added and the response at different scan rates was analyzed. The experiment was repeated with 30 equivalents of base. 15 equivalents of acid (triflic acid for pK_a under 15, otherwise trifluoroacetic acid).

Potential-$pK_{a,THF}$ diagram of **4.11**: 380 mg of tetrabutylammonium hexafluorophosphate was dissolved into dry tetrahydrofuran and the solution was sufficiently sparged with argon to deoxygenate. A blank voltammogram was run to ensure

no electroactive species or oxygen are present. Then 6.4 or 6.5 mg of **4.11** were dissolved and a voltammogram was obtained to ensure consistency. 30 mol equivalents of base followed by 15 mol equivalents of acid were then added to form the buffer solution. Voltammograms were obtained at doubling increments from 50 mV s^{-1} to 25 V s^{-1}.

Potential-$pK_{a,MeCN}$ diagram of **4.12**$^{+}$: 380 mg of tetrabutylammonium hexafluorophosphate was dissolved into dry acetonitrile and the solution was sufficiently sparged with argon to deoxygenate. A blank voltammogram was run to ensure no electroactive species or oxygen are present. Then 9.8 mg of **4.12**$^{+}$ were dissolved and a voltammogram was obtained to ensure consistency. 30 mol equivalents of base followed by 15 mol equivalents of acid were then added to form the buffer solution. Voltammograms were obtained at doubling increments from 50 mV s^{-1} to 25 V s^{-1}.

Bis-bipyridyl[*cis*-1*H*-indigo-bis(2,6-dimethylphenylimine)]ruthenium tetrafluoroborate H4.12^{+}**:** Silver (I) tetrafluoroborate (140 mg, 0.719 mmol) was weighed out and added to a round bottom flask in the glove box. $Ru(bipy)_2Cl_2 \cdot H_2O$ (160 mg, 0.318 mmol) was added to the flask out of the box, and the flask evacuated and backfilled with N_2 three times. To the solids was added 60 mL of absolute ethanol that was freshly distilled from CaH_2. The mixture was heated to reflux for 3 hours, cooled, and filtered under nitrogen into a flask containing indigo bis-(*para*-toluylimine) (139 mg, 0.316 mmol). NEt_3 (43 mg, 0.42 mmol) was added, and the mixture was heated to reflux for 24 hours. The mixture was cooled to room temperature and evaporated on a rotary evaporator. The residue was purified via alumina column chromatography: the residue was loaded and eluted with dichloromethane obtaining a blue band. An orange-brown band was then eluted using 20% acetonitrile in dichloromethane and the eluent was evaporated. The residue was

then dissolved in dichloromethane and washed twice with aqueous 0.5 M potassium hydroxide twice. The organic layer was dried over anhydrous magnesium sulfate, filtered, and concentrated to 5 mL. The solid was precipitated with addition of an equal volume of ether to yield black microcrystalline solid (154 mg, 51.6% yield). ^{1}H NMR (500 MHz, $(CD_3)_2SO$): δ 11.77 (s, 1H), 8.79 (d, 8.2 Hz, 2H), 8.74 (d, 8.2 Hz, 2H), 8.14 (td, 7.7, 1.2 Hz, 2H), 8.09 (d, 5 Hz, 2H), 8.04 (td, 7.3, 1.4 Hz, 2H), 7.86 (d, 5.5 Hz, 2H), 7.55 (td, 7.0, 1.0 Hz, 2H), 7.51 (t, 7.0 Hz), 7.21 (d, 8.2 Hz, 4H), 7.14 (d, 8.3 Hz, 4H), 6.96 (d, 8.0 Hz, 2H), 6.73 (td, 8.2, 1.0 Hz, 2H), 6.54 (d, 7.4 Hz, 2H), 5.19 (d, 8.4 Hz, 2H), 2.32 (s, 6H) ppm. ^{13}C NMR (125.793 MHz, $(CD_3)_2SO$): δ 158.2, 156.9, 154.2, 151.7, 151.1, 148.0, 141.8, 136.6, 136.0, 133.6, 130.2, 129.8, 127.3, 127.1, 124.4, 123.9, 123.6, 120.3, 120.0, 118.6, 113.6, 20.5 ppm. ^{19}F (282.5 MHz $(CD_3)_2SO$): δ -148.2 (s), -148.3 (s) ppm. FTIR (KBr pellet, air background): 2955 w, 2925 w, 2853 w, 1595 m, 1560 m, 1544 m, 1508 w, 1500 w, 1483 m, 1466 m, 1443 s, 1365 w, 1300 m, 1190 s, 1114 s, 928 w, 760 s, 584 w.

Acetylaceonato[*cis*-1*H*-indigo-bis(*para*-methylphenylimine)]palladium triflate H4.11^{+}·C$_7$H$_8$: An oven dried, nitrogen purged Schlenk tube was charged with silver (I) triflate (37 mg, 0.14 mmol) and **4.8** (93.8 mg, 0.146 mmol). Dry dichloromethane (6 mL) was added via syringe, and the mixture was stirred for 2 hours. The reddish mixture was cannula transferred onto a Celite layered glass frit, filtering into a second Schlenk tube, and washed through with 6 mL dichloromethane. To the resultant solution was added toluene (12 mL), and the solution held at -10 overnight. 91 mg (73% yield) of X-ray quality crystals were collected by filtration in air. Mp 260-262 ^{o}C. ^{1}H NMR (500 MHz, CD_2Cl_2): δ 7.27-8.00 (br), 7.11-7.26 (m, 8H), 2.34 (s, 4 H), 1.57 (s, 6H), -0.20-1.00 (br) ppm. Evans Method (CD_2Cl_2): 298 K on 300.27 instrument, 7.8 mg in 0.6435 g solvent gives 20.3 Hz

shift (μ_{eff} = 1.24). FT-IR (KBr pellet) cm^{-1}: 3465 w br, 2922 w, 1561 s, 1522 s, 1471 w, 1455 m, 1372 s, 1267 vs, 1222 w, 1193 w, 1150 m, 1116 w, 1030 s, 940 w, 824 w, 761 m, 636 s, 586 w, 516 m. Anal. Calc. for $C_{36}H_{30}F_3N_4O_5PdS \cdot C_7H_8$: C, 58.27; H, 4.32; N, 6.32. Expt. C, 58.05; H, 4.14; N, 5.88. UV-Vis-NIR (tetrahydrofuran) λ_{max}, nm (ε, $M^{-1}cm^{-1}$): 293 (17,000), 892 (5,800).

Bisbipyridyl[*cis*-1*H*-indigo-bis(2,6-dimethylphenyl)diiminato]ruthenium di-tetrafluoroborate H4.12^{2+}: Ferrocenium tetrafluoroborate (10 mg, 36 μmol) was dissolved in acetonitrile and the mixture was freeze-pump-thawed. On the final cycle, **H4.12**$^{+}$ (34 mg, 36 μmol) was added. The mixture was warmed to room temperature under nitrogen flow and stirred for 1 hour. The green liquid was evaporated, and the residue washed with several aliquots of tetrahydrofuran. After recrystallization from acetone/ethyl acetate, 27 mg of dark green solid were isolated (74% yield). Mp 245 ^{o}C decomp. Evans Method (CD_3CN): 298 K on 300.27 instrument, 2.8 mg in 0.452 g solvent gives 8.1 Hz shift (μ_{eff} = 1.7). Anal. Calc. for $C_{50}H_{39}B_2F_8N_8Ru \cdot H_2O$: C, 57.49; H, 3.96; N, 10.73. Expt. C, 57.81; H, 3.79; N, 10.43. UV-Vis-NIR (MeCN) λ_{max}, nm (ε, $M^{-1}cm^{-1}$) 244 (38,000), 285 (53,000), 445 (16,000), 493 (15,000), 623 (9,900) 834 (8,000), 1,254 (2,200). FTIR (KBr): 3411 br (H_2O), 2921 w, 1602 m, 1465 s, 1444 vs, 1375 w, 1310 w, 1284 w, 1162 w, 1055 vs (BF_4), 930 w, 903 w, 761 vs, 521 w. ESI-HRMS: theor 853.23412 (M^{+}), expt 853.23343.

Chapter 5 Non-innocence, Proton Transfer, and Electron Transfer in Ruthenium Acetylacetonate Complexes of Nindigo and Mindigo

5.1 Introduction

The thermodynamics of proton, hydrogen atom, and hydride transfer from redox-active ligands have been explored in Chapter 4 and by others. However, among the cases where a redox-active ligand can gain or lose a proton, there are only a handful of instances where both protonation states can be isolated (section 4.1). It is well known that changes in the protonation state of ligands can lead to large changes in metal-centered redox potentials.[132] Likewise, protonation or deprotonation can drastically affect redox potentials of redox-active conjugated systems. Therefore a change in the protonation state of a redox-active ligand should lead to drastic changes in the overall electronic structure of complexes containing redox-active ligands.

Complexes of *cis*-Mindigo and Nindigo provide a good scaffold to understand the role a proton can have on the electronic structure of RAL complexes when the proton is far removed from the metal. *Cis*-Mindigo and Nindigo differ from most other RALs in that the site of proton transfer is five bonds away from the metal. Coordination to a metal therefore should not greatly affect the acidity of the NH by electronics or electrostatics. Situated in the γ-diimine pocket, the proton is also orthogonal to the redox-active π-bonds of the ligand. As a result, there are no major changes in the geometry at the nitrogen atom upon protonation; the nitrogen remains sp^2 hybridized whether a proton is present or not. However, no routes to complexes of the deprotonated ligands have been successful to date.

We envisioned that $Ru(acac)_2$ complexes of Mindigo and Nindigo could be synthesized that were analogous to indigo complexes **5.1** and **H5.2**. These indigo complexes which were reported by Lahiri et al in 2016,[90] contained a *cis*-indigo ligand that is oxidized by two protons and two electrons (**5.1**), and a *trans*-indigoid ligand that is oxidized by one electron and one proton (**H5.2**). Complexes **5.1** and **H5.2** exhibited both ligand and metal centered redox activity. Mindigo and Nindigo analogues, which would have imines instead of ketones, were expected to be significantly more basic and would be amenable to reversible protonation.

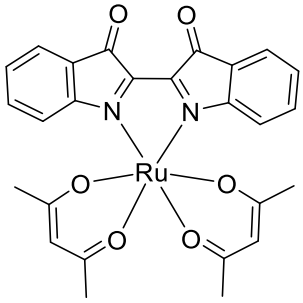

5.1

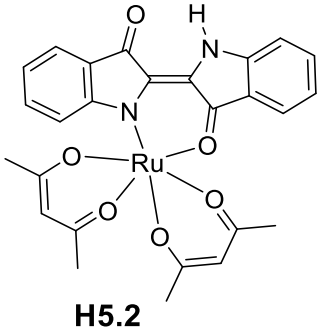

H5.2

Complexes of *cis*-Mindigo and Nindigo of the $Ru(acac)_2$ moiety were therefore targeted to compare the electronic structure of complexes with and without a proton. Furthermore, the potential for multiple ligand and metal redox processes allowed for the determination of the role played by ligand charge states in the NH bond strength. This chapter reports the synthesis of these *cis*-Nindigo and Mindigo ruthenium bisacetylacetonate complexes, their proton transfer reactivity, the effect of protonation on the complexes' electronic structure, and the thermodynamics of their proton-coupled electron transfer reactions.

5.2 Synthesis and Properties of Complexes

Reaction of $Ru(acac)_2(MeCN)_2$ with Mindigo in aerobic refluxing ethanol with triethylamine led to the formation of *cis*-Mindigo complex **5.3** and *trans*-Mindigo complex **H5.4** were obtained in 46% and 48% yield respectively by the depicted in **Scheme 5.1**. Like the indigo analogues **5.1** and **H5.2**, the ligand is oxidized by two electrons/protons in **5.3** and one electron/proton in **H5.4**. Like **H5.2**, **H5.4** is paramagnetic.

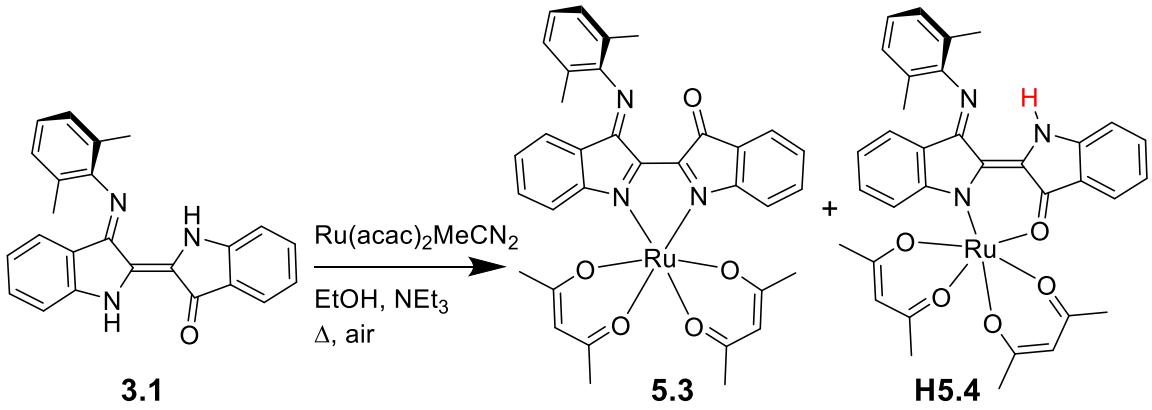

Scheme 5.1 Synthesis of **5.3** and **H5.4**.

Initial attempts to generate the Nindigo analogues by the same routes as used for compounds **5.1**-**5.4**, aerobic oxidation in basic media, led to hydrolysis of one imine. Only compound **5.3** could be isolated from these reactions in poor yields. To avoid the possibility of hydrolysis, further attempts to make a Nindigo ruthenium complex were carried out in dry benzene using p-benzoquinone as oxidant. Two-proton and two-electron oxidized complex **5.5** was obtained in 48% yield. In the absence of the ruthenium source, Nindigo is not oxidized by p-benzoquinone in refluxing benzene. Nindigo likewise does not react with the metal synthon $Ru(acac)_2(MeCN)_2$ in the absence of oxidant. Use of the (2,2,6,6-tetramethylpiperidin-1-yl)oxyl (TEMPO) radical as an oxidant also led to formation of **5.5**,

albeit in lower yield (34%). *Trans*-Nindigo complex **H5.6** was not isolated from any reaction mixture, although a dark band which likely contained the other 52-66% yield of other ruthenium containing species could not be obtained from the alumina column. **H5.6** differs from **5.2** and **5.4** by its coordination environment in that it must coordinate via the more sterically encumbered arylimine. As a result, formation of this compound as drawn in **Scheme 5.2** may be unfavorable.

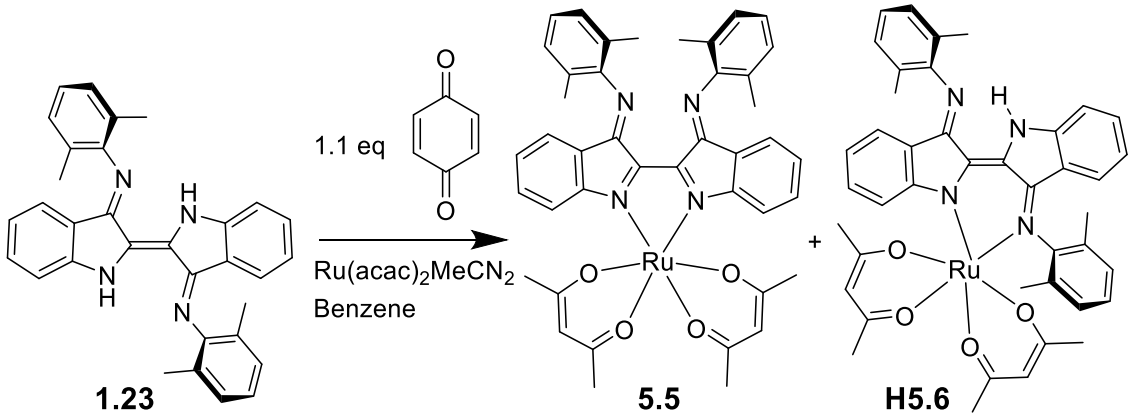

Scheme 5.2 Route to expected products **5.5** and **H5.6**.

Reddish-pink **5.3** and **5.5** were readily protonated to blue **H5.3**$^+$ and purple **H5.5**$^+$ by washing a dichloromethane solution of **5.3** or **5.5** with 48% aqueous tetrafluoroboric acid. **H5.3**$^+$ and **H5.5**$^+$ appear stable to the concentrated acid over several hours, however they are quite susceptible to hydrolysis in weakly acidic or neutral media; over the course of several minutes, the solutions of **H5.3**$^+$ or **H5.5**$^+$ become pink upon hydrolysis to **5.1** or **5.3** respectively.

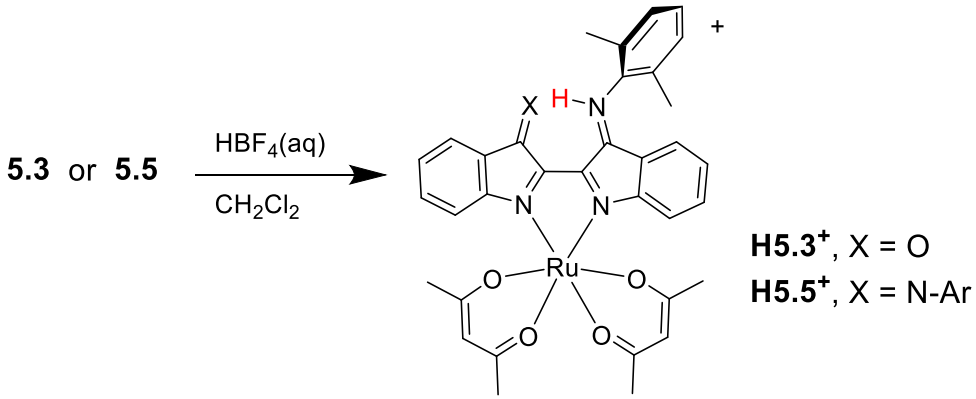

Scheme 5.3 The protonation of cis-Mindigo and Nindigo complexes.

The structures of **5.3** and **5.5** were investigated by X-ray crystallography. As **Table 5.1** shows, all three *cis*-indigoid chelates **5.1**, **5.3**, and **5.5** show similar bond metrics. There is a clear double-single-double bond character going from N1-C1-C2-O2 for **5.3** and N1-C1-C2-N2 for **5.5** which is indicative of fully oxidized ligands. The bond lengths of the α-diimine like chelate formed from N1-C1 are longer compared to the free ligand, dehydroNindigo **1.27**. The N1-C1 bond is 1.351 (2) Å in Nindigo complex **5.5** as opposed to 1.293 (2) Å in **1.27**. This discrepancy can be attributed primarily to significant π-back bonding character from the electron rich ruthenium (II) to the easily reduced, strongly π-accepting ligand. The structure of **H5.5**$^{+}$ confirms the presumed formula and connectivity, however the structure was of insufficient quality to compare bond lengths.

Table 5.1 Selected bond lengths (Å) for cis-indigo based compounds

	N1-C1	C1-C2	C2-N2/O2	C2-C3	C10-O1	C1-C1/C9	N1-Ru
5.1*	1.342 (6)	1.482 (9)	-	1.481 (8)	1.219 (6)	1.391 (8)	1.975 (5)
H5.2*	1.360 (5)	1.494 (6)	1.222 (5)	1.476 (7)	1.276 (5)	1.379 (7)	1.981 (3)
5.3	1.341 (4)	1.479 (4)	1.268 (4)	1.488 (4)	1.207 (5)	1.412 (4)	2.004 (3)

H5.4	1.358 (2)	1.484 (2)	1.291 (2)	1.473 (2)	1.277 (2)	1.383 (2)	1.996 (1)
5.5	1.351 (2)	1.476 (3)	1.285 (3)	1.479 (3)	-	1.413 (3)	1.999 (1)
H5.5^{+}	1.34 (2)	1.46 (2)	1.30 (2)	1.49 (2)	-	1.40 (2)	2.00 (1)
1.27	1.293 (2)	1.500 (2)	1.277 (2)	1.479 (2)	-	1.475 (2)	-

*Note: the numbering schemes for **5.1** differ, and are translated here for consistency. Bond lengths are taken for the low-number side of molecule A and are reported using the analogous number scheme. Differences in relative bond lengths between halves of indigo and each molecule are not statistically significant.

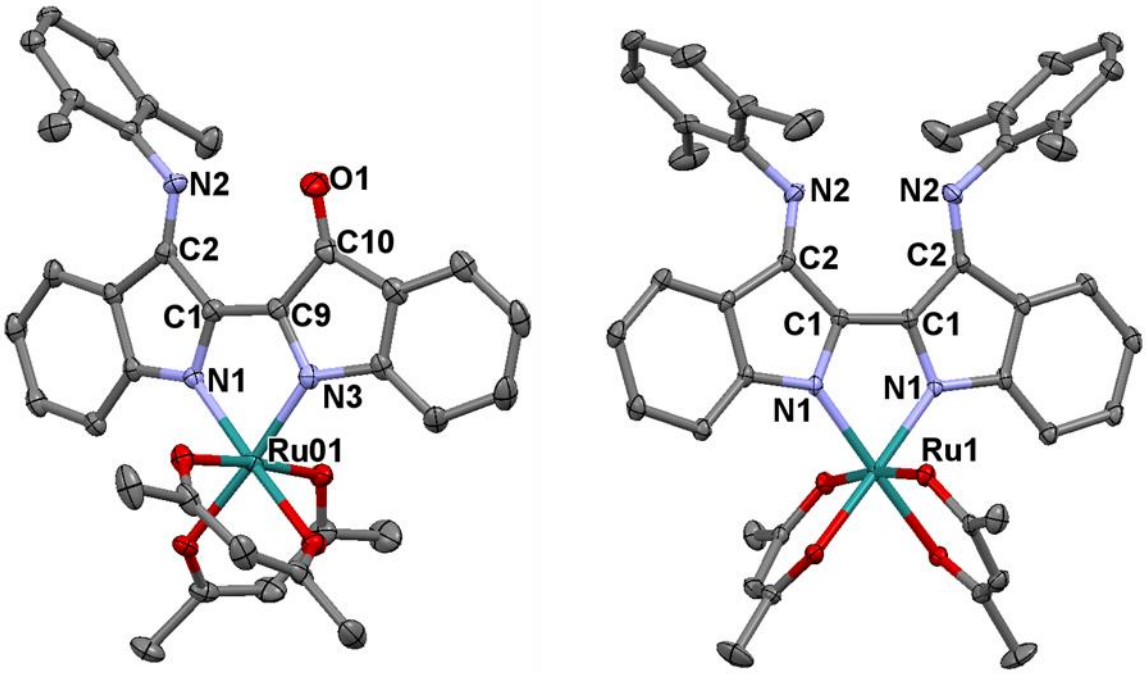

Figure 5.1 X-ray structures of **5.3** (left) and **5.5** (right) displayed at the 50% probability ellipsoids with cocrystallized solvent and hydrogen atoms removed for clarity.

All of the complexes that were studied showed one major band in the visible region of their electronic spectra. As shown in **Table 5.2**, the change of ketones to imines in the neutral compounds led to very minor changes in the absorption properties. The strong visible band in **5.3** and **5.5** tails slowly until absorption ends at around 800 nm. Protonation of **5.3** and **5.5** shifts the largest visible absorption bathochromically by 69 nm for **H5.3**$^{+}$ and 40 nm for **H5.5**$^{+}$. Protonated complexes **H5.3**$^{+}$ and **H5.5**$^{+}$ also gain a shoulder at 465

and 487 nm respectively, and they absorb weakly from 800 to ca. 1000 nm. The compounds obeyed Beer's law, and therefore were amenable to spectrophotometric titration for the determination of pK_a values (see section 5.3).

Table 5.2 Comparison of electronic spectra of compounds, λ_{max} in nm (ε in M^{-1} cm^{-1}) in acetonitrile.

5.1	**5.3**	**H5.3$^+$**	**5.5**	**H5.5$^+$**
275 (36,800)	267 (32,000)	270(25,000)	268 (29,000)	270 (31,000)
370 (13,600)	-	465 (9,700)	328 (9,600)	487 (12,000)
518 (17,400)	513 (16,000)	582 (12,000)	519 (18,000)	559 (16,000)

5.3 has C_1 symmetry, and all protons and carbons can be assigned through two-dimensional NMR techniques similar to those discussed in Chapter 3. The ^{1}H NMR spectrum of **5.5** indicate the compound has C_2 symmetry in solution. The ^{1}H NMR spectra of **H5.3$^+$** and **H5.5$^+$** in acetonitrile-d_3 have the same patterns as their non-protonated analogues except for the added N-H (which integrates reliably to 1 proton). All protons and carbons could be identified and assigned by NMR spectroscopy. The chemical shifts of **H5.3$^+$** and **H5.5$^+$** in acetonitrile-d_3 are *relatively* typical of diamagnetic structures, although some peaks appear slightly upfield.

The patterns of ^{1}H NMR spectra of **H5.3$^+$** and **H5.5$^+$** remained consistent in different solvents, but some peaks were shifted significantly from expected values. For instance, in CD_2Cl_2, the "aromatic region" of **H5.3$^+$** spans from 2-8 ppm, which is far outside the typical range of 6-8 ppm. A few control tests indicate these strange chemical shifts are not caused by ion pairing or impurities. When **H5.5$^+$** was protonated in situ with methanesulfonic acid, the spectrum showed very small changes in chemical shifts (±0 to 0.05 ppm for all peaks) indicating the anion does not play a role in the chemical shifts of

H5.5^{+}. Dilution of the samples did not lead to any significant change in chemical shift supporting the hypothesis that ion pairing does not play a role in the observed chemical shifts. Spectra taken from different batches also gave the same results.

Similar small deviations from typical diamagnetic values in proton NMR has been observed with complexes containing antiferromagnetically coupled radicals. Both metal-metal coupling[146] and metal-RAL coupling[147-149] has led to similar observations. In all of these cases, it is presumed that the ground state is a singlet that has no magnetic moment. A low-lying, paramagnetic excited state is thermally populated leading to the aberrant chemical shifts. The thermal population of a triplet excited state in these cases were investigated by variable temperature NMR.

Variable temperature ^{1}H NMR spectra were obtained for **H5.3**$^{+}$ and **H5.5**$^{+}$. The variable temperature measurement of **H5.5**$^{+}$ in acetonitrile-d_3 is shown in **Figure 5.4**. At lower temperatures, all signals approached typical diamagnetic values. As the temperature was increased from room temperature, a near linear change in chemical shifts of all peaks was observed. The methine proton of acetylacetonate ligands shift to the greatest degree in both cases, followed by the protons *ortho* and *para*- to coordinated nitrogen atoms. All three resonances shift to higher field with increasing temperature.

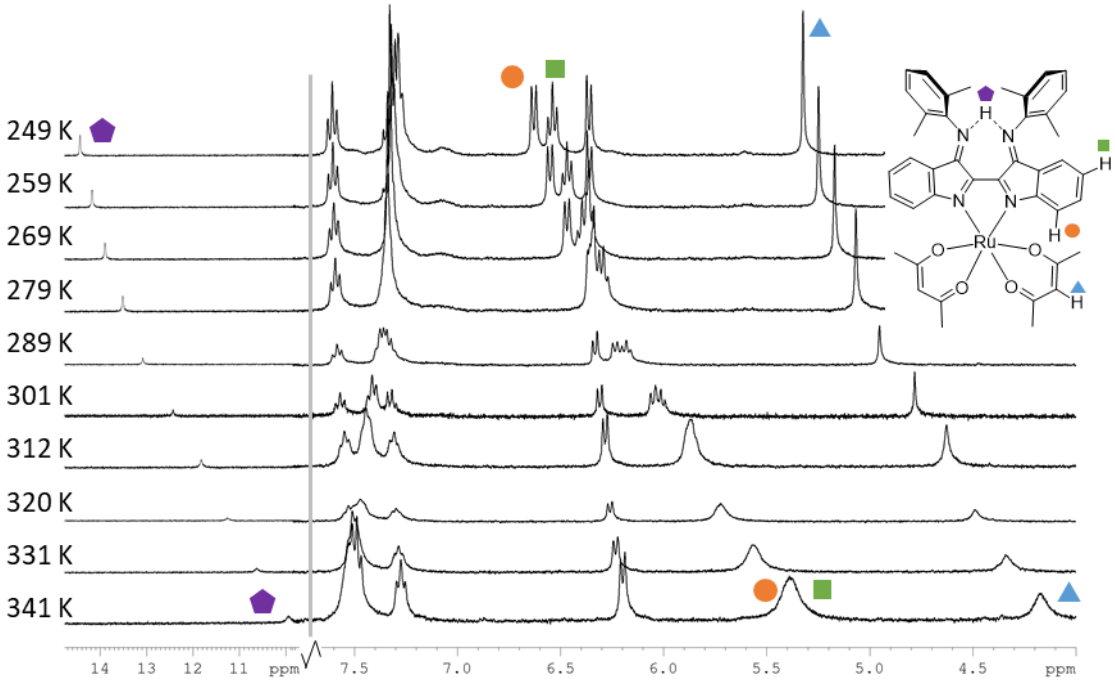

Figure 5.2 Variable temperature ^{1}H NMR spectra of **H5.5**$^{+}$ in d_3-acetonitrile.

Assuming that there is a thermally accessible excited state, the ratio of excited state to ground state population p(T) can be fit to the Boltzmann distribution:

$$p(T) = e^{\frac{-\Delta E}{kT}} \qquad \textbf{5.1}$$

To fit the experimental data to **Equation 5.1**, the role a paramagnetic excited state plays into the chemical shift in the fast exchange regime must be considered. In a paramagnetic substance, the observed chemical shift δ_{obs} can be determined as the sum of the chemical shift in the absence of unpaired electrons δ_0 and the paramagnetic shift component δ_{para}.[150] δ_{para} is itself the sum of the Fermi contact shift δ_{fc} and the pseudocontact shift δ_{pc} (**Equation 5.2**). δ_{fc} is proportional to the spin density on the observed atom by **Equation 5.3**, where μ_0 is the vacuum permeability (4π x 10^{-7} N A^{-2}), μ_B is the Bohr magneton (9.274 x 10^{-24} J T^{-1}), g_e is the free electron g factor (2.0023, k is the Boltzmann

constant, S is the total spin, and T is the temperature. $\rho_{\alpha\beta}$ represents the net spin density at the given atom.

$$\delta_{obs} = \delta_0 + \delta_{para} = \delta_0 + \delta_{fc} + \delta_{pc} \quad \textbf{5.2}$$

$$\delta_{fc} = \frac{\mu_0 \mu_B g_e^2 (S+1)}{9kT} \rho_{\alpha\beta} \; or \; \frac{2.350 \times 10^7 (S+1)}{T} \rho_{\alpha\beta} \quad \textbf{5.3}$$

The experimental data was fitted to **Equation 5.4** in order to determine the values of ΔE of **H5.3**$^+$ and **H5.5**$^+$. **Equation 5.4** accounts for the population of a paramagnetic state using **Equation 5.1**.

$$\delta_{obs} = \delta_0 + \delta_{para} * p(T) = \delta_0 + \left(\frac{2.350 \times 10^7 (S+1)}{T} \rho_{\alpha\beta} + \delta_{pc} \right) * p(T) \quad \textbf{5.4}$$

δ_0 and δ_{pc} in **Equation 5.2,** $\rho_{\alpha\beta}$ in **Equation 5.3**, and ΔE are not known. Attempts to fit experimental data using **Equations 5.4** were successful, and gave results identical to those shown in **Figure 5.3** below. The experimental fits showed that the value of $\rho_{\alpha\beta}$ was around -0.2% spin density on the acac methine protons. However, the data can also be fit to the much simpler **Equation 5.5** with roughly the same values of δ_0 and ΔE. In **Equation 5.5**, δ_{para} is treated as a constant because the change in paramagnetic shift is very small compared to the effect due to changes in the population of states. **Equation 5.5** was used for the remaining analysis to avoid over parameterization.

$$\delta_{obs} = \delta_0 + \delta_{para} * \left(e^{\frac{-\Delta E}{kT}} \right) \quad \textbf{5.5}$$

Figure 5.2 shows the temperature dependence on chemical shift of the highest field acac methine proton with the fits to **Equation 5.5**. These signals were chosen as the methine protons were the most sensitive to temperature, showed no overlap with other signals, and were singlets. At low temperatures, p(T) approaches zero so the observed chemical shift approaches the diamagnetic value, i.e. $\delta_{obs} = \delta_0$. At sufficiently high

temperatures, the paramagnetic components play a large role in the observed chemical shift leading to large deviance from expected diamagnetic chemical shifts.

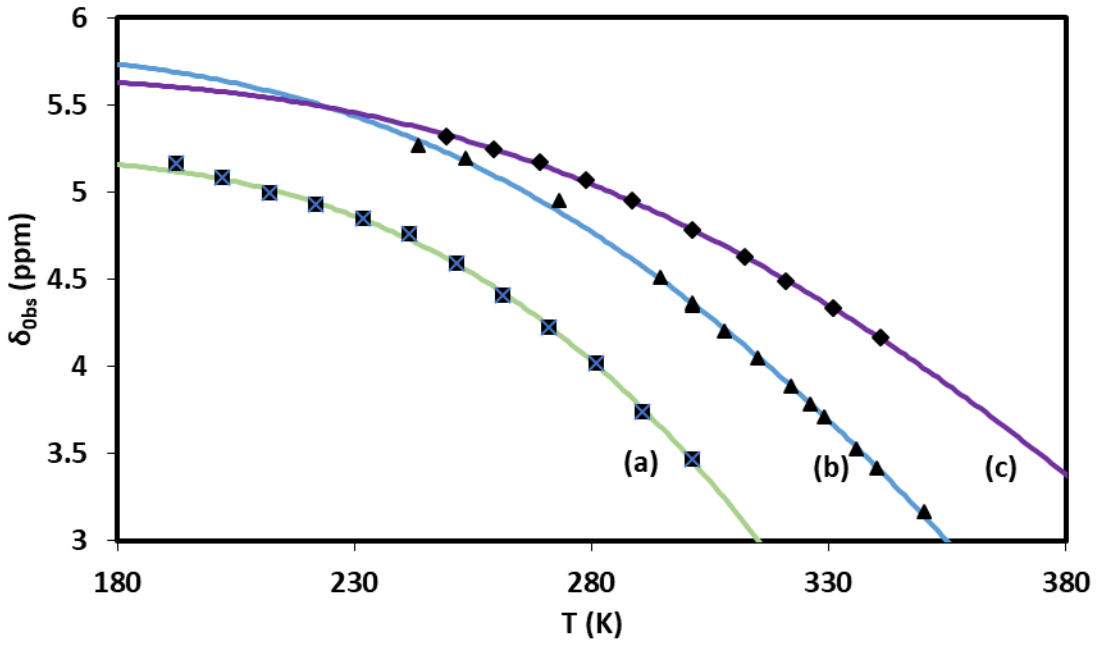

Figure 5.3 Observed ^{1}H NMR chemical shifts (black) with exponential fits at variable temperature for (a) **H5.5**$^{+}$ in dichloromethane, (b) **H5.3**$^{+}$ in MeCN, and (c) **H5.5**$^{+}$ in MeCN.

H5.3^{+} and **H5.5**$^{+}$ have large singlet-triplet gaps in the -900 to -1000 cm^{-1} range, as shown in **Table 5.3**. A gap of -920 cm^{-1} indicates an excited state population of 0.1% at 200 K to 1% at 300 K according to **Equation 5.1**.

Table 5.3 Fits to equation 5.4.

Compound	Solvent	δ_0 (ppm)	δ_{para}	ΔE (cm^{-1})
H5.3^{+}	CD_3CN	5.81	-116	-920
H5.5^{+}	CD_2Cl_2	5.21	-330	-1100
	CD_3CN	5.67	-88	-960

To test for a small paramagnetic impurity, ^{1}H NMR spectra at room temperature were acquired with and without an inner tube containing pure solvent to measure the magnetic moment of **H5.3**$^{+}$ and **H5.5**$^{+}$ by the Evans method. The spectra with the pure

solvent insert gained a small shoulder indicating the presence of a small, nearly undetectable magnetic moment.

The resonances corresponding to protons *para*- and *ortho*- to ruthenium bound nitrogen atoms were quite sensitive to temperature changes, but often overlapped with other signals making chemical shift determination difficult. Fitting these chemical shifts to **Equation 5.5** gave the same values of ΔE as above ($\pm$ 30 cm^{-1}) with different δ_{para} values. According to **Equation 5.2**, the paramagnetic shift observed is proportional to the spin density ρ_{ab} on an atom. Thus, the acac methine protons and the protons *para*- and *ortho*- to ruthenium bound nitrogen atoms have the largest magnitude (but still a very small amount) of negative spin density among protons. *Meta*- protons shifted positively to a small degree indicating a very small amount of positive spin density. The chemical shift of the N-H changed the most of all protons, however the large changes in the chemical shifts of trace water indicate that the chemical shift changes of the NH are likely due to exchange with trace water.

The low-lying excited state observed in **H5.3**$^+$ and **H5.5**$^+$ could arise from valence tautomerism (**Scheme 5.5**) wherein the closed shell cationic ligand is oxidizing the closed shell ruthenium(II). Alternatively, the singlet-triplet gap can arise from antiferromagnetic coupling between the metal and ligand radicals (**Scheme 5.5**). The metal would therefore be a ruthenium(III) and the ligand would be a neutral radical. The difference between these three electronic structures is the *placement* of a single electron.

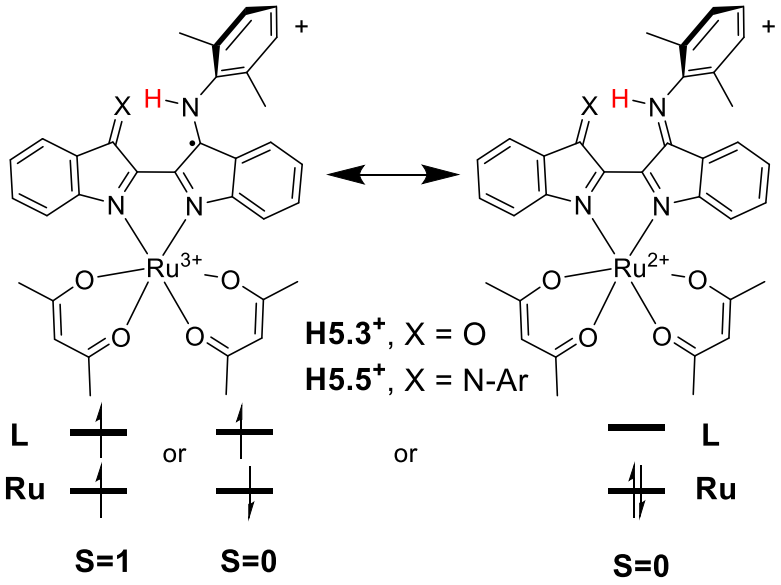

Scheme 5.4 Frontier orbitals of three possible electronic structures of **H5.3**$^+$ and **H5.5**$^+$.

Although both valence tautomerism and antiferromagnetic coupling have been observed for redox-active ligands as a whole, an antiferromagnetically coupled biradical is the most likely in this case based on the available data. In the complexes of other α-diimines with $Ru(acac)_2$ (**5.7**[151] and **5.8**[152]) computational studies suggest the presence of a radical ligand that is antiferromagnetically coupled to a ruthenium(III) moiety to give an overall singlet ground state. ^{1}H NMR spectra of these reported complexes appear within normal diamagnetic ranges without any apparent paramagnetic shifting. For example, the chemical shift of acac methine proton is 5.12-5.16 ppm in DMSO-d_6 for both **5.7** and **5.8**. Importantly, variable temperature studies were not done in those cases. It is likely that a deviation from diamagnetic chemical shifts were not observed due to the presence of a much larger singlet-triplet gap in **5.7** and **5.8** than **H5.3**$^+$ and **H5.5**$^+$. Assuming that *cis*-Nindigo and *cis*-Mindigo ligands can be considered as elaborate α-diimine ligands, antiferromagnetic coupling should be expected. If **H5.3**$^+$ and **H5.5**$^+$ are valence tautomers, it is likely that the biradical excited state would therefore be antiferromagnetically coupled.

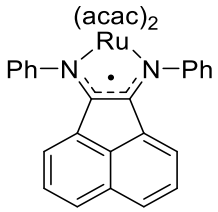

5.7

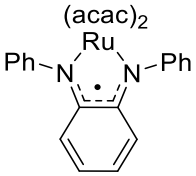

5.8

It stands to reason that **5.3** and **5.5** could likewise be antiferromagnetically coupled biradicals or valence tautomers, albeit with different gaps. In the variable temperature ^{1}H NMR in acetonitrile of **5.3** and **5.5**, negligible changes in chemical shifts were observed, ranging from 0 to 0.05 ppm (0 to 20 Hz on a 360 MHz instrument). The acac methine hydrogen resonance did not shift at all. Only resonances corresponding to the indigo- based ligand backbone changed in chemical shift. Due to the large changes in the chemical shifts of trace water, these small changes in chemical shifts likely arise from hydrogen bonding interactions with the trace water. Furthermore, Evans method measurements did not show the presence of any paramagnetism. Thus, no paramagnetic component could be detected for **5.3** or **5.5**. The absence of any paramagnetic shifting indicate that **5.3** and **5.5** likely contain a ruthenium(II) and a neutral indigoid ligand. This assignment is further supported by comparison to the computational results of *cis*-indigo complex **5.1** by Lahiri that indicate that the dominant electronic structure of **5.1** is likewise a ruthenium(II) and a neutral indigo ligand.

5.3 Determination of the NH bond Strengths of Complexes

The numerous possible ligand charge states endemic to Nindigo and Mindigo means there are many avenues for proton-coupled electron transfer reactions. Provided all reactions studied are electrochemically reversible and protonation is fully reversible, estimations of bond strengths are possible across several ligand charge states.

The pK_a values of **H5.3**$^+$ and **H5.5**$^+$ were determined by spectrophotometric titration in dry acetonitrile. Addition of sufficiently strong acid titrants to **5.3** and **5.5** led to clean conversion to **H5.3**$^+$ and **H5.5**$^+$; several isosbestic points can be seen in **Figure 5.3**. **H5.3**$^+$ or **H5.5**$^+$ were titrated with a suitably weak base to determine ΔpK_a values using values from the self-consistent acidity scale for acetonitrile.[135-136] The pK_a values of **H5.3**$^+$ and **H5.5**$^+$ could therefore be obtained through comparison of the ΔpK_a values with the known pK_a values for the reference bases. The $pK_{a,MeCN}$ of each were found to be 11 and 13 for **H5.3**$^+$ and **H5.5**$^+$ respectively. For reference, these values are close to the $pK_{a,MeCN}$ of anilinium (10.62) and pyridinium (12.53).

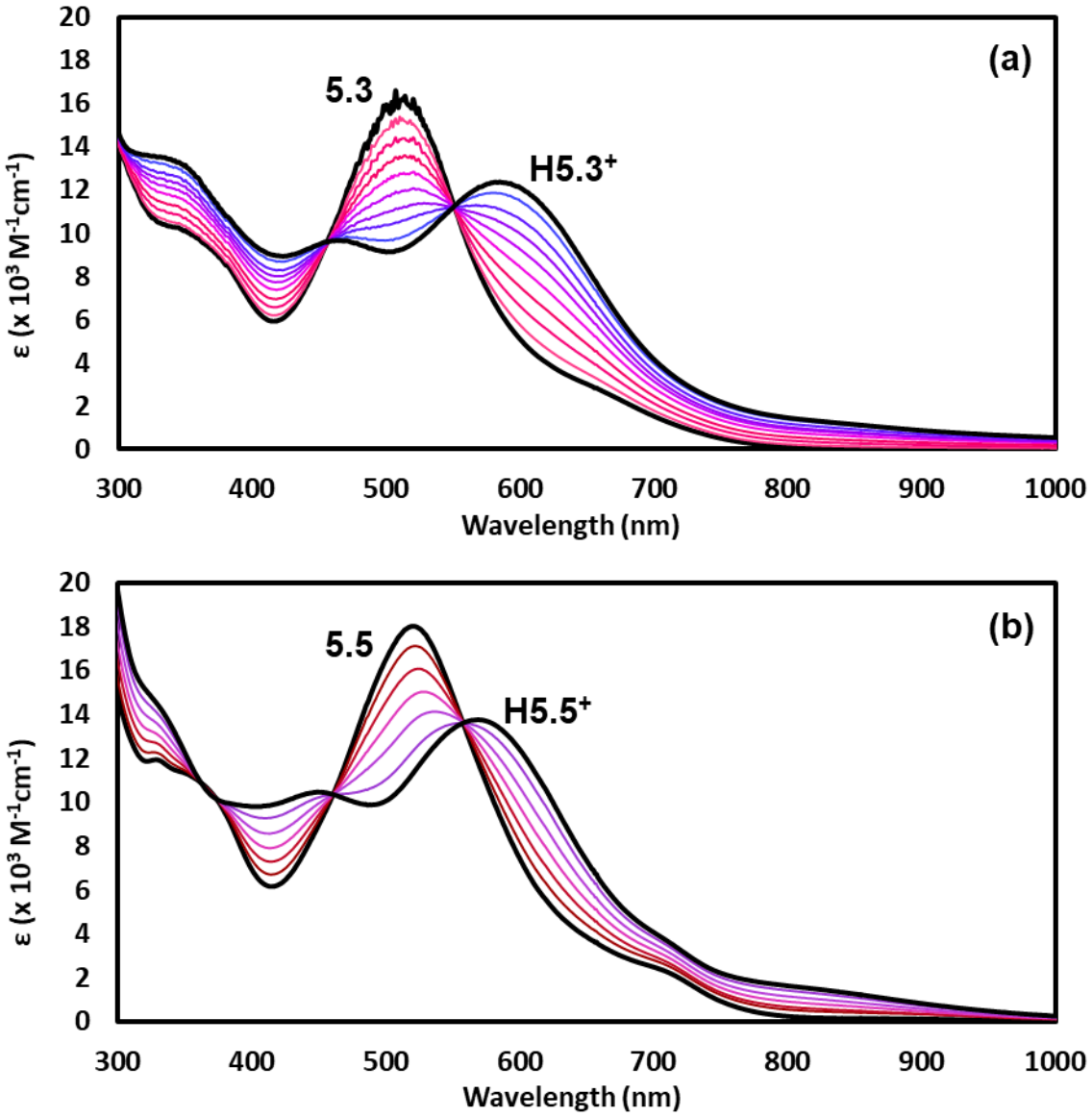

Figure 5.4 UV-Vis-NIR spectra of (a) **5.3** with increasing concentrations of *para*-toluene sulfonic acid and (b) **5.5** with increasing concentration of 2,6-lutidinium tetrafluoroborate. The black spectra are titration start and endpoints. The colors used in intermediate points are approximations of the colors observed.

This class of ligands normally has up to five accessible oxidation states (neutral to 4^-), and a $Ru(acac)_2$ moiety can access 3 oxidation states (II, III, IV). Thus up to 7 oxidation states are possible, in principle. Cyclic voltammetry (**Figure 5.4**) shows that only 3 or 4 oxidation state changes are seen in the cyclic voltammogram within the solvent window.

Those redox events that are detected have quite large comproportionation constants (10^6 to 10^{18}) indicating oxidation/reduction of the metal strongly affects the ligand (and vice versa).

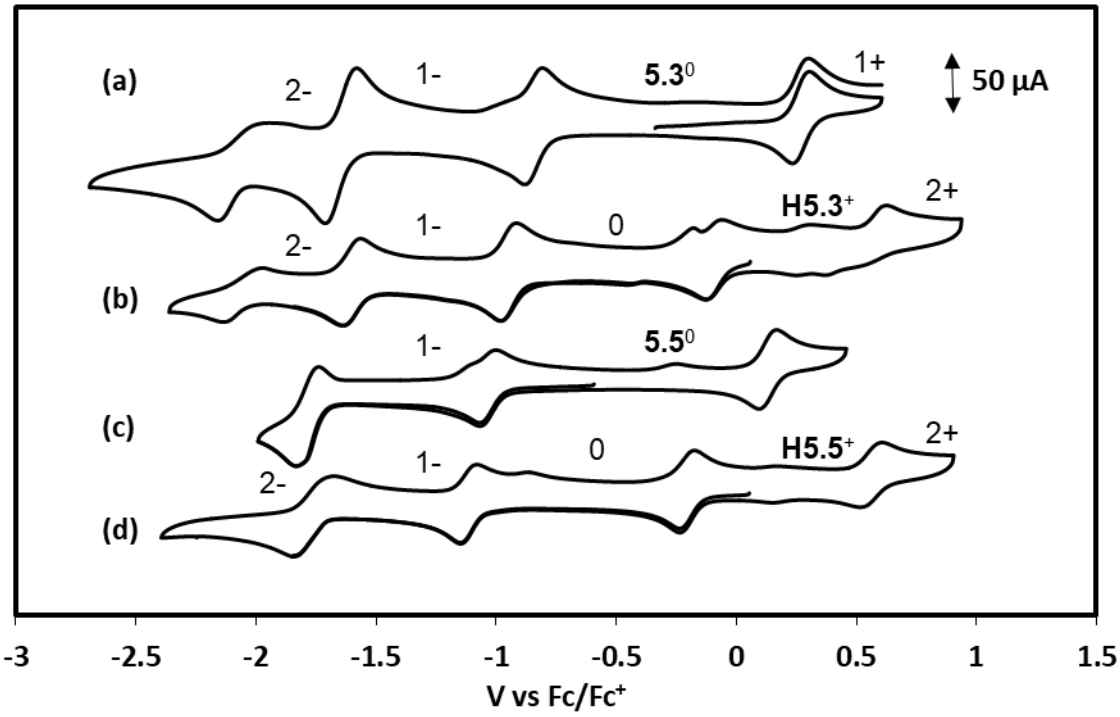

Figure 5.5 Cyclic voltammograms of (a) **5.3**, (b) **H5.3$^+$BF$_4$**, (c) **5.5**, and (d) **H5.5$^+$BF$_4$** in acetonitrile containing 0.1 M NBu_4PF_6.

Given the ligands' charge state assignment as fully oxidized in **5.1**, **5.3**, and **5.5,** oxidation of the complexes should be a Ru(II)/Ru(III) redox couple (ignoring the potential for redox non-innocence). The reductions are likely ligand based since coordination complexes of ruthenium(I) with these ligands are less likely. The first oxidation and reduction processes for **5.1**, **5.3** and **5.5** are fully reversible. Whereas the reductions of **5.1** appear quite reversible, the second and third reductions of **5.3** are only quasi-reversible. The second reduction gains a daughter peak at high scan-rates at ca. -0.95 V vs. Fc/Fc^+ which coincides with an oxidation potential observed in **H5.3$^+$**. The quasireversible second

reduction of **5.5** is double the current of the other redox events, occurs at almost exactly the same potential as a one electron process in the protonated compound, and has daughter peaks that coincide with the potentials of **H5.5**$^+$. This reduction likely includes the deprotonation of solvent given these observations.

Table 5.4 $E_{1/2}$ (ΔE) from cyclic voltammetry of *cis*-complexes in acetonitrile at 100 mV/s vs Fc/Fc^+. Non-bolded line indicates region of measured cell potential, indicative of the starting state of compound.

	5.1	**5.3**	**H5.3**$^+$	**5.5**	**H5.5**$^+$
1+/2+	-	-	+0.49 (205)	-	+0.56 (82)
0/1+	+0.31 (60)	+0.26 (62)	-0.09 (59)	+0.13 (62)	-0.22 (44)
1-/0	-0.76 (60)	-0.84 (61)	-0.95 (60)	-1.02 (66)	-1.12 (67)
2-/1-	-1.61 (80)	-1.64 (108)	-1.60 (60)	-1.79* (74)	-1.78 (126)
3-/2-	-1.99 (70)	-2.06 (145)	-2.04 (140)	-	-

*Quasi-reversible, 2-electron process.

Given the ambiguity of the oxidation/charge state of **H5.3**$^+$ and **H5.5**$^+$ discussed in section 5.2, it is very difficult to assign whether oxidation or reduction is metal or ligand centered. Nonetheless, the trends seen in the voltammograms leads to a few conclusions on the role of the ligand and metal. Protonation of the compounds leads to an anodic shift of all potentials. The oxidation waves shift by a smaller degree (+0.4 V) than the reduction (+0.8 V). A shift of +0.36 V for the Ru II/III couple was reported by the Mayer group upon protonation of a 2-pyridyl-2'-imidazole ligand bound to the $Ru(acac)_2$ moiety (compound **4.8**).[125] The similar shift in redox potentials, although noteworthy, may simply be a coincidence given the protonated complexes may already be a Ru(III) complex.

With electrochemical and acidity data in hand, thermochemical cycles (square schemes) for the $1H^+/1e^-$ oxidation or reduction can be generated as shown in **Scheme 5.6** and **5.7**. Bond dissociation free energy (BDFE) values can then be determined *via* the Bordwell equation (**Equation 4.1**) and hydricity values can be determined by **Equation**

4.3. The unknown pK_a values can be determined based on Hess's law to give the NH acidity, bond strengths, and hydricities across many oxidation states.

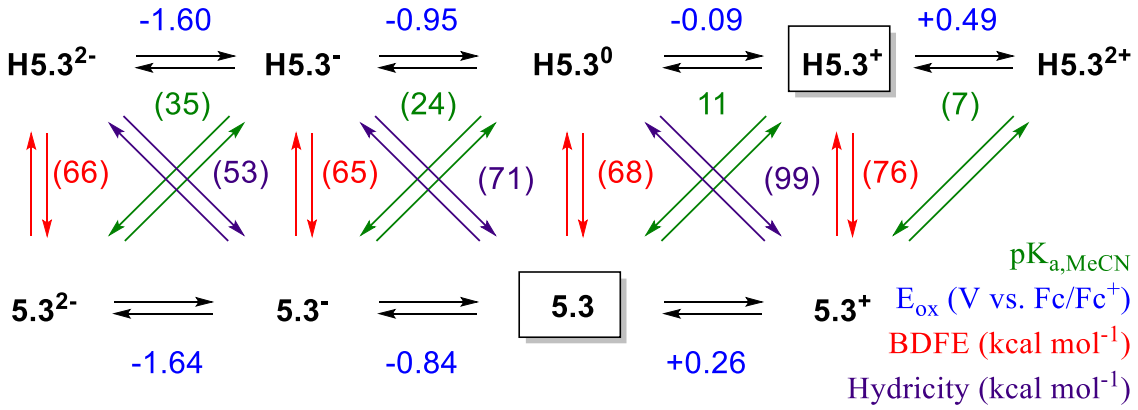

Scheme 5.5 Thermochemical cycles for a number of proton and charge states for compounds **(H)5.3^n**. Horizontal lines indicate electron transfer from cyclic voltammetry; vertical lines indicate hydrogen atom transfer. Up-right diagonal lines represent proton transfer. Down-right diagonal arrows represent hydride transfer. Boxes represent isolated compounds used for the analysis.

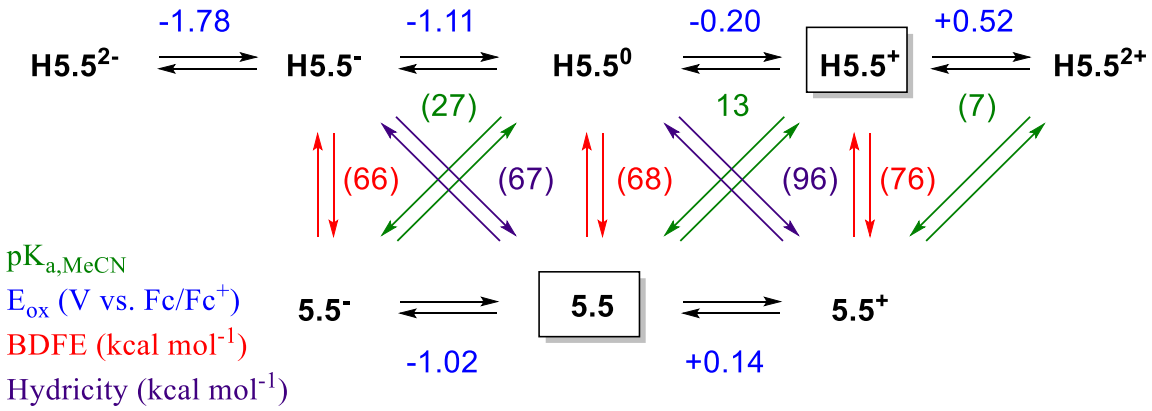

Scheme 5.6 Thermochemical cycles for a number of proton and charge states for compounds **(H)5.5^n**. Horizontal lines indicate electron transfer from cyclic voltammetry; vertical lines indicate hydrogen atom transfer. Up-right diagonal lines represent proton transfer. Down-right diagonal arrows represent hydride transfer. Boxes represent isolated compounds used for the analysis.

Generally speaking, the bond strengths of Mindigo are smaller than the Nindigo analogue by only about 1 kcal mol^{-1}, which is within the estimated error (±1 kcal mol^{-1})[119] of this method of bond strength determination. The NH bonds of **H5.3$^+$** and **H5.5$^+$** are

moderately strong, at around 76 kcal mol^{-1}. On the other hand, **5.3** and **5.5** have relatively weak NH bonds as the BDFE of **H5.3** and **H5.5** is around 68 kcal mol^{-1}. For reference, the bond strengths of TEMPOH and tBu_3PhOH in acetonitrile are 67 and 77 kcal mol^{-1} respectively. Further reduction to **H5.3**$^-$ and **H5.5**$^-$ does not change the NH bond strength (67 kcal mol^{-1}).

Comparison of the square schemes of **H4.11** and **H4.12**$^+$ with those of **5.3** and **5.5** is difficult as the metal oxidation states and ligand charge states are currently ambiguous, and the charges of related complexes in the two chapters are different. For the same electron count (ignoring acac or bipy ligands), the two related complexes **H5.5**$^+$ and **H4.12**$^{3+}$ have very similar $pK_{a,MeCN}$ values (13 and 12, respectively). On the other hand, **H5.5** ($pK_{a,MeCN}$ = 27) is much less acidic than **H4.12**$^{2+}$ ($pK_{a,MeCN}$ = 18) which also has the same electron count. It is unclear if this is due to a difference in overall charge or a difference in the ligand's charge state.

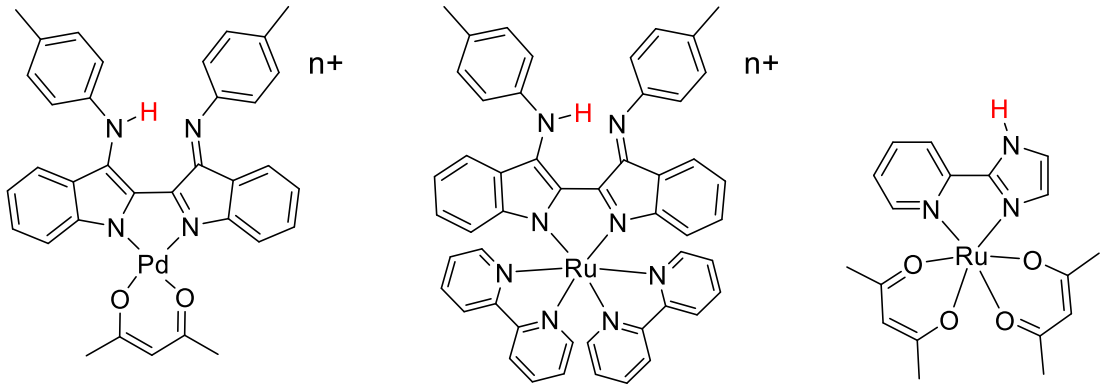

H4.11^n **H4.12**^{n} **4.8**

The NH bonds in $Ru(acac)_2$ complexes **H5.3**^{n} and **H5.5**^{n} are, in general, weaker by around 10 kcal mol^{-1} than **H4.11**^{n} and **H4.12**^{n}. This bond weakening is likely caused by the relative ease of oxidation of $Ru(acac)_2$ complexes **H5.3**^{n} and **H5.5**. For instance, the oxidation of **H5.5** occurs at -0.20 V which is negative of the $Ru(bipy)_2$ complex **H4.12**$^{2+}$

(+0.20 V); because the product of each oxidation, **H5.5**$^{+}$ and **H4.12**$^{2+}$ respectively, are equally stronger acids, the bond strength of **H5.5** is weaker by 0.4 V or 9 kcal mol^{-1}. The NH bond strengths of **H5.3^{n}** and **H5.5^{n}** (ca. 68 kcal mol^{-1}) are actually *stronger* by 5 kcal mol^{-1} than the related Ru(acac)$_2$ complex of 2-pyridyl-2'-imidazole **4.5**. In that case, the electron came from the ruthenium while the proton came from the ligand.

As with the complexes in Chapter 4, the accessibility of multiple charge states may allow these complexes to undergo net-hydride transfer. Oxidation of **5.3** and **5.5** should yield complexes that are potent hydride abstractors with hydride affinities greater than trityl (92 kcal mol^{-1}) or diphenylsilylium (96 kcal mol^{-1}) cations. **5.3**, **5.5**, and their reduced forms should be substantially weaker hydride abstractors. This observation follows the trend that the thermodynamics of hydride transfer follows electrostatic predictions, i.e. anions are better hydride donors while cations are better hydride acceptors.

5.4 Conclusions

It is interesting to note that, like **H4.11^{n}** and **H4.12^{n}**, the NH bond strength of **H5.3^{n}** and **H5.5^{n}** do not change much between differences in overall charge. On the other hand, acidity and hydricity are noticeably affected by the charge state; cations are better acids, and anions are better hydride donors. There are very few (if any) related systems with many possible ligand/metal charge states with which to compare. The NH bond in question is orthogonal to the electron reservoir. In these systems where the proton and electron are not in the same orbitals, it is possible that changes in charge do not change the observed bond strength.

Protonation of **5.3** and **5.5** has turned on some ligand non-innocence; the oxidation state of the metal is ambiguous. The proton, being cationic, is electron withdrawing.

Protonation of organic compounds, provided the basic site is coupled to the redox-active unit, is known to make the compound more oxidizing. It is possible that the use of this redox-active ligand with a basic site has played a role in the shuttling of electrons to and from the metal. Our lab is currently investigating the electronic structures of these complexes further *via* in depth quantum mechanical calculations.

Furthermore, the use of electron rich $Ru(acac)_2$ led to a significant NH bond weakening compared to $Ru(bipy)_2$ and Pd(acac) complexes. The hydride affinity was likewise reduced. The protic compounds reported in this chapter **H5.3^n** and **H5.5^n** are sufficiently weak such that they should be able to activate some substrates via hydrogen atom or hydride transfer which will be further discussed in chapter 6.

5.5 Experimental Methods

To determine ΔpK_a values, firstly a strong acid was standardized by titration of the acid into a proton sponge (1,8-bis(dimethylamino)naphthalene). The acid was then used to titrate the compound once, verifying its concentration. Then a known amount of base with no visible absorption and the compound are added to a cuvette. The mixture was titrated with acid, and the concentration of compound and its conjugate acids were determined by comparison of molar extinction coefficients, where $[Compound_{initial}]$=Abs. Using arithmetic, the concentration of added base and its conjugate can be determined by $[HA\ added]=[HB^+]+[HCompound^+]$. Variable temperature NMR data was fit using a non-linear fit function of Maple software using experimental data (chemical shift and temperature) and three constants (δ_0, δ_{para}, and ΔE).

Bisacetylacetonato[*cis*-indigo-mono(2,6-dimethylphenylimine)κ^2-*N,N'*]ruthenium 5.3 and **Bisacetylacetonato[*trans*-indigo-mono(2,6-dimethylphenylimine)-κ^2*N,O*]**

ruthenium 5.4: To a 1-neck round bottomed flask was added indigo-(2,6-dimethylphenyl)monoimine (58 mg, 0.16 mmol), bisacetonitrile bisacetylacetonate ruthenium (II) (61 mg, 0.16 mmol), and triethylamine (30 µL). The solids were dissolved in 15 mL of ethanol, and the mixture was refluxed in air for 18 hours. The mixture was cooled to room temperature, evaporated, and the residue purified by column chromatography on neutral alumina using 1:1 dichloromethane/hexanes eluent to obtain 48 mg **5.4** (46% yield). The solvent system was gradually shifted to 100% dichloromethane 50 mg **5.3** (48% yield). Single crystals suitable for x-ray diffraction of each were grown by slow diffusion of water into a concentrated ethanol solution.

5.3: mp 160 ^{o}C (decomp.). $C_{34}H_{31}N_3O_5Ru$-1/2 H_2O Calc C, 60.80; H, 4.80; N, 6.26. Expt C, 60.57; H, 4.72; N, 6.06. UV-Vis (MeCN) λ_{max}/ nm (ε/ M^{-1} cm^{-1}): 266 (30,000), 513 (16,000). FT-IR (KBr, air background): 2924 w, 1691 m, 1571 s, 1517 vs, 1384 s, 1271 w, 1199 w, 1180 w, 1085 w, 1020 w, 917 w, 846 w, 762 m, 694 w, 631 w cm^{-1}. ^{1}H NMR (500 MHz, CD_2Cl_2, 300 K) δ: 7.53 (1H, d, 8 Hz, H_{12}), 7.50 (1H, dt, 8 Hz, 2Hz, H_{14}), 7.44 (1H, d, 8 Hz, H_{15}), 7.36 (1H, d, 8 Hz, H_7), 7.32 (1H, dt, 7 Hz, 1 Hz, H_{13}), 7.28 (1H, dt, 8 Hz, 1 Hz, H_6), 7.13 (2H, d, 7 Hz, H_{22} and H_{20}), 7.08 (1H, dd, 8 Hz, 7 Hz, H_{21}), 7.00 (1H, t, 7 Hz, H_5), 6.31 (1H, d, 7 Hz, H_4), 5.59 (1H, s, H_{27}), 5.49 (1H, s, H_{32}), 2.32 (3H, s, H_{25}), 2.23 (3H, s, H_{34}), 2.15 (3H, s, H_{30}), 2.14 (3H, s, H_{29}), 2.029 and 2.027 (6H, 2 s, H_{19} and H_{24}) ppm. ^{13}C NMR (125.8 MHz, CD_2Cl_2, 300 K) δ: 191.4 (C_{33}) 191.0 (C_{28}), 190.5 (C_{26}), 190.1 (C_{31}), 183.6 (C_{10}), 158.4 (C_2), 158.1 (C_{16}), 135.9 (C_{14}), 134.5 (C_6), 128.58, 128.55, 128.54 (C_{13} or C_{22} or C_{20}), 127.1 (C_5), 126.5 (C_{11}), 124.8 (C_4), 124.5 (C_{21}), 123.85 (C_{20} or C_{22}), 123.82 (C_{20} or C_{22}), 122.3 (C_{12}), 117.6 (C_{15}), 117.2 (C_7), 99.5 (C_{27}), 99.2 (C_{32}), 27.40 (C_{34} or C_{25}), 27.38 (C_{34} or C_{25}), 27.1 (C_{30}), 27.0 (C_{29}), 18.25 and 18.16 (C_{19} and C_{24}) ppm.

H5.4: mp 180 °C (decomp.). Elemental analysis for $C_{34}H_{32}N_3O_5Ru$-1/2 CH_2Cl_2 Calc C, 58.68; H, 4.71; N, 5.95. Expt C, 58.74; H, 4.79; N, 5.61. UV-Vis (MeCN): λ_{max}/nm (ε/ M^{-1} cm^{-1}) 273 (32,000), 344 (15,000), 564 (18,000). FT-IR (KBr, air background): 3377 br, 1617 w, 1570 s, 1549 m, 1517 vs, 1491 w, 1464 w ,1449 w, 1391 s, 1327 w, 1283 m, 1181 s, 1112 s, 1024 w, 935 w, 862 w, 757 w, 685 w, 576 w, 460 w. ^{1}H NMR (300 MHz, $CDCl_3$, 300 K) δ: 22.44 (br), 19.39 (br), 6.30-9.32 (br), 7.40 (s), 5.86 (s), 5.80 (s), 5.31 (br), 4.42 (br), 4.16 (d, 8 Hz) 3.28 (br), 2.07 (s), 1.88 (s), 1.68 (s), 1.30 (s), 0.52 (s), 0.12 (s), -0.20 (s), -0.98 (s), -1.59 (s), -5.51 (s), -9.73 (br).

Bisacetylacetonato[*cis*-1*H*-indigo-mono(2,6-dimethylphenyl)diimine]ruthenium tetrafluoroborate H5.3$^+$: To a solution of pink **5.3** (32 mg, 0.048 mmol) in dichloromethane was added 0.2 mL 48% aqueous HBF_4. The mixture was shaken for 5 minutes, and the clear aqueous layer is removed. The dark blue organic layer was drained and the aqueous layer was extracted with a further 2 mL of dichloromethane. The combined organic layers were dried over $MgSO_4$, filtered, and evaporated. The resultant residue was recrystallized from dichloromethane/hexanes to give 29 mg of a black solid (76 % yield). Mp >320 °C. Elemental analysis for $C_{34}H_{32}BF_4N_3O_5Ru \cdot 0.5\ CH_2Cl_2$: Calc C, 52.26; H, 4.19; N, 5.30. Expt C, 52.42; H, 4.40; N, 5.02. UV-Vis-NIR (MeCN): λ_{max}/nm (ε/ M^{-1} cm^{-1}) 270 (25,000), 465 (9,700), 582 (12,000). FT-IR (KBr, air background): 2922 w, 1690 w, 1597 m, 1561 vs, 1551 vs, 1517 vs, 1448 m, 1376 s, 1272 m, 1181 m, 1084 m, 1054 s, 1029 m, 917 m, 766 m, 690 w, 458 w cm^{-1}. ^{1}H NMR (d_3-MeCN, 500 MHz, 298 K) δ: 7.94 (t, 8 Hz, 1H, H_{14}) 7.87 (d, 8 Hz, 1H, H_{12}), 7.74 (d, 8 Hz, 1H, H_{21} or H_{19}), 7.72 (d, 8 Hz, 1H, H_{21} or H_{19}), 7.43 (t, 8 Hz, 1H, H_{20}), 7.38 (t, 8 Hz, 1H, H_6), 6.09 (t, 8 Hz, 1H, H_{13}), 5.85 (d, 8 Hz, 1H, H_4), 5.64 (d, 8 Hz, 1H, H_{15}), 5.30 (d, 8 Hz, H_7), 5.12 (t, 8 Hz, 1H, H_5), 4.46 (s,

1H, H_{27}), 4.38 (s, 1H, H_{32}), 2.36 (s, 3H, H_{23} or H_{24}), 2.29 (s, 3H, H_{23} or H_{24}), 2.18 (s, 3H, H_{34}), 1.99 (s, 3H, H_{29}), 1.89 (s, 3H, H_{25}), 1.83 (s, 3H, H_{30}). ^{1}H NOESY correlations 5.30 to 1.99; 5.64 to 2.18. ^{13}C NMR (d_3-MeCN, 500 MHz, 298 K) δ: 195.1 (C_{28}), 192.3 (C_{33}), 190.5 (C_{26}), 189.2 (C_{31}), 180.4 (C_{10}), 151.0 (C_{16}), 148.6 (C_1 or C_9), 145.7 (C_{22} or C_{18}), 145.2 (C_{22} or C_{18}), 142.8 (C_8) 140.0 (C_2), 136.1 (C_1 or C_9), 135.9 (C_{14}), 134.6 (C_6), 134.1 (C_5), 133.6 (C_{13}), 132.9 (C_{20}), 130.7 (C_{19} or C_{21}), 130.6 (C_{19} or C_{21}), 127.7 (C_{11}), 125.5 (C_{17}), 124.5 (C_3), 121.6 (C_7), 121.4 (C_{15}), 121.0 (C_{12}), 119.8 (C_4), 111.4 (C_{27}), 110.5 (C_{32}), 26.0 (C_{34}), 25.9 (C_{25}), 25.6 (C_{30}), 25.0 (C_{29}), 17.9 (C_{23} or C_{24}), 17.7 (C_{23} or C_{24}).

Bisacetylacetonato[*cis*-indigo-bis-(2,6-dimethylphenyl)diimine]ruthenium 5.5: To a 1-neck round bottomed flask was added $Ru(acac)_2MeCN_2$ (80.8 mg, 0.212 mmol), H_2Nindigo (97.4 mg, 0.208 mmol), p-benzoquinone (23.3 mg, 0.216 mmol), and 20 mL dry benzene. The mixture was refluxed under a dinitrogen atmosphere for 14 hours. The solvent was evaporated to dryness with a small amount of activated alumina, and the resultant powder was loaded onto a 20 cm alumina column slurried with hexanes. 77.6 mg (48% yield) purple-red **5.5** was collected after evaporation by eluting with 10:100 ethyl acetate/hexanes. Single crystals of **5.5·CH_2Cl_2** were grown by layering a saturated solution in dichloromethane with hexamethyldisiloxane. MP: 155 ^{o}C (decomp.). Elemental analysis for $C_{42}H_{41}N_4O_4Ru\cdot$ ½CH_2Cl_2 Calc. C, 63.15; H, 5.11; N, 6.93. Expt C, 63.30; H, 5.09; N, 6.80. UV-Vis-NIR (MeCN): λ_{max}/nm (ε/ M^{-1} cm^{-1}) 202 (76,000), 241 (27,000), 268 (29,000), 328 (9,600), 519 (18,000). FT-IR (KBr, air background): 1624 w, 1571 s, 1515 vs, 1449 m, 1469 m, 1389 s, 1294 m, 1268 m, 1205 m, 1189 m, 1093 w, 1017 w, 928 m, 870 w, 759 s, 680 w, 630 w, 449 w cm^{-1}. ^{1}H NMR (500 MHz, CD_2Cl_2, 300 K) δ: 7.50 (2H, d, 7 Hz, H_7), 7.30 (2H, t, 7 Hz, H_6), 6.99-7.07 (8H, m), 6.33 (2H, d, 8 Hz, H_4), 5.54 (2H, s,

H_{19}), 2.26 (6H, s, H_{21}), 2.09 (6H, s, H_{17}), 2.03 (6H, s), 2.01 (6H, s). ^{13}C NMR (125.8 MHz, CD_2Cl_2) δ: 190.15 and 190.11 (C_{20} or C_{18}), 162.2, 161.0, 157.7, 150.8, 133.8 (C_6), 128.4, 127.5, 124.3(H_4), 124.0, 123.4, 123.2, 123.1, 117.6 (C_7), 99.5 (C_{19}), 27.6 (C_{21}), 27.2 (C_{17}), 18.3 (C_{16} and C_{15}).

Bisacetylacetonato[*cis*-1*H*-indigo-bis(2,6-dimethylphenyl)diimine]ruthenium tetrafluoroborate H5.5$^+$: To a solution of red **5.5·CH$_2$Cl$_2$** (33 mg, 0.043 mmol) in dichloromethane was added 0.2 mL 48% aqueous HBF_4. The mixture was shaken for 5 minutes, and the aqueous layer was removed. Deionized water (10 mL) was added and the separatory funnel was briefly swirled. The dark purple organic layer is drained. The aqueous layer wwas extracted with a further 2 mL of dichloromethane, and the combined organic layers were dried over $MgSO_4$, filtered, and evaporated. The resultant residue was recrystallized from dichloromethane/hexanes to give 24 mg black solid (65 % yield). Single crystals suitable for X-ray diffractometry were grown from slow evaporation of a concentrated solution of dichloromethane which was layered with 1:1 toluene/hexanes. Mp 142 ºC (decomp.). Elemental analysis for $C_{42}H_{41}BF_4N_4O_4Ru\cdot ½CH_2Cl_2$: Calc C, 56.96; H, 4.72; N, 6.25. Expt C, 57.22; H, 4.81; N, 6.29. UV-Vis-NIR (MeCN) λ_{max}/nm (ε/ M^{-1} cm^{-1}): 270 (32,000), 487 (12,000), 559 (16,000). FT-IR (KBr, air background): 2922 w, 1629 m, 1608 m, 1564 s, 1517 vs, 1502 m, 1444 m, 1368 m, 1275 m, 1194 m, 1060 vs, 938 m, 770 m, 732 w, 685 w, 460 w cm^{-1}. ^{1}H NMR (d_3-MeCN, 500 MHz, 298 K) δ: 12.52 (s, 1H, NH), 7.58 (t, 2H, 8 Hz, H_6), 7.42 (d, 8 Hz, 2H, H_{13}), 7.40 (d, 8 Hz, 2H, H_{11}), 7.32 (t, 8 Hz, 2H, H_{12}), 6.31 (d, 8 Hz, 2H, H_4), 6.07 (d, 8 Hz, 2H, H_7), 6.03 (t, 8 Hz, 2H, H_5), 4.80 (s, 2H, H_{19}), 2.20 (s, 6H, H_{15} or H_{16}), 2.14 (s, 6H, H_{21}), 2.11 (s, 6H, H_{15} or H_{16}), 2.06 (s, 6H, H_{17}). NOESY: 6.07 d to 2.14 s; 6.31 d to 2.11 s. ^{13}C NMR (d_3-MeCN, 500 MHz, 298 K) δ: 193.9

(C_{20}), 190.7 (C_{18}), 150.0 (C_2 or C_8), 149.7 (C_2 or C_8), 149.0 (C_1), 137.0 (C_5), 135.2 (C_6), 134.9 (C_{10} or C_{14}), 134.7 (C_{10} or C_{14}), 131.8 (C_5), 130.21 (C_{11} or C_{12}), 130.17 (C_{11} or C_{12}), 130.0 (C_{12}), 124.7(C_3), 121.7 (C_4), 119.7 (C_7), 106.7 (C_{19}), 26.3 (C_{21}), 25.9 (C_{17}), 18.3 (C_{15} or C_{16}), 18.2 (C_{15} or C_{16}).

Chapter 6 Concluding remarks

The unique electronic structures that are a defining trait of redox-active ligands drives the pursuit of the systems in this dissertation. The exploration of new and different redox-active ligands broadens the scope of applications that can benefit from these systems. This dissertation demonstrated the capability of two closely related redox-active ligands, Nindigo and Mindigo, to act as near-infrared absorbing proton and electron reservoirs, and it showed that nominally ligand centered properties can be controlled through different metal-ancillary ligand combinations.

In the first half of the dissertation, the thermodynamics of electron transfer involving Nindigo and Mindigo complexes was investigated. Chapters 2 and 3 demonstrated that the ligands ancillary to the redox-active ligand, Nindigo or Mindigo, affected the oxidation and absorption properties of the related complexes. For both ligands, complexes that contained electron rich, pi-donating acac ligands are more easily oxidized than their electron poor, pi-donating hfac congeners. Chapters 2 and 3 also show that Nindigo and in particular Mindigo can adopt several coordination modes, which play a significant role in the spectral and electrochemical properties of their corresponding complexes and are an important consideration in these systems.

Chapter 2 showed that the choice of aryl group can modulate both the steric environment around the arylimine unit and the reduction potentials of *cis*-Nindigo complexes. This result contrasts with those from the corresponding *trans*-Nindigo complexes, which showed that the choice of aryl groups had a negligible effect on the spectral and electrochemical properties of the resultant complexes. The ability to tune the

ligand's spectral properties through conjugation and functional group manipulation opens up the possibility of color tuning which was not possible with *trans*-complexes.

Chapter 3 demonstrated the coordination chemistry of Mindigo for the first time. The properties of Mindigo complexes shown in chapter 3 were confirmed to be the steric and electronic hybrid of indigo and Nindigo. As has been previously observed with indigo and Nindigo, complexes of *cis*- and *trans*-Mindigo were observed. Despite the possibility of at least four products with one metal per ligand, through careful optimization, the isolation of select products is possible. Indeed, when the palladium complexes discussed in chapter 3 are compared to the ruthenium complexes in chapter 5, it is clear that three chelates (*cis*-N,N; *trans*-N,N; and *trans*-N,O) can be formed in different conditions that have their own interesting properties and are independently isolable. *Trans*-Mindigo complexes are more difficult to reduce and are hypsochromically shifted from their *cis*-Mindigo analogues.

In the second half of this thesis, *cis*-Nindigo and *cis*-Mindigo ligands were shown to be both proton and electron reservoirs for the first time. Chapters 4 and 5 presented the thermodynamics of proton, hydrogen atom, and hydride transfer in these systems.

The weakening of the corresponding NH bond in metal complexes can be caused by increased acidity which arises from close proximity to an electropositive metal; by interactions of the metal with the ligand's π-system; and lastly, as a consequence of electron rich, redox-active metals behaving as separate electron reservoirs. Complexes found in chapters 4 and 5 differ from the previously reported complexes that are known to deliver protons and electrons. Firstly, the NH bond of the Nindigo and Mindigo complexes is relatively far removed from the metal; secondly, the basic nitrogen atom remain sp^2

hybridized; and lastly, up to *five* ligand centered charge states are possible. The ligands' acidity does not change noticeably among the complexes of similar ligand charge states, so the metal-ligand interactions effectively weaken the NH bond by causing the complexes to be more susceptible to oxidation. The absence of coordination induced acidity in all of the complexes and the wide separation of redox potentials show that different metals can weaken (or possibly strengthen) ligand centered NH bonds through the modulation of the ligand centered redox potentials.

The potential-pK_a (Pourbaix) diagrams presented in Chapter 4 further confirm the utility of these diagrams in the study of compounds involving proton and electron transfer. These diagrams are particularly helpful for analyzing compounds which are difficult to study by other means. Although these diagrams have been utilized for nearly a century, potential-pK_a diagrams in *aprotic* solvents are still quite new. Although these measurements have provided useful information on the thermodynamics of proton and electron transfer, the *identity* of the formed products remains ambiguous. This technique may be made extremely powerful by coupling the measurements to spectroscopy such as EPR and UV-Vis-NIR spectroscopy to determine the properties of proton-coupled oxidation *in situ*.

Chapter 5 explored the proton and electron transfer of the ruthenium bis(acetylacetonate) complexes of Nindigo and Mindigo. These complexes contrast with those reported in Chapter 4 in which metal centered redox activity was nominally absent. The presence of an electron rich metal weakens the NH bond strength in all of the oxidation/charge states.

Although the fine details of the electronic structure of **H5.3**$^{+}$ and **H5.5**$^{+}$ are not explicitly known, protonation clearly induced a dramatic change in the electronic structure of both the ligand and metal. Whether the observed low-lying paramagnetic state arises from antiferromagnetic coupling or valence tautomerism, protonation has turned on this non-innocence. The ambiguity of the compounds' electronic structures can be elucidated by comparison of singlet and triplet electronic structures, which can be obtained through computation.

Furthermore, the electronic structure of other oxidation and charge states of **H5.3**^{n} and **H5.5**^{n} are not known. The results of chapter 5 in general beg the question: how does the electronic structure of the complex affect the thermodynamics of proton and electron transfer? Both metal and ligand redox-activity is possible with these $Ru(acac)_2$ complexes and it is unclear if the proton and electron transfer processes proposed involve the metal or if the metal merely acts as a complicated functional group. **Scheme 6.1** displays a simplified depiction of oxidation and ligand charge states for (**H**)**5.3**^{n} and (**H**)**5.3**^{n}. Oxidation of forms A or B to **5.3** or **5.5** is ligand centered, however the metal is reduced from form A, i.e. redox-induced electron transfer. Likewise, oxidation of form C to **5.3** or **5.5** leads to a net reduction of the metal. In the future, spectroelectrochemical detection or synthesis and isolation of **H5.3**^{n} and **H5.5**^{n} (where n = +, 0, 1-, and 2-) must be completed alongside calculation of the electronic structures to develop a complete picture of the role that ruthenium plays in hydrogen atom non-innocence.

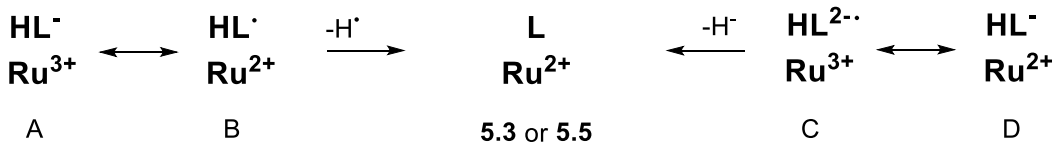

Scheme 6.1 Electronic structure possibilities for the hydrogen atom and hydride transfer reactions of **5.3** or **5.5**.

The effect of proton transfer to a redox-active ligand, in general, could affect the reactivity of the complex in dramatic ways. For instance, protonation (or deprotonation) could serve to increase the driving force of a reaction by making the complex more easily reduced (or oxidized). In chapter 4, this was demonstrated by the proton transfer induced disproportionation of **H4.12**$^{2+}$ and **4.12**$^{+}$. In Chapter 5, protonation resulted in the complex being easier to reduce by up to 0.78 V (18 kcal mol^{-1}). Proton transfer may therefore be used as a switch to turn the reactivity of a complex on or off by affecting its electronic structure. Furthermore, the complexes of Chapter 5 showed that this basic site need not be close to the metal to induce large effects on the complex. In general, proton responsive redox-active ligands allow for an orthogonal handle on the electronic structure beyond conventional ligand design or further changes to the coordination sphere.

Chapters 4 and 5 also revealed net two-electron/one-proton transfer processes. The products of two-electron one-proton oxidation, **4.11**$^{+}$ and **4.12**$^{2+}$, are predicted to be potent hydride abstractors, while Ru(acac)$_2$ complexes **5.3** and **5.5** are predicted to be moderate hydride abstractors. Hydride transfer to and from electronegative atoms such as nitrogen is somewhat unusual, although it is not unknown in cases where the proton and electrons are separated.[153] Typical hydride abstractors are Lewis acids such as BF_3, $B(C_6F_5)_3$, trityl cation, etc. As depicted in **Scheme 6.2,** the two electrons that are transferred go into forming the hydride's new bond in these examples. On the contrary, the examples in

Chapters 4 and 5 transfer proton and electrons to different orbitals as depicted in **Scheme 6.3**: the ligand's π-system and/or the metal's d-orbitals.

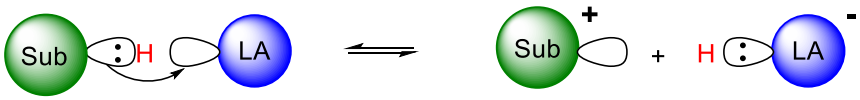

Scheme 6.2 Hydride transfer from a substrate (green) to a Lewis acid LA.

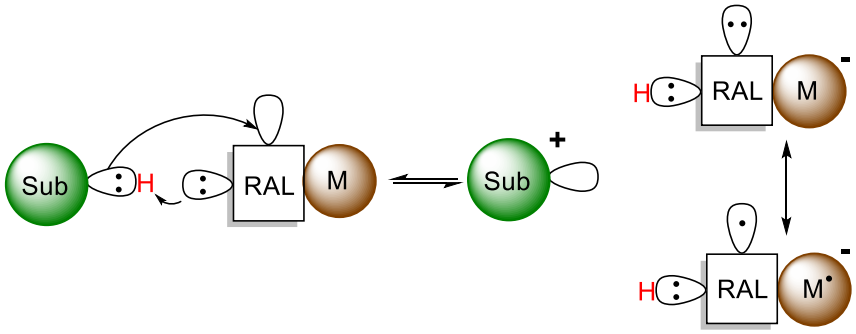

Scheme 6.3 Hydride transfer from a substrate (green) to a proton accepting RAL complex.

A potentially fruitful area of future research could be to investigate the hydride transfer reactivity of compounds **4.12**$^{2+}$, **5.3**, and **5.5**. These compound constitute a highly tunable series of hydride abstractors. The metal center is coordinatively saturated and is not likely to be a source of reactivity beyond electron transfer. The charge of the redox-active ligand is delocalized and, in the case of Nindigo, can be sterically shielded by the choice of the arylimine subunit. The thermodynamics of hydride transfer can therefore be modulated through changes to both the metal and the ancillary ligands. While the electrons end up in the metal/ligand system, the proton bonds to the arylimines. As a result, the choice of aryl group can change the sterics of the reactive site. The separation of proton and electrons also means the reactive site is not likely Lewis acidic in the traditional sense.

The results in Chapters 4 and 5 constitute an avenue of future exploratory reactivity using these non-Lewis acidic hydride acceptors. Like "frustrated Lewis pairs"[154], these

complexes likely would not react with Lewis bases but could work in concert to carry out small molecule activation reactions. Additionally, the absence of a Lewis acid allows for different substrate selectivity and availability. The hydride abstraction of dihydrogen shown in **Scheme 6.4**, which is known to require 76 kcal mol^{-1},[155] should be thermodynamically viable using **4.12**$^{2+}$ which has a hydride affinity of approximately 90 kcal mol^{-1}. This generates an equivalent of protons that can then be scavenged by added base. In principle, the same should apply for other substrates for their dehydrogenation. Likewise, the hydride affinity of **5.5** is only 3 kcal mol^{-1} less than $B(C_6F_5)_3$ which is known to reversibly (and usefully) split hydrogen in concert with weak ancillary bases. Thus, reactions similar to those accomplished by frustrated Lewis pairs should be thermodynamically accessible.

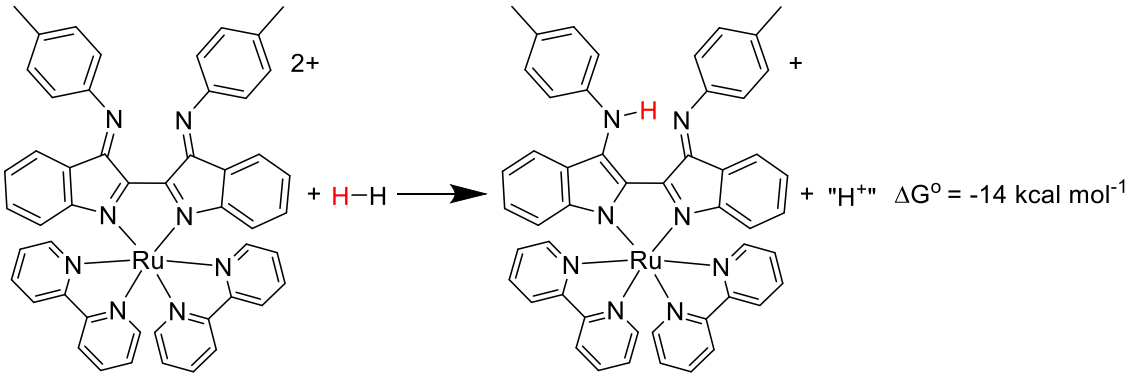

Scheme 6.4 Hydrogen splitting by **H4.12**$^{2+}$.

H4.12^{+} and **4.12**$^{2+}$ differ from more traditional Lewis acid reactivity as well in that they can be activated and regenerated readily by mild oxidants and bases such as ferrocenium and substituted pyridine bases, as shown in **Scheme 6.5**. Furthermore, **4.12**$^{2+}$ is predicted to have similar hydride affinities to some silylium cations in acetonitrile.[155] One potential application of this reaction is the defluorination of fluoroalkanes. The use of

catalytic amounts of hydride abstractors with silanes has previously been used to defluorinate fluorocarbons.[156]

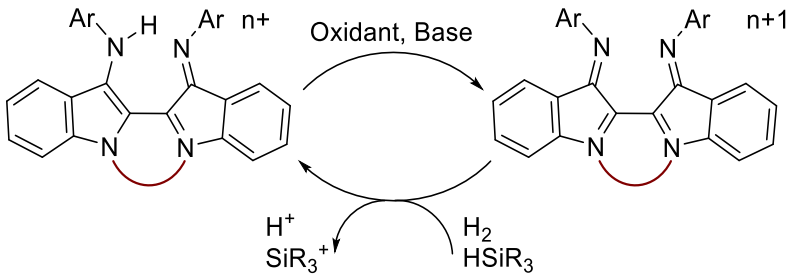

Scheme 6.5 Activation and hydride transfer of *cis*-Nindigo complexes. The brown loop implies a transition metal and ligand bridge such as, but not limited to, Pd(acac), $Ru(bipy)_2$ or $Ru(acac)_2$.

The lack of Lewis acidity in the *cis*-Nindigo complexes provides a potential kinetic problem. It is not known explicitly if the proton and both electrons would transfer together in a concerted manner, leading to a possibility of radical reactions (single electron or hydrogen atom transfer reactions) rather than hydride reactivity. Additionally, frustrated Lewis pairs typically form weak Lewis acid/base interactions that hold the pairs together. In the absence of a Lewis acid, interactions with neutral bases may not exist, thus requiring an unfavorable termolecular process. The use of anionic bases such as acetate as in adduct **6.1** alongside cationic hydride acceptors such as $\mathbf{4.12^{2+}}$ could allow for reactions between the substrate and the ion paired hydride acceptor and base. Alternatively, the use of basic arylimines such as a 2-pyridyl (**6.2**) or 2-aminophenyl groups provide the potential for an intramolecular proton/hydride transfer pair.

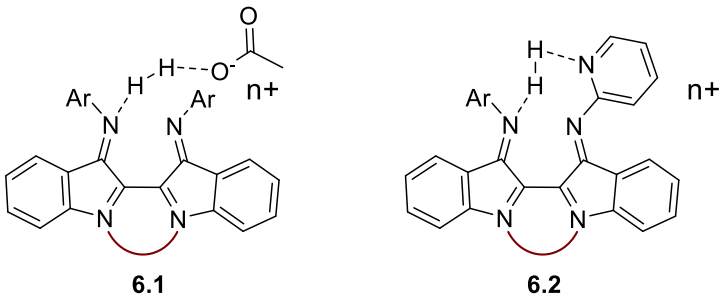

Scheme 6.6 Dihydrogen adducts of Nindigo complexes with ionically (**6.1**) and covalently (**6.2**) linked bases.

Bibliography

1. Constable, E. C.; Housecroft, C. E., *Chemical Society Reviews* **2013,** *42* (4), 1429-1439.

2. Crabtree, R. H., Applications of Organometallic Chemistry. In *The Organometallic Chemistry of the Transition Metals*, 4th ed.; John Wiley & Sons, Inc.: 2005; pp 343-377.

3. Atkins, P. W.; Shriver, D. F., *Inorganic chemistry*. 4th ed.; W.H. Freeman: New York, 2006; p xxi, 822 p.

4. Crabtree, R. H., *New Journal of Chemistry* **2011,** *35* (1), 18-23.

5. Karen, P.; McArdle, P.; Takats, J., Comprehensive definition of oxidation state (IUPAC Recommendations 2016). In *Pure and Applied Chemistry*, 2016; Vol. 88, p 831.

6. Chaudhuri, P.; Verani, C. N.; Bill, E.; Bothe, E.; Weyhermüller, T.; Wieghardt, K., *Journal of the American Chemical Society* **2001,** *123* (10), 2213-2223.

7. Jørgensen, C. K., *Coordination Chemistry Reviews* **1966,** *1* (1), 164-178.

8. Caulton, K. G., *European Journal of Inorganic Chemistry* **2012,** *2012* (3), 435-443.

9. Caulton, K. G., *European Journal of Inorganic Chemistry* **2012,** (3), 435-443.

10. Pierpont, C. G., *Coordination Chemistry Reviews* **2001,** *216–217*, 99-125.

11. Chirik, P. J., *Inorganic Chemistry* **2011,** *50* (20), 9737-9740.

12. Cohen, S. A.; Auburn, P. R.; Bercaw, J. E., *Journal of the American Chemical Society* **1983,** *105* (5), 1136-1143.

13. Miller, J. S.; Min, K. S., *Angewandte Chemie International Edition* **2009,** *48* (2), 262-272.

14. Muresan, N.; Chlopek, K.; Weyhermüller, T.; Neese, F.; Wieghardt, K., *Inorganic Chemistry* **2007,** *46* (13), 5327-5337.

15. Kaim, W., *Inorganic Chemistry* **2011,** *50* (20), 9752-9765.

16. Eisenberg, R.; Gray, H. B., *Inorganic Chemistry* **2011,** *50* (20), 9741-9751.

17. Dzik, W. I.; van der Vlugt, J. I.; Reek, J. N. H.; de Bruin, B., *Angewandte Chemie International Edition* **2011,** *50* (15), 3356-3358.

18. Luca, O. R.; Crabtree, R. H., *Chemical Society Reviews* **2013,** *42* (4), 1440-1459.

19. Kaim, W.; Schwederski, B., *Coordination Chemistry Reviews* **2010,** *254* (13), 1580-1588.

20. Guengerich, F. P.; Waterman, M. R.; Egli, M., *Trends in Pharmacological Sciences* **2016,** *37* (8), 625-640.

21. Rittle, J.; Green, M. T., *Science* **2010,** *330* (6006), 933-937.

22. Newcomb, M.; Zhang, R.; Chandrasena, R. E. P.; Halgrimson, J. A.; Horner, J. H.; Makris, T. M.; Sligar, S. G., *Journal of the American Chemical Society* **2006,** *128* (14), 4580-4581.

23. Laszlo Kurti, B. C., *Strategic Applications of Named Reactions in Organic Synthesis*. 1 ed.; Elsevier: 2005; p 864.

24. Chirik, P. J.; Wieghardt, K., *Science* **2010,** *327* (5967), 794-795.

25. Blackmore, K. J.; Ziller, J. W.; Heyduk, A. F., *Inorganic Chemistry* **2005,** *44* (16), 5559-5561.

26. Haneline, M. R.; Heyduk, A. F., *Journal of the American Chemical Society* **2006,** *128* (26), 8410-8411.

27. Zarkesh, R. A.; Ziller, J. W.; Heyduk, A. F., *Angewandte Chemie-International Edition* **2008,** *47* (25), 4715-4718.

28. Munhá, R. F.; Zarkesh, R. A.; Heyduk, A. F., *Dalton Transactions* **2013,** *42* (11), 3751-3766.

29. Smith, A. L.; Clapp, L. A.; Hardcastle, K. I.; Soper, J. D., *Polyhedron* **2010,** *29* (1), 164-169.

30. Smith, A. L.; Hardcastle, K. I.; Soper, J. D., *Journal of the American Chemical Society* **2010,** *132* (41), 14358-14360.

31. Friedfeld, M. R.; Shevlin, M.; Margulieux, G. W.; Campeau, L.-C.; Chirik, P. J., *Journal of the American Chemical Society* **2016,** *138* (10), 3314-3324.

32. Chirik, P. J., *Accounts of Chemical Research* **2015,** *48* (6), 1687-1695.

33. Pappas, I.; Treacy, S.; Chirik, P. J., *ACS Catalysis* **2016,** *6* (7), 4105-4109.

34. Palmer, W. N.; Diao, T.; Pappas, I.; Chirik, P. J., *ACS Catalysis* **2015,** *5* (2), 622-626.

35. Aimoto, Y.; Koshiba, K.; Yamauchi, K.; Sakai, K., *Chemical Communications* **2018,** *54* (91), 12820-12823.

36. Koshiba, K.; Yamauchi, K.; Sakai, K., *Angewandte Chemie International Edition* **2017,** *56* (15), 4247-4251.

37. Koshiba, K.; Yamauchi, K.; Sakai, K., *Dalton Transactions* **2019**.

38. Zarkadoulas, A.; Koutsouri, E.; Mitsopoulou, C. A., *Coordination Chemistry Reviews* **2012,** *256* (21), 2424-2434.

39. Uzelac, E. J.; Rasmussen, S. C., *European Journal of Inorganic Chemistry* **2017,** *2017* (33), 3878-3883.

40. Amb, C. M.; Heth, C. L.; Evenson, S. J.; Pokhodnya, K. I.; Rasmussen, S. C., *Inorganic Chemistry* **2016,** *55* (21), 10978-10989.

41. Demir, S.; Jeon, I.-R.; Long, J. R.; Harris, T. D., *Coordination Chemistry Reviews* **2015,** *289–290*, 149-176.

42. Dou, J.-H.; Sun, L.; Ge, Y.; Li, W.; Hendon, C. H.; Li, J.; Gul, S.; Yano, J.; Stach, E. A.; Dincă, M., *Journal of the American Chemical Society* **2017,** *139* (39), 13608-13611.

43. Sheberla, D.; Bachman, J. C.; Elias, J. S.; Sun, C.-J.; Shao-Horn, Y.; Dincă, M., *Nature Materials* **2016,** *16*, 220.

44. Li, W.; Sun, L.; Qi, J.; Jarillo-Herrero, P.; Dincă, M.; Li, J., *Chemical Science* **2017,** *8* (4), 2859-2867.

45. DeGayner, J. A.; Jeon, I.-R.; Sun, L.; Dincă, M.; Harris, T. D., *Journal of the American Chemical Society* **2017,** *139* (11), 4175-4184.

46. Cozzolino, A. F.; Brozek, C. K.; Palmer, R. D.; Yano, J.; Li, M. Y.; Dinca, M., *Journal of the American Chemical Society* **2014,** *136* (9), 3334-3337.

47. Ferreira, E. S. B.; Hulme, A. N.; McNab, H.; Quye, A., *Chemical Society Reviews* **2004,** *33* (6), 329-336.

48. Nusca, A. Tablets, Lasers, and Time to Market: How Levi Strauss Reinvented the Way It Makes Jeans. http://fortune.com/2018/02/27/levi-strauss-tablets-lasers-market-jeans-model/ (accessed 1/7/2019).

49. Baeyer, A., *Berichte der deutschen chemischen Gesellschaft* **1883,** *16* (2), 2188-2204.

50. Lindstedt, A. Alfred von Baeyer Nobel Award ceremony speech. https://www.nobelprize.org/prizes/chemistry/1905/ceremony-speech/ (accessed 1-7-2019).

51. Christie, R. M., *Colour Chemistry: Edition 2*. Royal Society of Chemistry: Cambridge, UK, 2015.

52. Clark, R. J. H.; Cooksey, C. J.; Daniels, M. A. M.; Withnall, R., *Endeavour* **1993,** *17* (4), 191-199.

53. Luttke, W.; Klessinger, M., *Chemie Berichte* **1964,** *97* (8), 2342-&.

54. Kunz, K., *Berichte Der Deutschen Chemischen Gesellschaft* **1922,** *55*, 3688-3691.

55. Kunz, K.; Stuhlinger, W., *Berichte Der Deutschen Chemischen Gesellschaft* **1925,** *58*, 1860-1868.

56. Larkworthy, L. F.; Nyholm, R. S., *Nature* **1959,** *183* (4672), 1377-1380.

57. Lenz, A.; Sunkel, K.; Beck, W., *Zeitschrift Fur Naturforschung Section B-a Journal of Chemical Sciences* **1996,** *51* (11), 1639-1643.

58. Andreas Lenz, C. S., Annette Lehmann, Barbara Wagner, Wolfgang Beck, *Zeitschrift Fur Naturforschung* **1996,** *52 b*, 474-484.

59. Lenz, A.; Schmidt, C.; Lehmann, A.; Wagner, B.; Beck, W., *Zeitschrift Fur Naturforschung Section B* **1997,** *52* (4), 474-484.

60. Beck, W.; Schmidt, C.; Wienold, R.; Steimann, M.; Wagner, B., *Angewandte Chemie-International Edition in English* **1989,** *28* (11), 1529-1531.

61. Schmidt, C.; Wagner, H. U.; Beck, W., *Chemische Berichte Recueil* **1992,** *125* (11), 2347-2350.

62. Wu, J. Y.; Chang, C. H.; Thanasekaran, P.; Tsai, C. C.; Tseng, T. W.; Lee, G. H.; Peng, S. M.; Lu, K. L., *Dalton Transactions* **2008,** (44), 6110-6112.

63. Oakley, S. R.; Nawn, G.; Waldie, K. M.; MacInnis, T. D.; Patrick, B. O.; Hicks, R. G., *Chemical Communications* **2010,** *46* (36), 6753-5.

64. Nawn, G.; Waldie, K. M.; Oakley, S. R.; Peters, B. D.; Mandel, D.; Patrick, B. O.; McDonald, R.; Hicks, R. G., *Inorganic chemistry* **2011,** *50* (20), 9826-37.

65. Nawn, G.; Oakley, S. R.; Majewski, M. B.; McDonald, R.; Patrick, B. O.; Hicks, R. G., *Chemical Science* **2013,** *4* (2), 612.

66. Nawn, G.; McDonald, R.; Hicks, R. G., *Inorganic Chemistry* **2013,** *52* (19), 10912-9.

67. Mondal, P.; Ehret, F.; Bubrin, M.; Das, A.; Mobin, S. M.; Kaim, W.; Lahiri, G. K., *Inorganic Chemistry* **2013,** *52* (15), 8467-75.

68. Mondal, P.; Plebst, S.; Ray, R.; Mobin, S. M.; Kaim, W.; Lahiri, G. K., *Inorganic Chemistry* **2014,** *53* (17), 9348-56.

69. Fortier, S.; Moral, O. G.-d.; Chen, C.-H.; Pink, M.; Le Roy, J. J.; Murugesu, M.; Mindiola, D. J.; Caulton, K. G., *Chemical Communications* **2012,** *48* (90), 11082-11084.

70. Fortier, S.; Le Roy, J. J.; Chen, C. H.; Vieru, V.; Murugesu, M.; Chibotaru, L. F.; Mindiola, D. J.; Caulton, K. G., *Journal of the American Chemical Society* **2013,** *135* (39), 14670-8.

71. Bhattacharya, D.; Chang, C. H.; Cheng, Y. H.; Lai, L. L.; Lu, H. Y.; Lin, C. Y.; Lu, K. L., *Chemistry-a European Journal* **2012,** *18* (17), 5275-5283.

72. Mondal, P.; Chatterjee, M.; Paretzki, A.; Beyer, K.; Kaim, W.; Lahiri, G. K., *Inorganic Chemistry* **2016,** *55* (6), 3105-3116.

73. Chatterjee, M.; Mondal, P.; Beyer, K.; Paretzki, A.; Kaim, W.; Lahiri, G. K., *Dalton Transactions* **2017,** *46* (15), 5091-5102.

74. Mondal, P.; Das, A.; Lahiri, G. K., *Inorganic Chemistry* **2016,** *55* (3), 1208-1218.

75. Chatterjee, M.; Ghosh, P.; Beyer, K.; Paretzki, A.; Fiedler, J.; Kaim, W.; Lahiri, G. K., *Chem-Asian J* **2018,** *13* (1), 118-125.

76. Guo, F. S.; Layfield, R. A., *Chemical Communications* **2017,** *53* (21), 3130-3133.

77. Konarev, D. V.; Khasanov, S. S.; Kuzmin, A. V.; Shestakov, A. F.; Otsuka, A.; Yamochi, H.; Saito, G.; Lyubovskaya, R. N., *Dalton Transactions* **2016,** *45* (43), 17095-17099.

78. Konarev, D. V.; Kuzmin, A. V.; Khasanov, S. S.; Fatalov, A. M.; Yudanova, E. I.; Lyubovskaya, R. N., *Chemistry-a European Journal* **2018,** *24* (33), 8415-8423.

79. Complexes of Bulky β-Diketiminate Ligands. In *Inorganic Syntheses*, John Wiley & Sons, Inc.: 2010; pp 1-55.

80. Nicholls-Allison, E. C.; Nawn, G.; Patrick, B. O.; Hicks, R. G., *Chemical Communications* **2015,** *51* (62), 12482-12485.

81. Hajjar, L.; Hicks, R. G.; Zeng, T., *The Journal of Physical Chemistry A* **2016,** *120* (38), 7569-7576.

82. Sarkar, B.; Schweinfurth, D.; Deibel, N.; Weisser, F., *Coordination Chemistry Reviews* **2015,** *293-294*, 250-262.

83. Chiang, L.; Allan, L. E. N.; Alcantara, J.; Wang, M. C. P.; Storr, T.; Shaver, M. P., *Dalton Transactions* **2014,** *43* (11), 4295-4304.

84. Herebian, D.; Bothe, E.; Neese, F.; Weyhermüller, T.; Wieghardt, K., *Journal of the American Chemical Society* **2003,** *125* (30), 9116-9128.

85. Sanz, C. A.; McKay, Z. R.; MacLean, S. W. C.; Patrick, B. O.; Hicks, R. G., *Dalton Transactions* **2017,** *46* (37), 12636-12644.

86. Cui, P.; Iluc, V. M., *Chemical Science* **2015,** *6* (12), 7343-7354.

87. Broere, D. L. J.; Metz, L. L.; de Bruin, B.; Reek, J. N. H.; Siegler, M. A.; van der Vlugt, J. I., *Angewandte Chemie International Edition* **2015,** *54* (5), 1516-1520.

88. Broere, D. L. J.; Plessius, R.; Tory, J.; Demeshko, S.; de Bruin, B.; Siegler, M. A.; Hartl, F.; van der Vlugt, J. I., *Chemistry – A European Journal* **2016,** *22* (39), 13965-13975.

89. Sanz, C. A.; Ferguson, M. J.; McDonald, R.; Patrick, B. O.; Hicks, R. G., *Chemical Communications* **2014,** *50* (79), 11676-11678.

90. Mondal, P.; Das, A.; Lahiri, G. K., *Inorganic Chemistry* **2016,** *55* (3), 1208-1218.

91. Oakley, S. Synthesis, characterization and coordination chemistry of indigo diimines. University of Victoria, 2008.

92. Rosenkoetter, K. E.; Wojnar, M. K.; Charette, B. J.; Ziller, J. W.; Heyduk, A. F., *Inorganic Chemistry* **2018,** *57* (16), 9728-9737.

93. Whittaker, J. W., *Chemical Reviews* **2003,** *103* (6), 2347-2364.

94. Whittaker, J. W., *Archives of Biochemistry and Biophysics* **2005,** *433* (1), 227-239.

95. Baron, A. J.; Stevens, C.; Wilmot, C.; Seneviratne, K. D.; Blakeley, V.; Dooley, D. M.; Phillips, S. E.; Knowles, P. F.; McPherson, M. J., *Journal of Biological Chemistry* **1994,** *269* (40), 25095-105.

96. Humphreys, K. J.; Mirica, L. M.; Wang, Y.; Klinman, J. P., *Journal of the American Chemical Society* **2009,** *131* (13), 4657-4663.

97. Tolman, W. B., 8.26 - Metal–Radical Arrays. In *Comprehensive Coordination Chemistry II*, McCleverty, J. A.; Meyer, T. J., Eds. Pergamon: Oxford, 2003; pp 715-737.

98. Königsmann, M.; Donati, N.; Stein, D.; Schönberg, H.; Harmer, J.; Sreekanth, A.; Grützmacher, H., *Angewandte Chemie International Edition* **2007,** *46* (19), 3567-3570.

99. Chaudhuri, P.; Hess, M.; Müller, J.; Hildenbrand, K.; Bill, E.; Weyhermüller, T.; Wieghardt, K., *Journal of the American Chemical Society* **1999,** *121* (41), 9599-9610.

100. Wang, Y.; Stack, T. D. P., *Journal of the American Chemical Society* **1996,** *118* (51), 13097-13098.

101. Que, L.; Tolman, W. B., *Nature* **2008,** *455* (7211), 333-340.

102. Sherbow, T. J.; Fettinger, J. C.; Berben, L. A., *Inorganic Chemistry* **2017,** *56* (15), 8651-8660.

103. Solis, B. H.; Maher, A. G.; Dogutan, D. K.; Nocera, D. G.; Hammes-Schiffer, S., *Proceedings of the National Acadamy of Sciences USA* **2016,** *113* (3), 485-492.

104. Haddad, A. Z.; Kumar, D.; Sampson, K. O.; Matzner, A. M.; Mashuta, M. S.; Grapperhaus, C. A., *Journal of the American Chemical Society* **2015,** *137* (29), 9238-9241.

105. Haddad, A. Z.; Cronin, S. P.; Mashuta, M. S.; Buchanan, R. M.; Grapperhaus, C. A., *Inorganic Chemistry* **2017,** *56* (18), 11254-11265.

106. Sherbow, T. J.; Carr, C. R.; Saisu, T.; Fettinger, J. C.; Berben, L. A., *Organometallics* **2016,** *35* (1), 9-14.

107. Thompson, E. J.; Berben, L. A., *Angewandte Chemie-International Edition* **2015,** *54* (40), 11642-11646.

108. Haddad, A. Z.; Garabato, B. D.; Kozlowski, P. M.; Buchanan, R. M.; Grapperhaus, C. A., *Journal of the American Chemical Society* **2016,** *138* (25), 7844-7847.

109. Matsumoto, T.; Chang, H. C.; Wakizaka, M.; Ueno, S.; Kobayashi, A.; Nakayama, A.; Taketsugu, T.; Kato, M., *Journal of the American Chemical Society* **2013,** *135* (23), 8646-8654.

110. Kwon, Y. M.; Delgado, M.; Zakharov, L. N.; Seda, T.; Gilbertson, J. D., *Chemical Communications* **2016,** *52* (73), 11016-11019.

111. Lu, F.; Zarkesh, R. A.; Heyduk, A. F., *European Journal of Inorganic Chemistry* **2012,** (3), 467-470.

112. Pramanick, R.; Bhattacharje, R.; Sengupta, D.; Datta, A.; Goswami, S., *Inorganic Chemistry* **2018,** *57* (12), 6816-6824.

113. Henthorn, J. T.; Lin, S. B.; Agapie, T., *Journal of the American Chemical Society* **2015,** *137* (4), 1458-1464.

114. Horak, K. T.; Agapie, T., *Journal of the American Chemical Society* **2016,** *138* (10), 3443-3452.

115. Schneck, F.; Finger, M.; Tromp, M.; Schneider, S., *Chemistry – A European Journal* **2017,** *23* (1), 33-37.

116. Sherbow, T. J.; Thompson, E. J.; Arnold, A.; Sayler, R. I.; Britt, R. D.; Berben, L. A., *Chemistry – A European Journal* **2018,** *25* (2), 454-458.

117. Conner, K. M.; Arostegui, A. C.; Swanson, D. D.; Brown, S. N., *Inorganic Chemistry* **2018,** *57* (16), 9696-9707.

118. Carter, S. M.; Sia, A.; Shaw, M. J.; Heyduk, A. F., *Journal of the American Chemical Society* **2008,** *130* (18), 5838-5839.

119. Warren, J. J.; Tronic, T. A.; Mayer, J. M., *Chemical Reviews* **2010,** *110* (12), 6961-7001.

120. Weinberg, D. R.; Gagliardi, C. J.; Hull, J. F.; Murphy, C. F.; Kent, C. A.; Westlake, B. C.; Paul, A.; Ess, D. H.; McCafferty, D. G.; Meyer, T. J., *Chemical Reviews* **2012,** *112* (7), 4016-4093.

121. Wayner, D. D. M.; Parker, V. D., *Accounts of Chemical Research* **1993,** *26* (5), 287-294.

122. Mader, E. A.; Davidson, E. R.; Mayer, J. M., *Journal of the American Chemical Society* **2007,** *129* (16), 5153-5166.

123. Cappellani, E. P.; Drouin, S. D.; Jia, G.; Maltby, P. A.; Morris, R. H.; Schweitzer, C. T., *Journal of the American Chemical Society* **1994,** *116* (8), 3375-3388.

124. Manner, V. W.; Mayer, J. M., *Journal of the American Chemical Society* **2009,** *131* (29), 9874-9875.

125. Wu, A.; Masland, J.; Swartz, R. D.; Kaminsky, W.; Mayer, J. M., *Inorganic Chemistry* **2007,** *46* (26), 11190-11201.

126. Roth, J. P.; Lovell, S.; Mayer, J. M., *Journal of the American Chemical Society* **2000,** *122* (23), 5486-5498.

127. Yoder, J. C.; Roth, J. P.; Gussenhoven, E. M.; Larsen, A. S.; Mayer, J. M., *Journal of the American Chemical Society* **2003,** *125* (9), 2629-2640.

128. Tarantino, K. T.; Miller, D. C.; Callon, T. A.; Knowles, R. R., *Journal of the American Chemical Society* **2015,** *137* (20), 6440-6443.

129. Semproni, S. P.; Milsmann, C.; Chirik, P. J., *Journal of the American Chemical Society* **2014,** *136* (25), 9211-9224.

130. Bezdek, M. J.; Guo, S.; Chirik, P. J., *Science* **2016,** *354* (6313), 730-733.

131. Kapovsky, M.; Dares, C.; Dodsworth, E. S.; Begum, R. A.; Raco, V.; Lever, A. B. P., *Inorganic Chemistry* **2013,** *52* (1), 169-181.

132. Pourbaix, M., *Atlas of electrochemical equilibria in aqueous solutions*. 1 ed.; Pergamon Press: New York, 1966; p 644.

133. Horvath, S.; Fernandez, L. E.; Appel, A. M.; Hammes-Schiffer, S., *Inorganic Chemistry* **2013,** *52* (7), 3643-3652.

134. McNaught, A. D.; Wilkinson, A.; Jenkins, A. D.; International Union of, P.; Applied, C., *IUPAC compendium of chemical terminology : the gold book*. International Union of Pure and Applied Chemistry: [Research Triangle Park, N.C.], 2006.

135. Kaljurand, I.; Kutt, A.; Soovali, L.; Rodima, T.; Maemets, V.; Leito, I.; Koppel, I. A., *The Journal of Organic Chemistry* **2005,** *70* (3), 1019-1028.

136. Kütt, A.; Leito, I.; Kaljurand, I.; Sooväli, L.; Vlasov, V. M.; Yagupolskii, L. M.; Koppel, I. A., *The Journal of Organic Chemistry* **2006,** *71* (7), 2829-2838.

137. Garrido, G.; Koort, E.; Rafols, C.; Bosch, E.; Rodima, T.; Leito, I.; Roses, M., *The Journal of Organic Chemistry* **2006,** *71* (24), 9062-9067.

138. McCarthy, B. D.; Dempsey, J. L., *Inorganic Chemistry* **2017,** *56* (3), 1225-1231.

139. Rountree, E. S.; McCarthy, B. D.; Dempsey, J. L., *Inorganic Chemistry* **2019**.

140. Reed, C. J.; Agapie, T., *Journal of the American Chemical Society* **2018,** *140* (34), 10900-10908.

141. Morris, R. H., *Journal of the American Chemical Society* **2014,** *136* (5), 1948-1959.

142. Rakowski DuBois, M.; DuBois, D. L., *Chemical Society Reviews* **2009,** *38* (1), 62-72.

143. Morris, R. H., *Chemical Reviews* **2016,** *116* (15), 8588-8654.

144. Brunner, E., *Journal of Chemical & Engineering Data* **1985,** *30* (3), 269-273.

145. Ilic, S.; Alherz, A.; Musgrave, C. B.; Glusac, K. D., *Chemical Society Reviews* **2018,** *47* (8), 2809-2836.

146. Pfirrmann, S.; Limberg, C.; Herwig, C.; Knispel, C.; Braun, B.; Bill, E.; Stösser, R., *Journal of the American Chemical Society* **2010,** *132* (39), 13684-13691.

147. Lu, C. C.; Weyhermüller, T.; Bill, E.; Wieghardt, K., *Inorganic Chemistry* **2009,** *48* (13), 6055-6064.

148. Bowman, A. C.; Milsmann, C.; Bill, E.; Lobkovsky, E.; Weyhermüller, T.; Wieghardt, K.; Chirik, P. J., *Inorganic Chemistry* **2010,** *49* (13), 6110-6123.

149. Stieber, S. C. E.; Milsmann, C.; Hoyt, J. M.; Turner, Z. R.; Finkelstein, K. D.; Wieghardt, K.; DeBeer, S.; Chirik, P. J., *Inorganic Chemistry* **2012,** *51* (6), 3770-3785.

150. Mao, J. H.; Zhang, Y.; Oldfield, E., *Journal of the American Chemical Society* **2002,** *124* (46), 13911-13920.

151. Mondal, P.; Agarwala, H.; Jana, R. D.; Plebst, S.; Grupp, A.; Ehret, F.; Mobin, S. M.; Kaim, W.; Lahiri, G. K., *Inorganic Chemistry* **2014,** *53* (14), 7389-7403.

152. Das, A.; Ghosh, P.; Plebst, S.; Schwederski, B.; Mobin, S. M.; Kaim, W.; Lahiri, G. K., *Inorganic Chemistry* **2015,** *54* (7), 3376-3386.

153. McLoughlin, E. A.; Waldie, K. M.; Ramakrishnan, S.; Waymouth, R. M., *Journal of the American Chemical Society* **2018,** *140* (41), 13233-13241.

154. Stephan, D. W.; Erker, G., *Angewandte Chemie International Edition* **2015,** *54* (22), 6400-6441.

155. Heiden, Z. M.; Lathem, A. P., *Organometallics* **2015,** *34* (10), 1818-1827.

156. Douvris, C.; Ozerov, O. V., *Science* **2008,** *321* (5893), 1188.

Appendix A. Appendix Table of Contents

Appendix B. NMR spectra

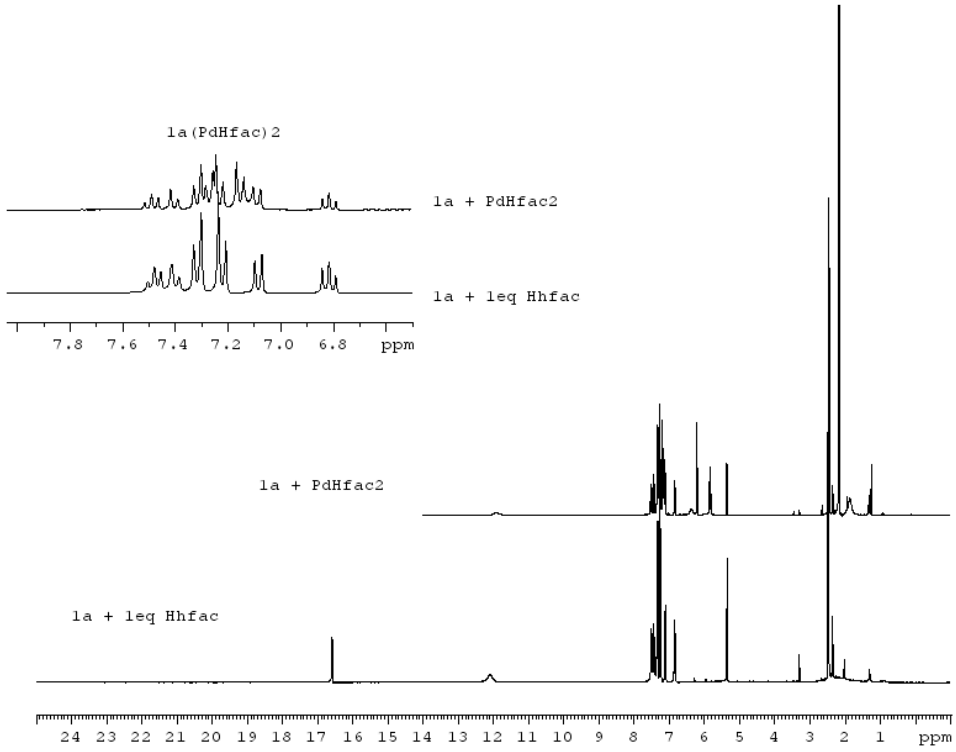

Appendix B-1 ^{1}H NMR of crude reaction mixture after 10 minutes (top) of **2.4a**, and **1.25** with 1 eq Hhfac (bottom).

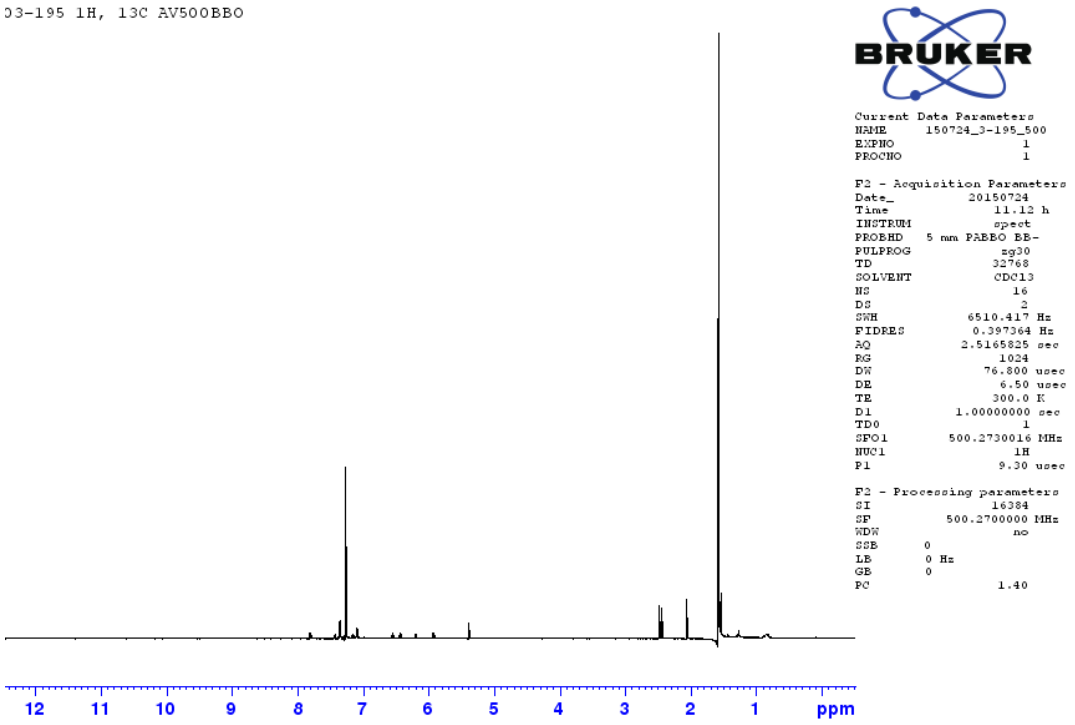

Appendix B-2 ^{1}H NMR of **2.3a** in $CDCl_3$.

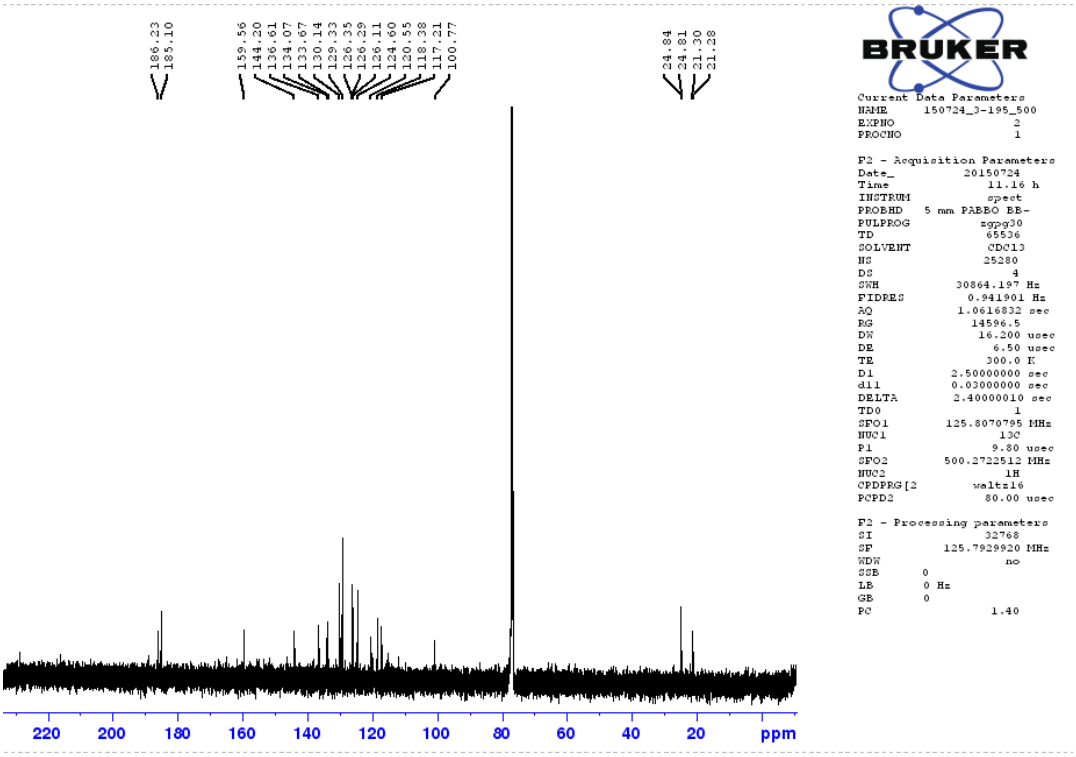

Appendix B-3 ^{13}C NMR of **2.3a** in $CDCl_3$.

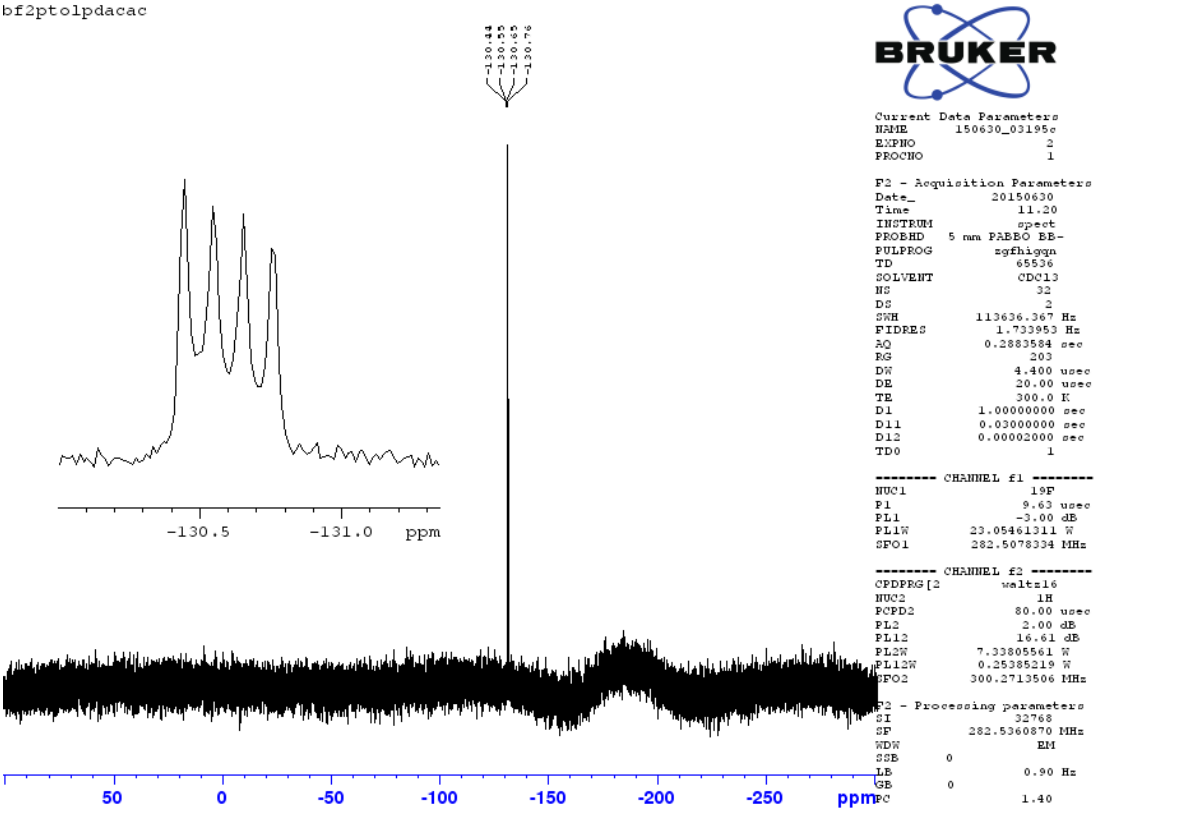

Appendix B-4 ^{19}F of **2.3a** in $CDCl_3$.

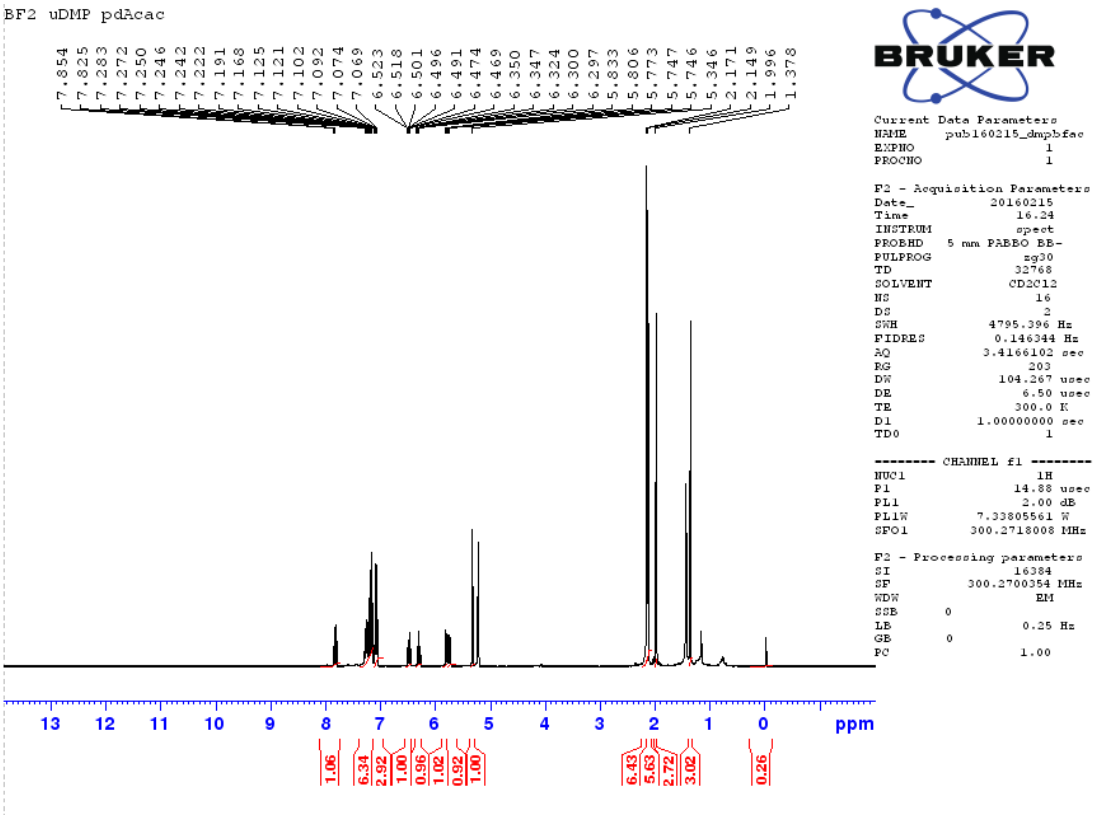

Appendix B-5 ^{1}H NMR of **2.3b** in CD_2Cl_2.

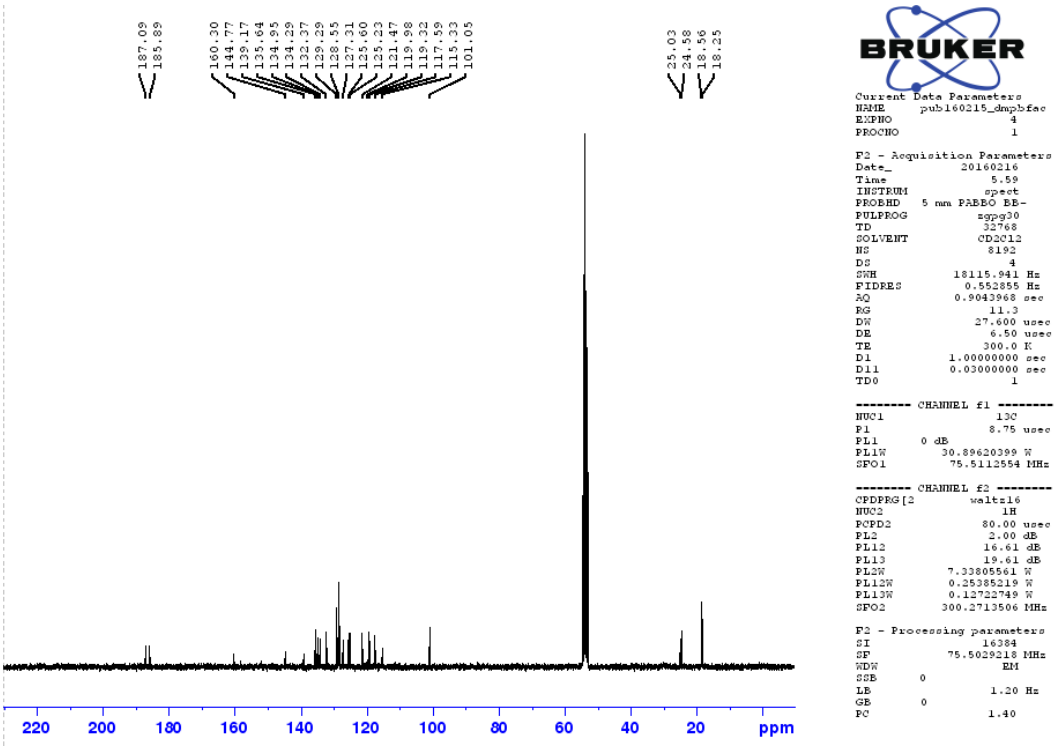

Appendix B-6^{13}C NMR of **2.2b** in CD_2Cl_2.

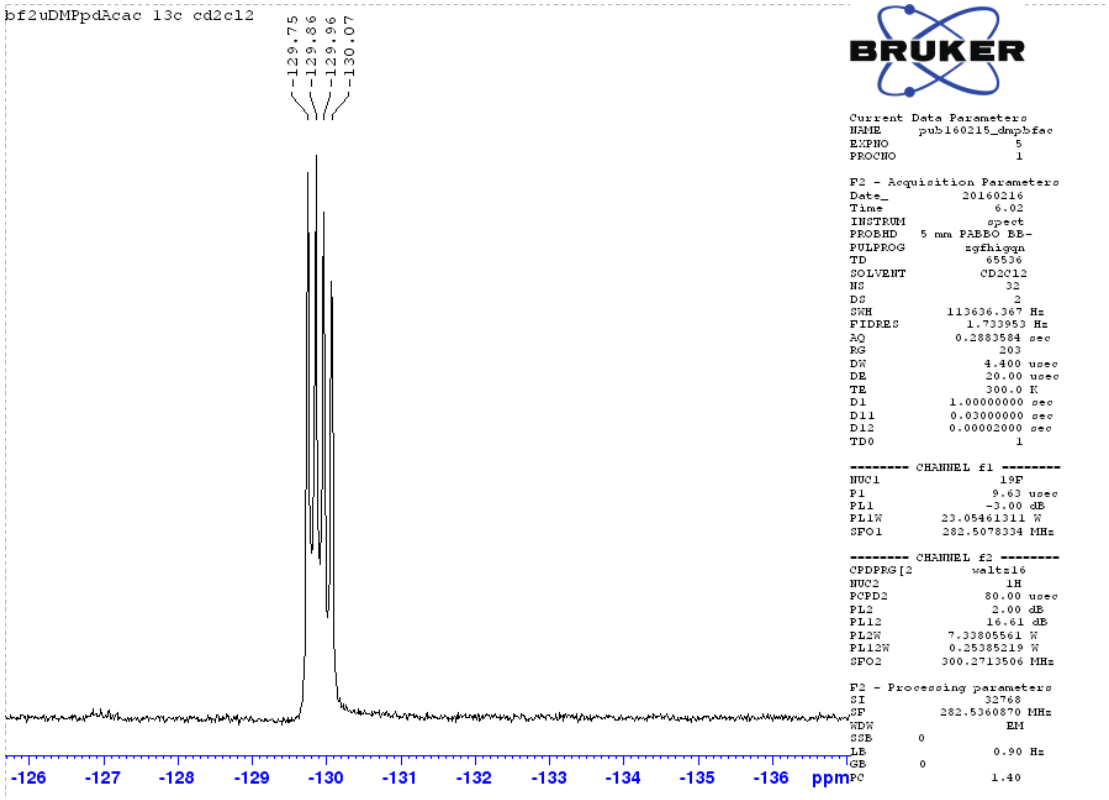

Appendix B-7 ^{19}F NMR of **2.2b** in CD_2Cl_2.

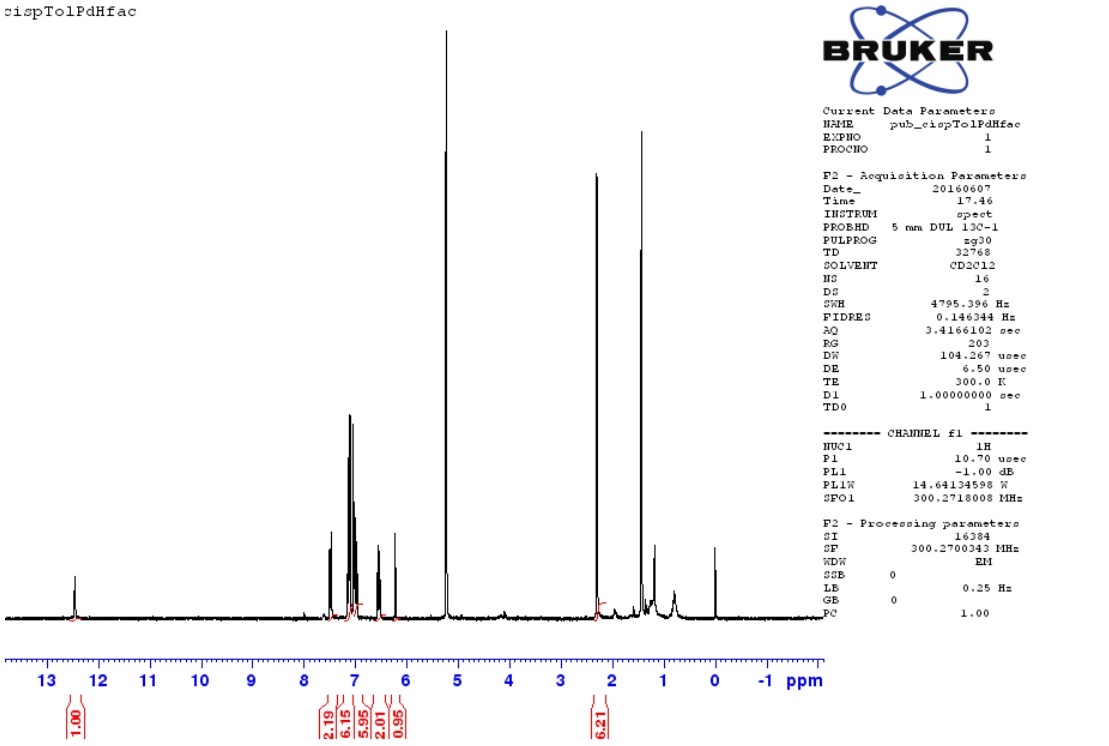

Appendix B-8 ^{1}H NMR of **2.4a** in CD_2Cl_2.

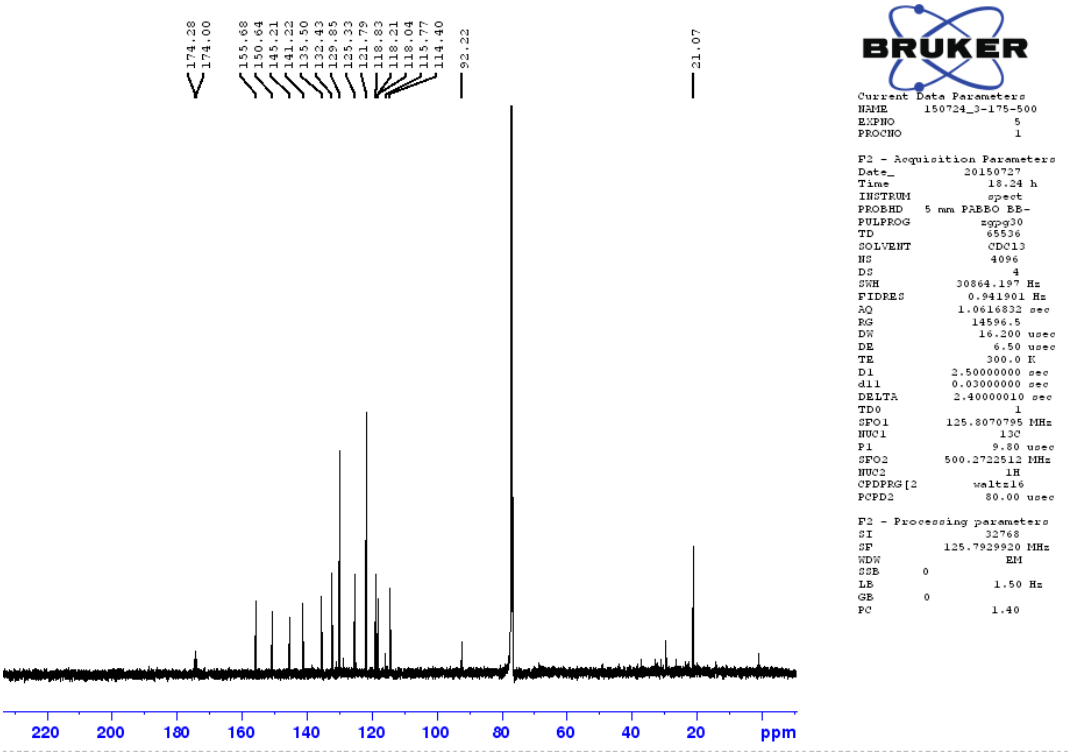

Appendix B-9 ^{13}C NMR of **2.4a** in CD_2Cl_2.

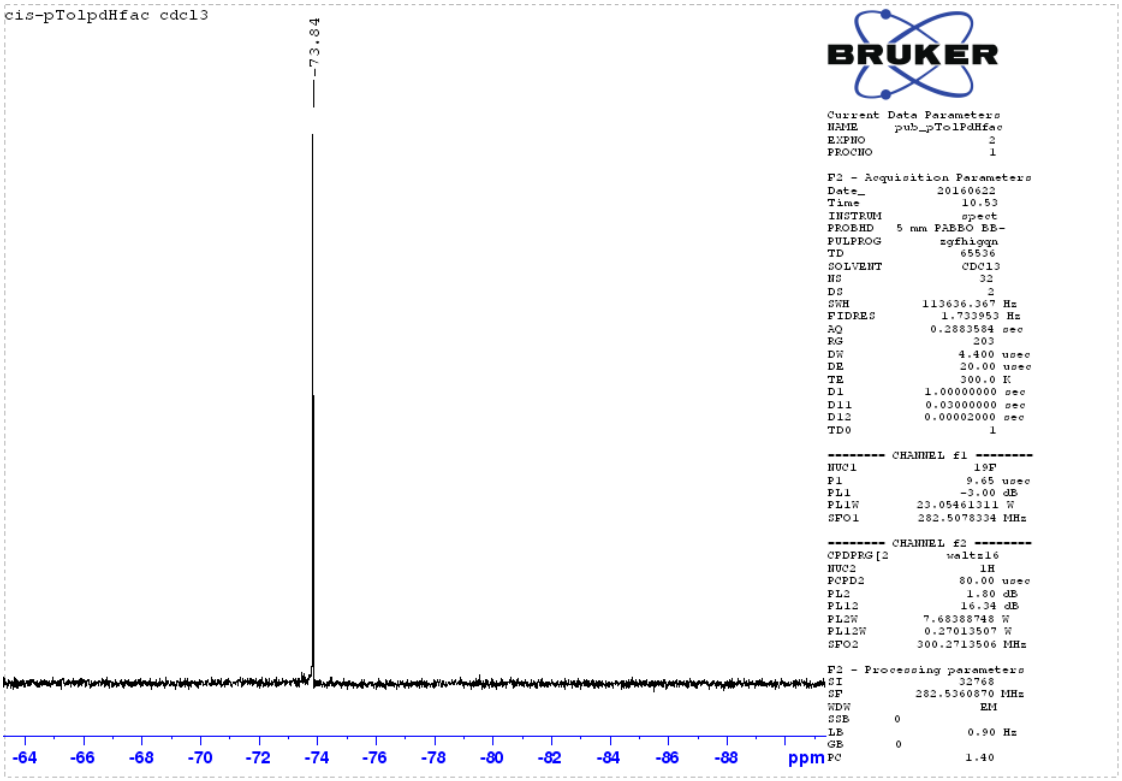

Appendix B-10 ^{19}F NMR of **2.4a** in $CDCl_3$.

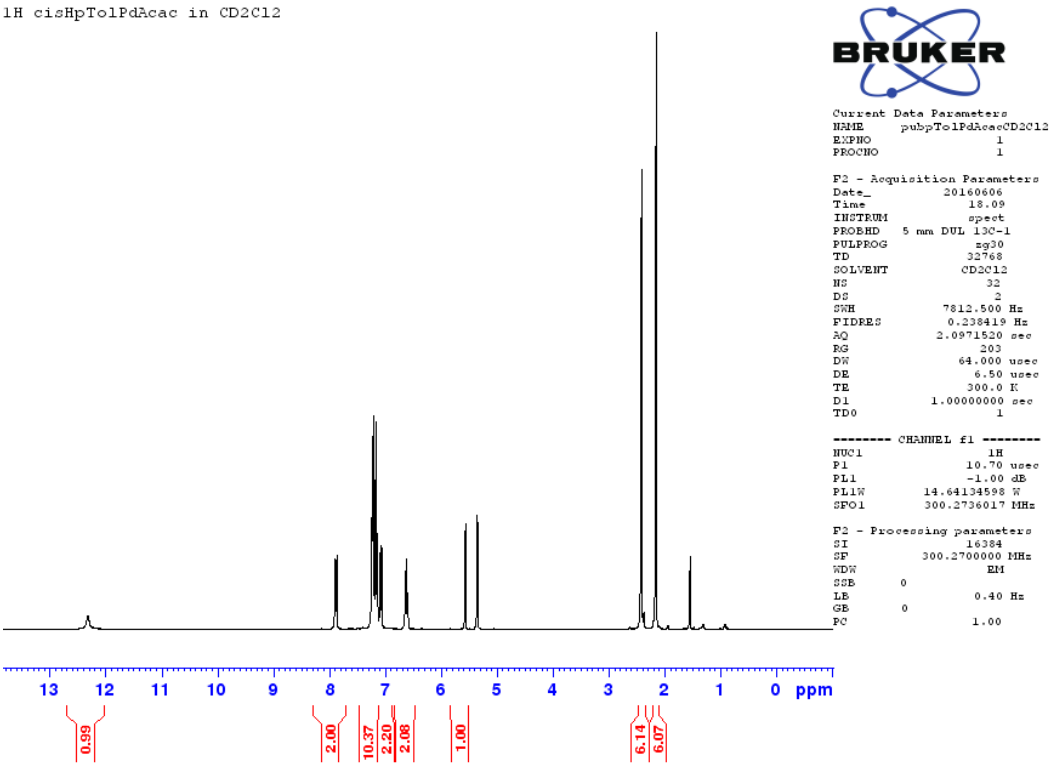

Appendix B-11 ^{1}H NMR of **2.5a** in CD_2Cl_2.

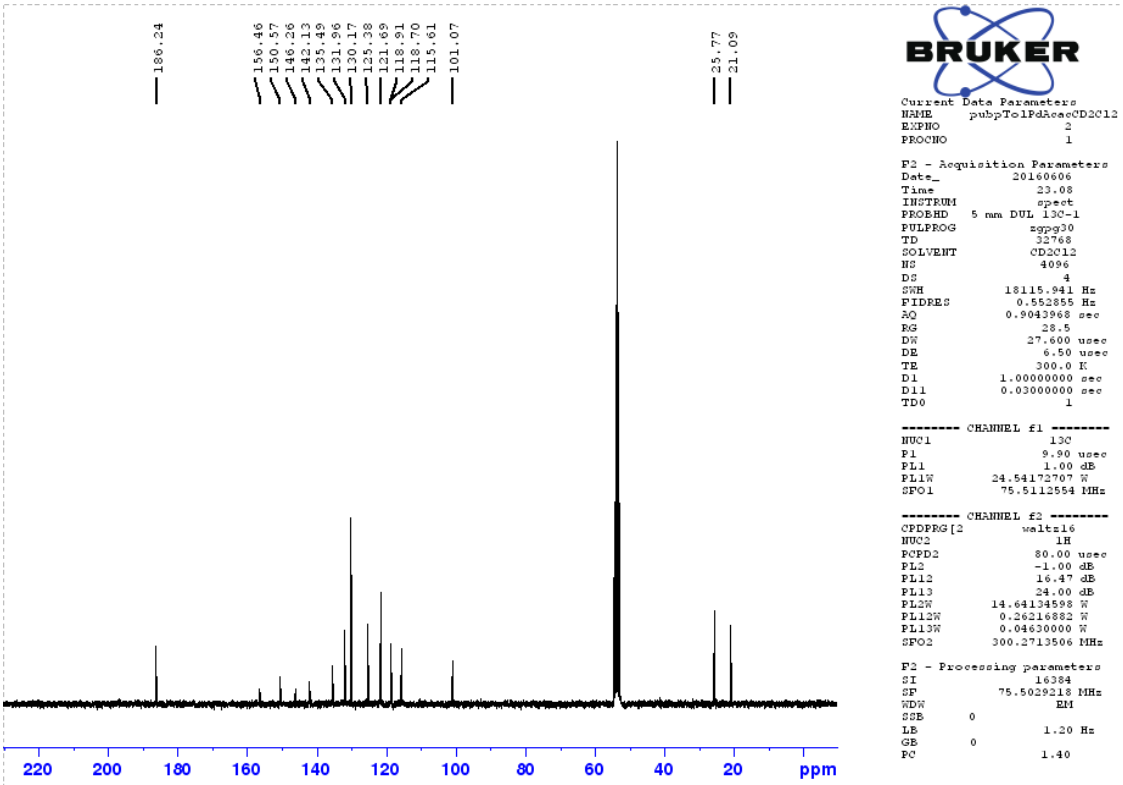

Appendix B-12 ^{13}C NMR of **2.5a** in CD_2Cl_2.

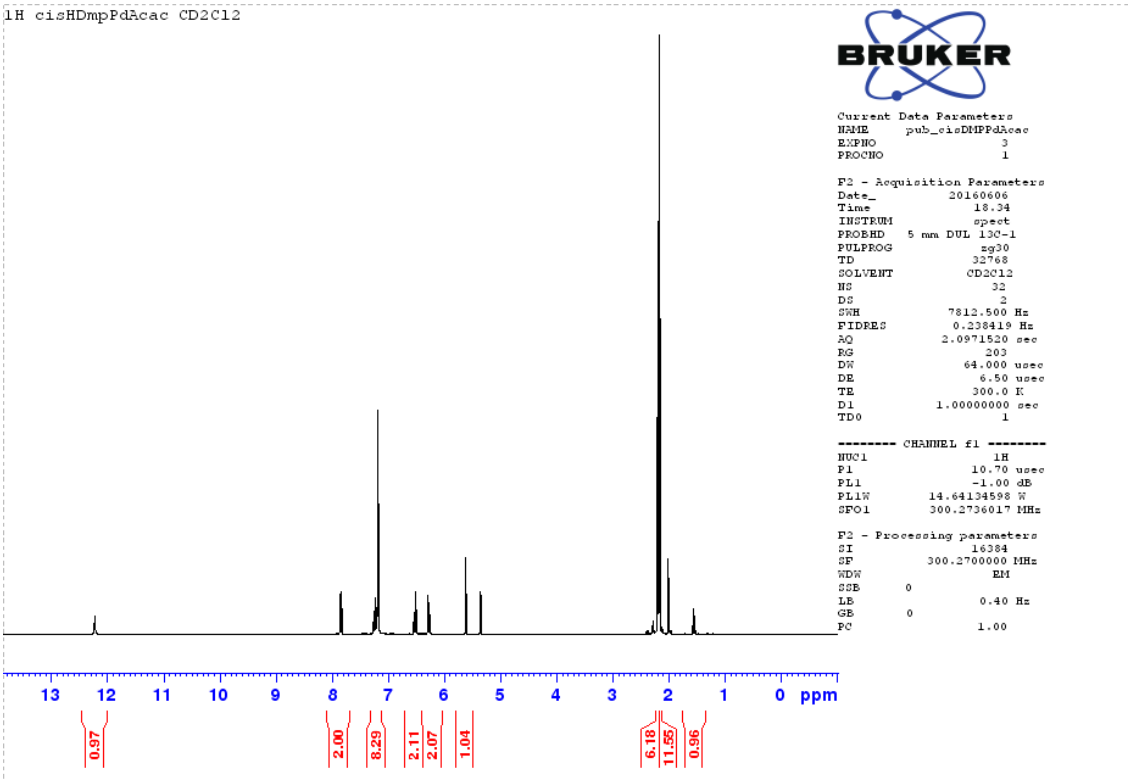

Appendix B-13 ^{1}H NMR of **2.5b** in CD_2Cl_2.

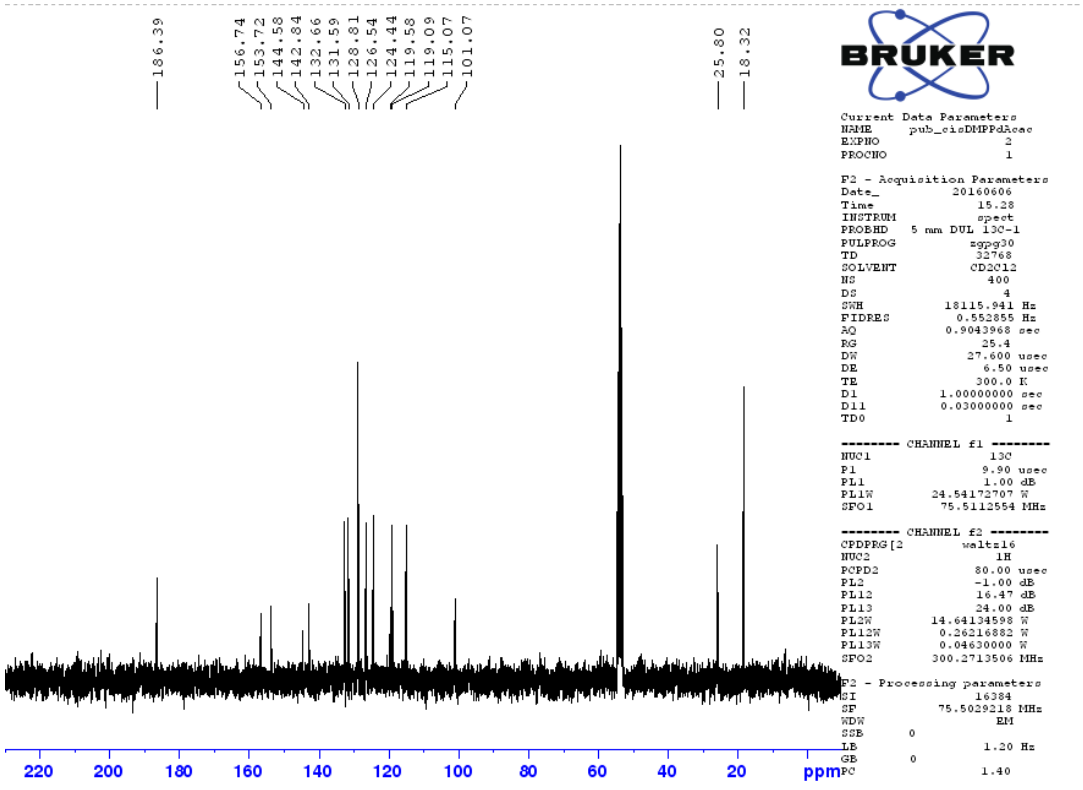

Appendix B-14 ^{13}C of **2.5b** in CD_2Cl_2.

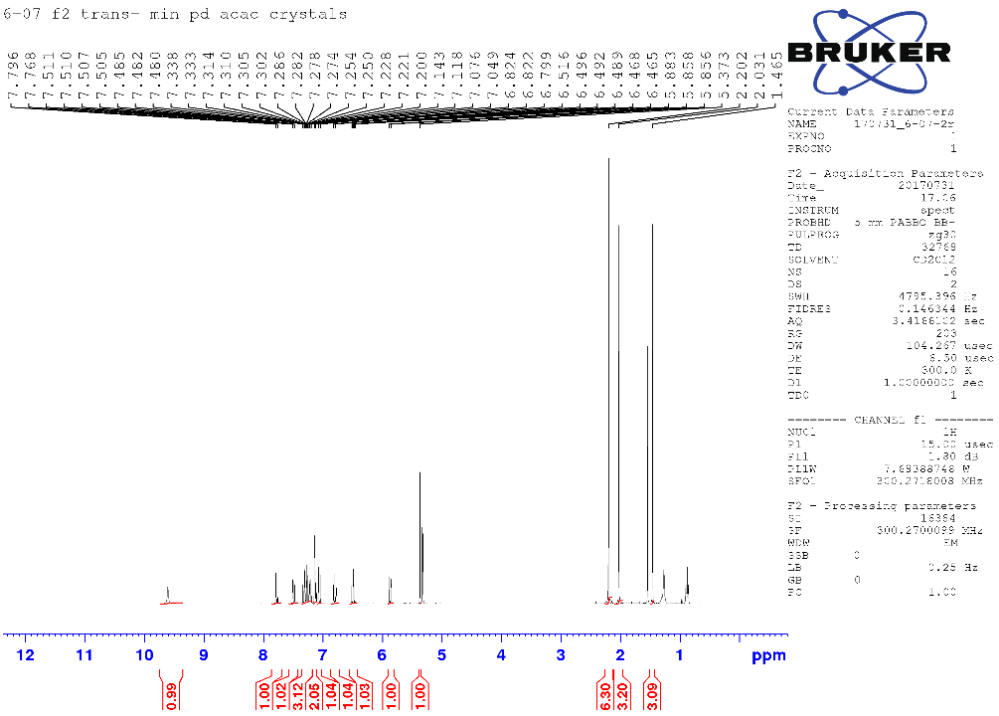

Appendix B-15 ^{1}H NMR of **3.2** in CD_2Cl_2.

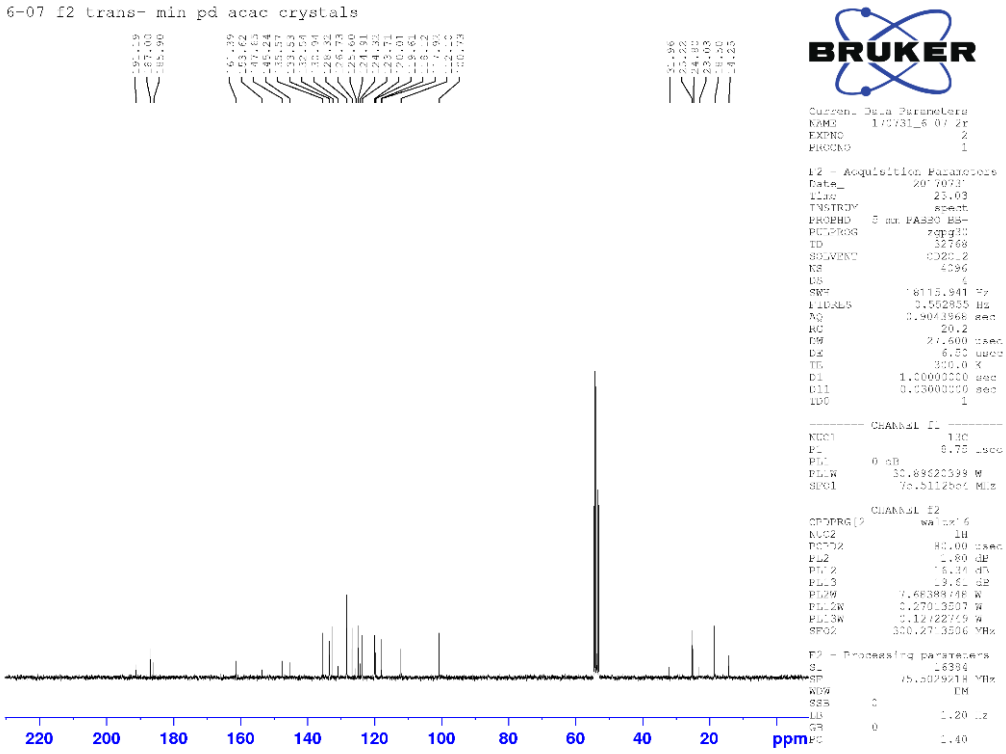

Appendix B-16 ^{13}C NMR of **3.2** in CD_2Cl_2.

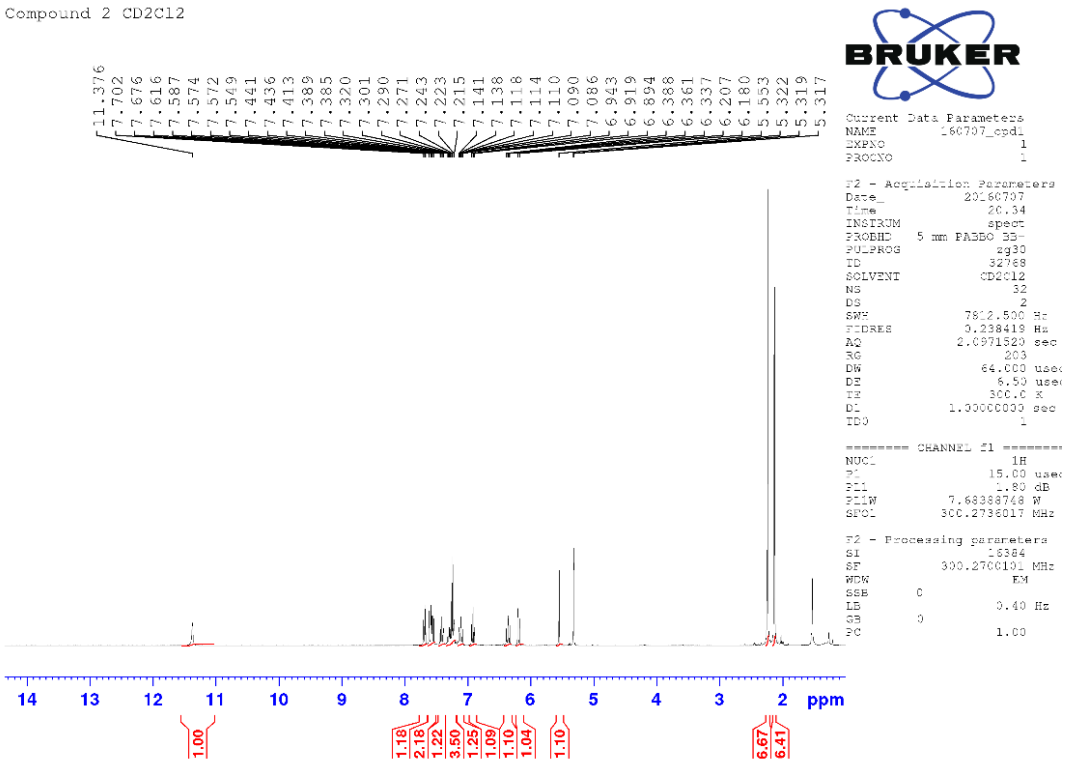

Appendix B-17 ^{1}H NMR of **3.3** in CD_2Cl_2.

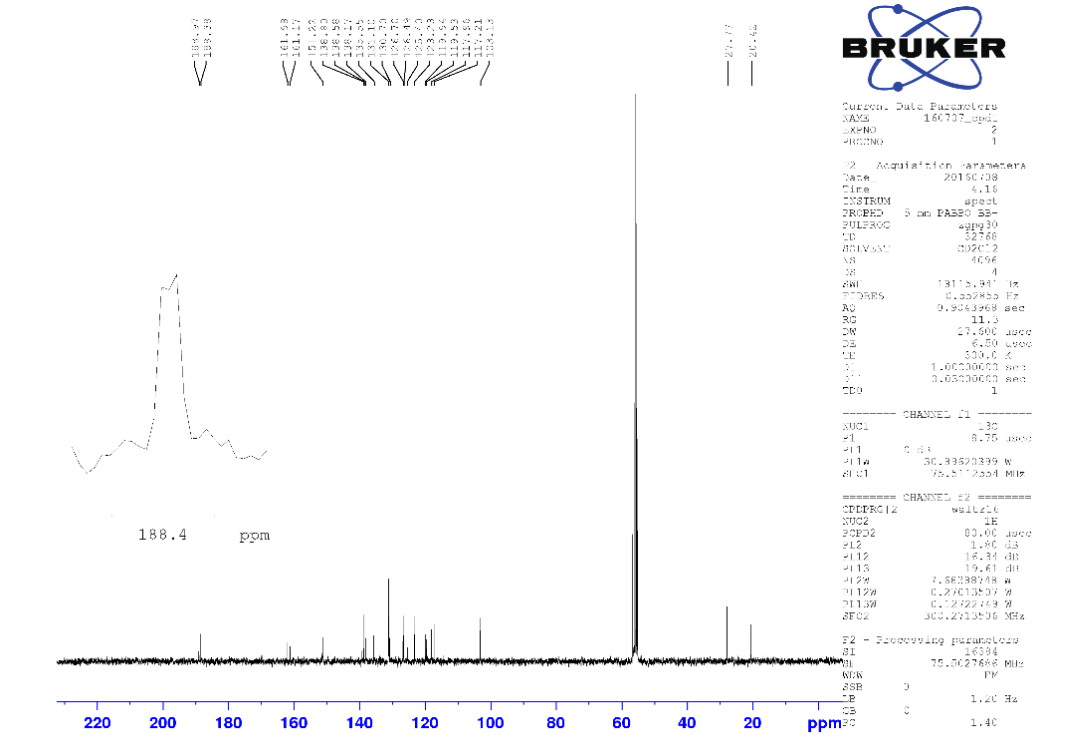

Appendix B-18 ^{13}C NMR of **3.3** in CD_2Cl_2.

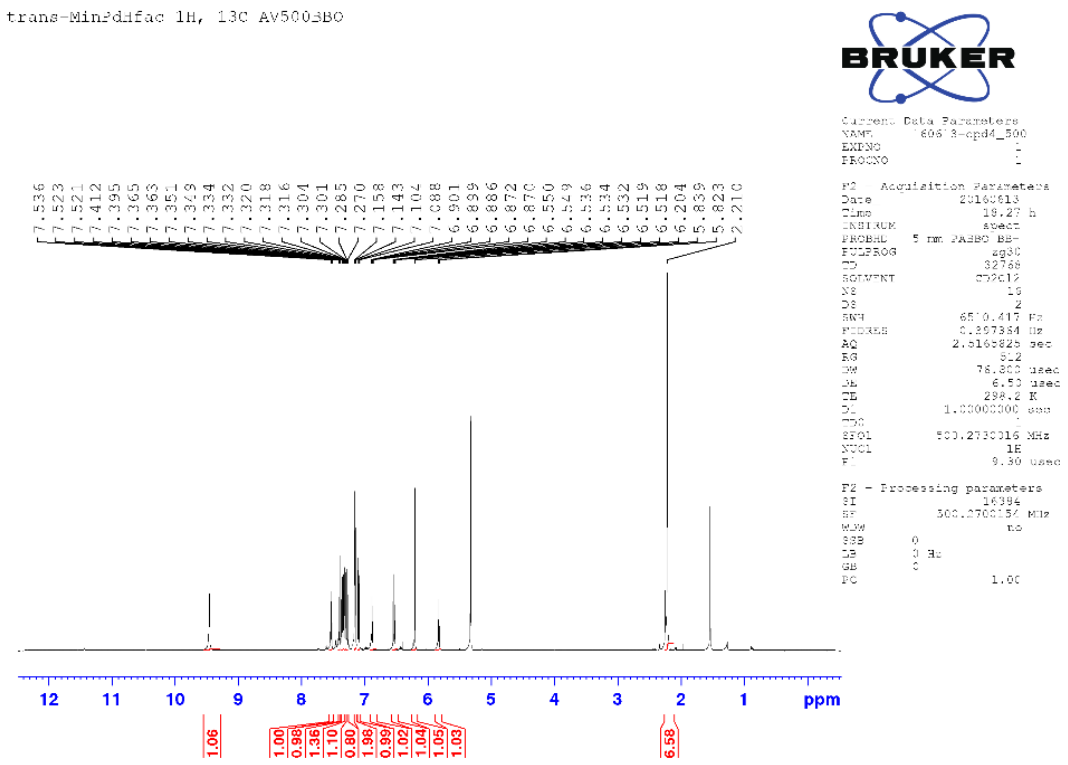

Appendix B-19 ^{1}H NMR of **3.4** in CD_2Cl_2.

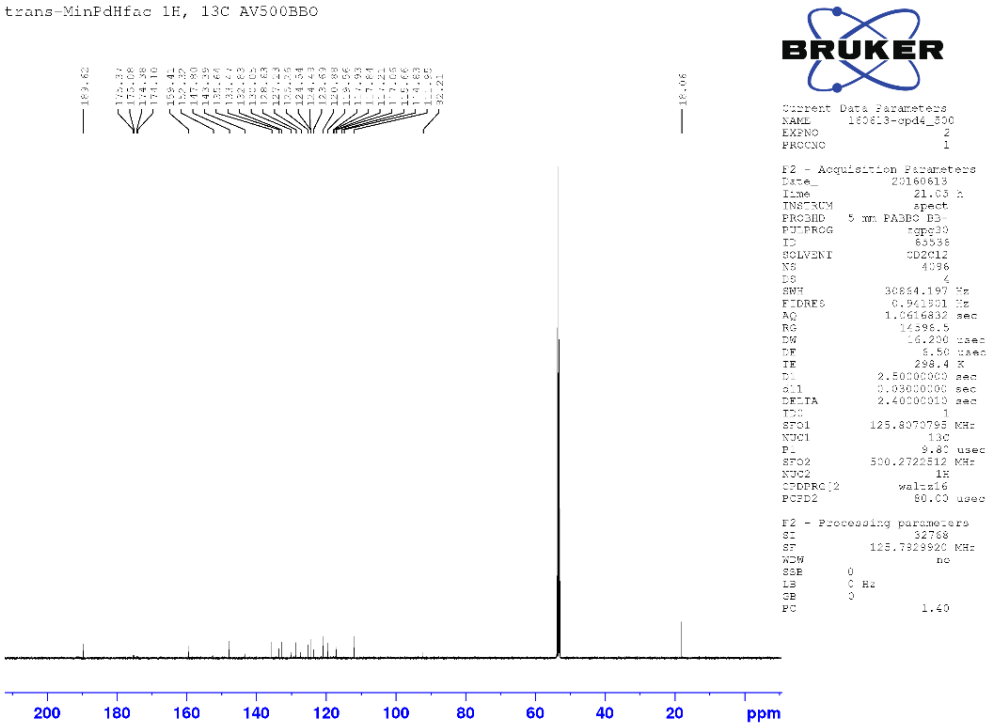

Appendix B-20 ^{13}C NMR of **3.4** in CD_2Cl_2.

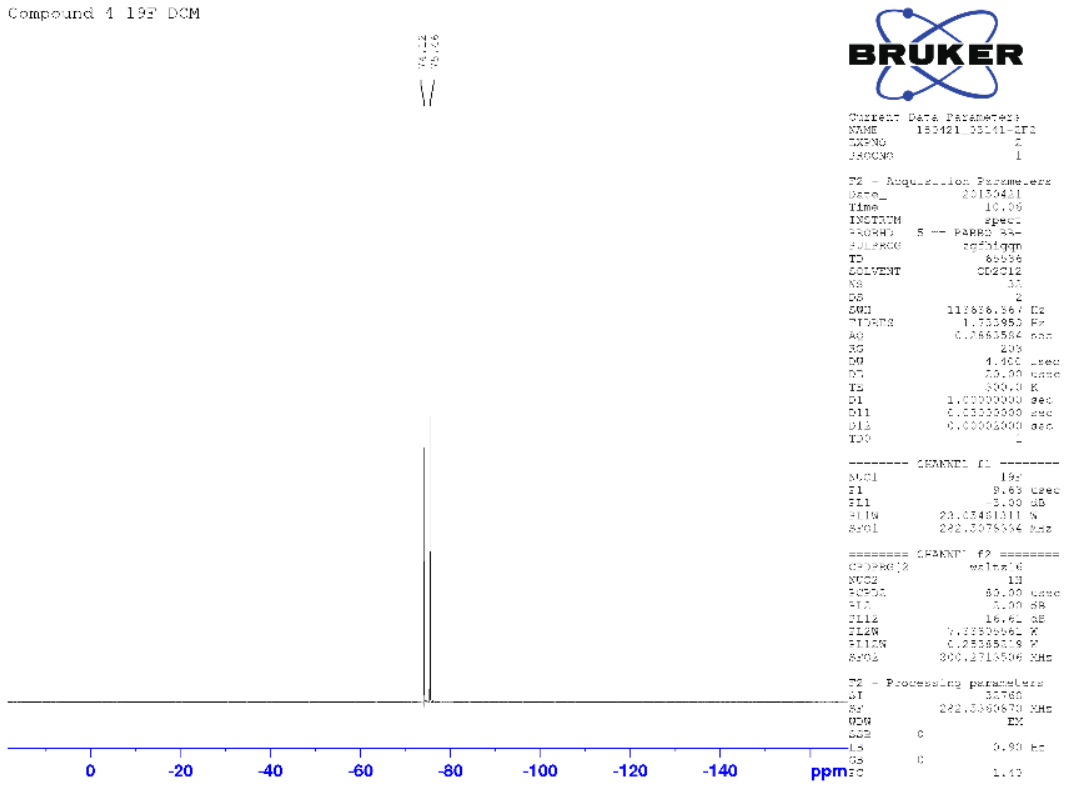

Appendix B-21 ^{19}F NMR of **3.4** in CD_2Cl_2.

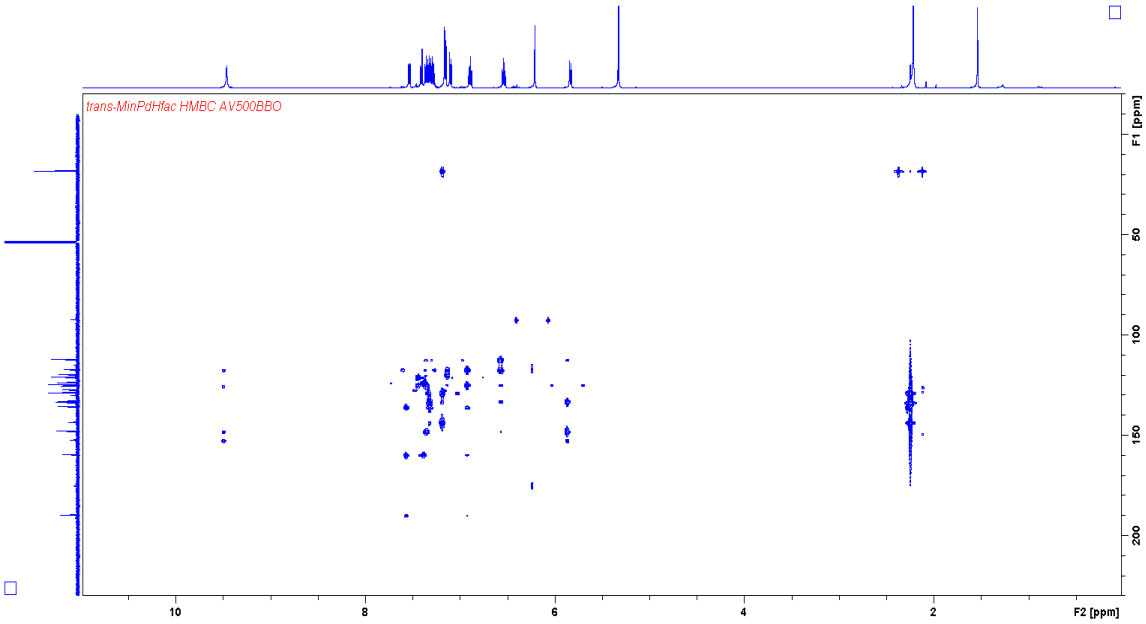

Appendix B-22 HMBC ($3j^1H$-^{13}C) of **3.4** in CD_2Cl_2.

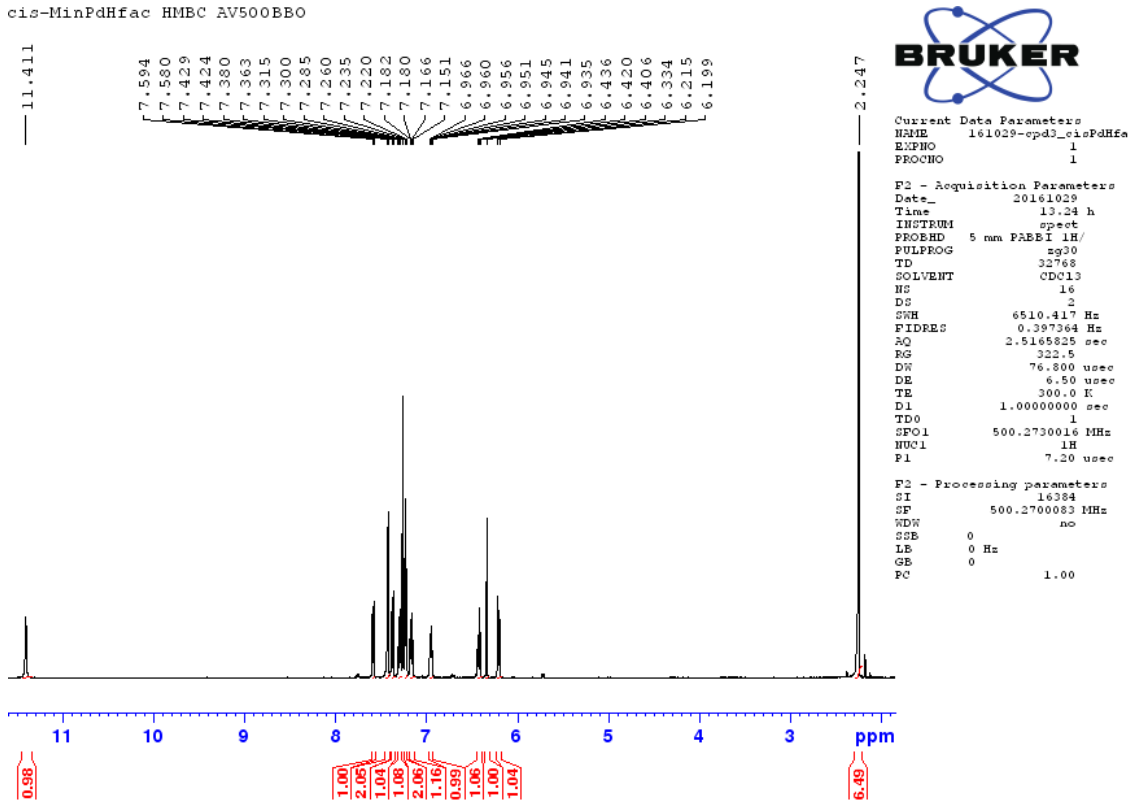

Appendix B-23 ^{1}H NMR of **3.5** in CD_2Cl_2.

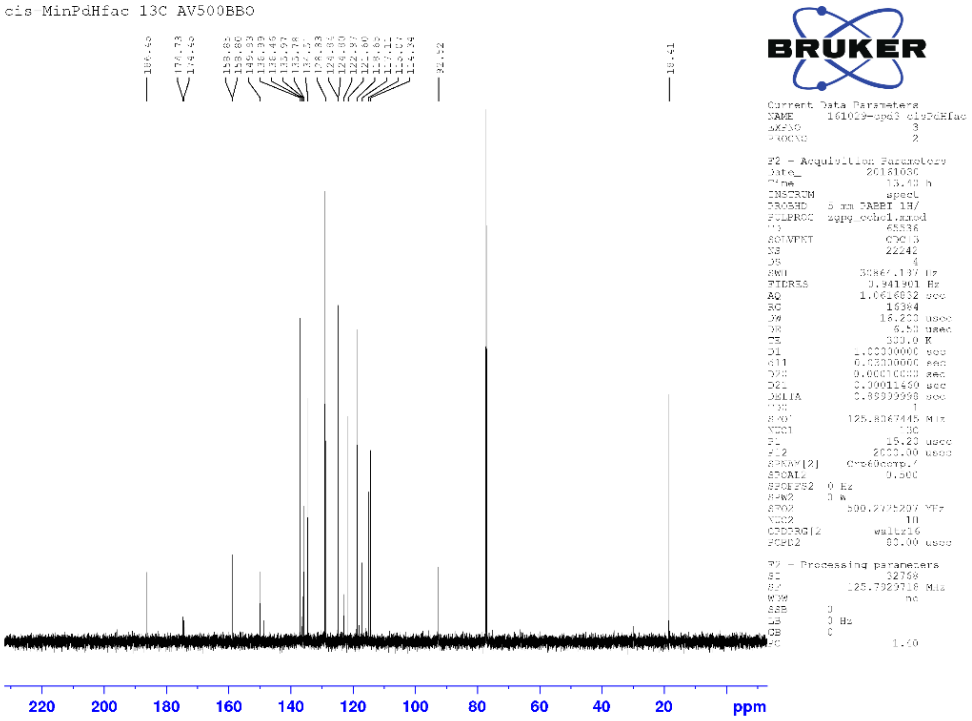

Appendix B-24 ^{13}C NMR of **3.5** in CD_2Cl_2.

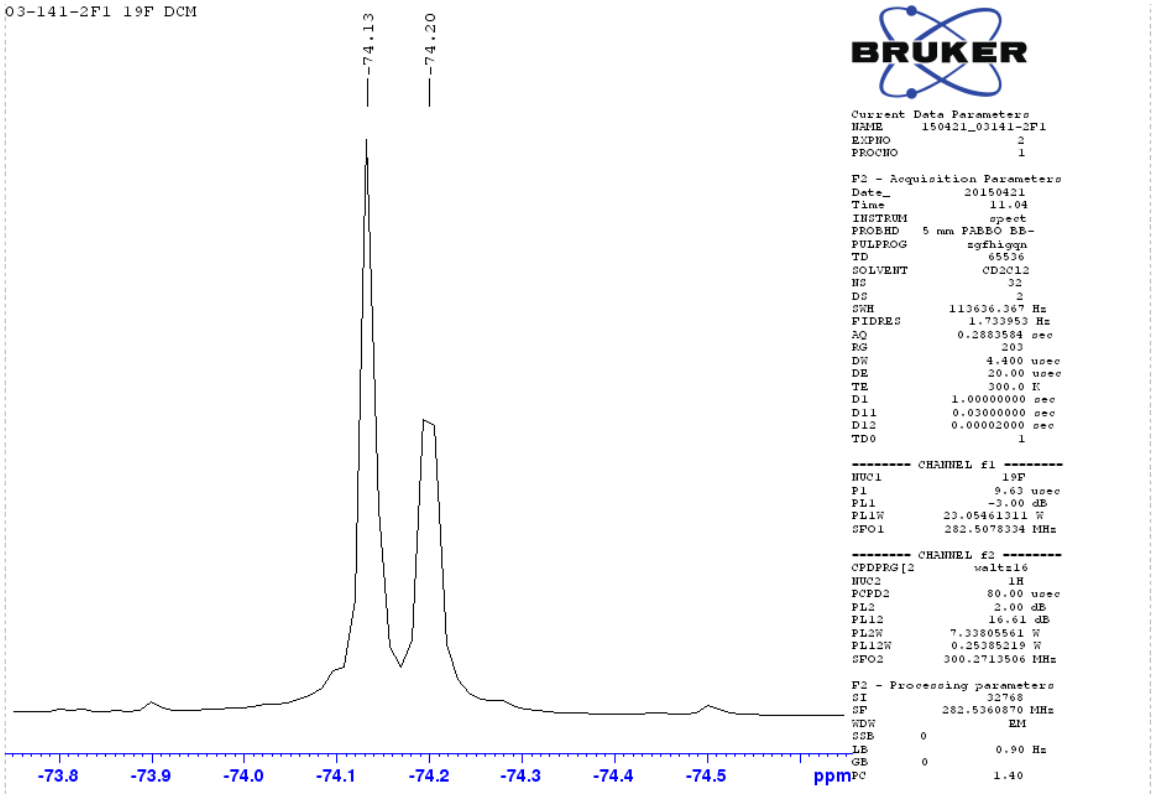

Appendix B-25 ^{19}F NMR of **3.5** in CD_2Cl_2.

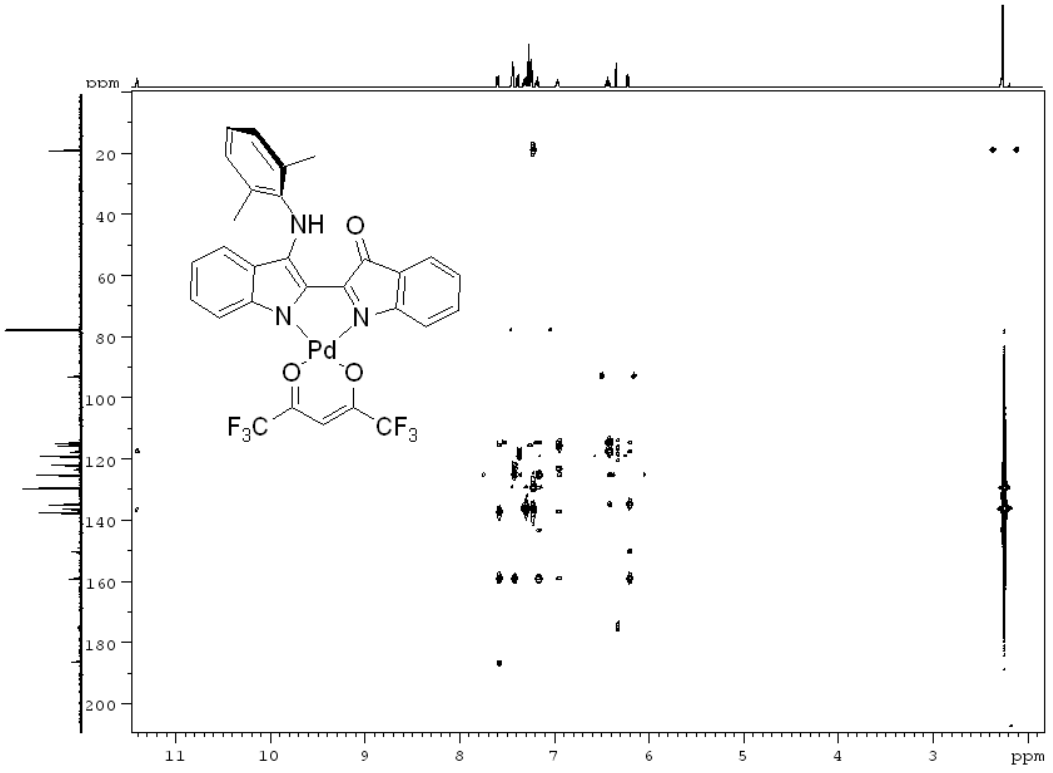

Appendix B-26 HMBC ($3j^1H$-^{13}C) of **3.4** in CD_2Cl_2.

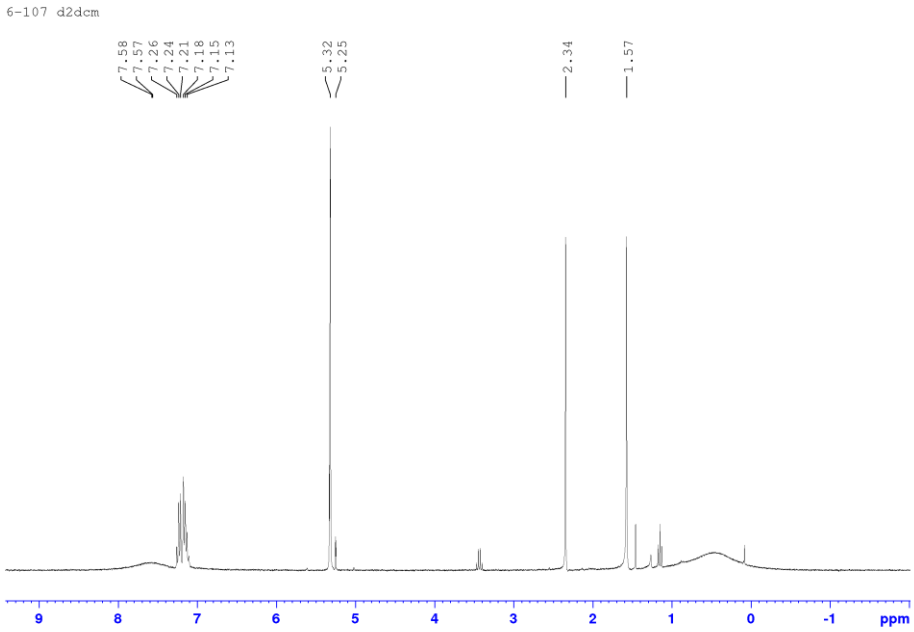

Appendix B-27 ^{1}H NMR of **H4.11**$^{+}$ in CD_2Cl_2 (at 5.32 ppm) with a coaxial insert containing pure solvent (at 5.25 ppm).

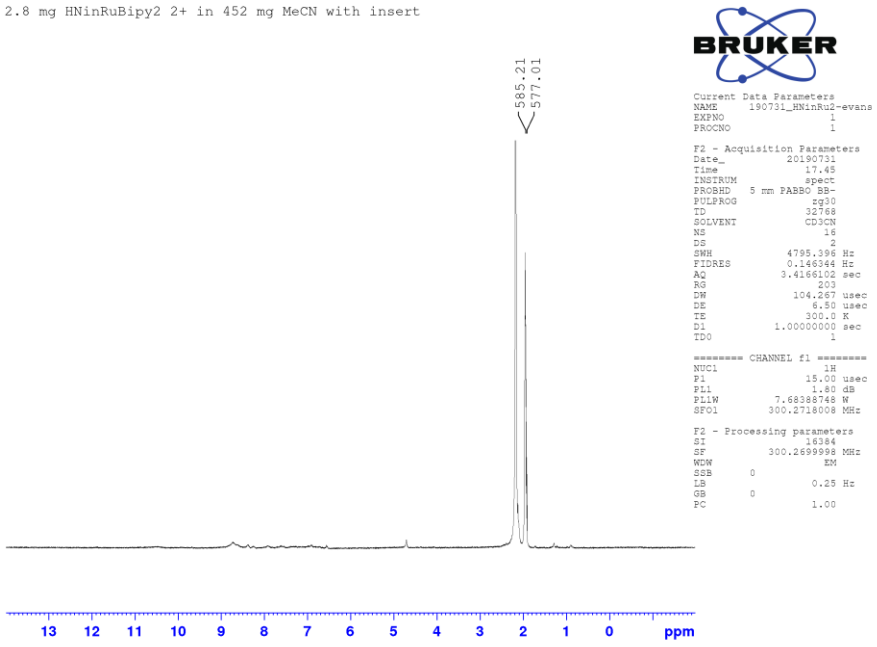

Appendix B-28 ^{1}H NMR of **H4.11**$^{+}$ in CD_3CN (at 1.95 ppm) with a coaxial insert containing pure solvent (at 1.92 ppm).

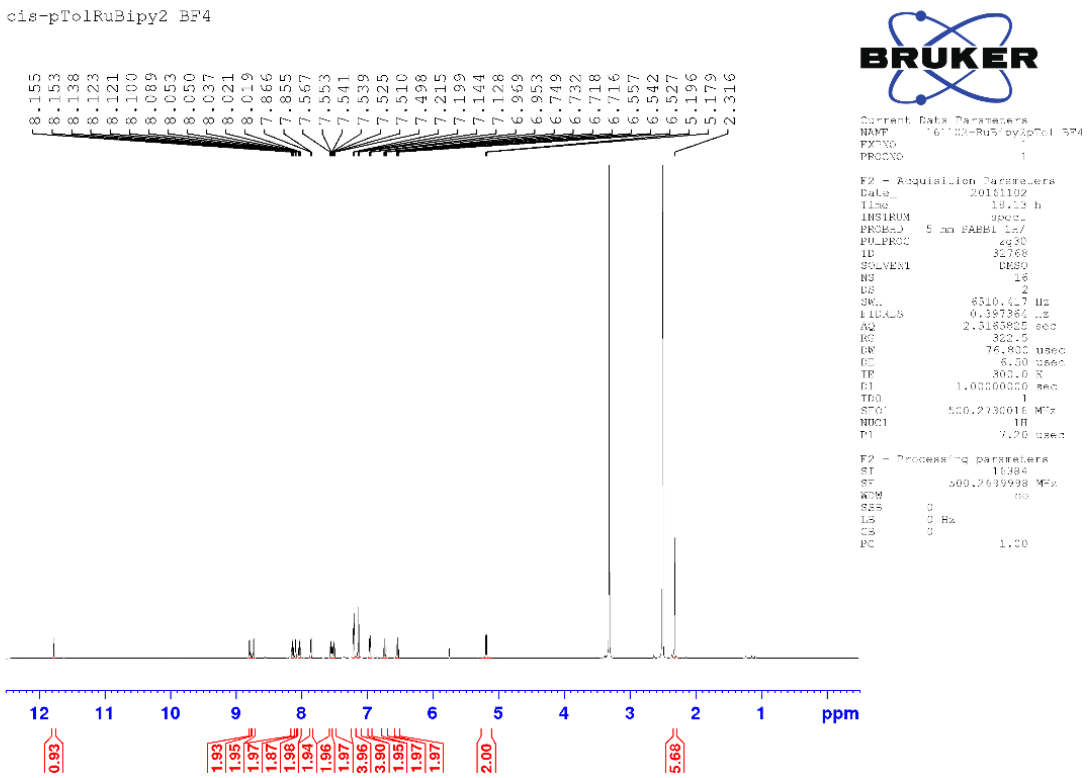

Appendix B-29 ^{1}H NMR of **H4.12**$^{+}$ in d_6-DMSO.

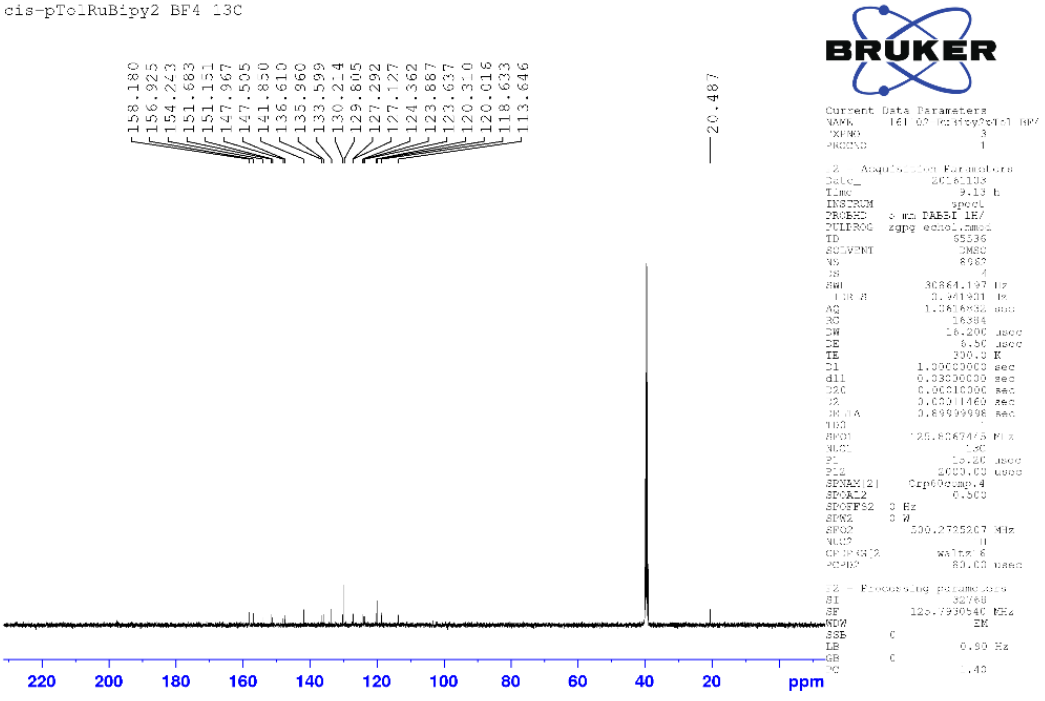

Appendix B-30 ^{13}C NMR of **H4.12**$^{+}$ in d_6-DMSO.

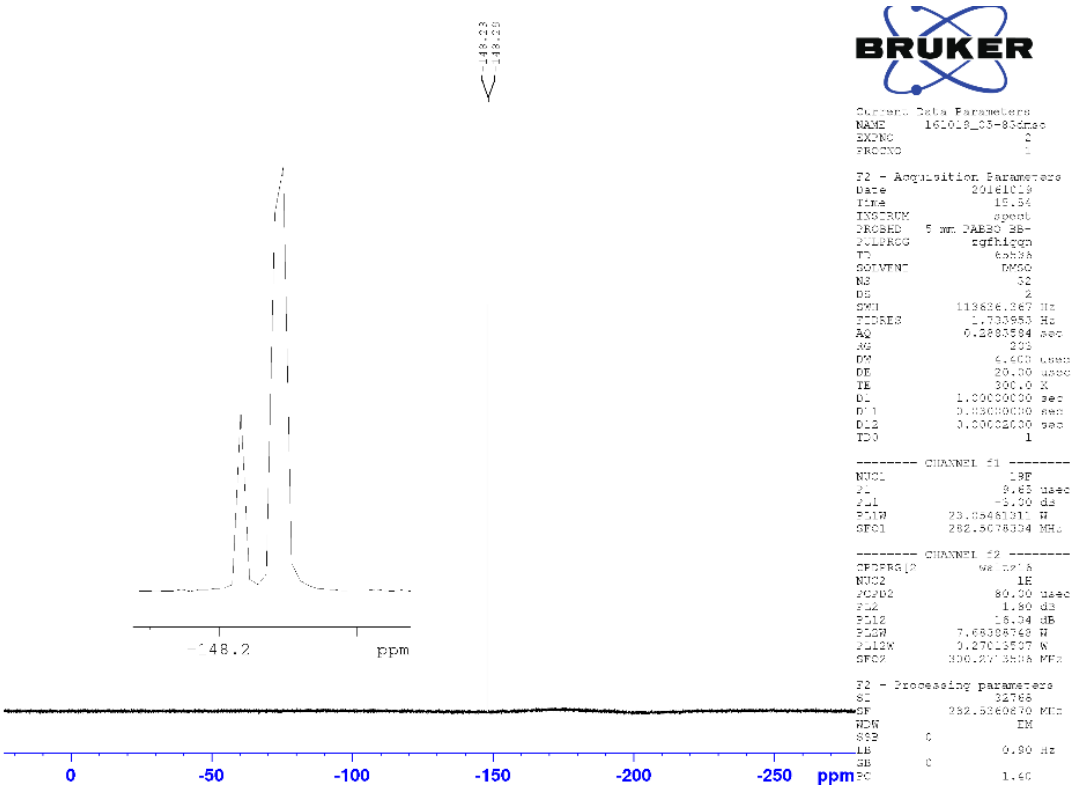

Appendix B-31 ^{19}F NMR of **H4.12**$^{+}$ in d_6-DMSO.

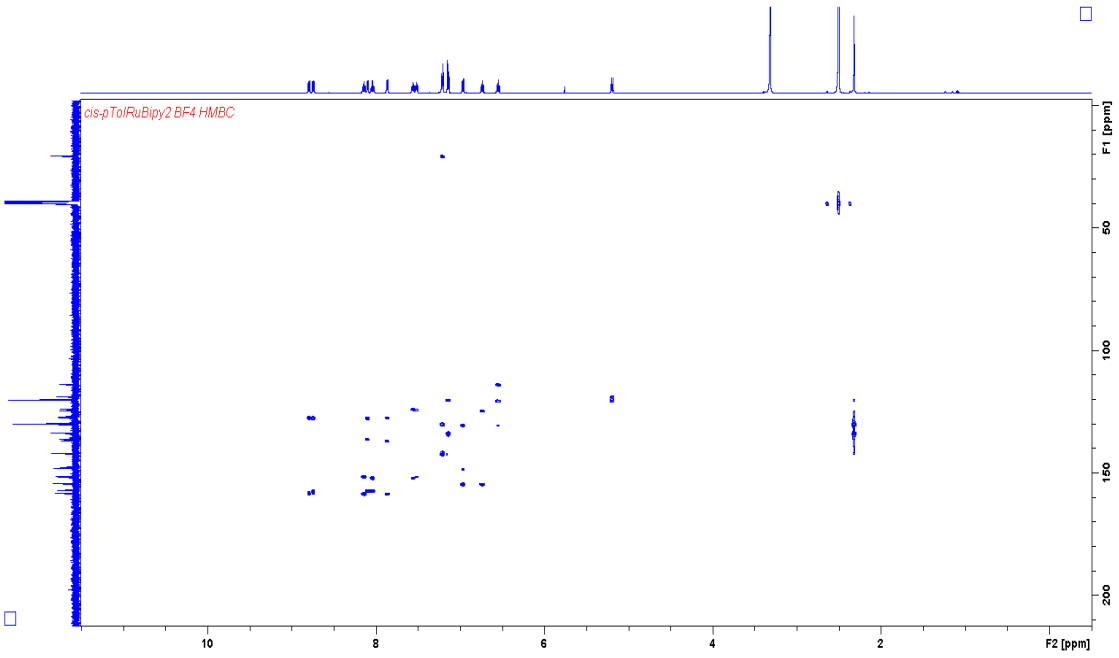

Appendix B-32 HMBC ($3j^{1}H$-^{13}C) of **H4.12**$^{+}$ in d_6-DMSO.

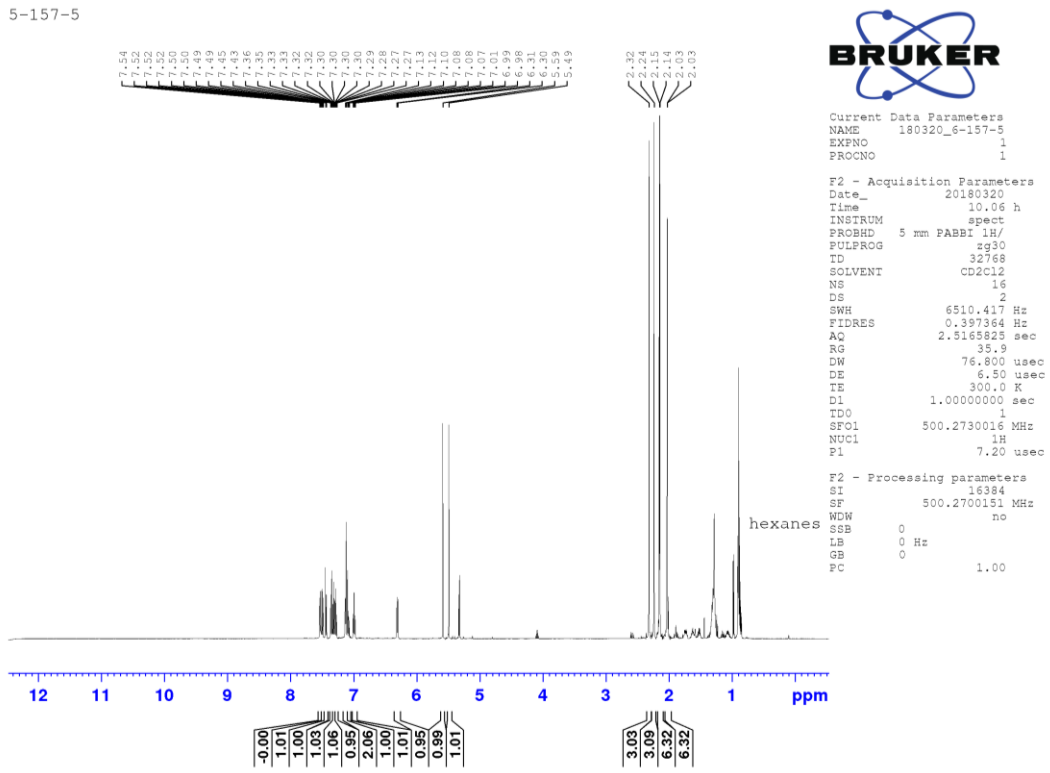

Appendix B-33 ^{1}H NMR of **5.3** in d^{2}-dichloromethane at 300 K.

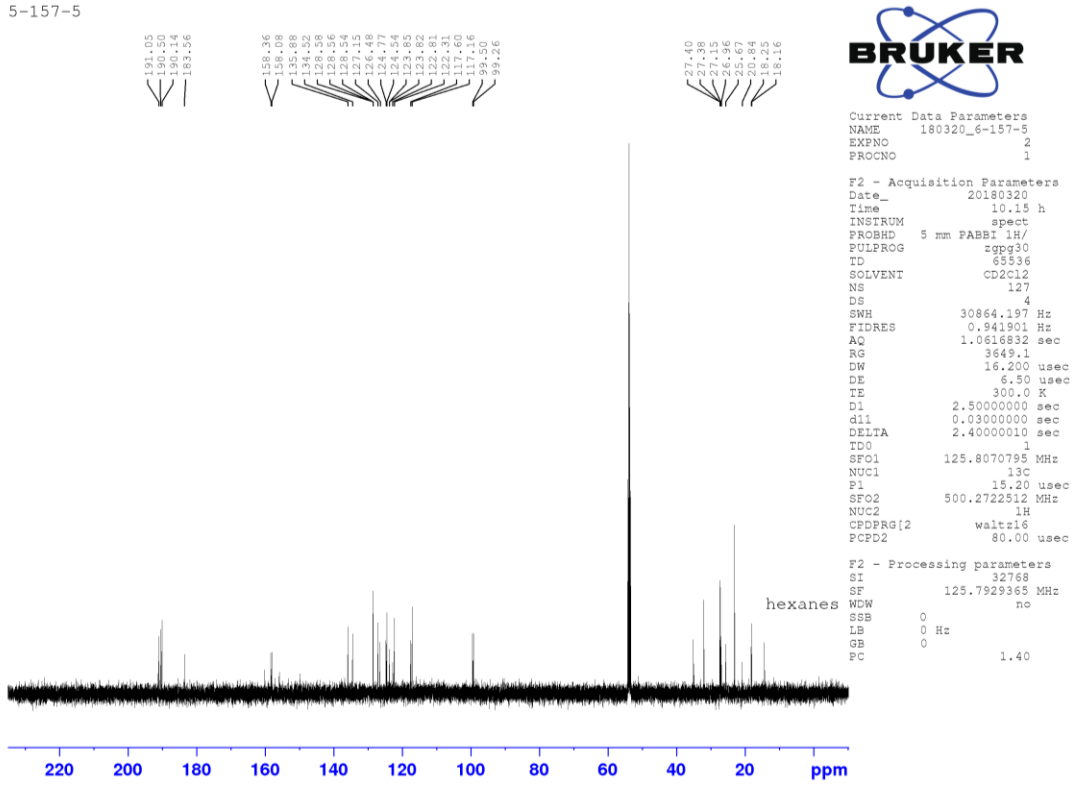

Appendix B-34 ^{13}C NMR of **5.3** in d^{2}-dichloromethane at 300 K.

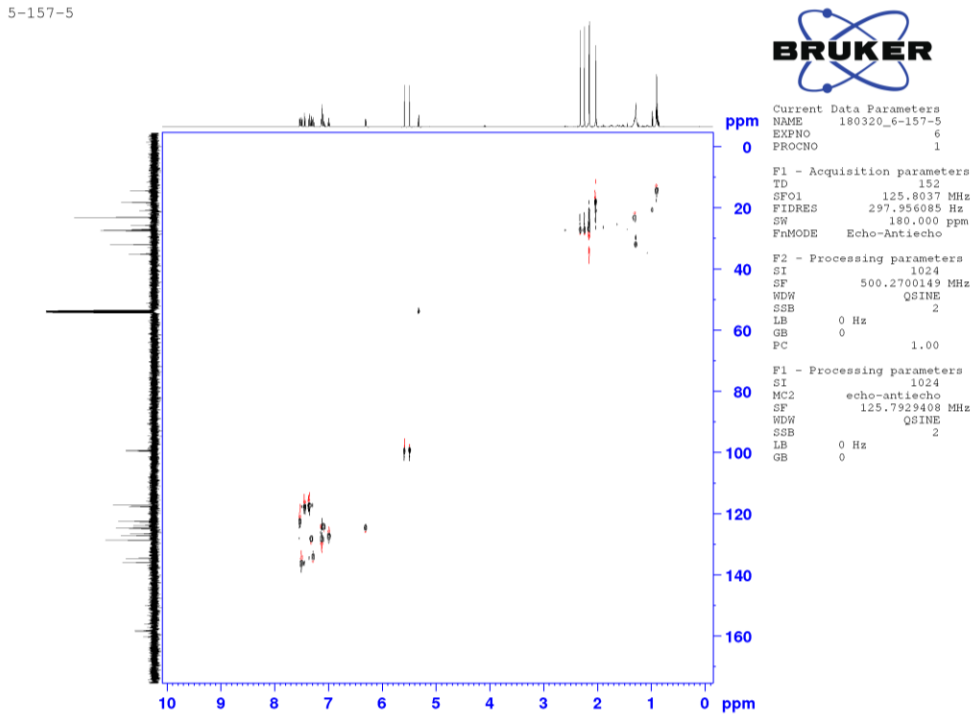

Appendix B-35 HSQC (1j ^{1}H-^{13}C) of **5.3** in d^2-dichloromethane.

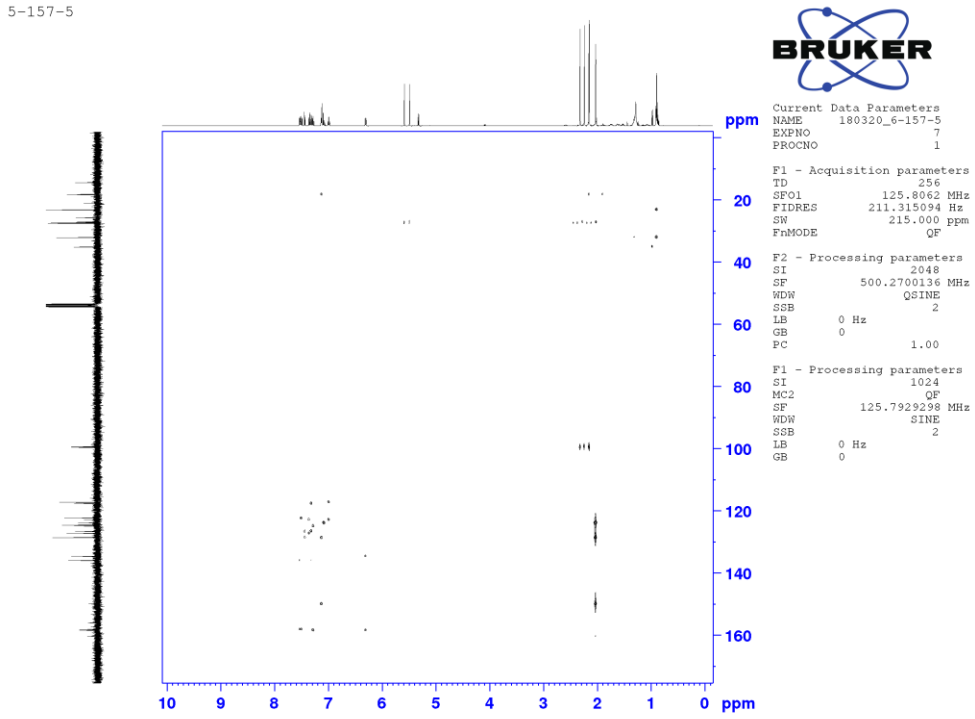

Appendix B-36 HMBC (3j ^{1}H-^{13}C) of **5.3** in d^2-dichloromethane.

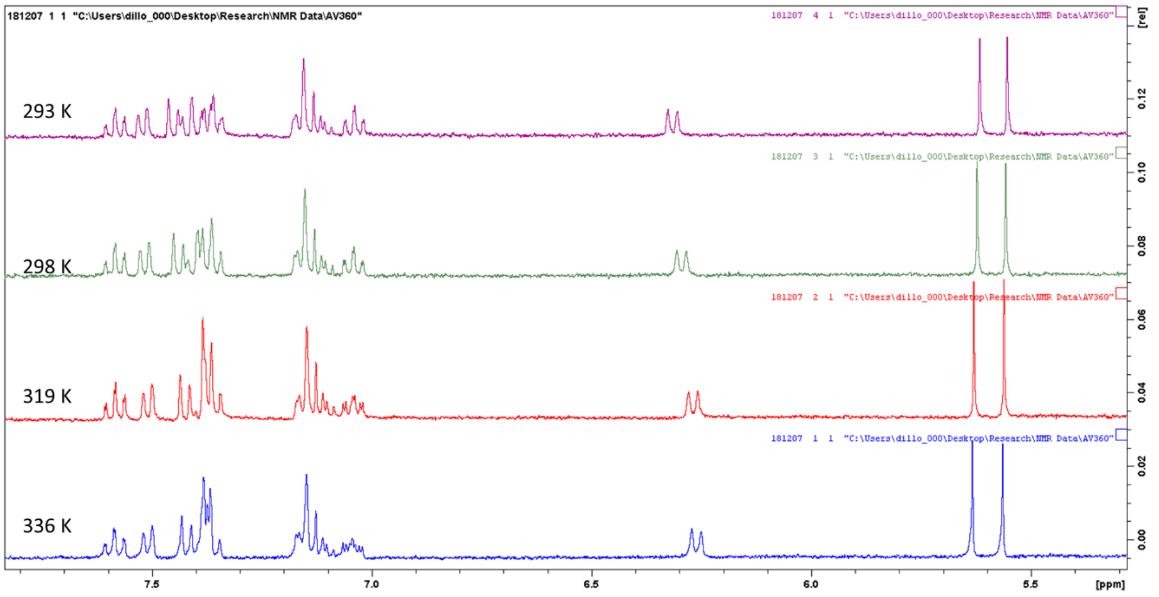

Appendix B-37 ^{1}H NMR of **5.3** in d^{3}-MeCN at various temperatures.

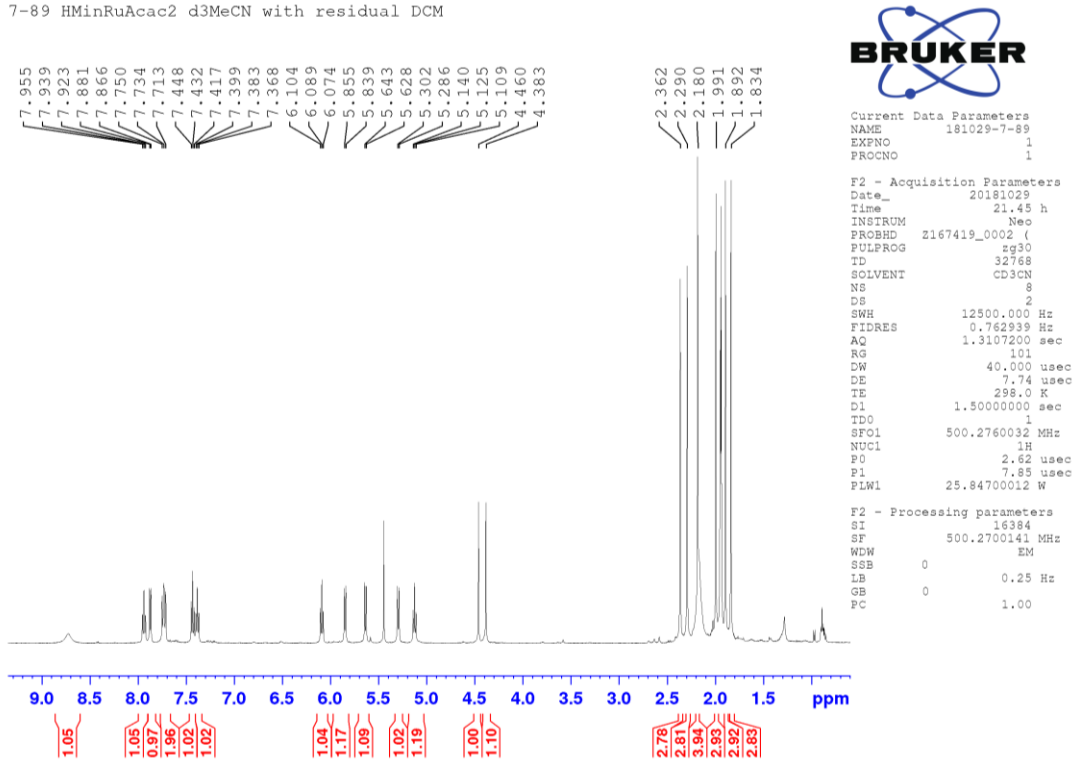

Appendix B-38 ^{1}H NMR of **H5.3**$^{+}$ in d^{3}-MeCN at 300 K.

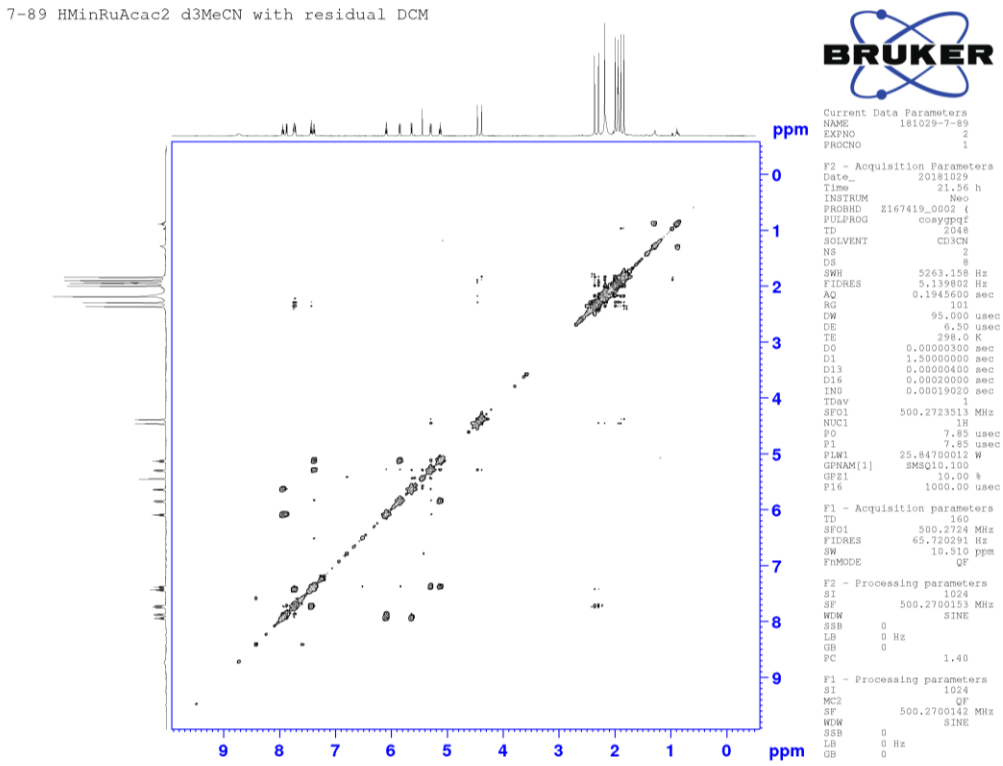

Appendix B-39 ^{1}H-^{1}H COSY NMR of **H5.3**$^{+}$ in d^{3}-MeCN at 300 K.

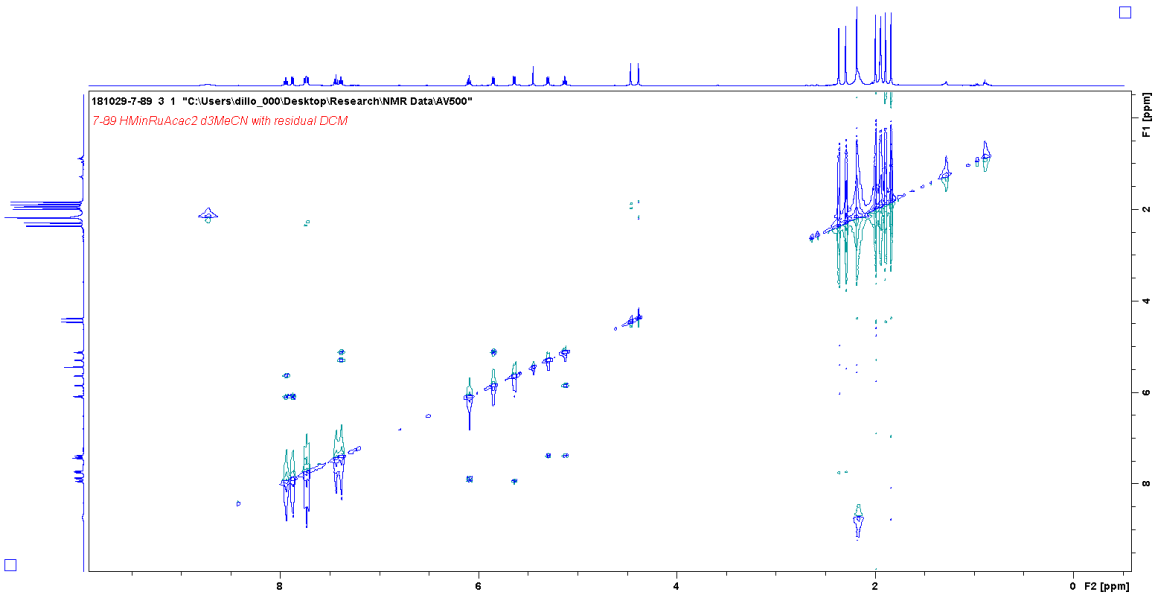

Appendix B-40 ^{1}H-^{1}H NOESY NMR of **H5.3**$^{+}$ in d^{3}-MeCN at 300 K.

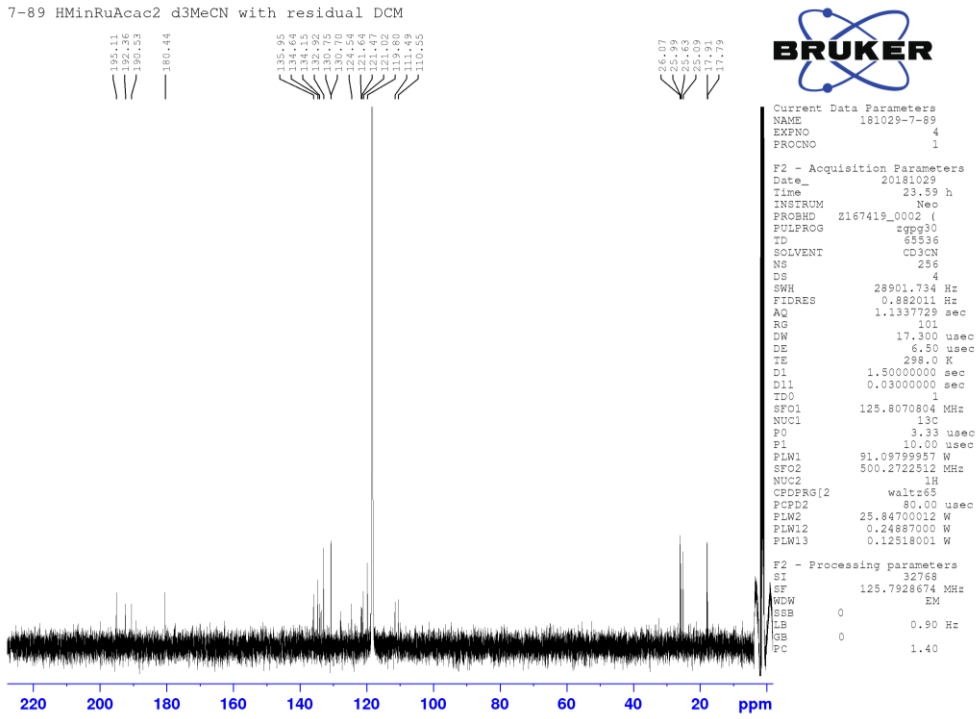

Appendix B-41 ^{13}C NMR of **H5.3**$^{+}$ in d^{3}-MeCN at 300 K.

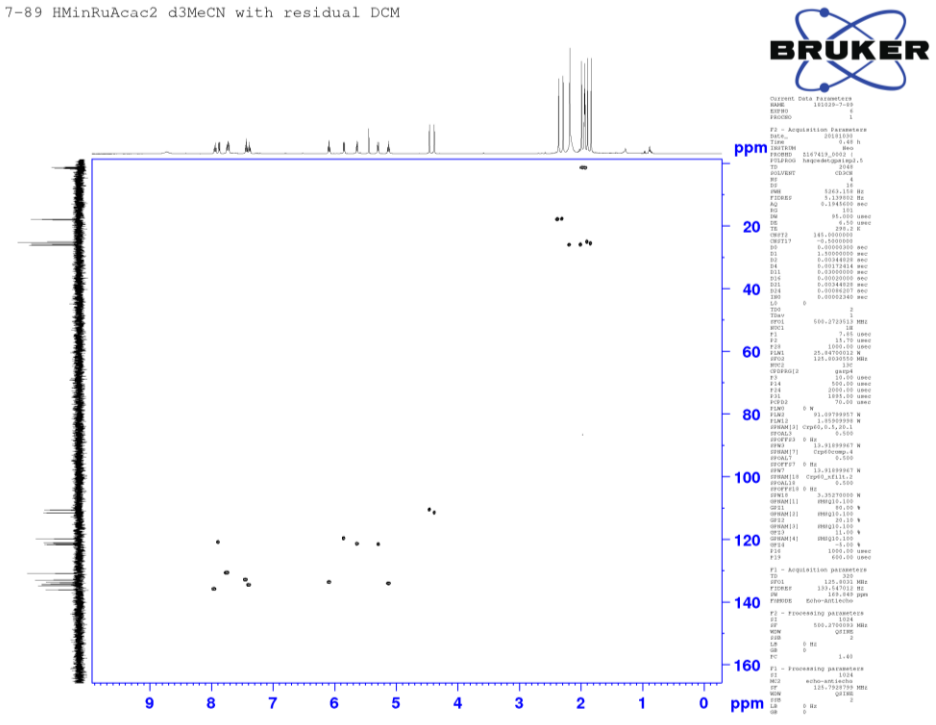

Appendix B-42 HSQC (1j ^{1}H-^{13}C) of **H5.3**$^{+}$ in d$_{3}$-MeCN at 300 K.

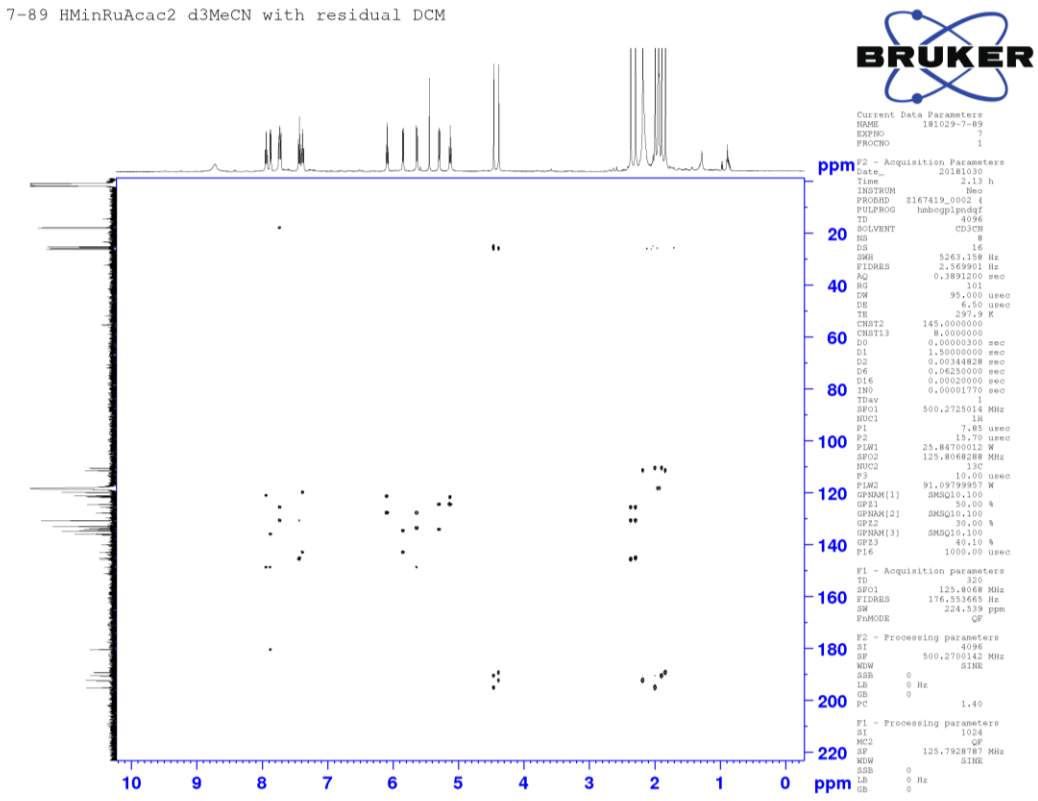

Appendix B-43 HMBC (3j ^{1}H-^{13}C) of **H5.3**$^{+}$ in d_3-MeCN at 300 K.

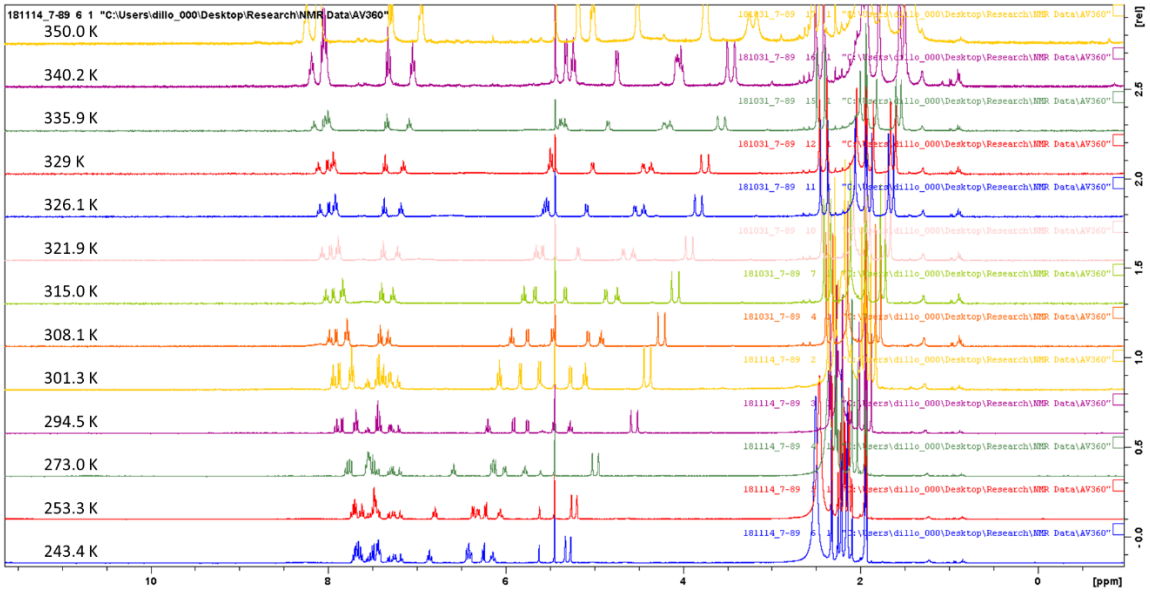

Appendix B-44 ^{1}H NMR of **H5.3**$^{+}$ in d^{3}-MeCN at various temperatures.

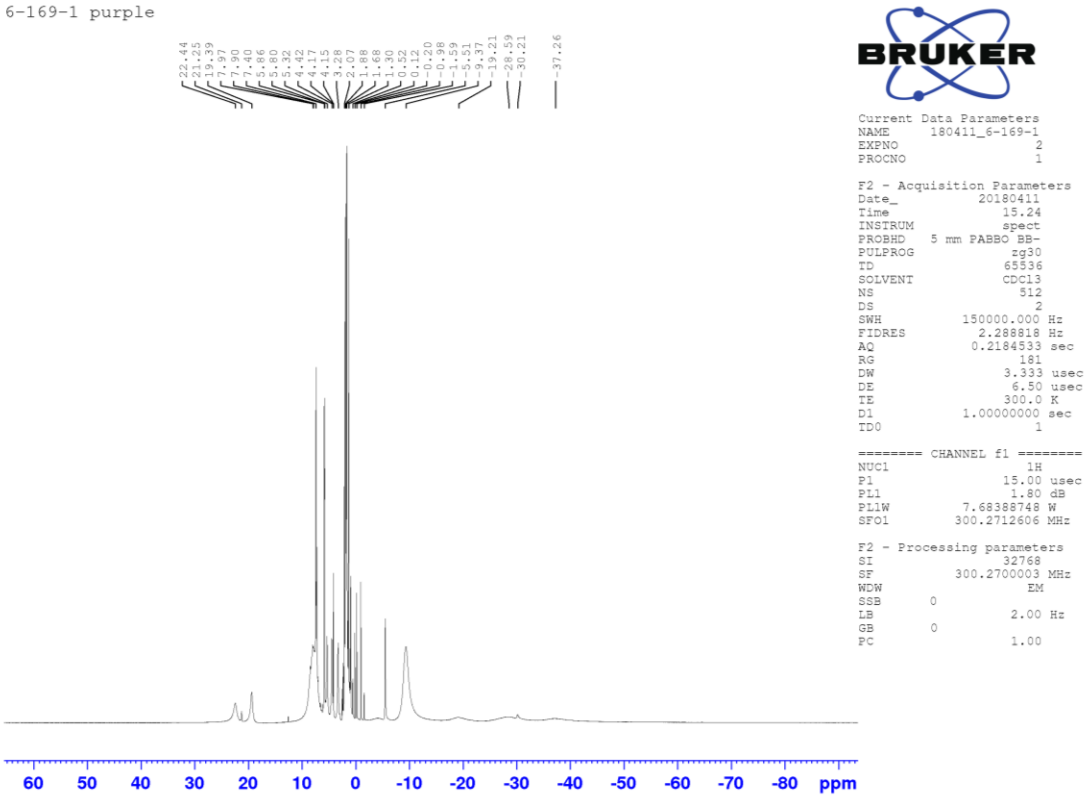

Appendix B-45 ^{1}H NMR of **H5.4** in $CDCl_3$ at 300 K.

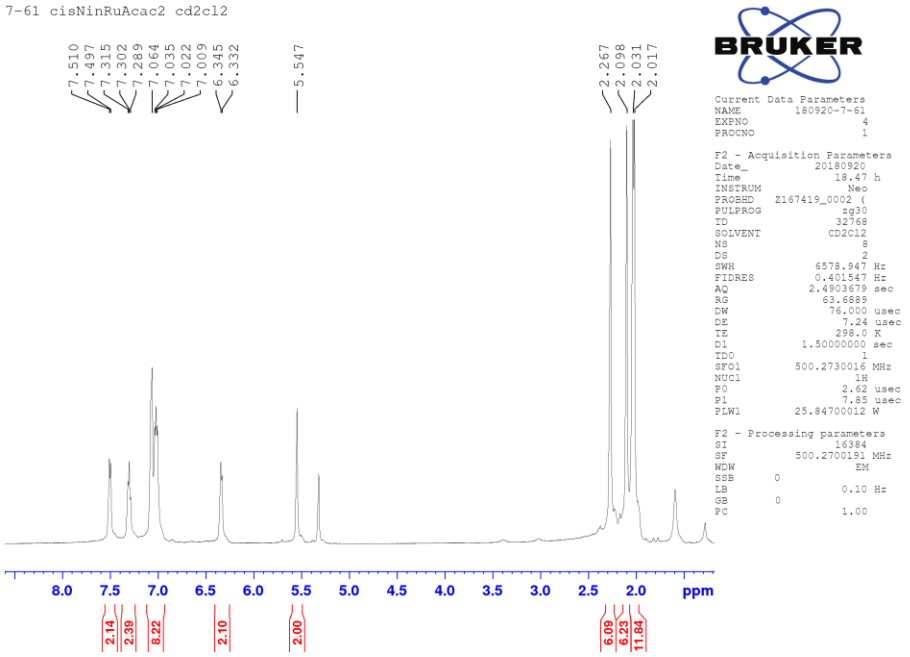

Appendix B-46 ^{1}H NMR of **5.5** in d^{2}-dichloromethane at 300 K.

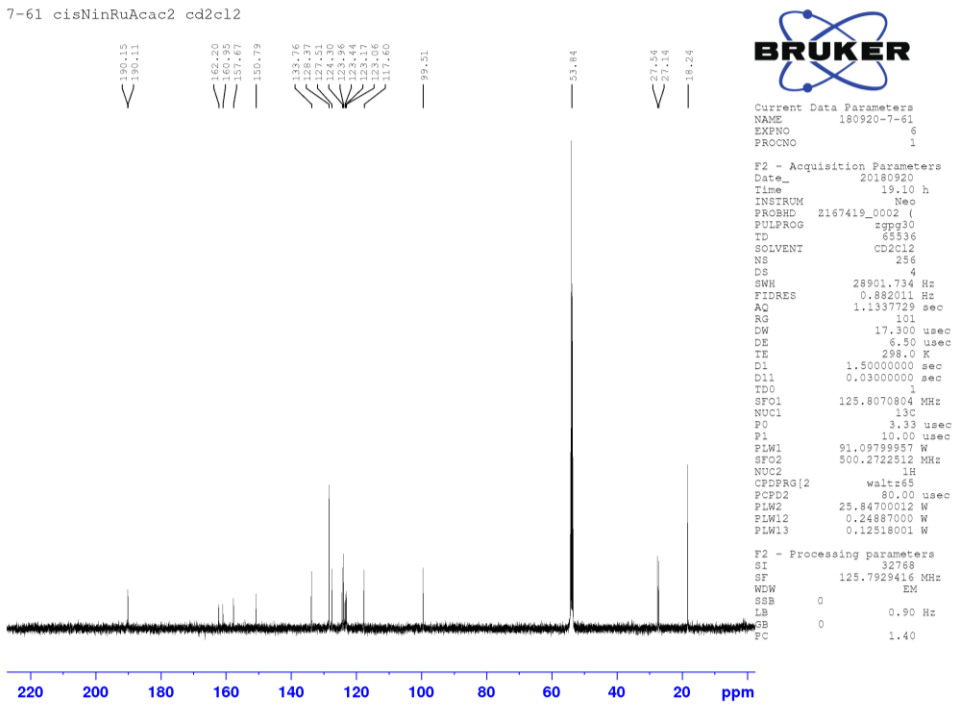

Appendix B-47 ^{13}C NMR of **5.5** in d^2-dichloromethane at 300 K.

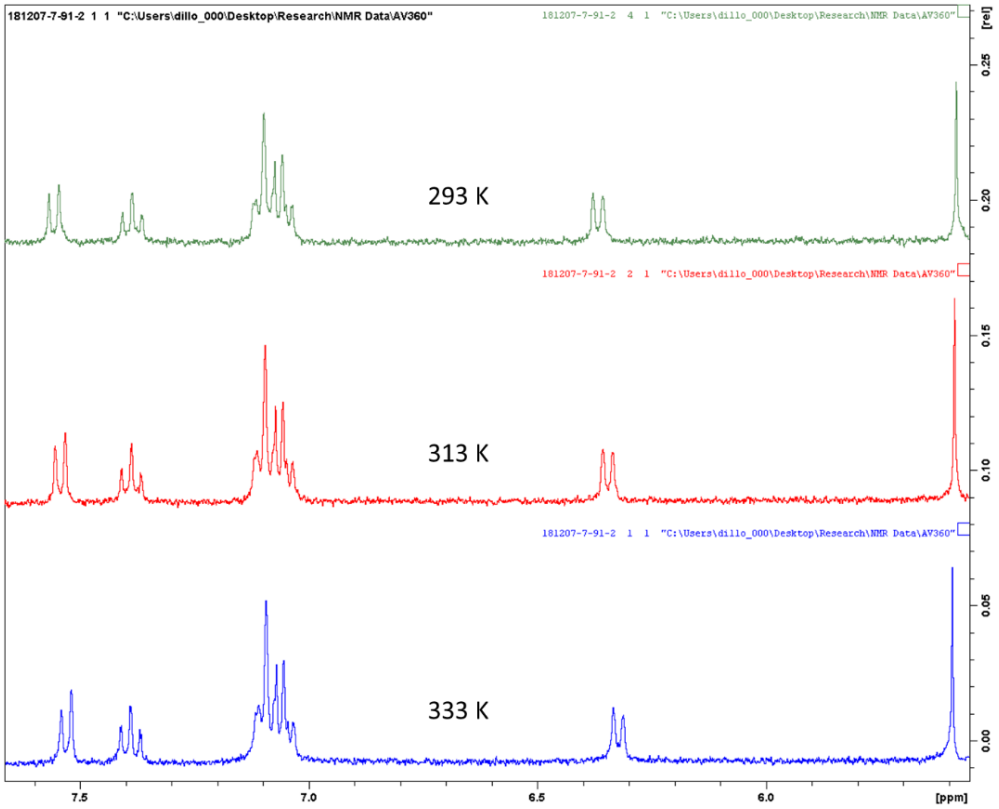

Appendix B-48 ^{1}H NMR of **5.5** in d^3-MeCN at various temperatures.

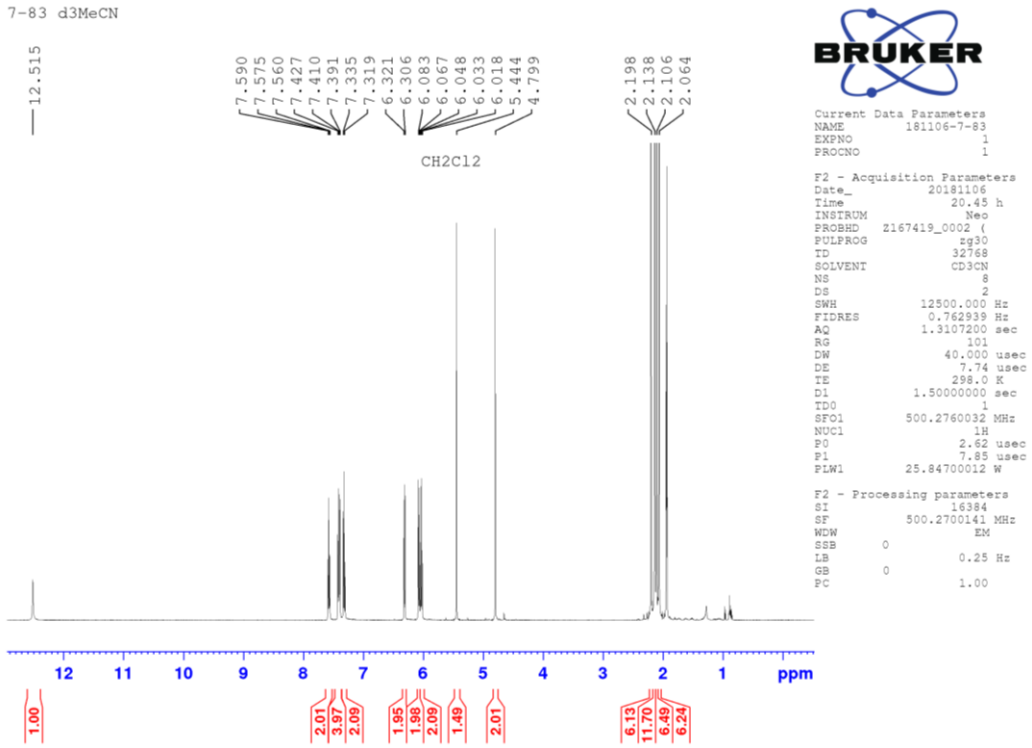

Appendix B-49 ^{1}H NMR of **H5.5**$^{+}$ in d^{3}-MeCN at 300 K.

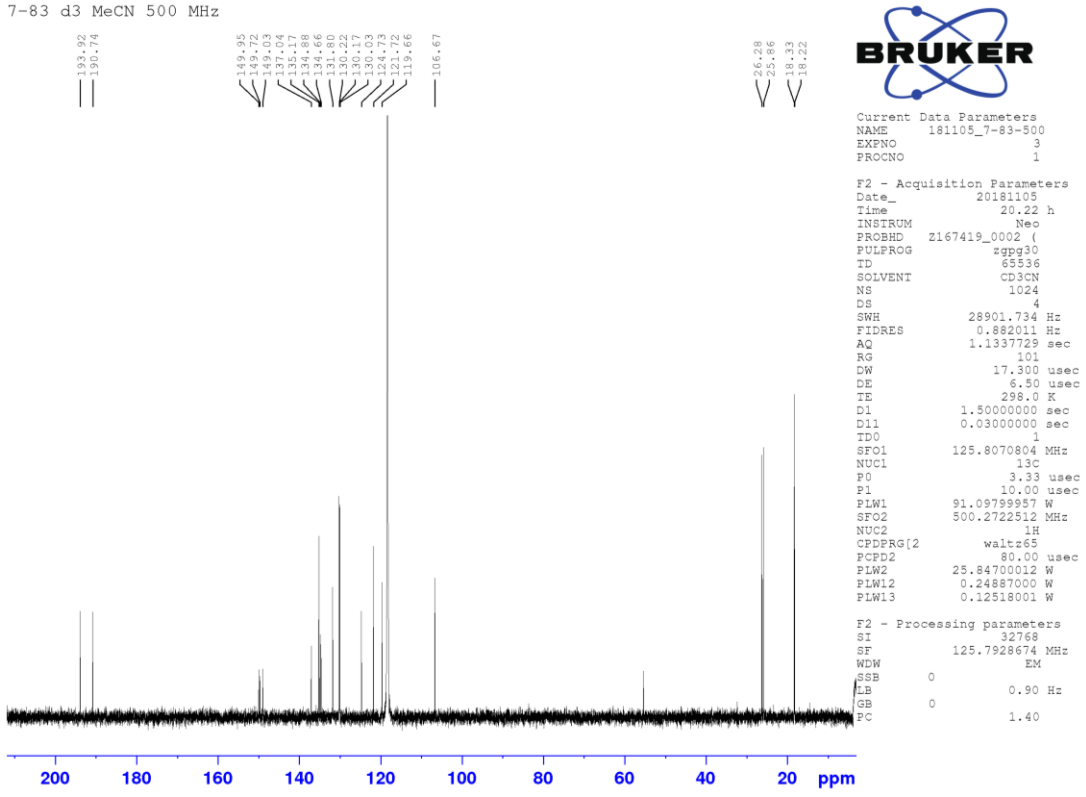

Appendix B-50 ^{13}C NMR of **H5.5**$^{+}$ in d^{3}-MeCN at 300 K.

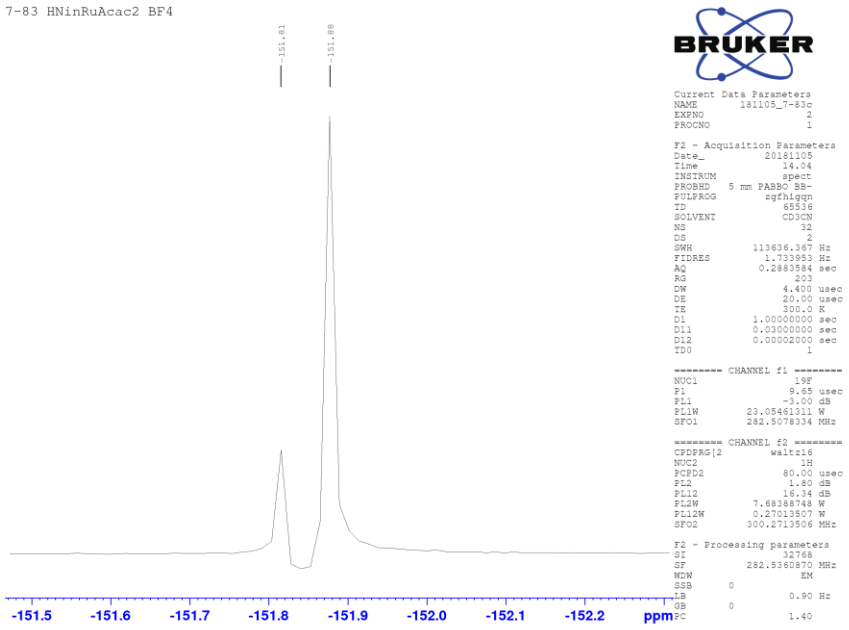

Appendix B-51 ^{19}F NMR of **H5.5**$^{+}$ in d^{3}-MeCN at 300 K.

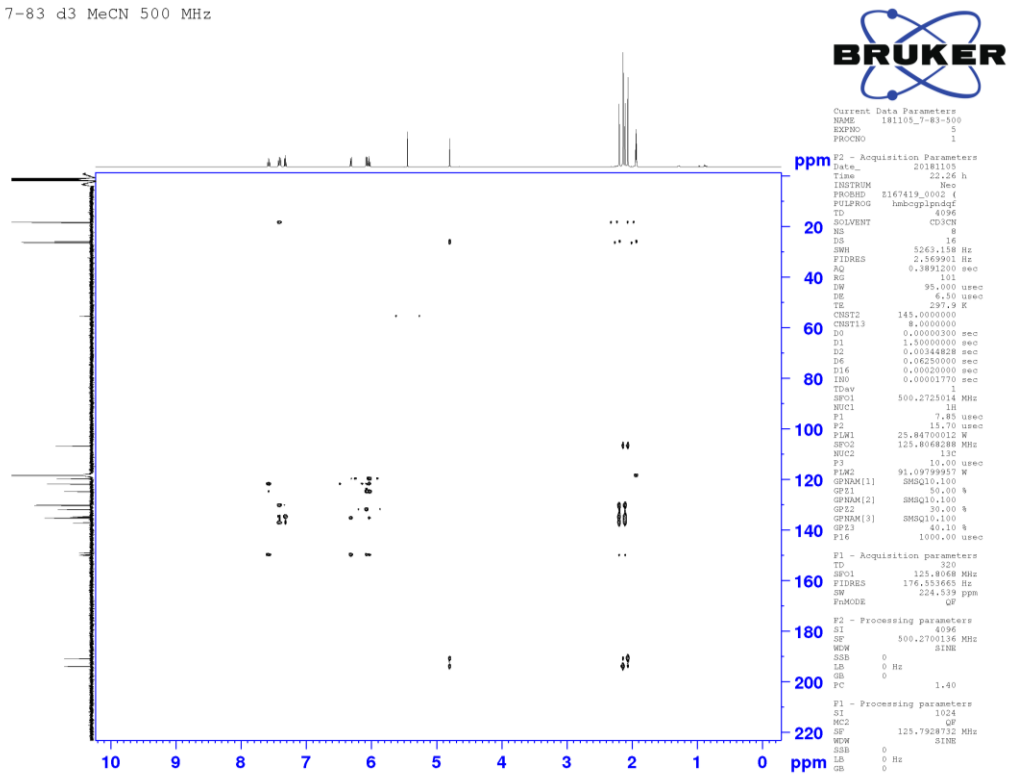

Appendix B-52 HMBC (3j ^{1}H-^{13}C) of **H5.5**$^{+}$ in d$_{3}$-MeCN.

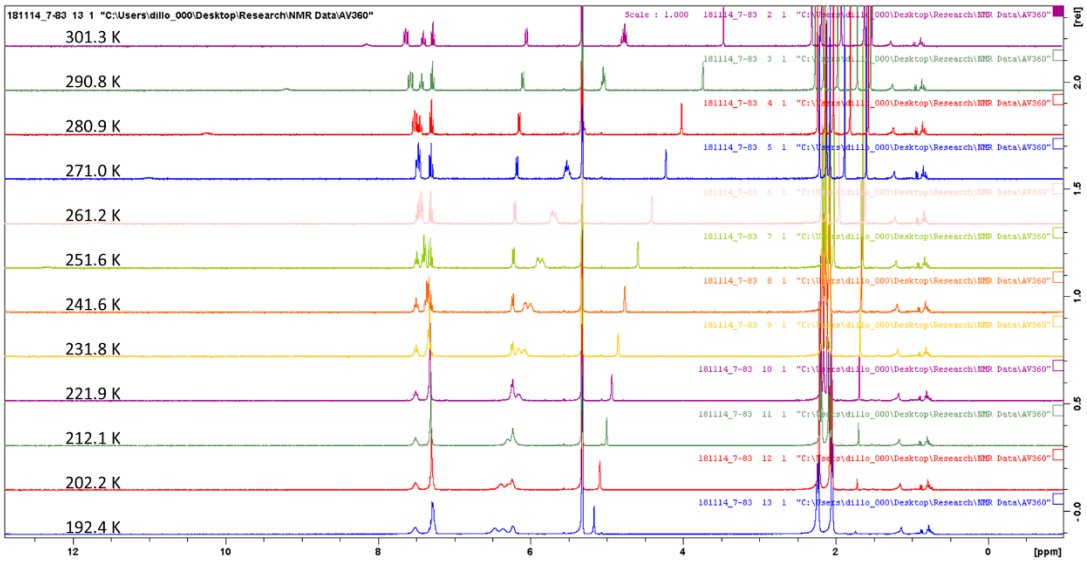

Appendix B-53 ^{1}H NMR of **H5.5**$^{+}$ in d^{2}-dichloromethane at various temperatures.

Appendix C. FT-IR spectra

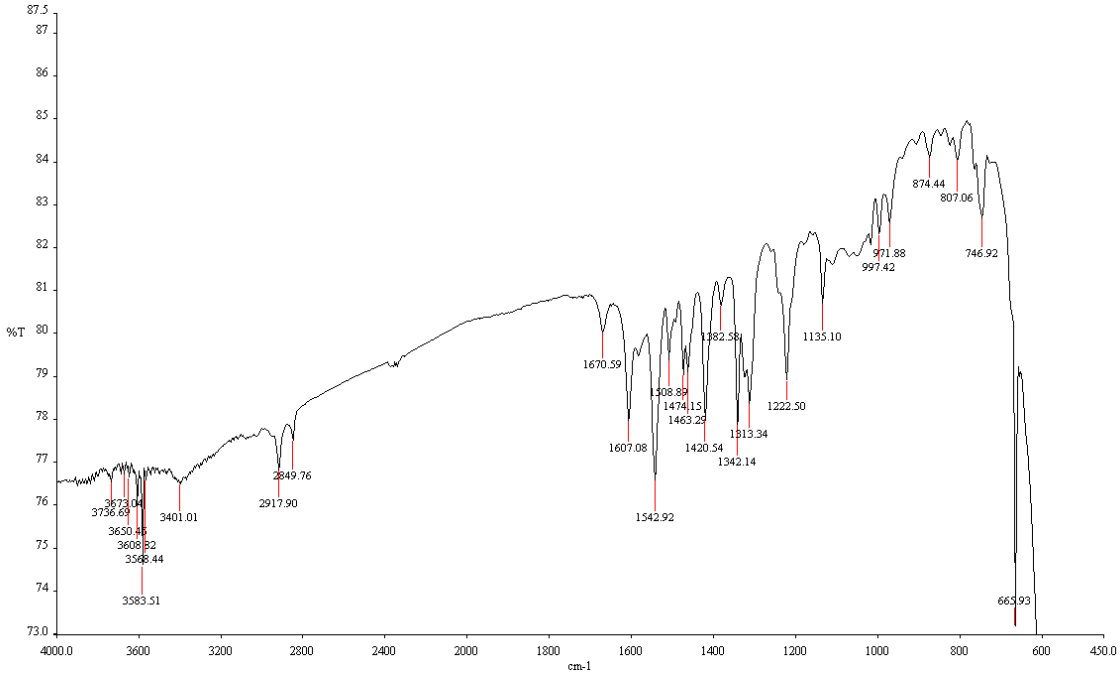

Appendix C-1 FT-IR of **2.3a**.

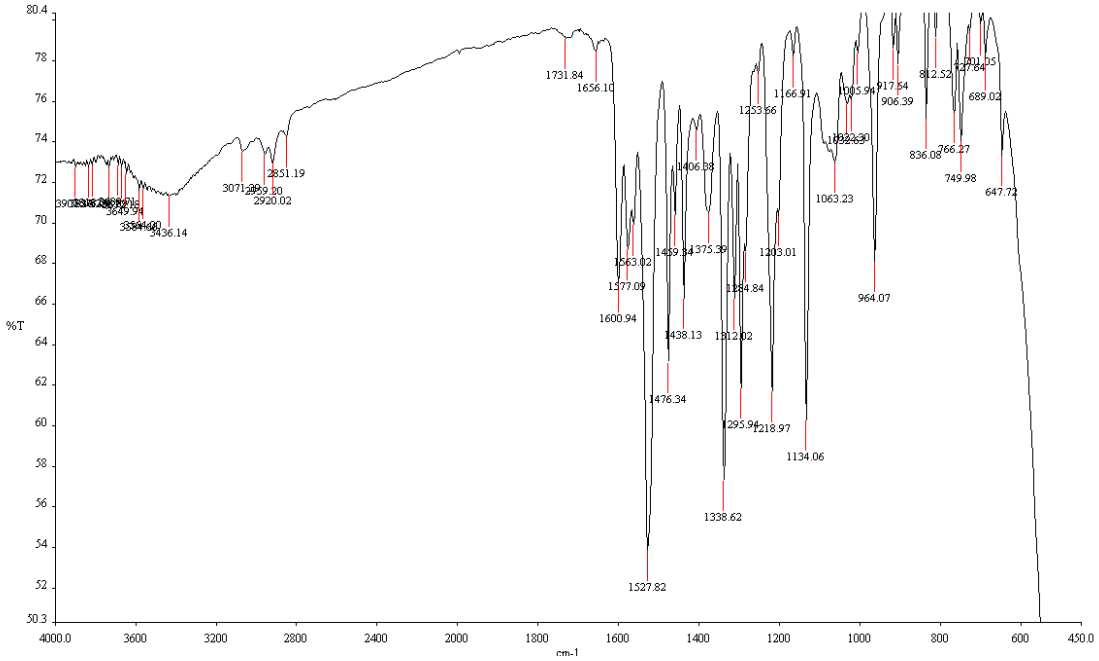

Appendix C-2 FT-IR of **2.3b**.

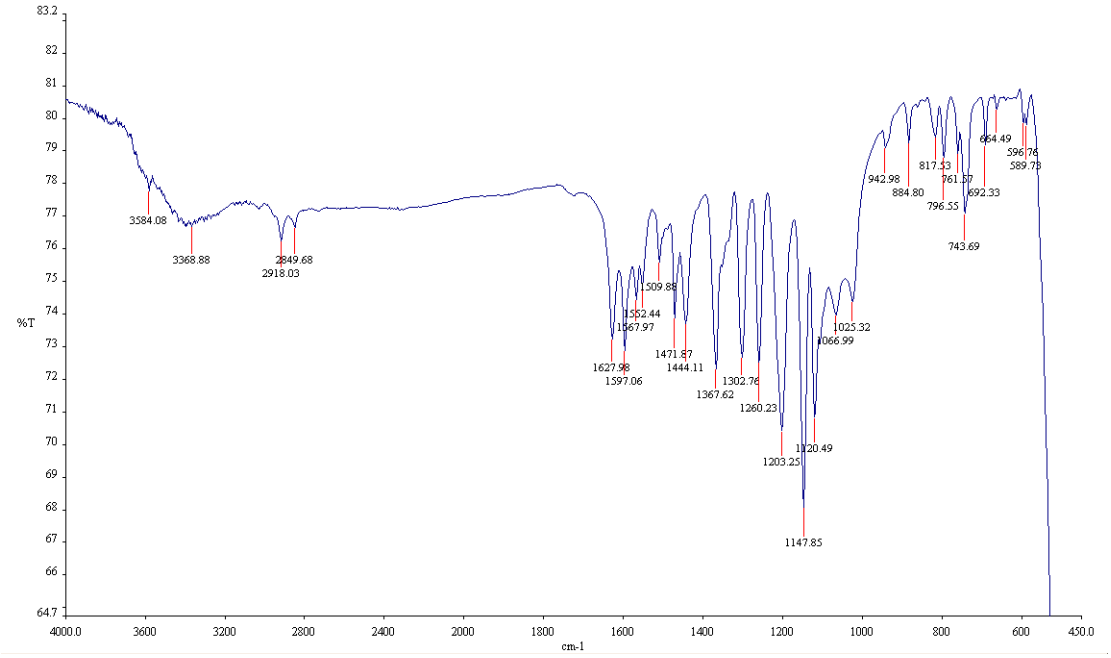

Appendix C-3 FT-IR of **2.4a**.

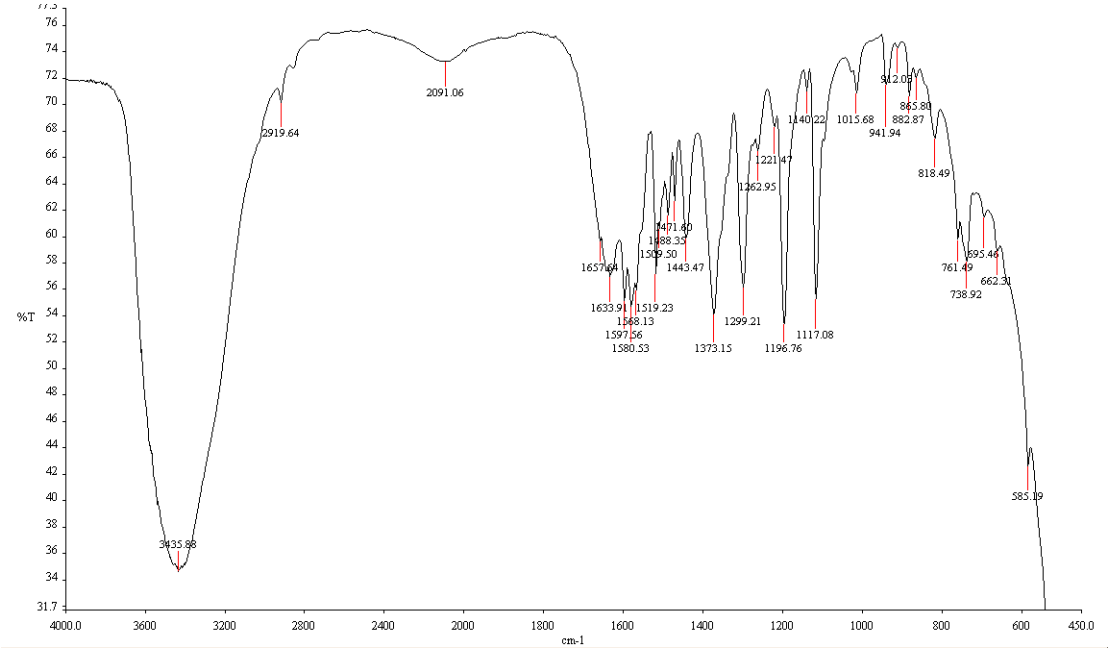

Appendix C-4 FT-IR of **2.5a**.

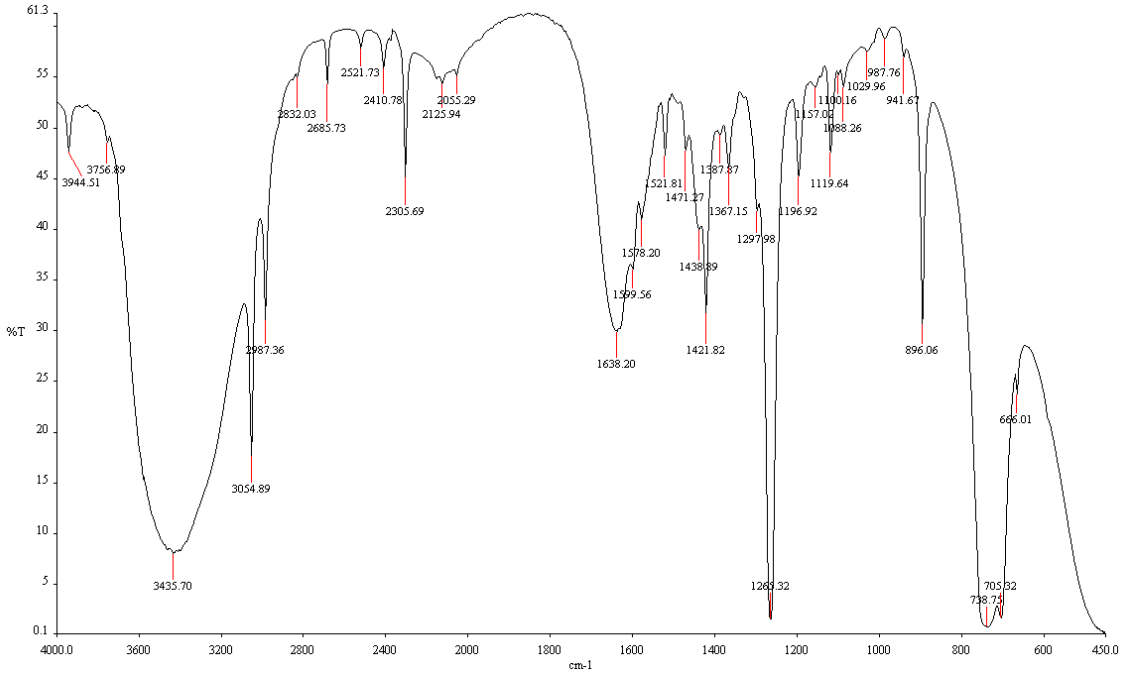

Appendix C-5 FT-IR of **2.5b**.

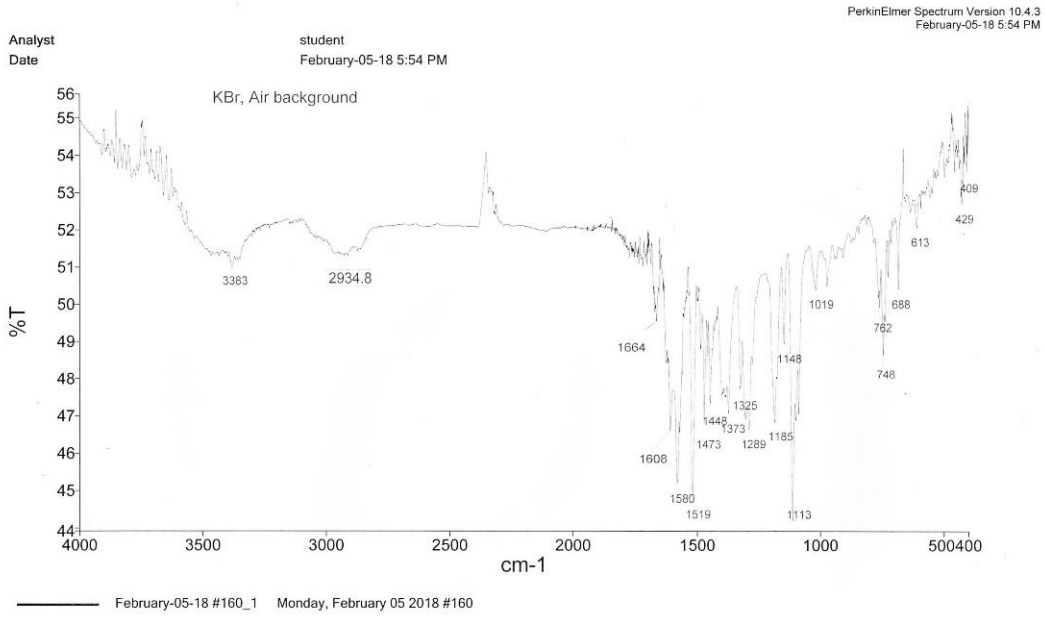

Appendix C-6 FT-IR of **3.2**, KBr pellet, Air background.

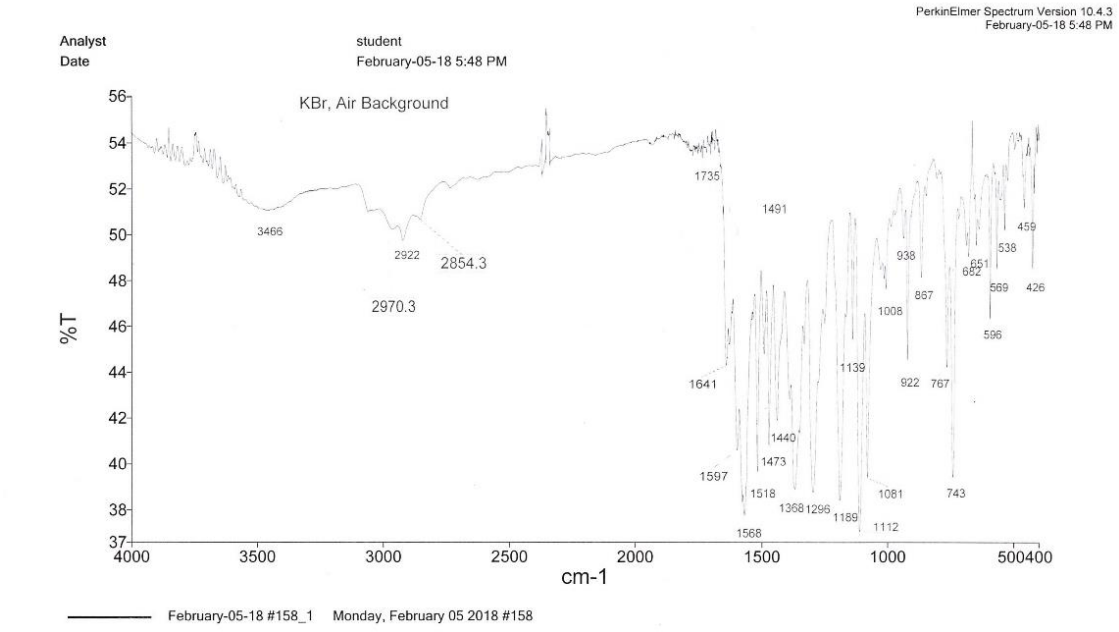

Appendix C-7 FT-IR of **3.3**, KBr pellet, Air background.

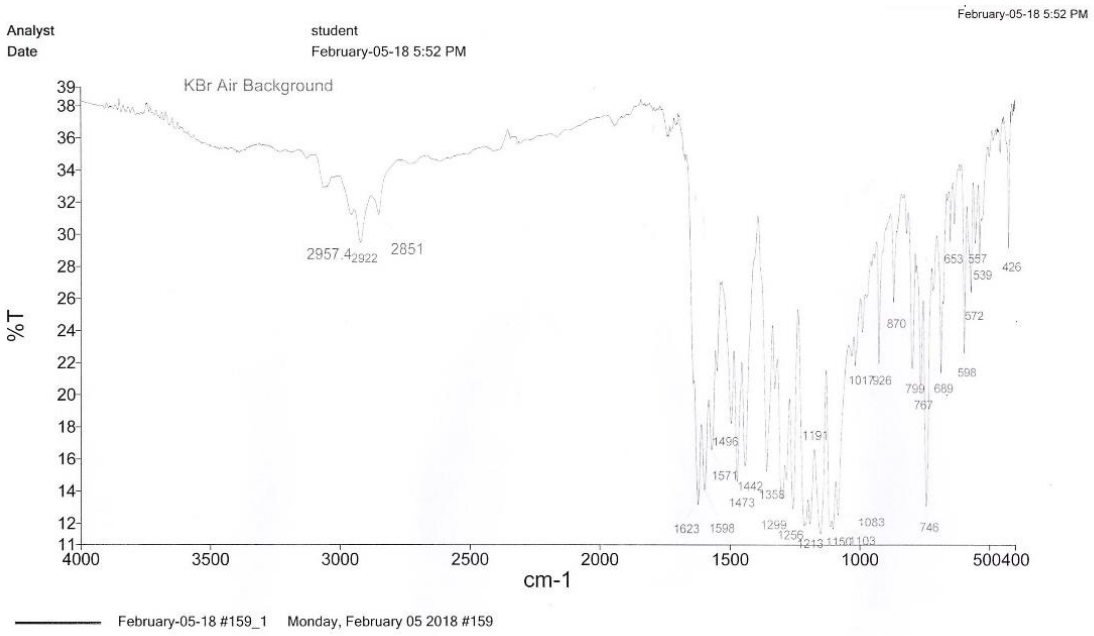

Appendix C-8 FT-IR of **3.4**, KBr pellet, Air background.

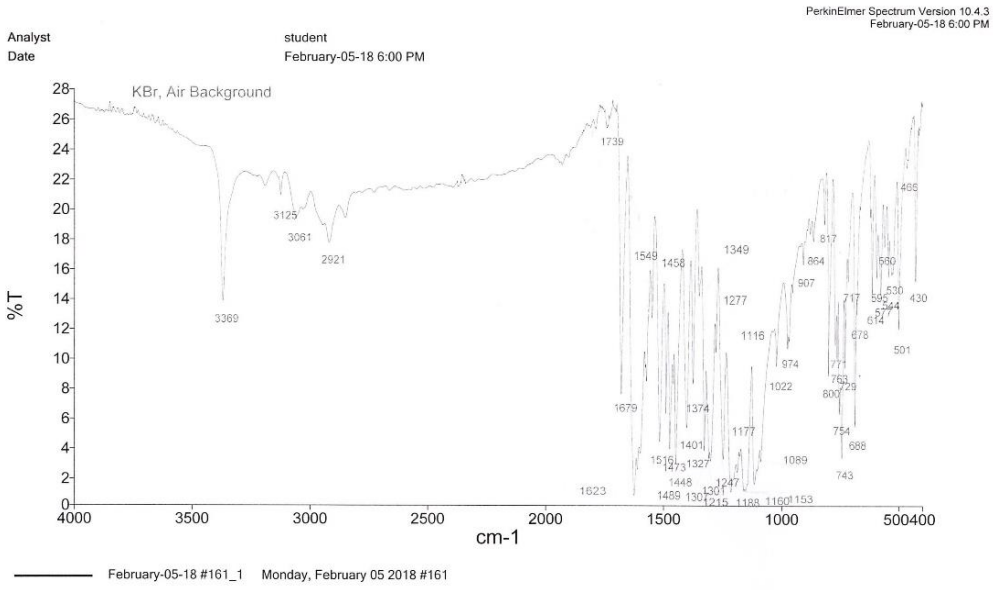

Appendix C-9 FT-IR of **3.5**, KBr pellet, Air background.

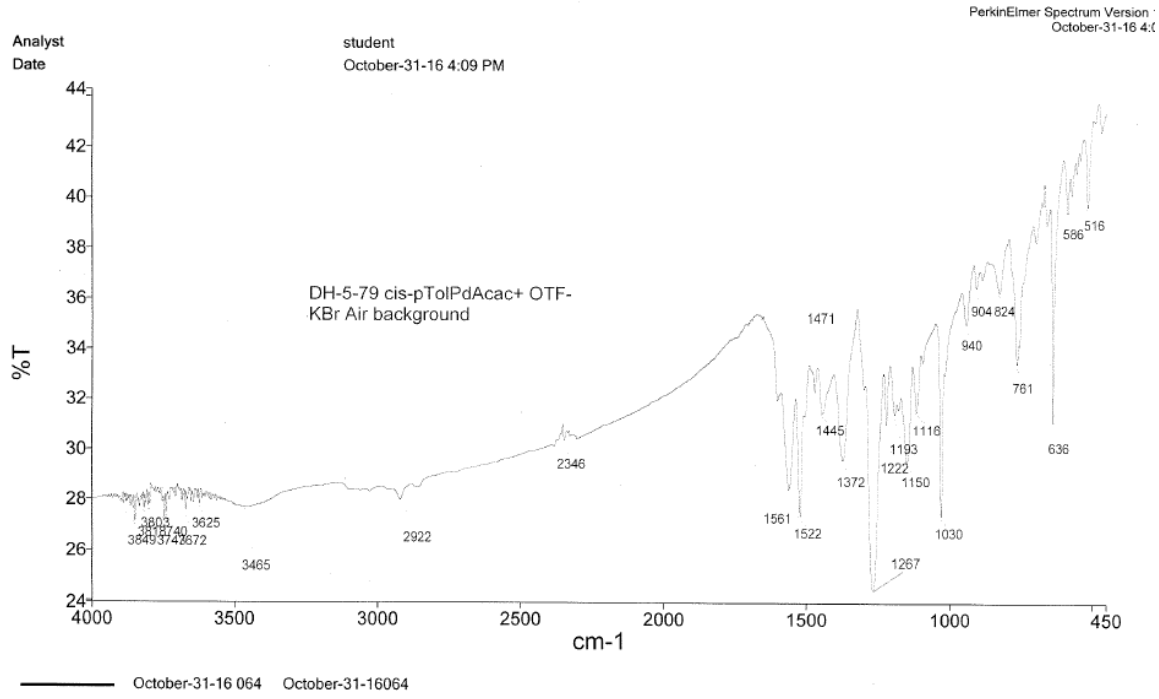

Appendix C-10 FT-IR of **H4.11**$^{+}$, KBr pellet, Air background.

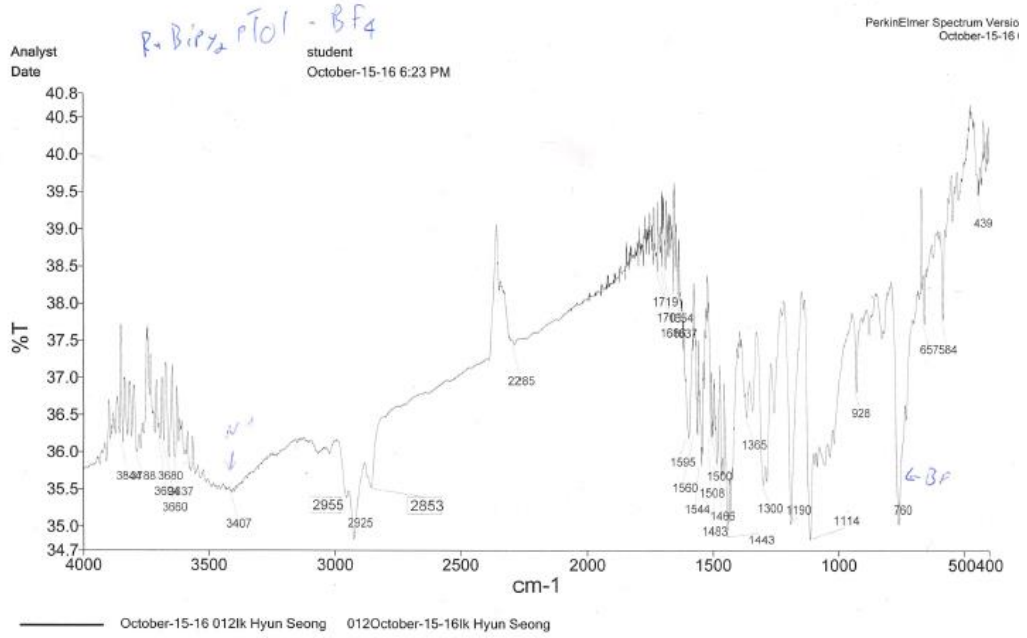

Appendix C-11 FT-IR of **H4.12**$^{+}$, KBr pellet, Air background.

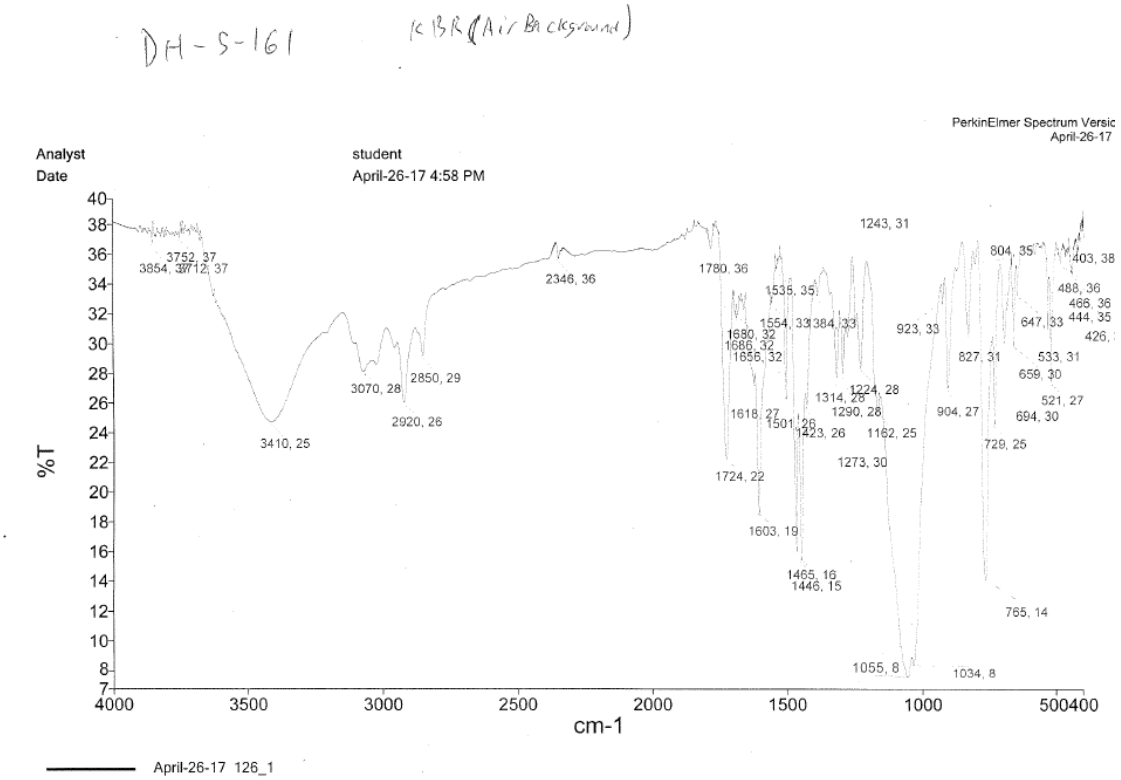

Appendix C-12 FT-IR of **H4.12**$^{2+}$, KBr pellet, Air background.

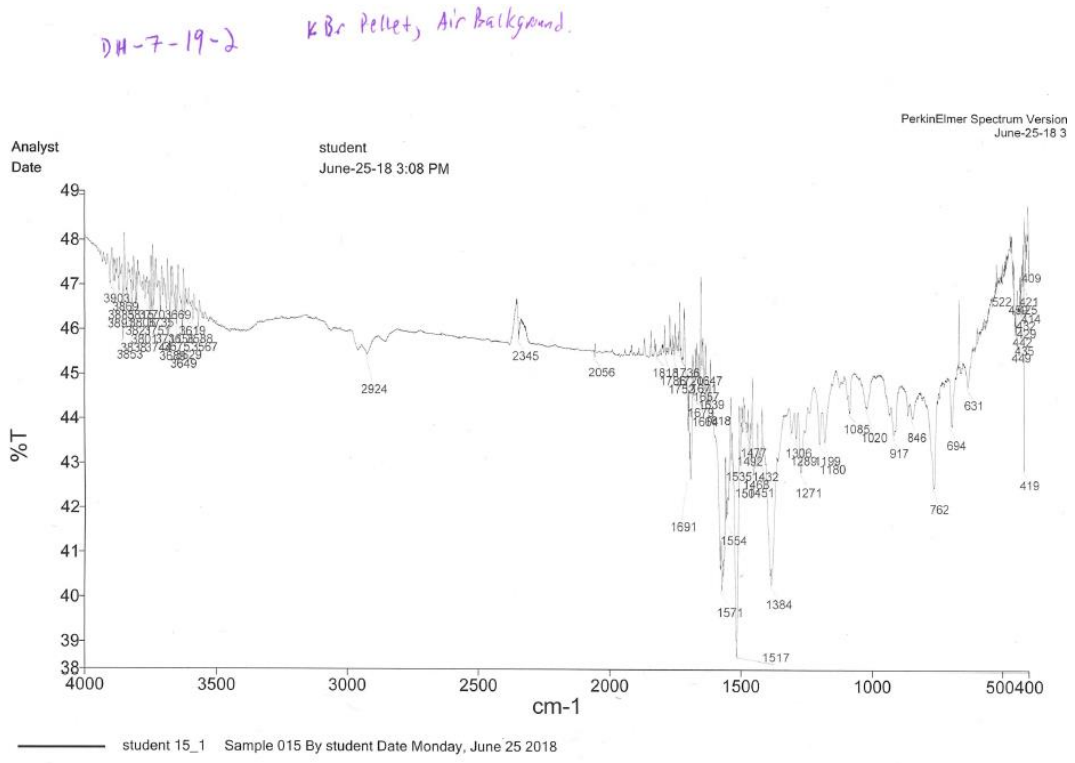

Appendix C-13 FT-IR of **5.3**, KBr pellet, Air background.

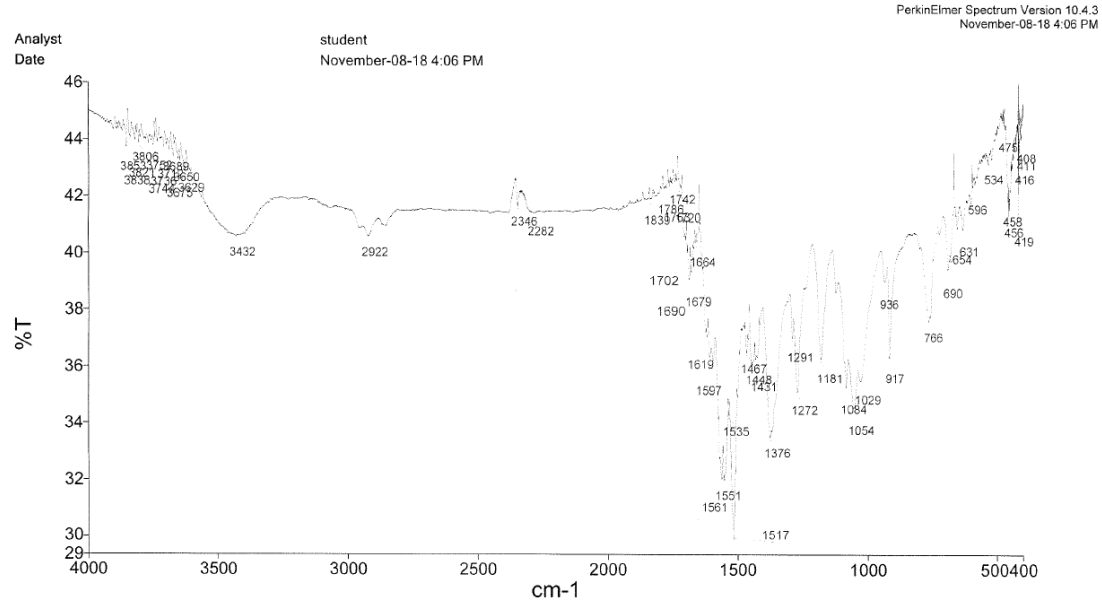

Appendix C-14 FT-IR of **H5.3**$^{+}$, KBr pellet, Air background.

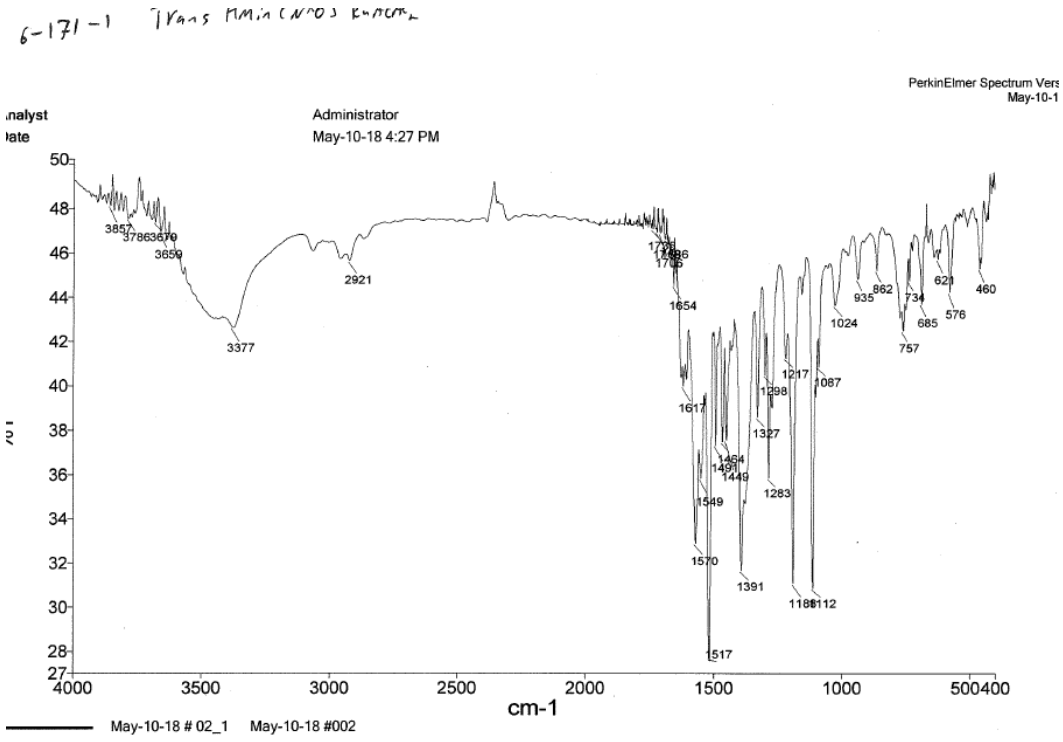

Appendix C-15 FT-IR of **H5.4**, KBr pellet, Air background.

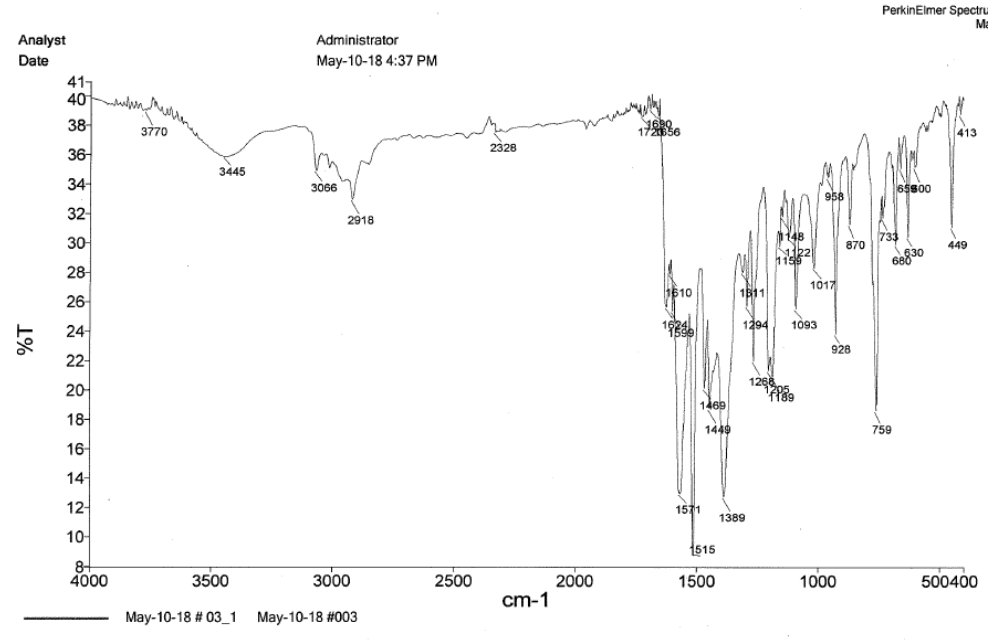

Appendix C-16 FT-IR of **5.5**, KBr pellet, Air background.

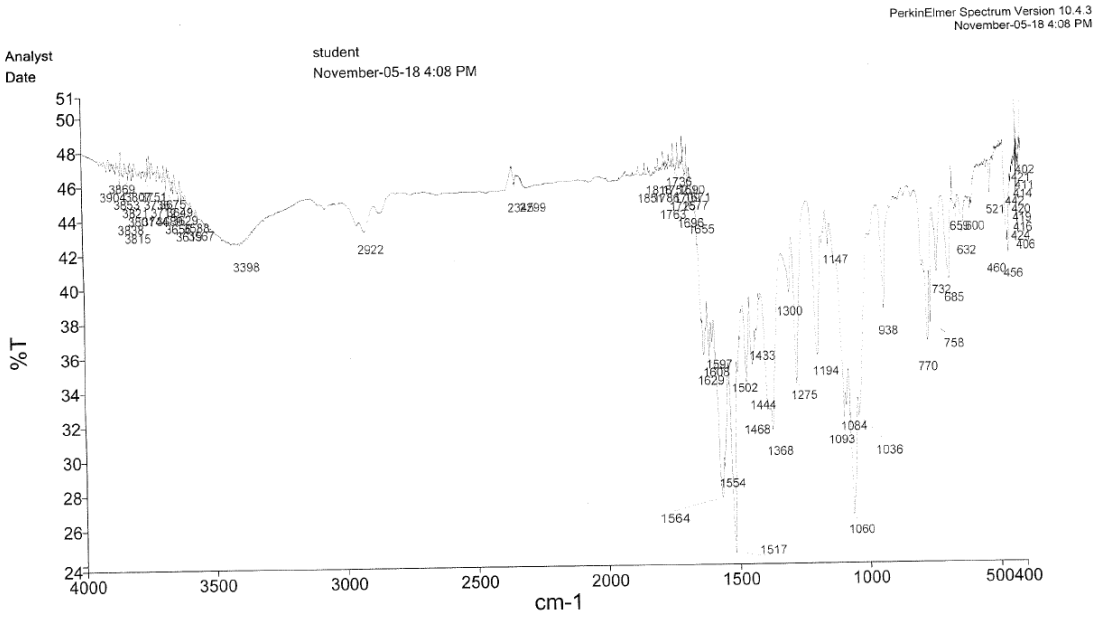

Appendix C-17 FT-IR of **H5.5**$^{+}$, KBr pellet, Air background.

Appendix D. Mass Spectra

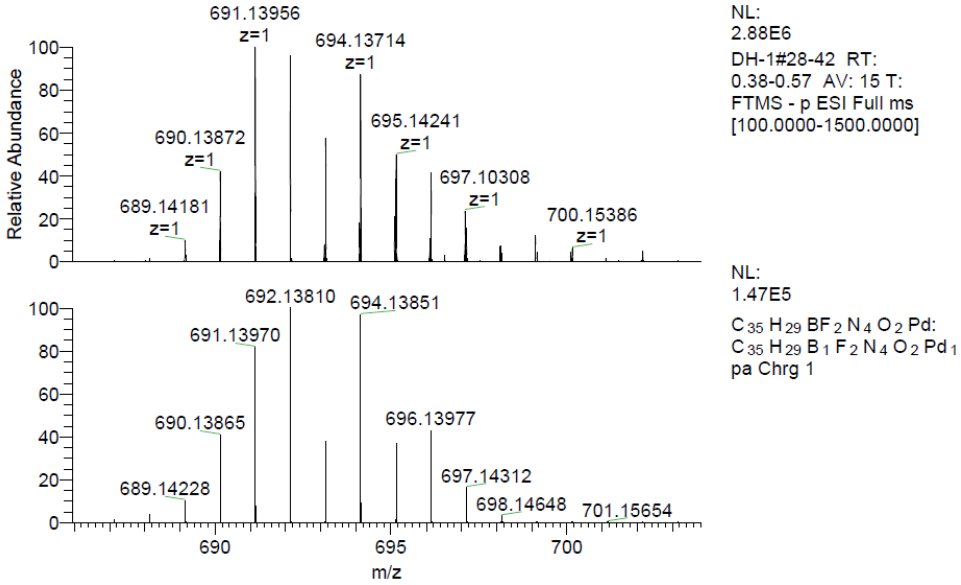

Appendix D-1 HR-MS of **2.3a** and simulation.

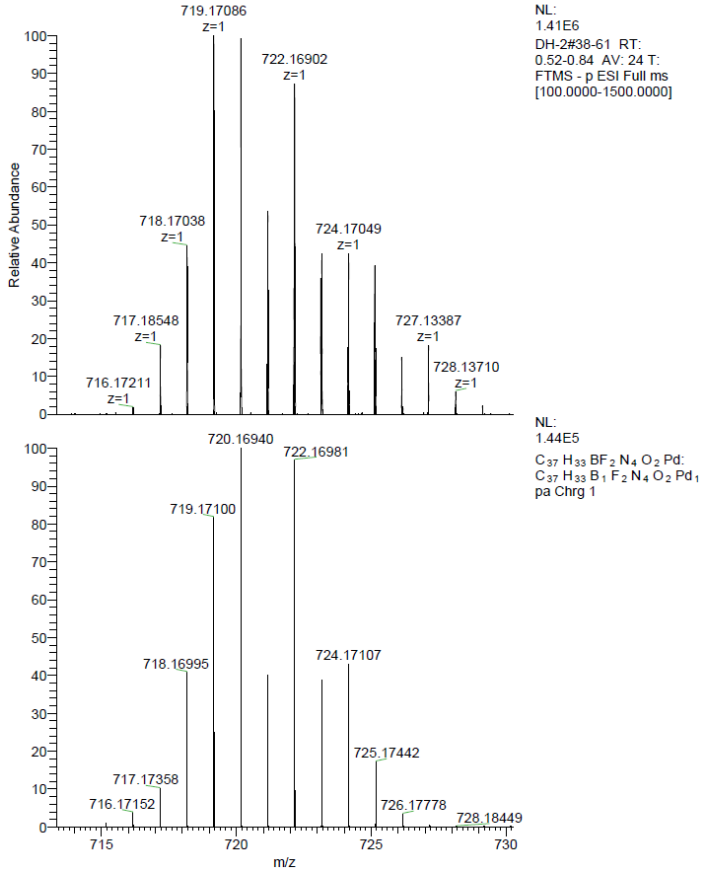

Appendix D-2 HR-MS of **2.3b** and simulation.

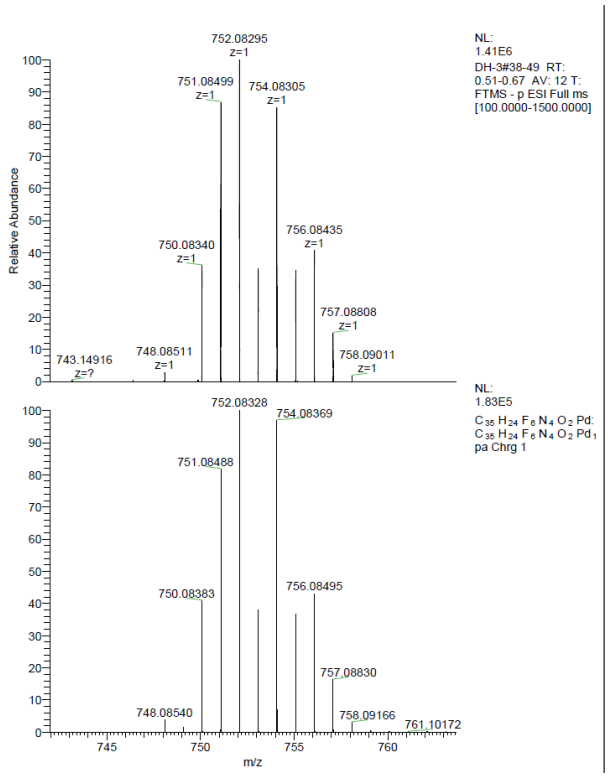

Appendix D-3 HR-MS of **2.4a** and simulation.

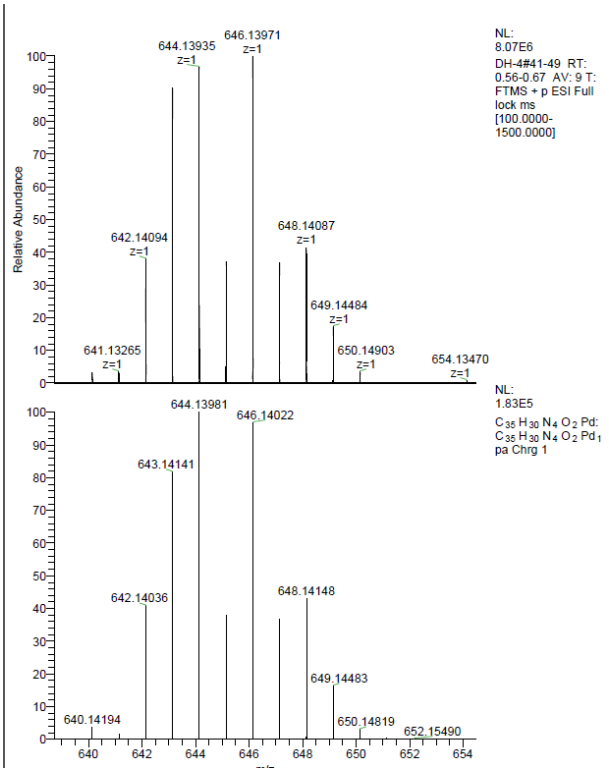

Appendix D-4 HR-MS of **2.5a** and simulation.

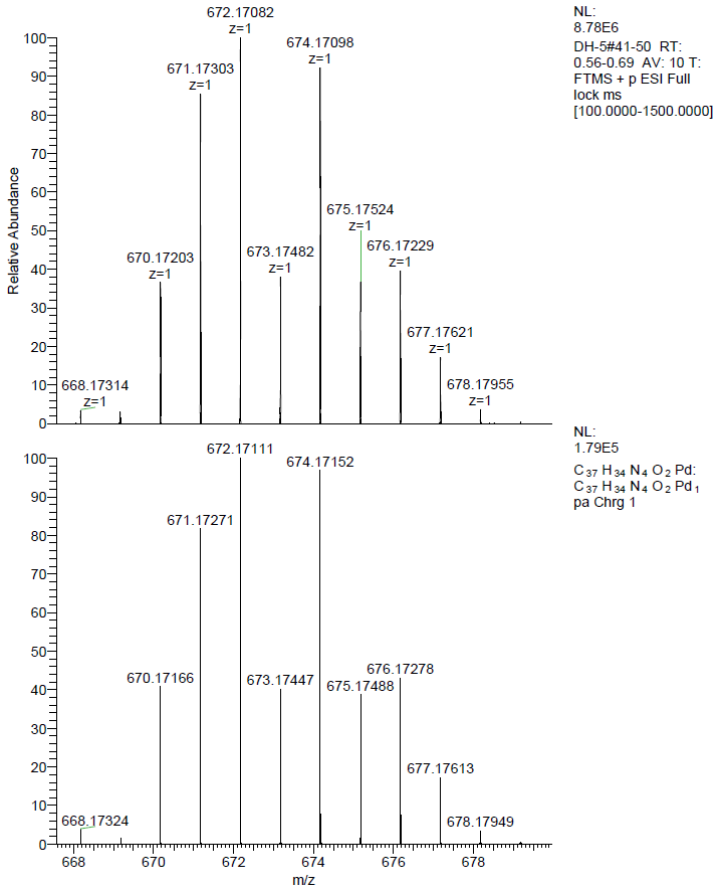

Appendix D-5 HR-MS of **2.5b** and simulation.

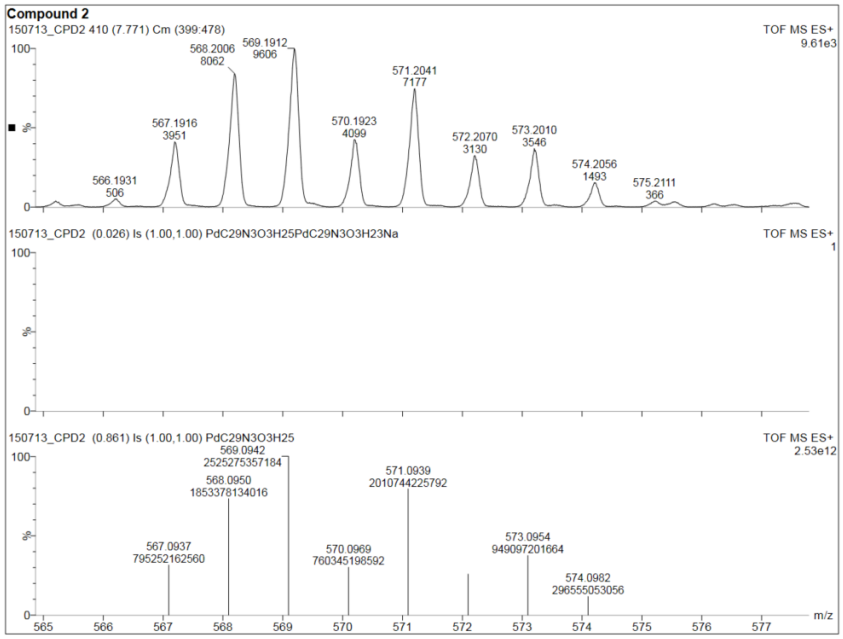

Appendix D-6 ESI-MS of **3.2** and simulation.

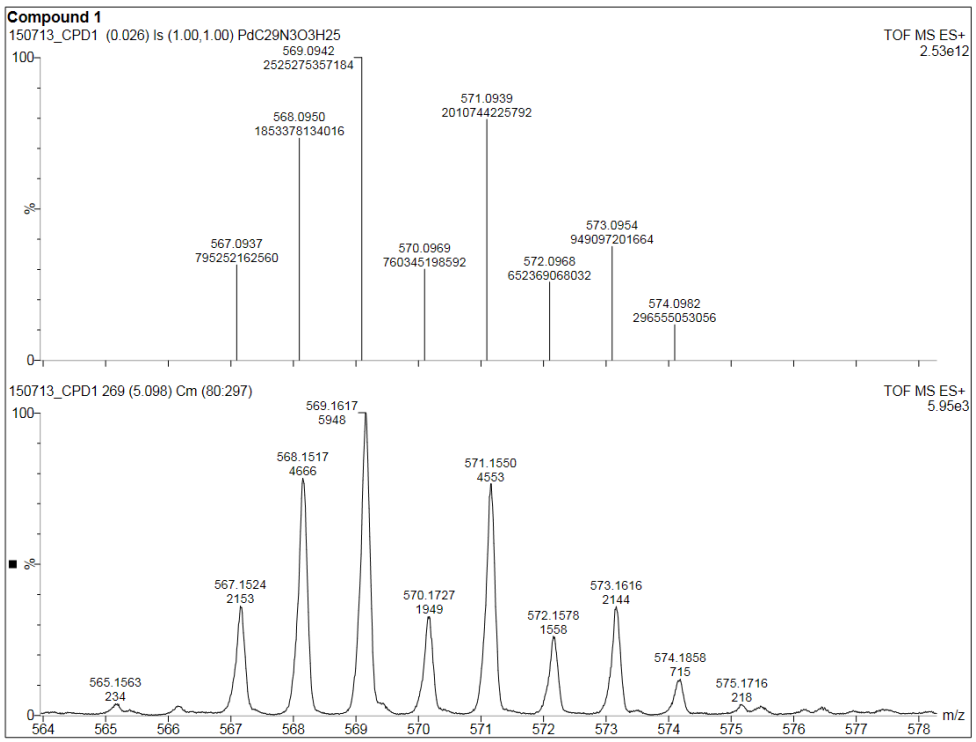

Appendix D-7 ESI-MS of **3.3** and simulation.

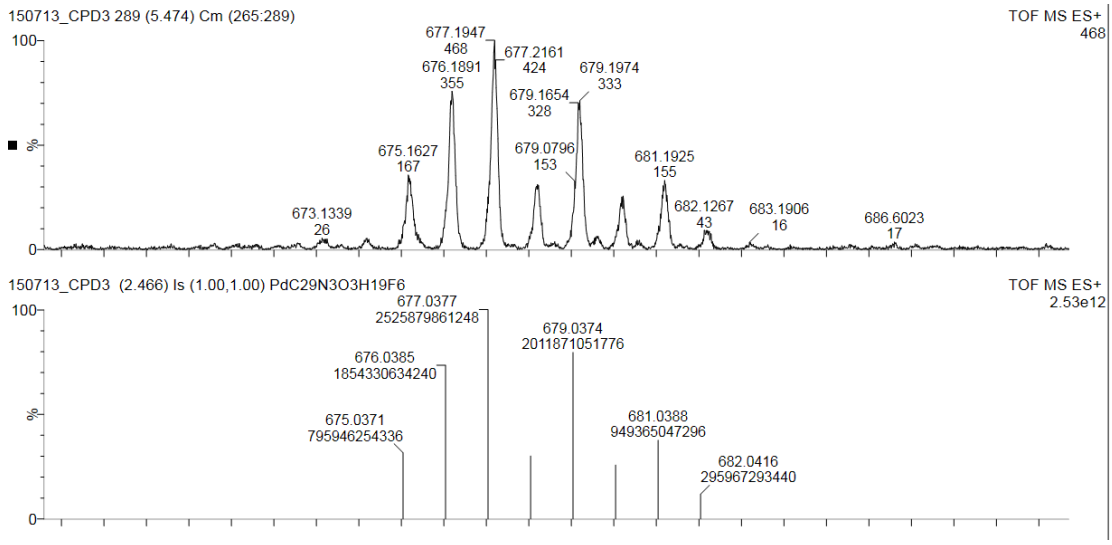

Appendix D-8 ESI-MS of **3.4** and simulation.

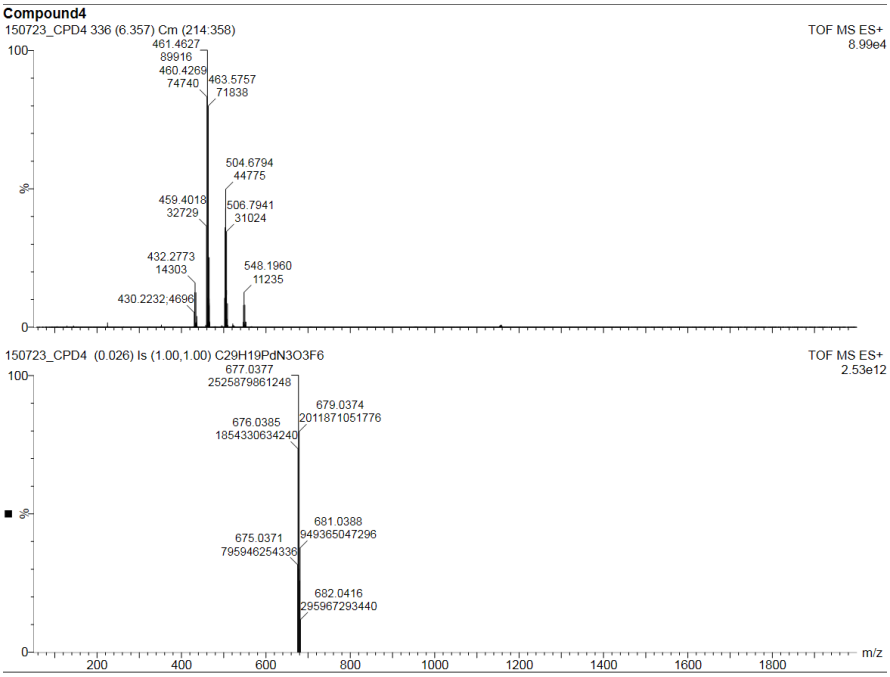

Appendix D-9 ESI-MS of **3.5**.

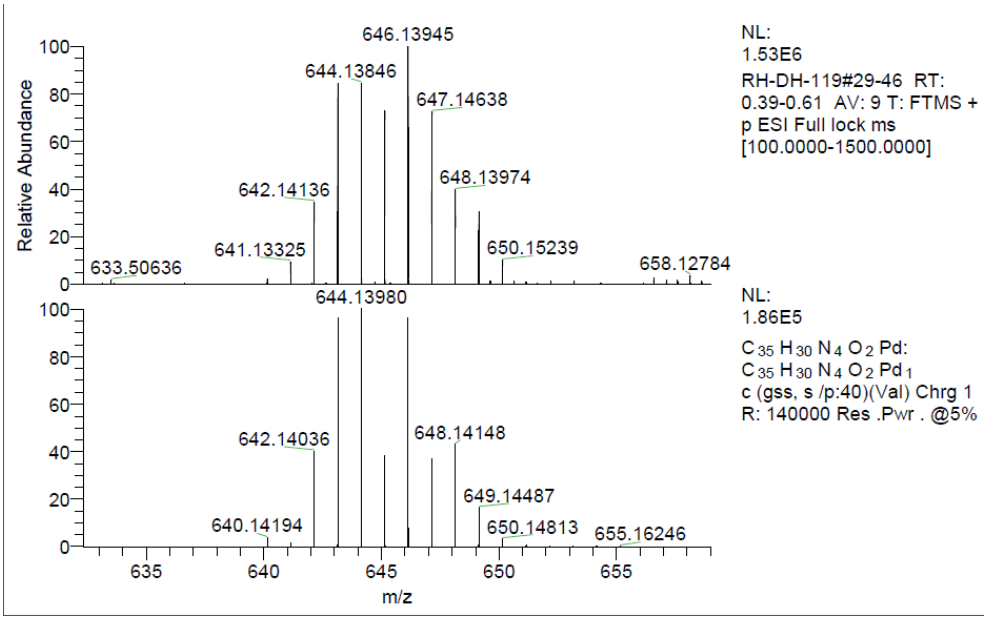

Appendix D-10 HR-MS of **H4.11**$^{+}$.

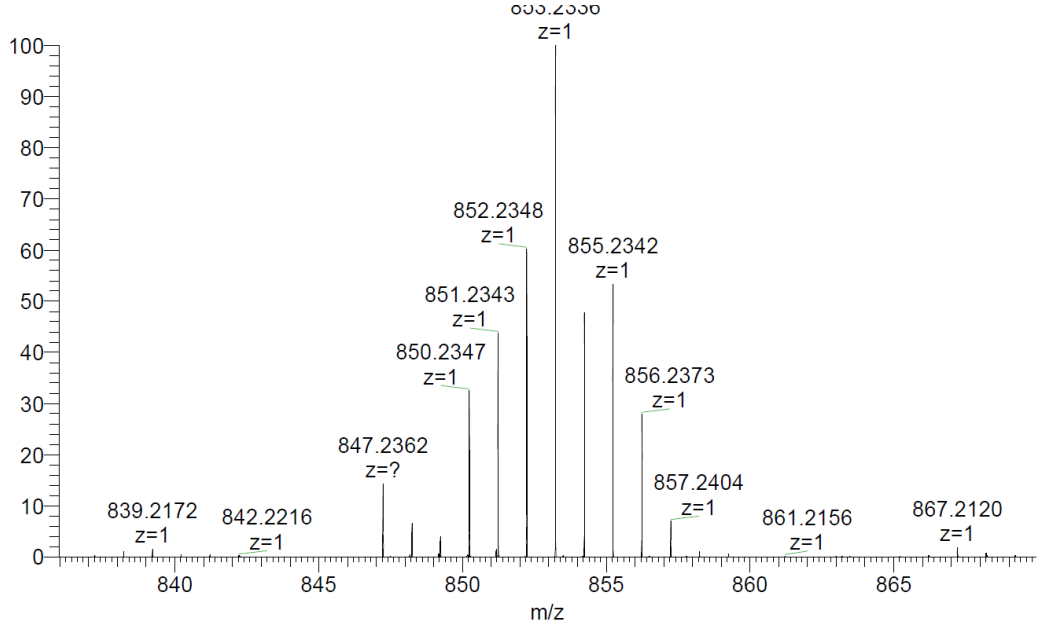

Appendix D-11 HR-MS of **H4.12**$^{2+}$.

Appendix E. UV-Vis-NIR Spectra

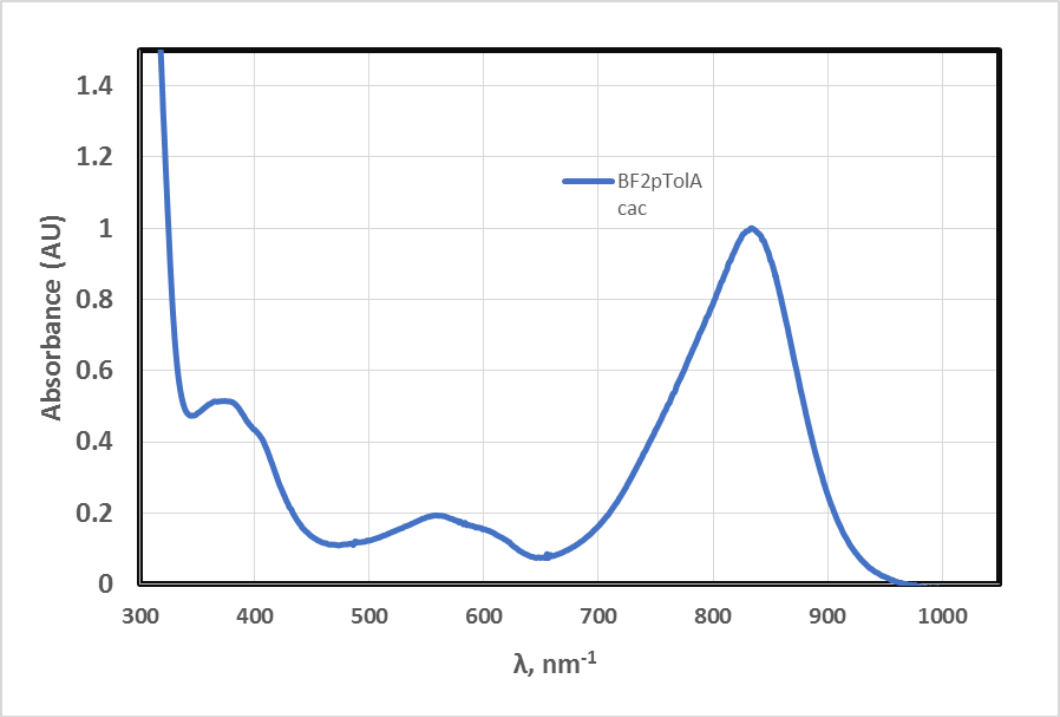

Appendix E-1 UV-Vis of **2.3a** in CH_2Cl_2, 50 µM, 298 K.

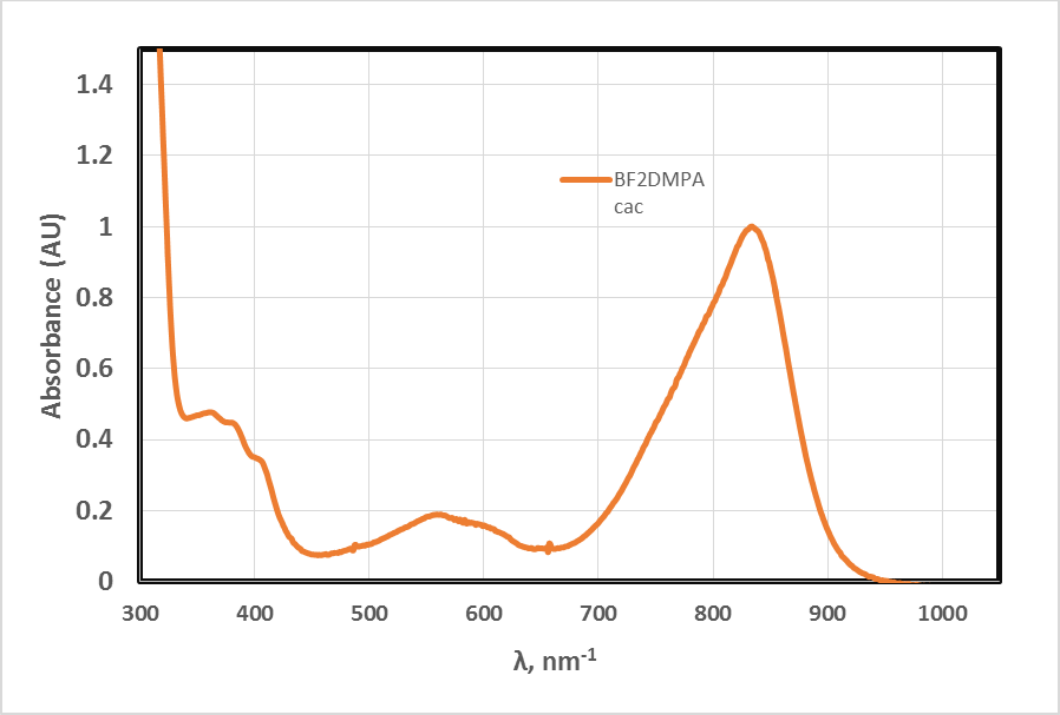

Appendix E-2 UV-Vis of **2.3b** in CH_2Cl_2, 50 µM, 298 K.

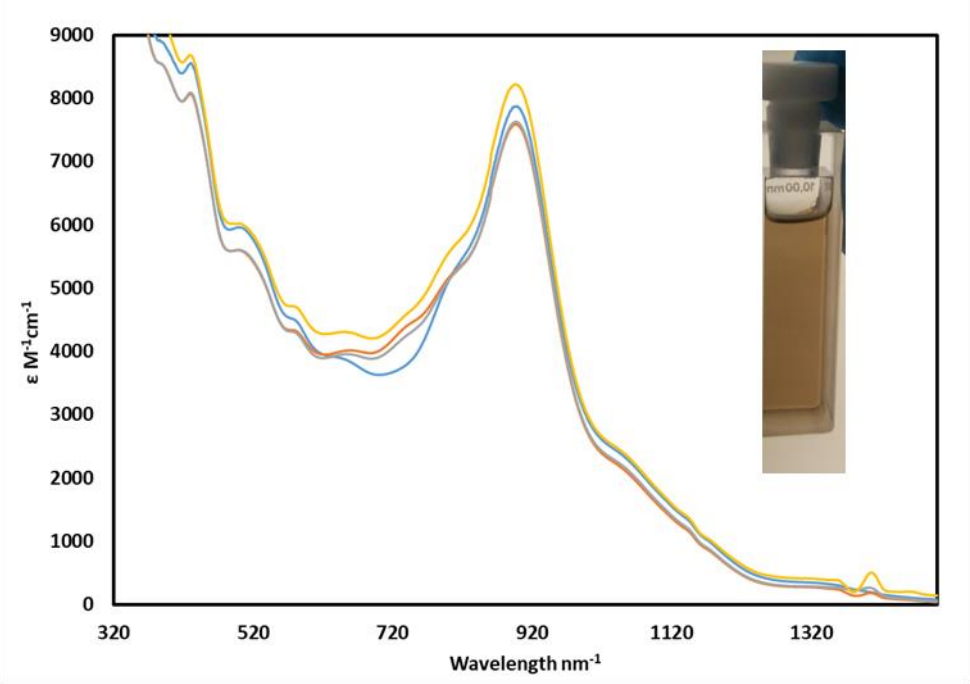

Appendix E-3 UV-Vis of **H4.11**$^{+}$ in CH_2Cl_2, ca. 20 µM, 298 K.

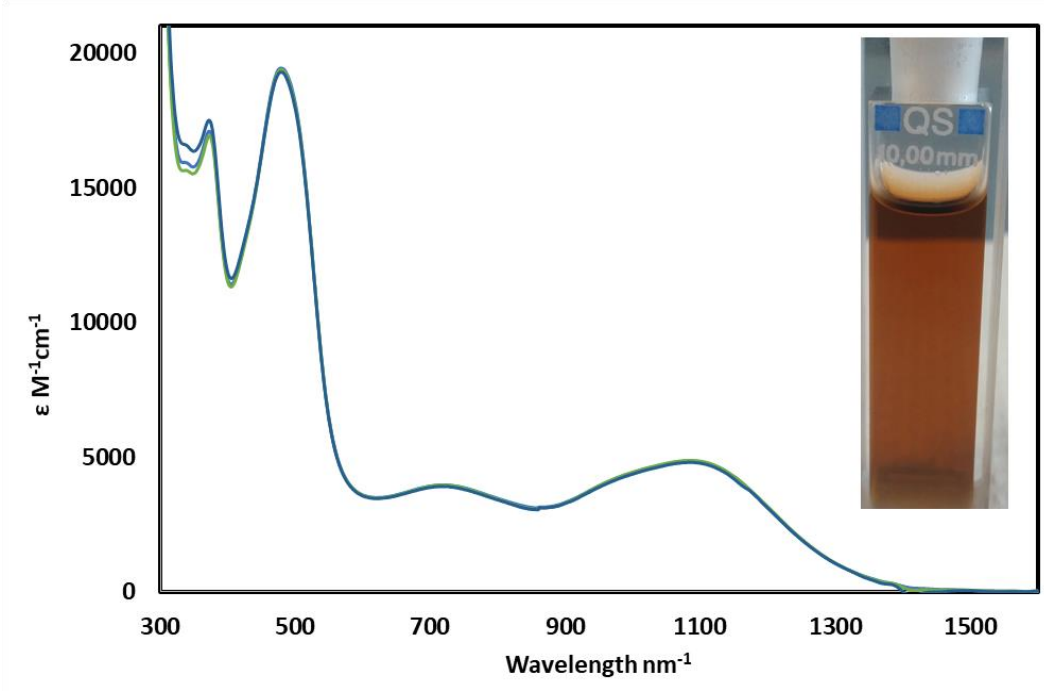

Appendix E-4 UV-Vis of **H4.12**$^{+}$ in MeCN, ca. 20 µM, 298 K.

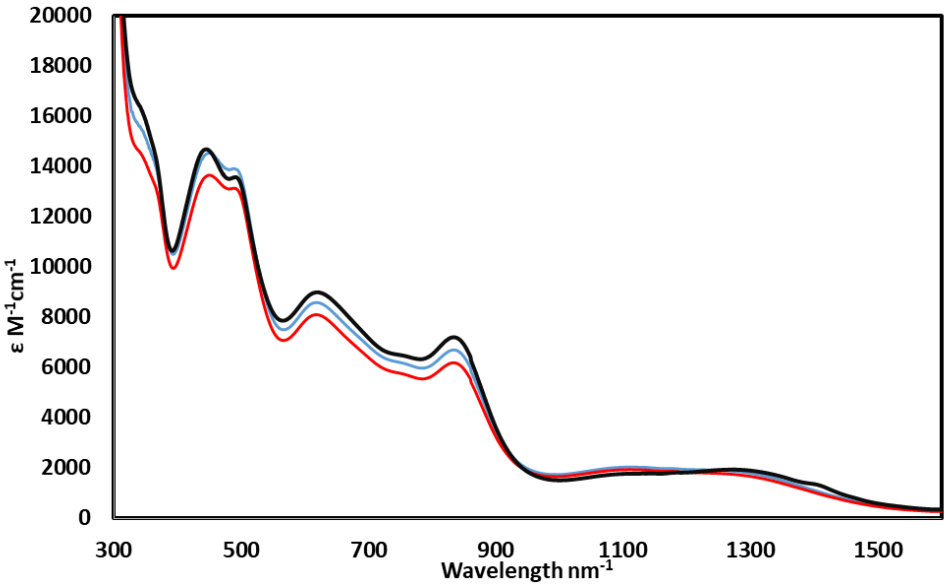

Appendix E-5 UV-Vis of **H4.12**$^{2+}$ in MeCN, ca. 20 µM, 298 K.

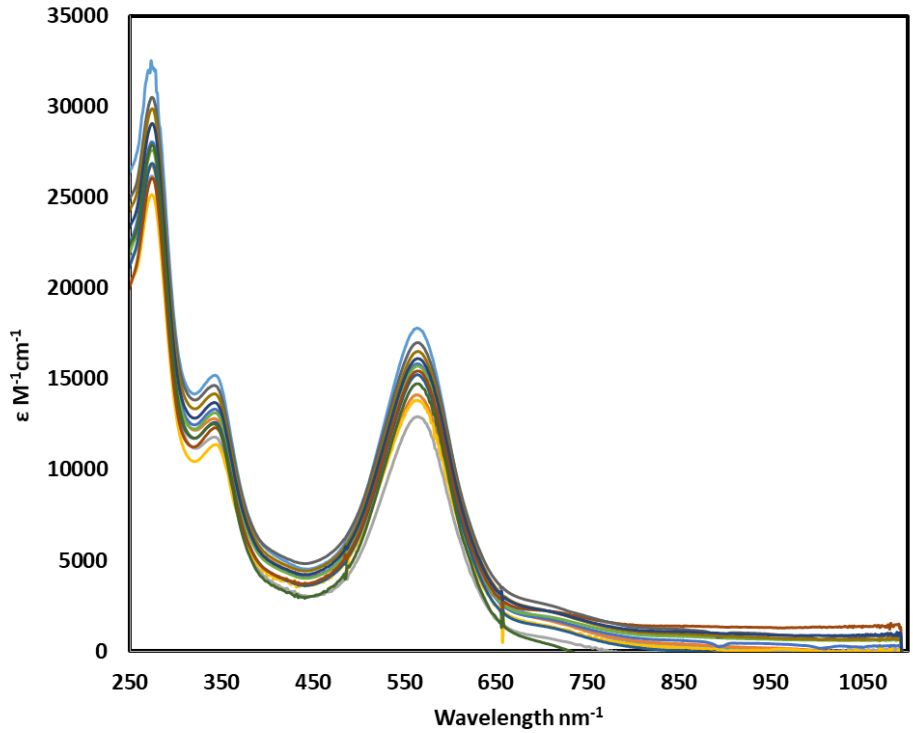

Appendix E-6 UV-Vis of **H5.4** in MeCN at 298 K.

Appendix F. Cyclic Voltammograms

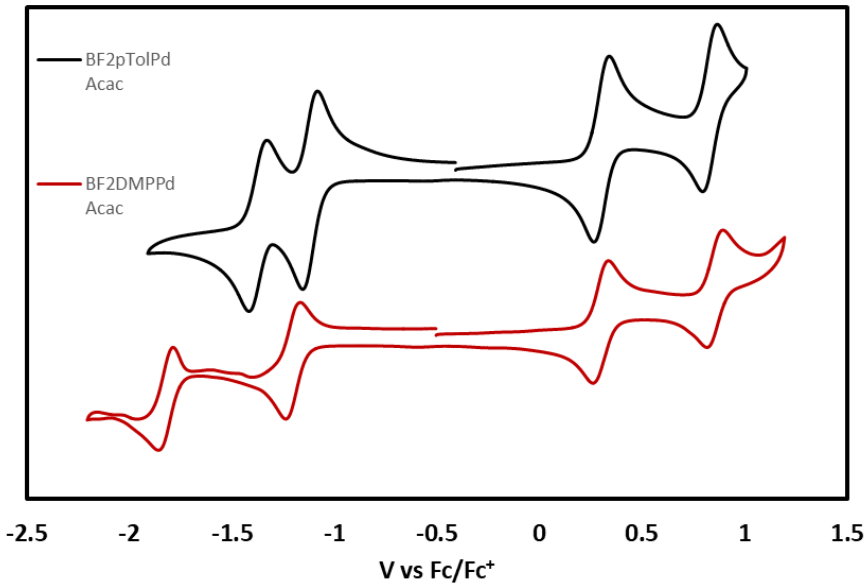

Appendix F-1 Cyclic voltammetry of 1 mM **2.3a** (top) and **2.3b** (bottom) 0.1 M NBu_4BF_4 dichloromethane.

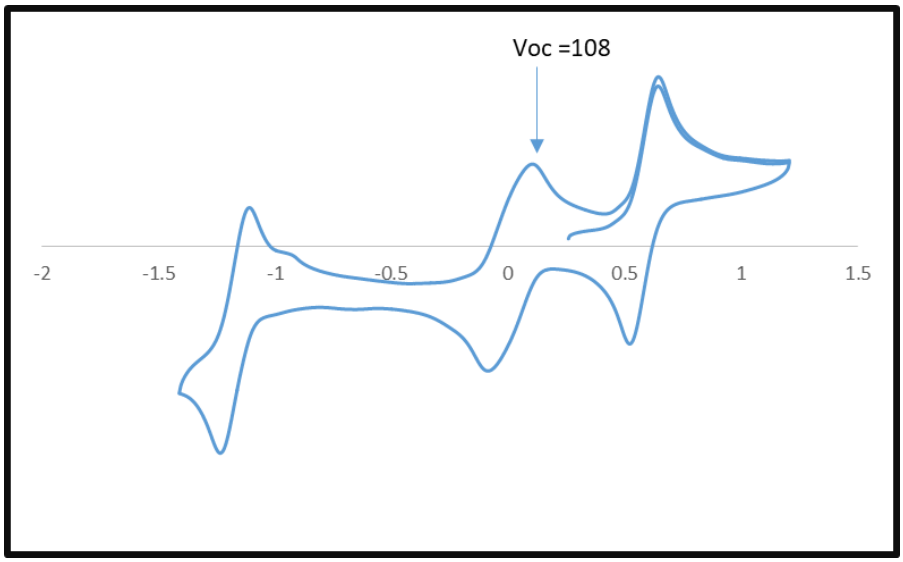

Appendix F-2 Cyclic voltammogram of 1 mM **H4.11**$^+$, 0.1 M NBu_4BF_4, THF.

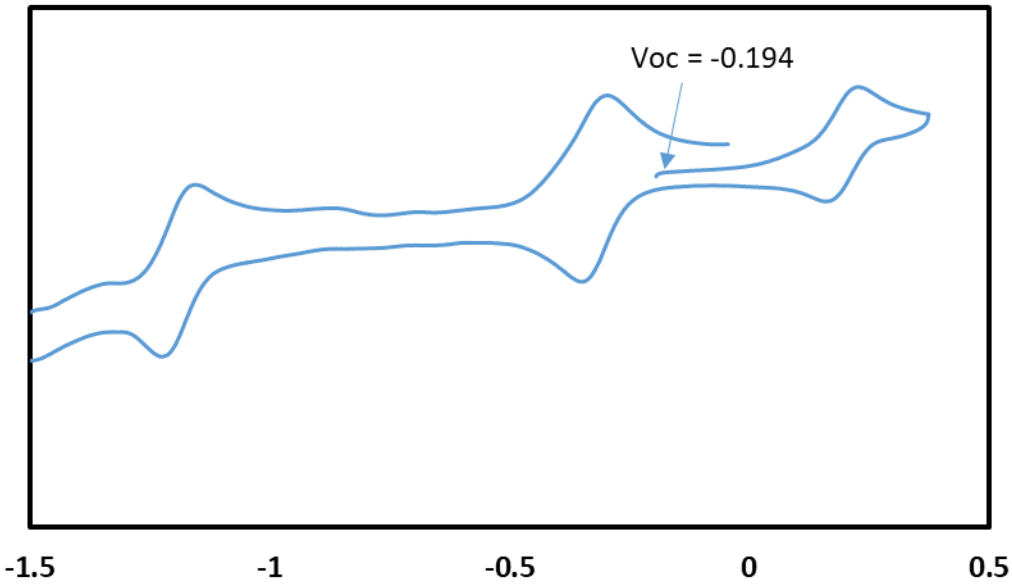

Appendix F-3 Cyclic voltammogram of 1 mM **H4.12**$^{2+}$, 0.1 M NBu_4BF_4, MeCN.

Appendix F-4 Table of oxidation potentials used for the construction of potential-pK_a diagram for **4.11**.

Base	$pK_{a,THF}$	E_{ox} (V)	$E_{1/2}$ (V)
None	None	+0.106; +0.463	+0.058; +0.401
4-$BrPhNH_2$	6.2	+0.428	+0.349
Pyridine	7.8	+0.117	+0.024
2,6-Me_2Pyridine	9.5	+0.091	+0.012
4-(Me_2N)Pyridine	13.6	-0.027	-0.065
Pyrrolidine	16	-0.068	-0.047
Tetramethylguanidine	17.8	-0.152	N/A
1,8-diazabicyclo [5.4.0]undec-7-ene	19.1	-0.201	-0.149

Appendix F-5 Table of values used for the construction of potential-pK_a diagram for **H4.12**$^+$.

Base	$pK_{a,MeCN}$	$E_{1/2}$ (V)
None	-	-0.322; +0.192*
Pyridine	12.53	-0.315; +0.191*
2,6-Me_2Pyridine	14.43	-0.321; +0.071*
2,4,6-Me_3Pyridine	14.98	-0.313; +0.055*
2-aminobenzimidazole	16.08	-0.317*; obscured
Benzylamine	16.91	-0.321
4-(Me_2N)Pyridine	17.95	-0.322
NEt_3	18.82	-0.356
Pyrrolidine	19.56	-0.376
2,4,6-Br_3-phenolate	20.35	-0.324
Benzoate	21.51	-0.318
tetramethylguanidine	23.30	-0.453
1,8-diazabicyclo [5.4.0]undec-7-ene	24.34	-0.458
7-Methyl-1,5,7-Triaza bicyclo[4.4.0]dec-5-ene	25.49	-0.465

*from square wave voltammetry

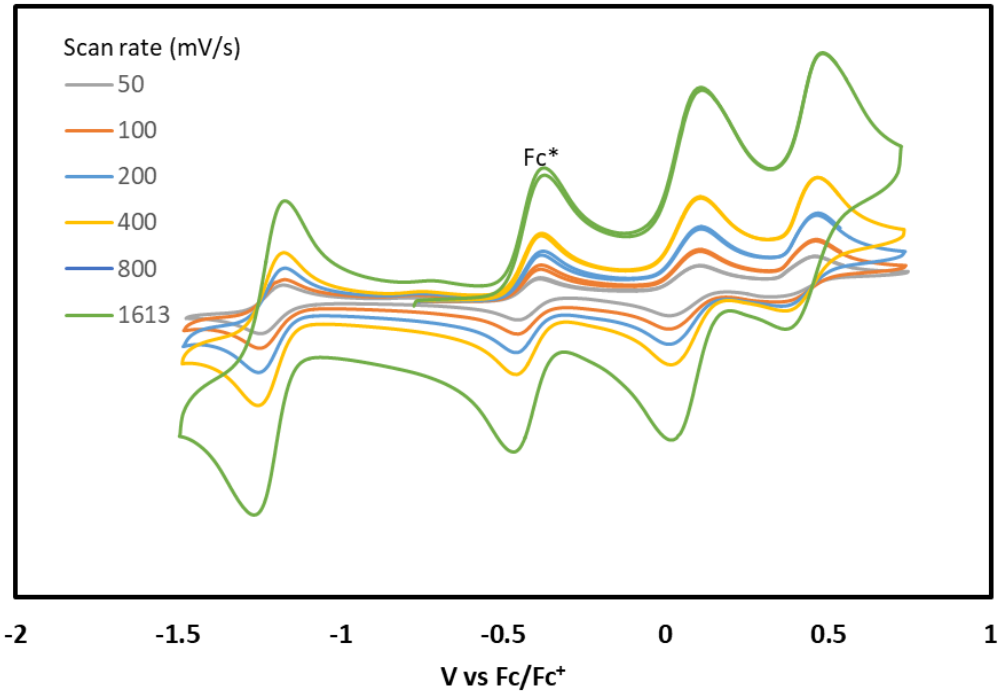

Appendix F-6 Cyclic voltammogram of 1 mM **H4.11** in 0.1 M NBu_4PF_6 in tetrahydrofuran with decamethylferrocene as internal standard at scan rates of 50 to 1613 mV/s.

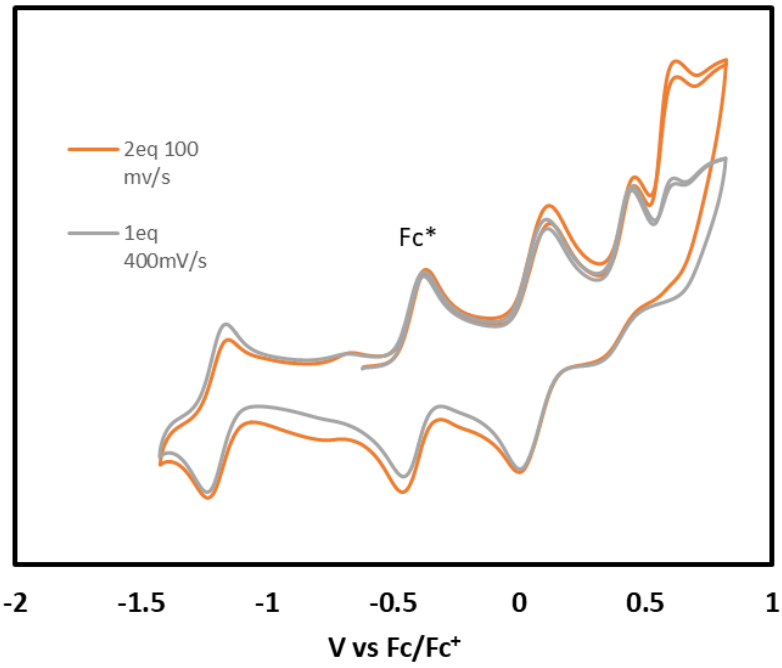

Appendix F-7 Cyclic voltammogram of 1 mM **H4.11** in 0.1 M NBu_4PF_6 in tetrahydrofuran with 1 and 2 mM 4-$BrPhNH_2$ 100 mV/s.

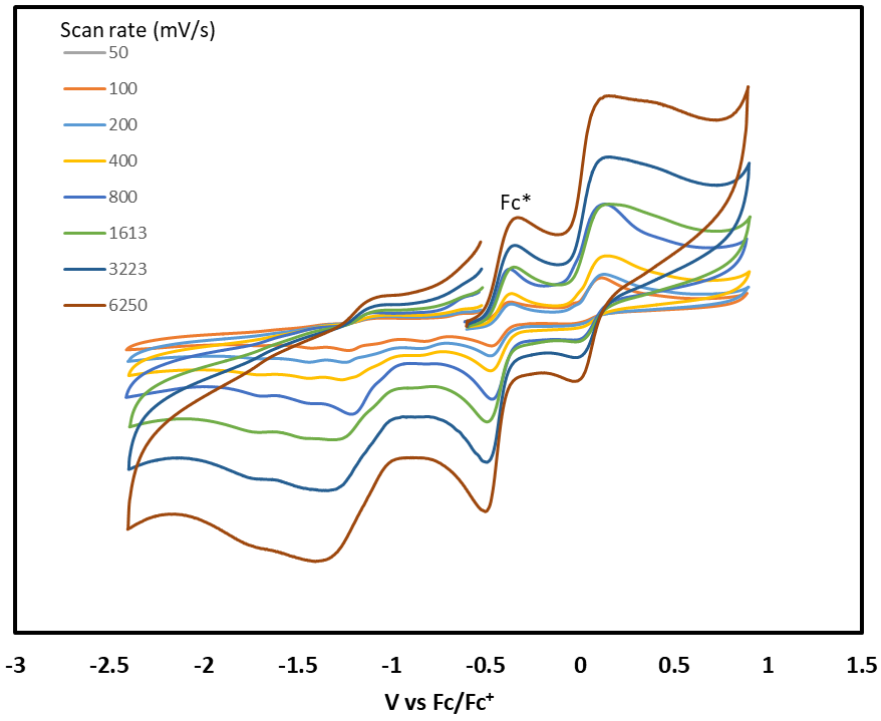

Appendix F-8 Cyclic voltammogram of 1 mM **H4.11** in 0.1 M NBu_4PF_6 in tetrahydrofuran with 15/15 mM pyridine/pyridinium methane sulfonate at scan rates of 50 to 6250 mV/s.

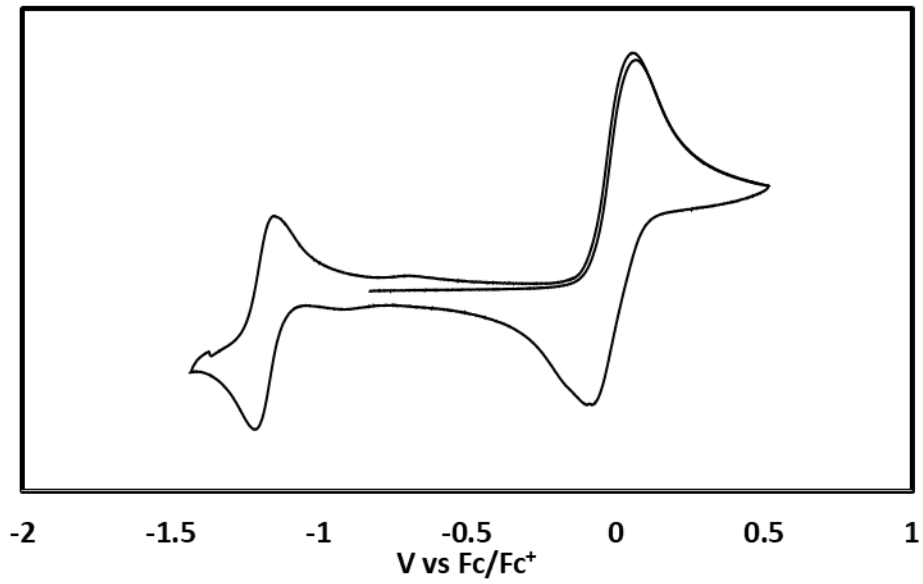

Appendix F-9 Cyclic voltammogram of 1 mM **H4.11** in 0.1 M NBu_4PF_6 in tetrahydrofuran with 1 mM 2,6-Me_2pyridine 100 mV/s.

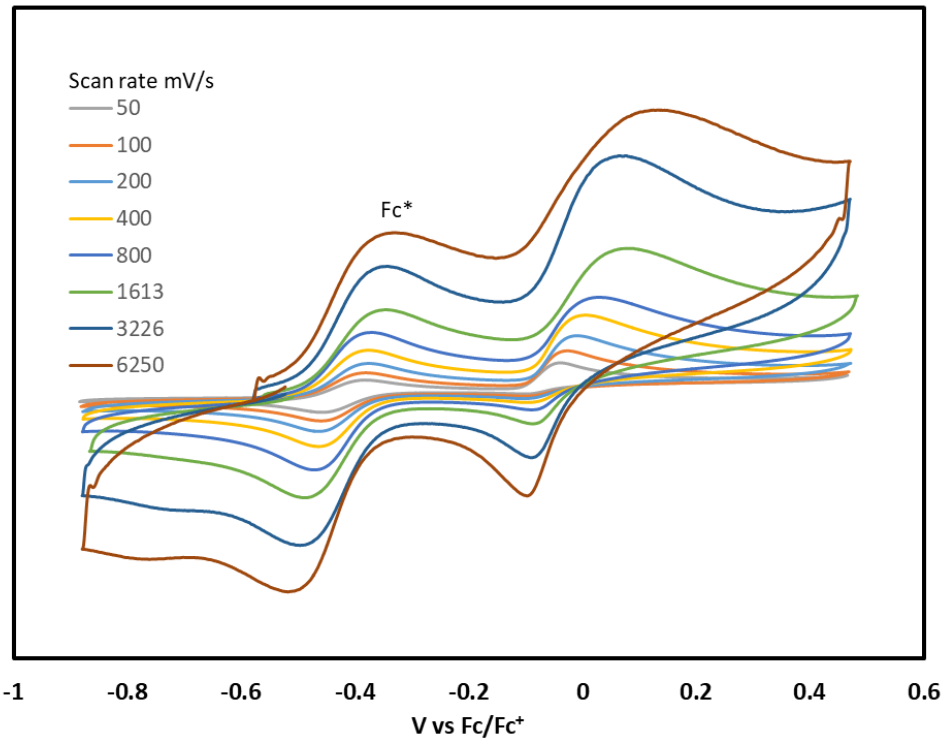

Appendix F-10 Cyclic voltammogram of 1 mM **H4.11** in 0.1 M NBu_4PF_6 in tetrahydrofuran with 15/15 mM 4-dimethylaminopyridine/4-dimethylaminopyridinium methane sulfonate at scan rates of 50 to 6250 mV/s.

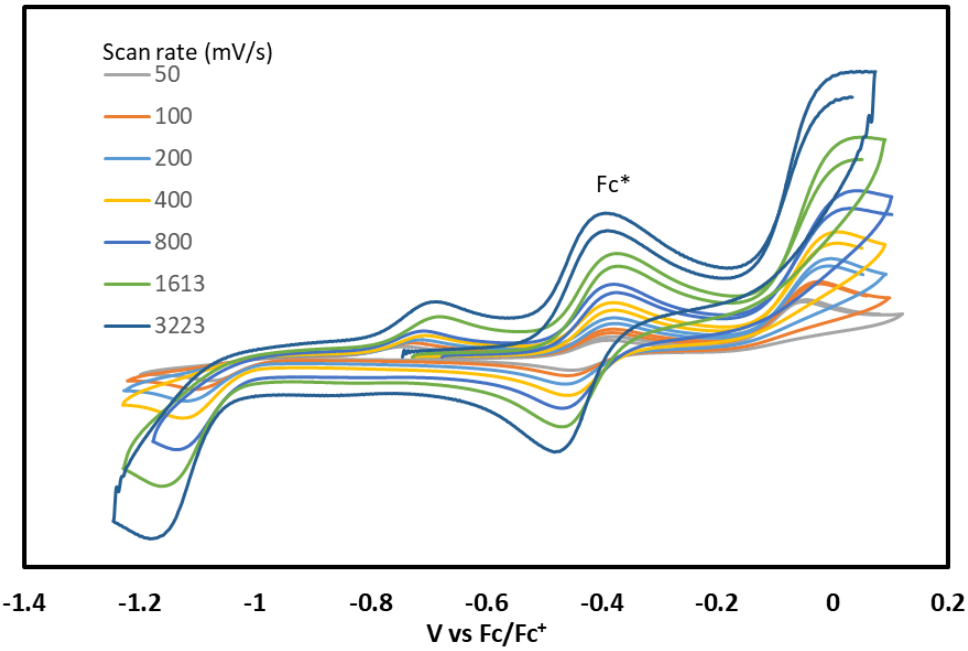

Appendix F-11 Cyclic voltammogram of 1 mM **H4.11** in 0.1 M NBu_4PF_6 in tetrahydrofuran with 15/15 mM pyrrolidine /pyrrolidinium methane sulfonate at scan rates of 50 to 6250 mV/s.

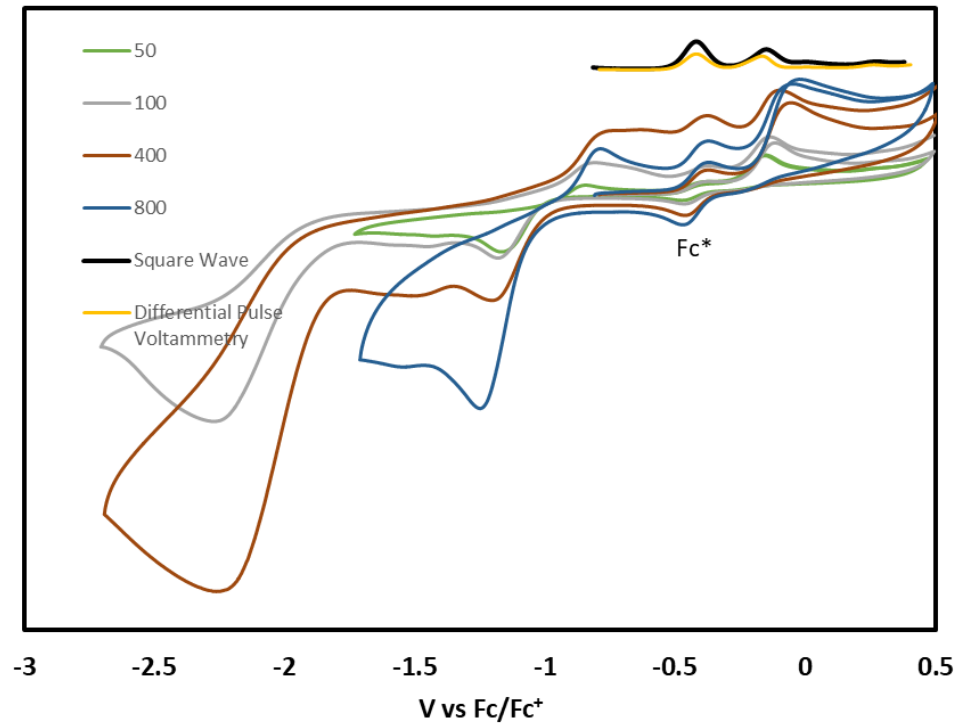

Appendix F-12 Cyclic voltammogram of 1 mM **H4.11** in 0.1 M NBu_4PF_6 in tetrahydrofuran with 15/15 mM tetramethylguanidine / tetramethylguanidinium methane sulfonate at scan rates of 50 to 6250 mV/s.

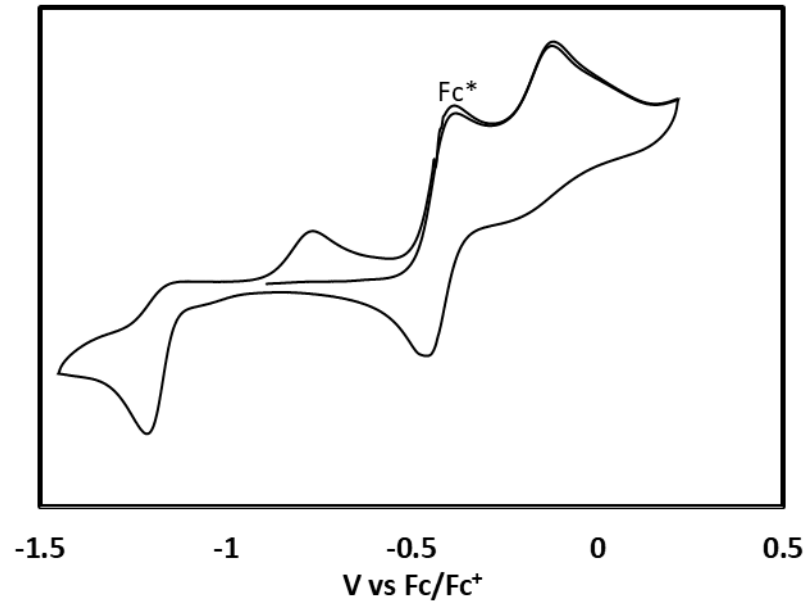

Appendix F-13 Cyclic voltammogram of 1 mM **H4.11** in 0.1 M NBu_4PF_6 in tetrahydrofuran with 2 mM 1,8-diazabicyclo [5.4.0]undec-7-ene at 100 mV/s.

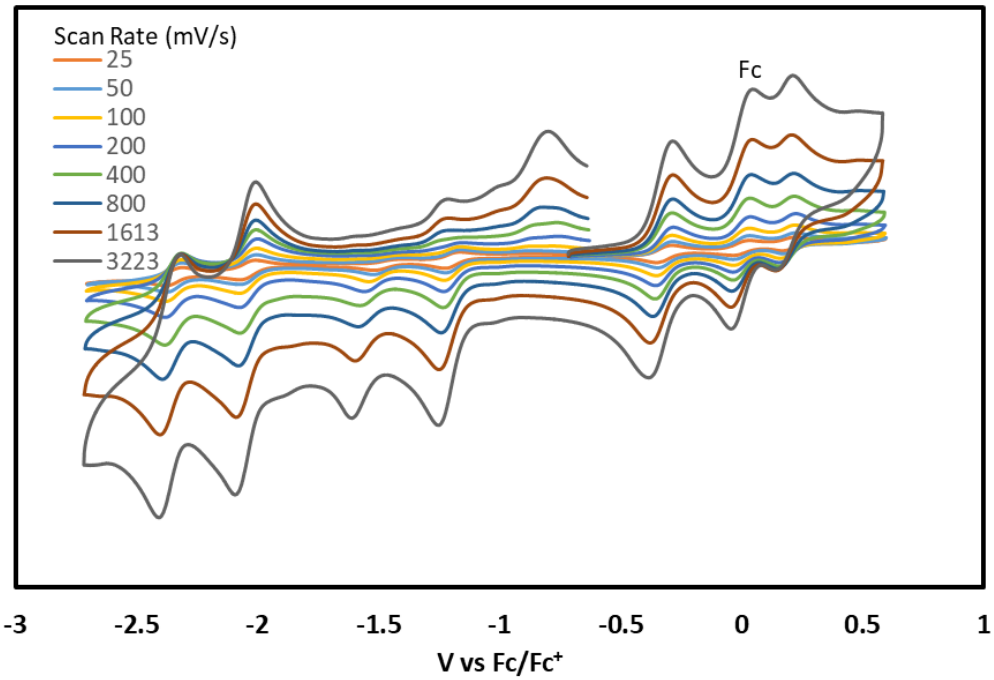

Appendix F-14 Cyclic voltammogram of 1 mM **H4.12**$^+$ in 0.1 M NBu_4PF_6 in MeCN at scan rates of 25 to 3226 mV/s.

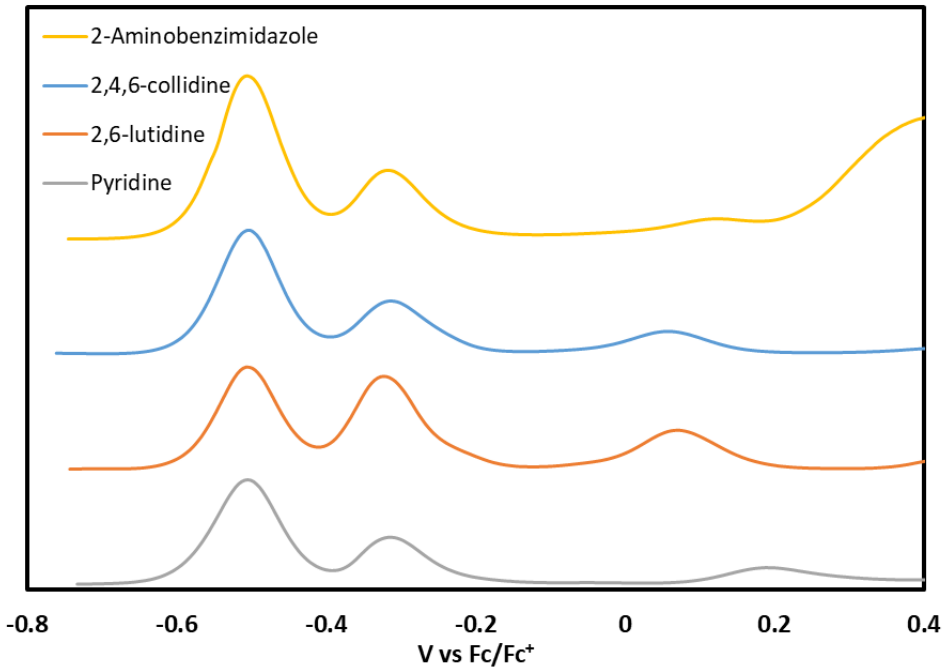

Appendix F-15 Square wave voltammetry of 1 mM **H4.12**$^{+}$ in 0.1 M NBu_4PF_6 in MeCN with 15/15 mM base / conjugate base methane sulfonate.

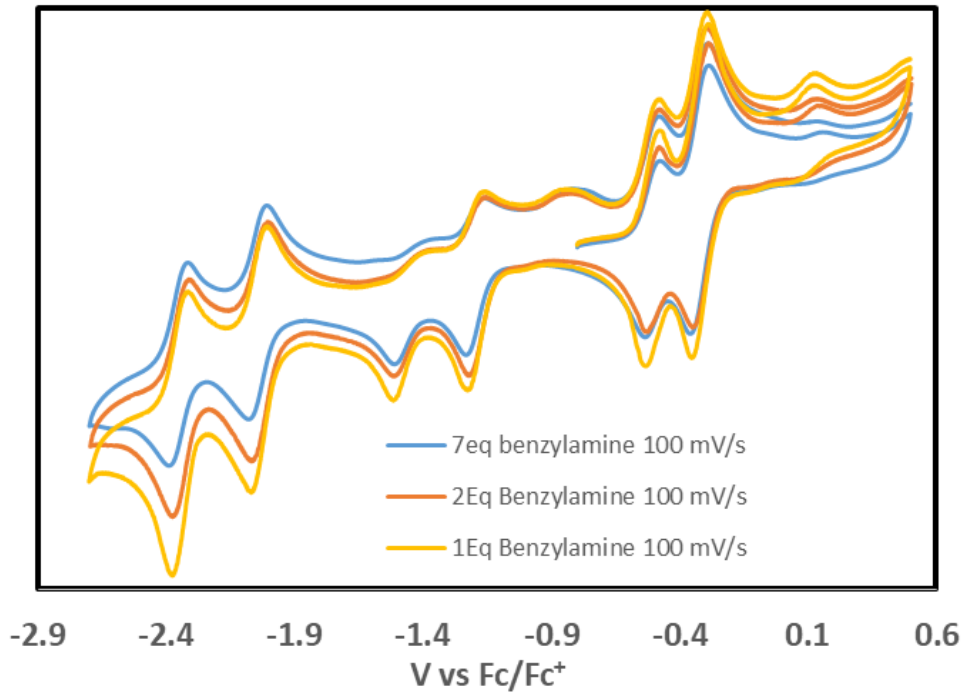

Appendix F-16 Cyclic voltammogram of 1 mM **H4.11** in 0.1 M NBu_4PF_6 in MeCN with various molar equivalents of benzylamine at 100 mV/s.

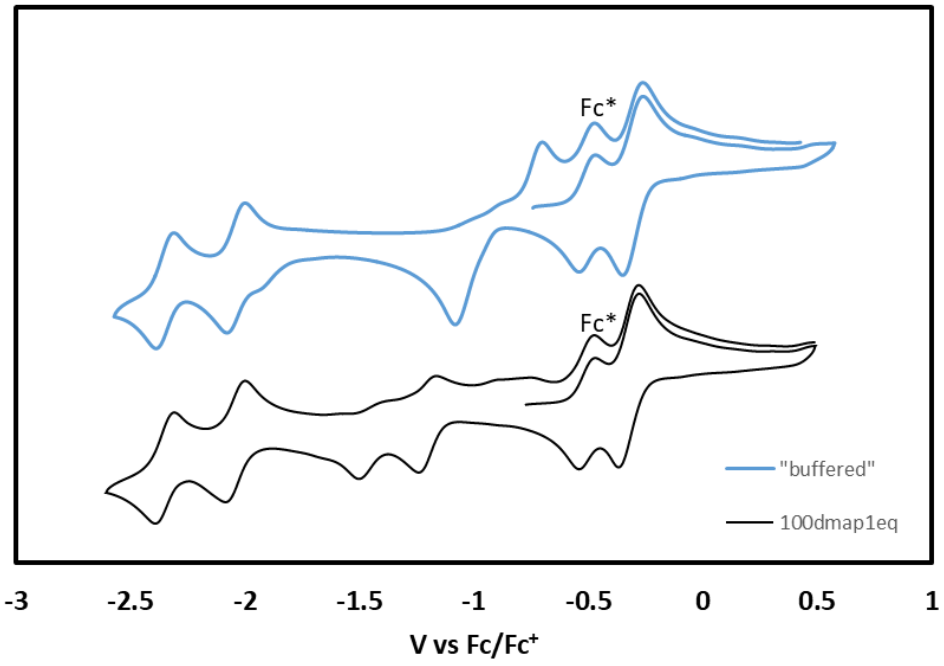

Appendix F-17 Cyclic voltammogram of 1 mM **H4.12**$^{+}$ in 0.1 M NBu_4PF_6 in MeCN with 1 mM p-dimethylaminopyridine and 15/15 mM p-dimethylaminopyridine / p-dimethylaminopyridinium methane sulfonate "buffer" at 100 mV/s.

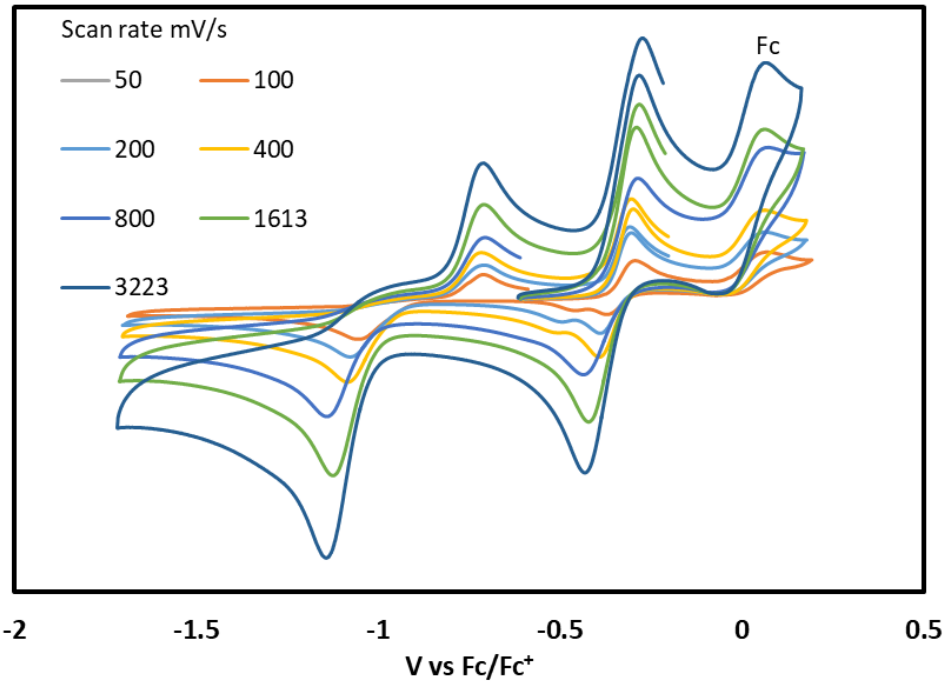

Appendix F-18 Cyclic voltammogram of 1 mM **H4.12**$^{+}$ in 0.1 M NBu_4PF_6 in MeCN with 15/15 mM pyrrolidine / pyrrolidinium methane sulfonate "buffer" at scan rates of 50 to 3223 mV/s s.

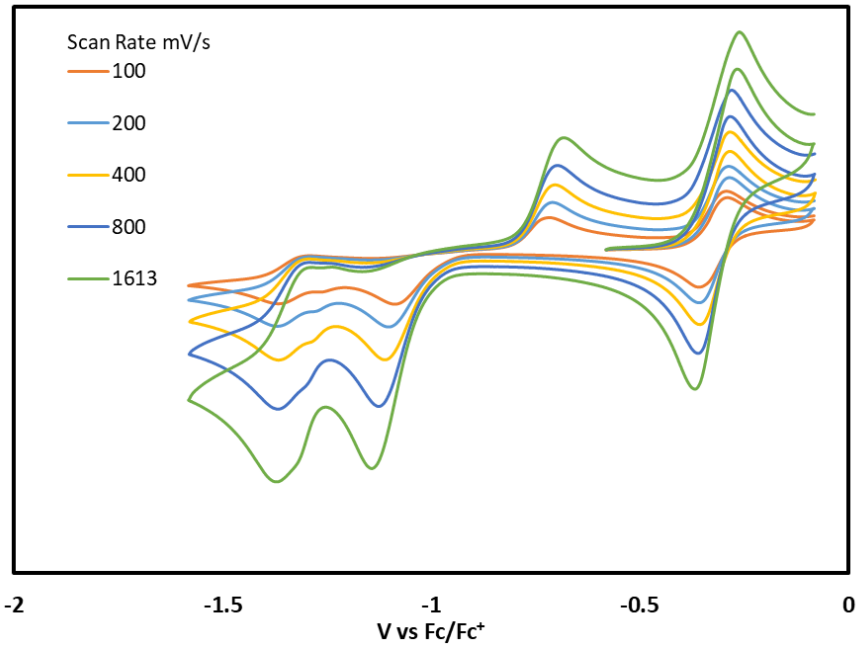

Appendix F-19 Cyclic voltammogram of 1 mM **H4.12**$^+$ in 0.1 M NBu_4PF_6 in MeCN with 15/15 mM 2,4,6-Br_3phenol / 1,8-diazabicyclo [5.4.0]undec-7-enium 2,4,6-Br_3phenolate "buffer" at scan rates of 100 to 1613 mV/s.

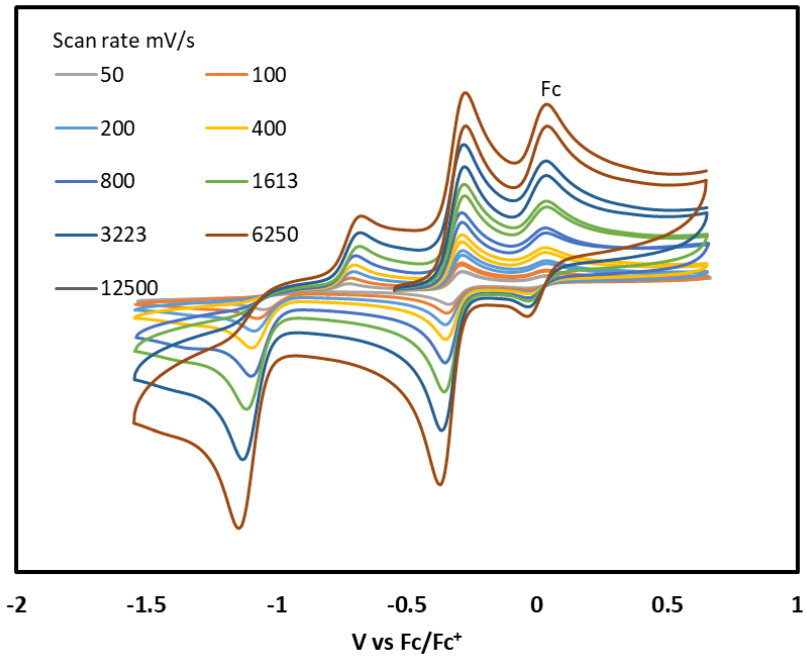

Appendix F-20 Cyclic voltammogram of 1 mM **H4.12**$^+$ in 0.1 M NBu_4PF_6 in MeCN with 15/15 mM Benzoic acid / 1,8-diazabicyclo [5.4.0]undec-7-enium benzoate "buffer" at scan rates of 50 to 12500 mV/s.

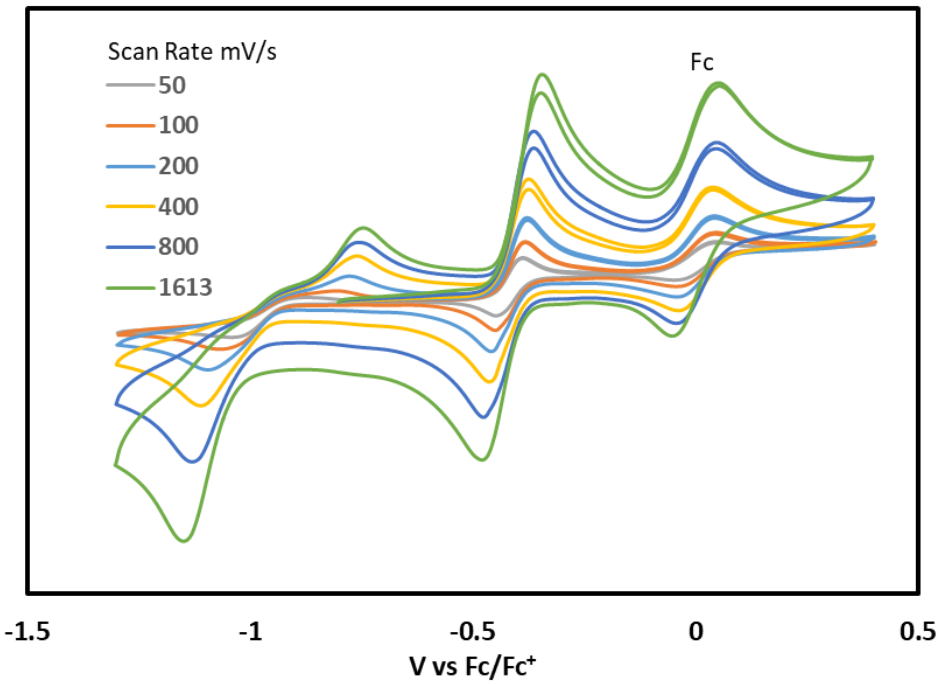

Appendix F-21 Cyclic voltammogram of 1 mM **H4.12**$^{+}$ in 0.1 M NBu_4PF_6 in MeCN with 15/15 mM tetramethylguanidine / tetramethylguanidinium "buffer" at scan rates of 50 to 1613 mV/s.

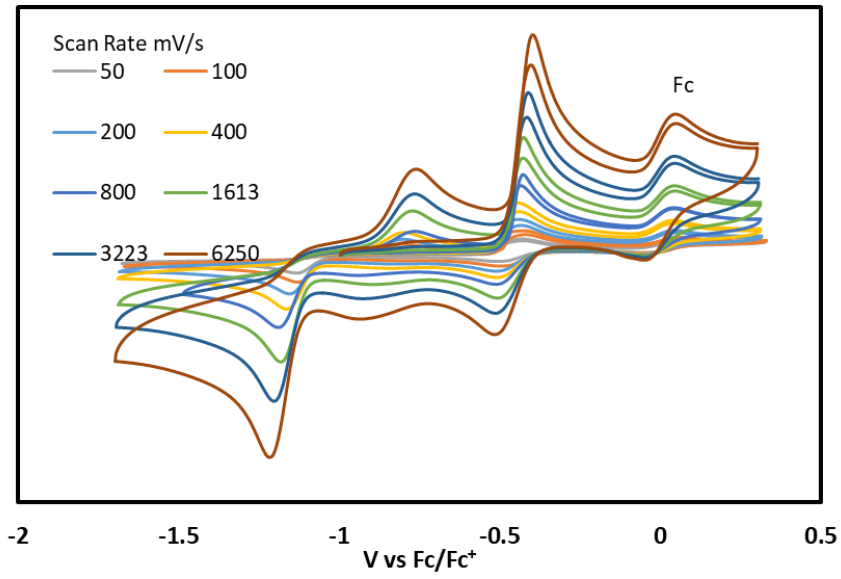

Appendix F-22 Cyclic voltammogram of 1 mM **H4.12**$^{+}$ in 0.1 M NBu_4PF_6 in MeCN with 15/15 mM 1,8-diazabicyclo [5.4.0]undec-7-ene / 1,8-diazabicyclo [5.4.0]undec-7-enium methane sulfonate "buffer" at scan rates of 50 to 6250 mV/s.

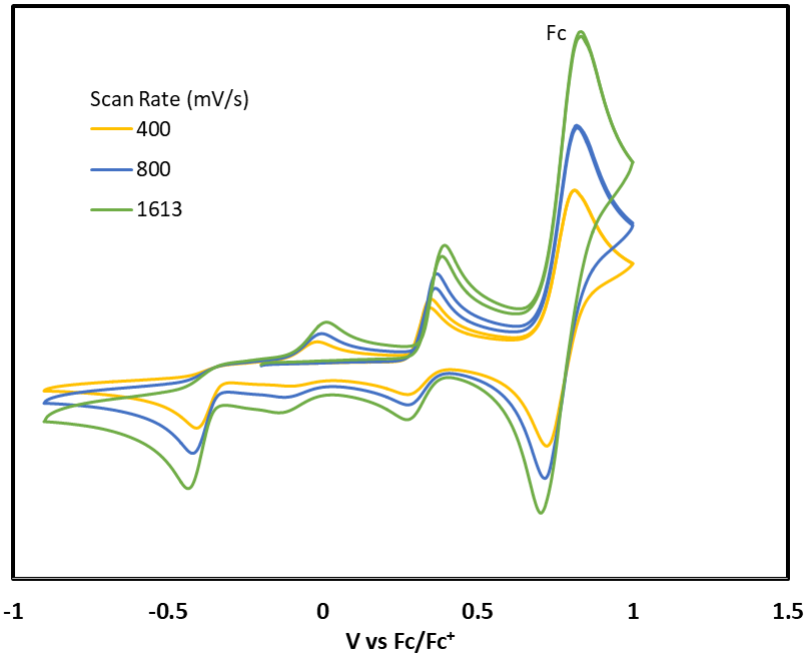

Appendix F-23 Cyclic voltammogram of 1 mM **H4.12**$^{+}$ in 0.1 M NBu_4PF_6 in MeCN with 15/15 mM 7-Methyl-1,5,7-Triaza bicyclo[4.4.0]dec-5-ene / 7-Methyl-1,5,7-Triaza bicyclo[4.4.0]dec-5-enium methane sulfonate "buffer" at scan rates of 400 to 1613 mV/s.

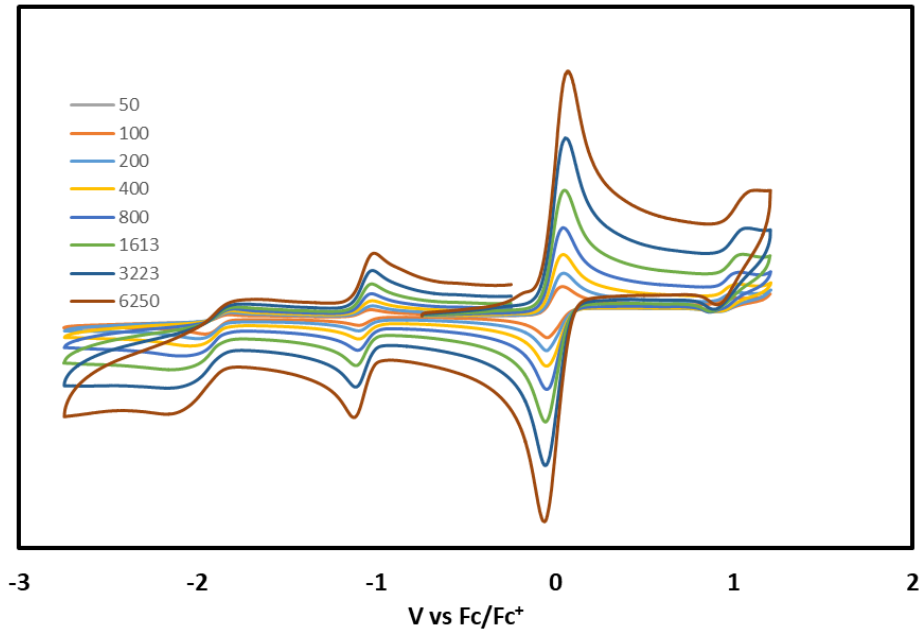

Appendix F-24 Cyclic voltammogram of 1 mM **H5.4** in 0.1 M NBu_4PF_6 in acetonitrile at scan rates of 50 to 6250 mV/s.

Appendix G. Crystallography

Appendix G-1 Table of crystallographic parameters for **2.2b**, **2.4a**, and **2.4b·0.5 MeCN**.

Crystal	**2.2b**	**2.4a**	**2.4b·0.5 MeCN**
Empirical formula	$C_{44}H_{41}BF_2N_4O_2Pd$	$C_{35}H_{30}N_4O_2Pd$	$C_{304}H_{284}N_{36}O_{16}Pd_8$
Formula weight	813.02	645.03	5548.85
Temperature/K	90	90	90
Crystal system	monoclinic	monoclinic	monoclinic
Space group	$P2_1/c$	$P2_1/n$	C2/c
a/Å	11.8862(6)	13.8893(6)	23.3242(19)
b/Å	27.3264(12)	24.7608(11)	14.2799(11)
c/Å	12.7997(6)	17.7292(8)	22.0138(18)
α/°	90	90	90
β/°	116.4920(10)	109.713(3)	117.678(2)
γ/°	90	90	90
Volume/Å^3	3720.9(3)	5739.9(5)	6493.1(9)
Z	4	8	1
ρ_{calc}g/cm^3	1.451	1.493	1.419
μ/mm^{-1}	0.553	0.686	0.613
F(000)	1672.0	2640.0	2856.0
Crystal size/mm^3	0.34 × 0.15 × 0.15	0.66 × 0.14 × 0.08	0.31 × 0.27 × 0.24
Radiation	MoKα (λ = 0.71073)	MoKα (λ = 0.71073)	MoKα (λ = 0.71073)
2Θ range for data collection/°	2.98 to 60.196	2.942 to 55.876	3.468 to 61.106
Index ranges	-16 ≤ h ≤ 16, -38 ≤ k ≤ 38, -18 ≤ l ≤ 18	-18 ≤ h ≤ 18, -32 ≤ k ≤ 32, -23 ≤ l ≤ 23	-33 ≤ h ≤ 33, -19 ≤ k ≤ 20, -31 ≤ l ≤ 31
Reflections collected	74025	84489	74782

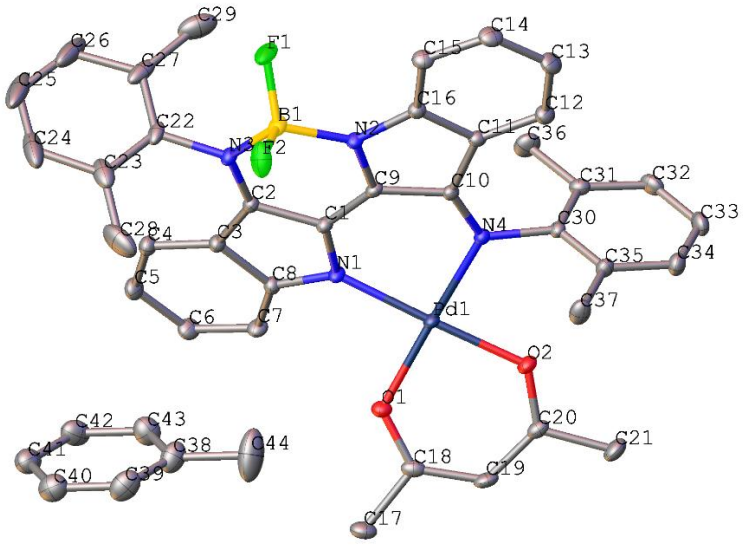

Appendix G-2 X-ray structure of **2.3b**. Hydrogen atoms are omitted for clarity. Thermal ellipsoids are shown at the 50% probability.

Appendix G-3 Table of bond lengths (Å) for **2.3b**.

Pd1	O1	1.9950(13)	C12	C13	1.390(3)
Pd1	O2	1.9929(13)	C13	C14	1.401(3)
Pd1	N1	1.9963(14)	C14	C15	1.388(3)
Pd1	N4	2.0508(14)	C15	C16	1.394(2)
F1	B1	1.385(2)	C17	C18	1.506(3)
F2	B1	1.390(2)	C18	C19	1.390(3)
O1	C18	1.284(2)	C19	C20	1.398(3)
O2	C20	1.277(2)	C20	C21	1.504(3)
N1	C1	1.360(2)	C22	C23	1.390(3)
N1	C8	1.388(2)	C22	C27	1.406(3)
N2	C9	1.366(2)	C23	C24	1.410(4)
N2	C16	1.398(2)	C23	C28	1.492(4)
N2	B1	1.536(2)	C24	C25	1.370(5)
N3	C2	1.330(2)	C25	C26	1.361(5)
N3	C22	1.444(2)	C26	C27	1.393(3)
N3	B1	1.573(2)	C27	C29	1.498(4)
N4	C10	1.310(2)	C30	C31	1.399(2)
N4	C30	1.444(2)	C30	C35	1.397(2)
C1	C2	1.442(2)	C31	C32	1.396(3)
C1	C9	1.371(2)	C31	C36	1.508(3)
C2	C3	1.437(2)	C32	C33	1.385(3)
C3	C4	1.407(2)	C33	C34	1.385(3)
C3	C8	1.432(2)	C34	C35	1.398(3)
C4	C5	1.380(3)	C35	C37	1.503(3)
C5	C6	1.410(3)	C38	C39	1.392(4)
C6	C7	1.386(3)	C38	C43	1.392(3)
C7	C8	1.403(2)	C38	C44	1.502(4)
C9	C10	1.453(2)	C39	C40	1.387(4)
C10	C11	1.462(2)	C40	C41	1.383(3)
C11	C12	1.396(2)	C41	C42	1.385(3)
C11	C16	1.415(2)	C42	C43	1.383(3)

Appendix G-4 Table of bond angles (°) for **2.3b**.

O1	Pd1	N1	87.79(6)	N2	C16	C11	111.00(14)
O1	Pd1	N4	171.25(6)	C15	C16	N2	127.37(16)
O2	Pd1	O1	93.05(5)	C15	C16	C11	121.63(16)
O2	Pd1	N1	177.39(6)	O1	C18	C17	113.77(17)
O2	Pd1	N4	86.80(5)	O1	C18	C19	126.65(17)
N1	Pd1	N4	92.74(6)	C19	C18	C17	119.58(16)
C18	O1	Pd1	123.46(12)	C18	C19	C20	125.73(17)

C20	O2	Pd1	124.51(12)	O2	C20	C19	126.02(17)
C1	N1	Pd1	120.15(11)	O2	C20	C21	114.15(17)
C1	N1	C8	105.81(14)	C19	C20	C21	119.81(16)
C8	N1	Pd1	133.75(11)	C23	C22	N3	119.12(19)
C9	N2	C16	107.14(14)	C23	C22	C27	122.8(2)
C9	N2	B1	123.56(14)	C27	C22	N3	118.06(19)
C16	N2	B1	129.26(14)	C22	C23	C24	116.1(3)
C2	N3	C22	117.75(15)	C22	C23	C28	122.1(2)
C2	N3	B1	123.07(14)	C24	C23	C28	121.7(2)
C22	N3	B1	119.16(14)	C25	C24	C23	121.6(3)
C10	N4	Pd1	123.52(12)	C26	C25	C24	121.1(2)
C10	N4	C30	118.54(14)	C25	C26	C27	120.4(3)
C30	N4	Pd1	117.74(10)	C22	C27	C29	123.28(19)
N1	C1	C2	112.04(14)	C26	C27	C22	118.0(3)
N1	C1	C9	126.97(15)	C26	C27	C29	118.8(2)
C9	C1	C2	120.60(15)	C31	C30	N4	117.62(15)
N3	C2	C1	120.64(15)	C35	C30	N4	119.84(15)
N3	C2	C3	134.11(16)	C35	C30	C31	122.43(16)
C3	C2	C1	105.19(14)	C30	C31	C36	120.96(17)
C4	C3	C2	134.29(16)	C32	C31	C30	117.73(17)
C4	C3	C8	120.40(16)	C32	C31	C36	121.31(17)
C8	C3	C2	105.28(14)	C33	C32	C31	120.98(18)
C5	C4	C3	118.64(17)	C32	C33	C34	120.18(17)
C4	C5	C6	120.74(17)	C33	C34	C35	120.86(18)
C7	C6	C5	121.93(17)	C30	C35	C34	117.78(17)
C6	C7	C8	118.13(16)	C30	C35	C37	121.64(16)
N1	C8	C3	111.61(15)	C34	C35	C37	120.59(16)
N1	C8	C7	128.17(16)	F1	B1	F2	108.79(15)
C7	C8	C3	120.14(16)	F1	B1	N2	110.28(16)
N2	C9	C1	121.08(15)	F1	B1	N3	109.73(15)
N2	C9	C10	111.03(14)	F2	B1	N2	110.94(15)
C1	C9	C10	127.57(15)	F2	B1	N3	109.61(16)
N4	C10	C9	122.16(15)	N2	B1	N3	107.47(14)
N4	C10	C11	133.15(16)	C39	C38	C44	121.1(2)
C9	C10	C11	104.69(14)	C43	C38	C39	118.4(2)
C12	C11	C10	134.06(16)	C43	C38	C44	120.4(2)
C12	C11	C16	119.82(16)	C40	C39	C38	120.6(2)
C16	C11	C10	106.08(14)	C41	C40	C39	120.3(2)
C13	C12	C11	118.61(17)	C40	C41	C42	119.5(2)
C12	C13	C14	120.83(17)	C43	C42	C41	120.3(2)
C15	C14	C13	121.62(17)	C42	C43	C38	120.9(2)
C14	C15	C16	117.47(17)				

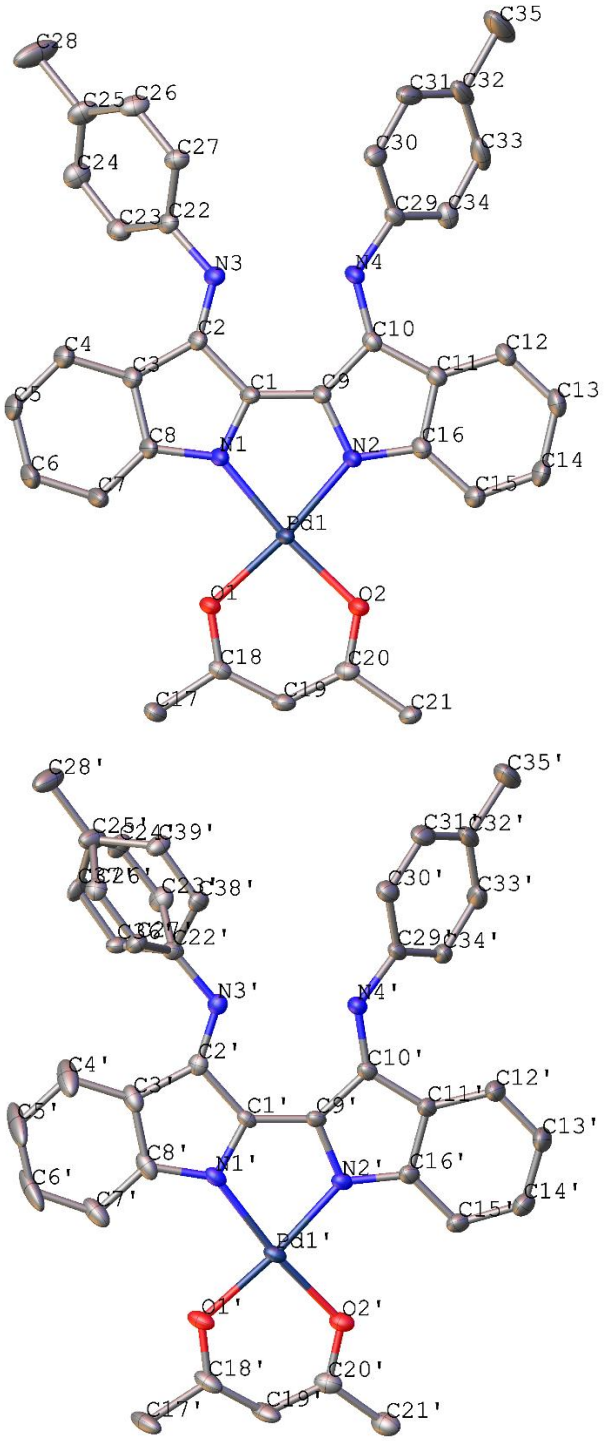

Appendix G-5 X-ray structure of **2.5a** (top) and **2.5a'** (bottom). Hydrogen atoms are omitted for clarity. Thermal ellipsoids are shown at the 50% probability.

Appendix G-6 Table of bond lengths (**Å**) for **2.5a**.

Pd1'	O1'	1.9965(19)	C33'	C34'	1.388(4)
Pd1'	O2'	1.987(2)	C36'	C37'	1.393(7)
Pd1'	N1'	2.007(2)	C38'	C39'	1.398(7)
Pd1'	N2'	1.992(2)	Pd1	O1	1.9972(18)
O1'	C18'	1.278(4)	Pd1	O2	1.9894(19)
O2'	C20'	1.283(3)	Pd1	N1	2.002(2)
N1'	C1'	1.332(3)	Pd1	N2	2.005(2)
N1'	C8'	1.407(4)	O1	C18	1.280(3)
N2'	C9'	1.395(3)	O2	C20	1.275(3)
N2'	C16'	1.361(3)	N1	C1	1.350(3)
N3'	C2'	1.289(3)	N1	C8	1.396(3)
N3'	C22'	1.416(3)	N2	C9	1.382(3)
N4'	C10'	1.364(4)	N2	C16	1.366(3)
N4'	C29'	1.407(3)	N3	C2	1.301(3)
C1'	C2'	1.491(4)	N3	C22	1.412(3)
C1'	C9'	1.403(4)	N4	C10	1.350(4)
C2'	C3'	1.476(4)	N4	C29	1.409(3)
C3'	C4'	1.386(4)	C1	C2	1.474(4)
C3'	C8'	1.410(4)	C1	C9	1.396(4)
C4'	C5'	1.391(5)	C2	C3	1.467(4)
C5'	C6'	1.380(6)	C3	C4	1.391(4)
C6'	C7'	1.381(5)	C3	C8	1.415(4)
C7'	C8'	1.386(4)	C4	C5	1.390(4)
C9'	C10'	1.417(4)	C5	C6	1.387(5)
C10'	C11'	1.421(4)	C6	C7	1.380(4)
C11'	C12'	1.414(4)	C7	C8	1.387(4)
C11'	C16'	1.428(4)	C9	C10	1.428(4)
C12'	C13'	1.373(4)	C10	C11	1.425(4)
C13'	C14'	1.407(5)	C11	C12	1.415(4)
C14'	C15'	1.374(4)	C11	C16	1.433(4)
C15'	C16'	1.402(4)	C12	C13	1.370(4)
C17'	C18'	1.513(4)	C13	C14	1.405(4)
C18'	C19'	1.383(4)	C14	C15	1.372(4)
C19'	C20'	1.392(4)	C15	C16	1.413(4)
C20'	C21'	1.491(4)	C17	C18	1.508(4)
C22'	C23'	1.395(6)	C18	C19	1.392(4)
C22'	C27'	1.463(6)	C19	C20	1.391(4)
C22'	C36'	1.350(6)	C20	C21	1.502(4)
C22'	C38'	1.358(6)	C22	C23	1.394(4)
C23'	C24'	1.389(8)	C22	C27	1.391(4)
C24'	C25'	1.245(7)	C23	C24	1.383(4)

C25'	C26'	1.455(6)	C24	C25	1.391(4)
C25'	C28'	1.509(4)	C25	C26	1.387(4)
C25'	C37'	1.438(7)	C25	C28	1.508(4)
C25'	C39'	1.438(6)	C26	C27	1.382(4)
C26'	C27'	1.381(8)	C29	C30	1.391(4)
C29'	C30'	1.383(4)	C29	C34	1.388(4)
C29'	C34'	1.400(4)	C30	C31	1.387(4)
C30'	C31'	1.393(4)	C31	C32	1.378(5)
C31'	C32'	1.383(5)	C32	C33	1.382(5)
C32'	C33'	1.388(5)	C32	C35	1.512(5)
C32'	C35'	1.513(4)	C33	C34	1.388(4)

Appendix G-7 Table of bond angles for **2.5a**.

O1'	Pd1'	N1'	93.59(8)	C33'	C34'	C29'	120.1(3)
O2'	Pd1'	O1'	93.31(8)	C22'	C36'	C37'	117.2(5)
O2'	Pd1'	N1'	172.63(8)	C36'	C37'	C25'	123.7(5)
O2'	Pd1'	N2'	93.06(9)	C22'	C38'	C39'	116.9(5)
N2'	Pd1'	O1'	173.06(9)	C38'	C39'	C25'	123.7(5)
N2'	Pd1'	N1'	80.18(9)	O1	Pd1	N1	93.15(8)
C18'	O1'	Pd1'	123.6(2)	O1	Pd1	N2	173.31(9)
C20'	O2'	Pd1'	124.11(19)	O2	Pd1	O1	93.30(8)
C1'	N1'	Pd1'	114.59(18)	O2	Pd1	N1	173.54(8)
C1'	N1'	C8'	108.8(2)	O2	Pd1	N2	93.14(8)
C8'	N1'	Pd1'	136.37(19)	N1	Pd1	N2	80.43(9)
C9'	N2'	Pd1'	114.27(17)	C18	O1	Pd1	124.04(18)
C16'	N2'	Pd1'	138.43(19)	C20	O2	Pd1	123.78(18)
C16'	N2'	C9'	107.0(2)	C1	N1	Pd1	114.30(18)
C2'	N3'	C22'	122.7(2)	C1	N1	C8	108.7(2)
C10'	N4'	C29'	127.9(3)	C8	N1	Pd1	136.95(19)
N1'	C1'	C2'	110.4(2)	C9	N2	Pd1	113.58(17)
N1'	C1'	C9'	117.1(2)	C16	N2	Pd1	139.27(19)
C9'	C1'	C2'	132.5(2)	C16	N2	C9	107.1(2)
N3'	C2'	C1'	121.1(2)	C2	N3	C22	123.8(2)
N3'	C2'	C3'	135.0(3)	C10	N4	C29	129.9(2)
C3'	C2'	C1'	103.9(2)	N1	C1	C2	110.3(2)
C4'	C3'	C2'	134.5(3)	N1	C1	C9	116.4(2)
C4'	C3'	C8'	119.4(3)	C9	C1	C2	133.3(2)
C8'	C3'	C2'	106.1(2)	N3	C2	C1	121.6(2)
C3'	C4'	C5'	118.8(4)	N3	C2	C3	134.2(3)
C6'	C5'	C4'	120.8(3)	C3	C2	C1	104.2(2)
C5'	C6'	C7'	121.8(3)	C4	C3	C2	133.8(3)

C6'	C7'	C8'	117.5(3)	C4	C3	C8	119.6(3)
N1'	C8'	C3'	110.7(2)	C8	C3	C2	106.5(2)
C7'	C8'	N1'	127.5(3)	C5	C4	C3	118.6(3)
C7'	C8'	C3'	121.7(3)	C6	C5	C4	121.0(3)
N2'	C9'	C1'	113.9(2)	C7	C6	C5	121.3(3)
N2'	C9'	C10'	110.6(2)	C6	C7	C8	118.1(3)
C1'	C9'	C10'	135.4(3)	N1	C8	C3	110.3(2)
N4'	C10'	C9'	124.4(3)	C7	C8	N1	128.4(3)
N4'	C10'	C11'	130.2(3)	C7	C8	C3	121.3(3)
C9'	C10'	C11'	105.3(2)	N2	C9	C1	115.2(2)
C10'	C11'	C16'	107.0(2)	N2	C9	C10	110.5(2)
C12'	C11'	C10'	133.7(3)	C1	C9	C10	134.3(3)
C12'	C11'	C16'	119.0(3)	N4	C10	C9	121.6(2)
C13'	C12'	C11'	119.1(3)	N4	C10	C11	132.6(3)
C12'	C13'	C14'	121.0(3)	C11	C10	C9	105.7(2)
C15'	C14'	C13'	121.7(3)	C10	C11	C16	106.2(2)
C14'	C15'	C16'	118.2(3)	C12	C11	C10	134.8(3)
N2'	C16'	C11'	110.0(2)	C12	C11	C16	119.0(3)
N2'	C16'	C15'	129.1(3)	C13	C12	C11	119.7(3)
C15'	C16'	C11'	120.9(3)	C12	C13	C14	120.5(3)
O1'	C18'	C17'	113.7(3)	C15	C14	C13	122.4(3)
O1'	C18'	C19'	126.5(3)	C14	C15	C16	117.9(3)
C19'	C18'	C17'	119.8(3)	N2	C16	C11	110.5(2)
C18'	C19'	C20'	126.5(3)	N2	C16	C15	129.1(3)
O2'	C20'	C19'	125.7(3)	C15	C16	C11	120.5(3)
O2'	C20'	C21'	114.6(3)	O1	C18	C17	114.4(2)
C19'	C20'	C21'	119.6(3)	O1	C18	C19	125.7(3)
N3'	C22'	C27'	121.0(3)	C19	C18	C17	119.8(2)
C23'	C22'	N3'	125.4(3)	C20	C19	C18	126.3(3)
C23'	C22'	C27'	113.4(4)	O2	C20	C19	126.6(3)
C36'	C22'	N3'	121.3(3)	O2	C20	C21	114.5(2)
C36'	C22'	C38'	124.4(4)	C19	C20	C21	118.9(2)
C38'	C22'	N3'	112.9(3)	C23	C22	N3	123.1(3)
C24'	C23'	C22'	123.7(5)	C27	C22	N3	118.1(3)
C25'	C24'	C23'	121.1(5)	C27	C22	C23	118.4(3)
C24'	C25'	C26'	122.8(4)	C24	C23	C22	120.8(3)
C24'	C25'	C28'	121.2(4)	C23	C24	C25	120.8(3)
C26'	C25'	C28'	115.8(4)	C24	C25	C28	120.8(3)
C37'	C25'	C28'	124.3(3)	C26	C25	C24	118.0(3)
C39'	C25'	C28'	123.1(3)	C26	C25	C28	121.1(3)
C39'	C25'	C37'	111.9(4)	C27	C26	C25	121.6(3)
C27'	C26'	C25'	116.5(5)	C26	C27	C22	120.2(3)

C26' C27' C22'	122.2(5)	C30 C29 N4	116.6(3)
C30' C29' N4'	118.4(3)	C34 C29 N4	123.5(3)
C30' C29' C34'	119.0(3)	C34 C29 C30	119.7(3)
C34' C29' N4'	122.4(3)	C31 C30 C29	119.7(3)
C29' C30' C31'	119.7(3)	C32 C31 C30	121.7(3)
C32' C31' C30'	122.2(3)	C31 C32 C33	117.6(3)
C31' C32' C33'	117.5(3)	C31 C32 C35	120.5(4)
C31' C32' C35'	122.0(3)	C33 C32 C35	121.9(4)
C33' C32' C35'	120.5(4)	C32 C33 C34	122.4(3)
C32' C33' C34'	121.4(3)	C29 C34 C33	118.9(3)

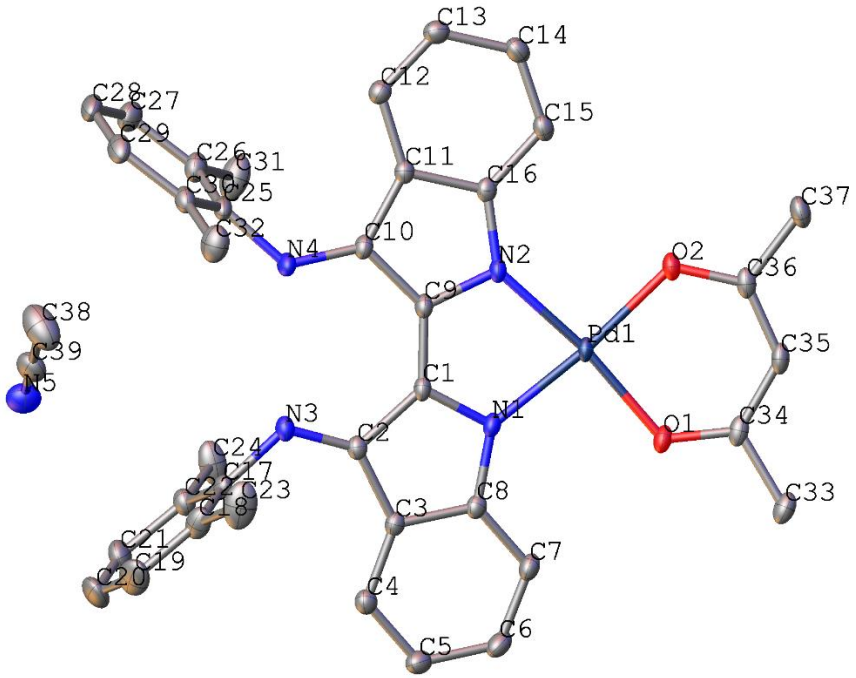

Appendix G-8 X-ray structure of **2.5b·1/2 MeCN**. Hydrogen atoms are omitted for clarity. Thermal ellipsoids are shown at the 50% probability.

Appendix G-9 Table of bond lengths (**Å**) for **2.5b·1/2 MeCN**.

Pd1 O2	2.0008(10)	C17 C18	1.398(2)
Pd1 O1	1.9934(10)	C36 C35	1.396(2)
Pd1 N2	2.0065(11)	C36 C37	1.507(2)
Pd1 N1	2.0113(12)	C34 C33	1.505(2)
O2 C36	1.2827(16)	C34 C35	1.398(2)
O1 C34	1.2786(16)	C8 C7	1.3952(19)
N2 C9	1.3851(16)	C7 C6	1.394(2)

N2	C16	1.3666(18)	C15	C14	1.379(2)
N1	C1	1.3563(16)	C15	C16	1.4078(19)
N1	C8	1.4007(18)	C25	C26	1.400(2)
N3	C2	1.2978(17)	C25	C30	1.400(2)
N3	C17	1.4251(17)	C5	C6	1.402(2)
N4	C10	1.3470(17)	C14	C13	1.421(2)
N4	C25	1.4287(18)	C28	C29	1.380(3)
N5	C39	1.141(4)	C28	C27	1.384(3)
C1	C9	1.3865(19)	C22	C21	1.391(2)
C1	C2	1.4783(18)	C22	C24	1.505(2)
C3	C2	1.4649(19)	C29	C30	1.397(2)
C3	C4	1.394(2)	C27	C26	1.400(2)
C3	C8	1.4189(18)	C39	C38	1.449(4)
C10	C9	1.4363(18)	C26	C31	1.503(2)
C10	C11	1.4304(19)	C30	C32	1.503(2)
C11	C12	1.4094(19)	C21	C20	1.375(3)
C11	C16	1.4348(18)	C18	C23	1.496(3)
C4	C5	1.388(2)	C18	C19	1.409(3)
C12	C13	1.378(2)	C20	C19	1.377(3)
C17	C22	1.400(2)			

Appendix G-10 Table of bond angles for **2.5b·1/2 MeCN**.

O2	Pd1	N2	93.32(4)	O2	C36	C37	114.26(14)
O2	Pd1	N1	172.89(4)	C35	C36	C37	119.04(13)
O1	Pd1	O2	93.67(4)	O1	C34	C33	114.34(14)
O1	Pd1	N2	172.44(4)	O1	C34	C35	126.16(14)
O1	Pd1	N1	92.12(4)	C35	C34	C33	119.50(13)
N2	Pd1	N1	80.71(5)	N1	C8	C3	110.78(11)
C36	O2	Pd1	123.26(10)	C7	C8	N1	128.39(12)
C34	O1	Pd1	123.96(10)	C7	C8	C3	120.82(13)
C9	N2	Pd1	113.13(9)	C6	C7	C8	117.46(13)
C16	N2	Pd1	140.04(9)	C14	C15	C16	117.99(13)
C16	N2	C9	106.83(11)	C26	C25	N4	120.12(13)
C1	N1	Pd1	113.20(9)	C30	C25	N4	117.97(13)
C1	N1	C8	107.96(11)	C30	C25	C26	121.77(13)
C8	N1	Pd1	138.77(9)	C4	C5	C6	120.40(14)
C2	N3	C17	120.34(12)	C15	C14	C13	121.93(13)
C10	N4	C25	125.91(12)	N2	C16	C11	110.88(12)
N1	C1	C9	117.09(12)	N2	C16	C15	128.73(12)
N1	C1	C2	110.60(12)	C15	C16	C11	120.38(13)
C9	C1	C2	132.27(12)	C7	C6	C5	122.07(14)

C4	C3	C2	132.92(12)	C29	C28	C27	120.06(15)
C4	C3	C8	120.67(13)	C17	C22	C24	120.56(14)
C8	C3	C2	106.41(12)	C21	C22	C17	118.73(15)
N4	C10	C9	123.82(13)	C21	C22	C24	120.71(15)
N4	C10	C11	130.84(13)	C28	C29	C30	121.15(15)
C11	C10	C9	105.32(11)	C36	C35	C34	126.10(13)
N2	C9	C1	115.52(12)	C28	C27	C26	120.92(16)
N2	C9	C10	110.79(12)	N5	C39	C38	180.0
C1	C9	C10	133.65(12)	C25	C26	C31	122.02(15)
N3	C2	C1	122.76(12)	C27	C26	C25	118.04(15)
N3	C2	C3	133.01(13)	C27	C26	C31	119.94(16)
C3	C2	C1	104.23(11)	C25	C30	C32	120.95(14)
C10	C11	C16	106.17(12)	C29	C30	C25	118.06(15)
C12	C11	C10	133.58(12)	C29	C30	C32	120.98(15)
C12	C11	C16	120.23(12)	C12	C13	C14	120.84(14)
C5	C4	C3	118.58(13)	C20	C21	C22	120.70(17)
C13	C12	C11	118.61(13)	C17	C18	C23	120.80(16)
C22	C17	N3	118.45(12)	C17	C18	C19	116.85(16)
C18	C17	N3	119.53(14)	C19	C18	C23	122.33(16)
C18	C17	C22	121.87(14)	C21	C20	C19	120.03(16)
O2	C36	C35	126.68(14)	C20	C19	C18	121.78(16)

Appendix G-11 Table of crystallographic parameters for **3.2-3.5**.

Structure	**3.2**	**3.3**	**3.4**	**3.5**
Empirical formula	$C_{232}H_{200}N_{24}O_{24}Pd_8$	$C_{29.5}H_{26}ClN_3O_3Pd$	$C_{29}H_{19}F_6N_3O_3Pd$	$C_{29}H_{19}N_3O_3F_6Pd$
Formula weight	4559.35	612.38	677.87	677.87
Temperature/K	90	90	90	90
Crystal system	monoclinic	monoclinic	monoclinic	triclinic
Space group	C2/c	$P2_1/c$	C2/c	P-1
a/Å	36.389(6)	15.399(2)	35.499(4)	7.0269(10)
b/Å	7.6084(14)	22.831(3)	7.8925(9)	17.185(2)
c/Å	18.489(3)	7.5024(10)	18.785(2)	23.413(3)
α/°	90	90	90	82.473(4)
β/°	101.998(3)	96.139(3)	101.829(2)	86.674(4)
γ/°	90	90	90	82.943(4)
Volume/$Å^3$	5007.1(15)	2622.6(6)	5151.2(10)	2779.1(7)
Z	1	4	8	4
$\rho_{calc}g/cm^3$	1.512	1.551	1.748	1.620
μ/mm^{-1}	0.777	0.846	0.803	0.744
Reflections collected	32686	9972	16567	12927
Independent reflections	7618	9972	6396	12927
Data/restraints/parameters	7618/0/329	9972/0/361	6396/0/385	12927/0/768
Goodness-of-fit on F^2	1.087	1.076	1.095	0.969
R_1	0.0362	0.1005	0.0516	0.0747
wR_2	0.0639	0.1950	0.0859	0.1228

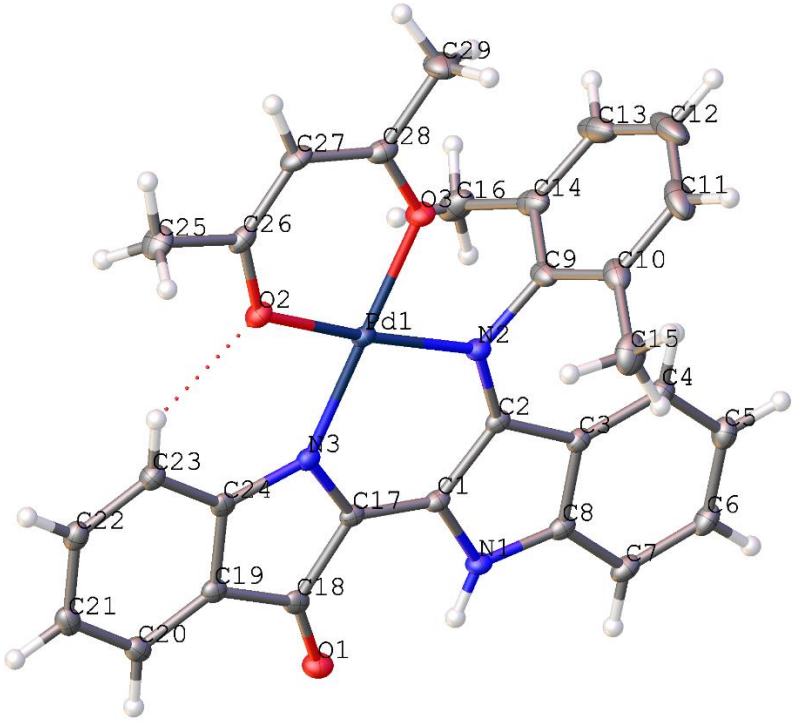

Appendix G-12 X-ray structure of **3.2**. Thermal ellipsoids are shown at the 50% probability.

Appendix G-13 Table of bond lengths (Å) for **3.2**.

Pd1	O2	2.0113(12)	C9	C10	1.401(3)
Pd1	O3	2.0062(13)	C9	C14	1.404(3)
Pd1	N2	2.0280(14)	C23	C22	1.396(2)
Pd1	N3	2.0327(14)	C21	C20	1.387(3)
O2	C26	1.280(2)	C21	C22	1.398(3)
O3	C28	1.278(2)	C3	C8	1.418(2)
O1	C18	1.233(2)	C3	C4	1.410(2)
N2	C2	1.324(2)	C8	C7	1.405(2)
N2	C9	1.439(2)	C26	C25	1.514(2)
N3	C17	1.358(2)	C26	C27	1.392(3)
N3	C24	1.429(2)	C6	C5	1.404(3)
N1	C1	1.392(2)	C6	C7	1.382(3)
N1	C8	1.371(2)	C5	C4	1.390(2)
C17	C18	1.506(2)	C28	C27	1.397(3)
C17	C1	1.377(2)	C28	C29	1.510(3)
C2	C1	1.443(2)	C10	C11	1.404(3)
C2	C3	1.465(2)	C10	C15	1.498(3)
C18	C19	1.452(2)	C14	C16	1.501(3)

C19	C24	1.412(2)	C14	C13	1.398(3)
C19	C20	1.394(2)	C13	C12	1.381(4)
C24	C23	1.397(2)	C11	C12	1.382(4)

Appendix G-14 Table of bond angles for **3.2**.

O2	Pd1	N2	173.99(5)	C10	C9	N2	119.15(17)
O2	Pd1	N3	91.76(5)	C10	C9	C14	122.38(17)
O3	Pd1	O2	89.93(5)	C14	C9	N2	118.47(17)
O3	Pd1	N2	84.72(5)	C22	C23	C24	118.01(16)
O3	Pd1	N3	177.90(5)	C20	C21	C22	119.55(16)
N2	Pd1	N3	93.65(6)	C21	C20	C19	118.13(16)
C26	O2	Pd1	125.95(12)	C8	C3	C2	105.94(14)
C28	O3	Pd1	126.35(12)	C4	C3	C2	134.83(15)
C2	N2	Pd1	125.98(12)	C4	C3	C8	119.23(15)
C2	N2	C9	116.30(14)	N1	C8	C3	110.27(14)
C9	N2	Pd1	117.73(11)	N1	C8	C7	127.79(16)
C17	N3	Pd1	122.01(11)	C7	C8	C3	121.94(16)
C17	N3	C24	106.45(13)	O2	C26	C25	114.27(16)
C24	N3	Pd1	131.53(11)	O2	C26	C27	126.46(16)
C8	N1	C1	109.35(14)	C27	C26	C25	119.24(16)
N3	C17	C18	111.21(14)	C23	C22	C21	122.80(17)
N3	C17	C1	127.33(15)	C7	C6	C5	121.50(16)
C1	C17	C18	121.46(15)	C4	C5	C6	121.40(17)
N2	C2	C1	123.05(15)	O3	C28	C27	126.07(17)
N2	C2	C3	130.85(15)	O3	C28	C29	113.84(16)
C1	C2	C3	106.10(14)	C27	C28	C29	120.03(16)
O1	C18	C17	125.99(15)	C6	C7	C8	117.49(16)
O1	C18	C19	130.28(16)	C9	C10	C11	117.5(2)
C19	C18	C17	103.71(14)	C9	C10	C15	121.50(17)
C24	C19	C18	107.35(14)	C11	C10	C15	120.9(2)
C20	C19	C18	129.97(16)	C5	C4	C3	118.44(16)
C20	C19	C24	122.68(16)	C26	C27	C28	124.09(16)
N1	C1	C2	108.33(14)	C9	C14	C16	121.26(17)
C17	C1	N1	123.76(15)	C13	C14	C9	117.7(2)
C17	C1	C2	127.91(15)	C13	C14	C16	121.0(2)
C19	C24	N3	111.28(14)	C12	C13	C14	121.0(2)
C23	C24	N3	129.89(16)	C12	C11	C10	120.9(2)
C23	C24	C19	118.83(15)	C13	C12	C11	120.5(2)

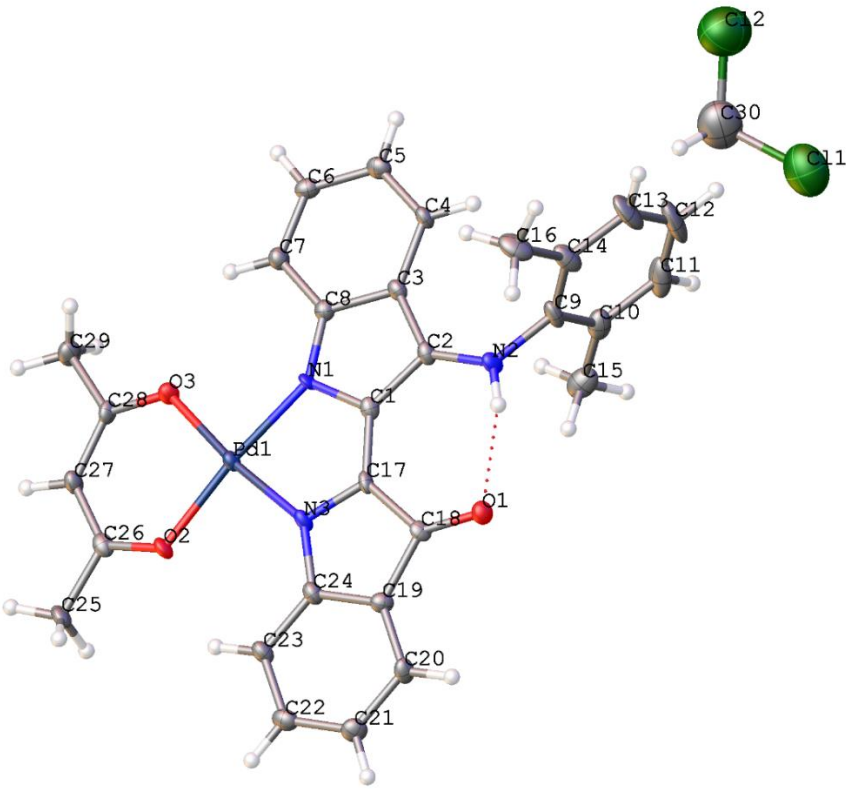

Appendix G-15 X-ray structure of **3.3**. Thermal ellipsoids are shown at the 50% probability.

Appendix G-16 Table of bond lengths (Å) for **3.3**.

C1	C2	1.434(8)	C18	C19	1.475(8)
C1	C17	1.393(8)	C18	O1	1.235(7)
C1	N1	1.387(7)	C19	C20	1.400(8)
C2	C3	1.434(8)	C19	C24	1.403(8)
C2	N2	1.356(7)	C20	C21	1.403(9)
C3	C4	1.426(8)	C21	C22	1.393(9)
C3	C8	1.435(8)	C22	C23	1.403(8)
C4	C5	1.383(9)	C23	C24	1.403(8)
C5	C6	1.412(9)	C24	N3	1.406(7)
C6	C7	1.385(8)	C25	C26	1.504(8)
C7	C8	1.422(8)	C26	C27	1.405(8)
C8	N1	1.374(7)	C26	O2	1.265(7)
C9	C10	1.397(9)	C27	C28	1.411(8)
C9	C14	1.410(9)	C28	C29	1.509(8)
C9	N2	1.434(8)	C28	O3	1.273(7)
C10	C11	1.398(11)	N1	Pd1	2.021(5)
C10	C15	1.506(11)	N3	Pd1	2.009(5)
C11	C12	1.393(14)	O2	Pd1	2.020(4)
C12	C13	1.392(13)	O3	Pd1	2.009(4)

C13	C14	1.390(10)	C30	Cl1	1.80(3)
C14	C16	1.515(10)	C30	Cl2	1.73(3)
C17	C18	1.504(8)	Cl1	Cl2[1]	1.826(12)
C17	N3	1.360(7)	Cl2	Cl1[2]	1.826(12)

Appendix G-17 Table of bond angles for **3.3**.

C17	C1	C2	133.1(5)	C20	C19	C24	122.0(6)
N1	C1	C2	111.4(5)	C24	C19	C18	107.2(5)
N1	C1	C17	115.4(5)	C19	C20	C21	118.0(6)
C1	C2	C3	105.0(5)	C22	C21	C20	119.6(5)
N2	C2	C1	124.7(5)	C21	C22	C23	122.9(6)
N2	C2	C3	130.3(5)	C24	C23	C22	117.3(6)
C2	C3	C8	106.4(5)	C19	C24	N3	111.6(5)
C4	C3	C2	133.6(5)	C23	C24	C19	120.1(5)
C4	C3	C8	119.9(5)	C23	C24	N3	128.3(5)
C5	C4	C3	118.3(5)	C27	C26	C25	118.8(5)
C4	C5	C6	121.3(6)	O2	C26	C25	114.6(5)
C7	C6	C5	122.3(6)	O2	C26	C27	126.6(6)
C6	C7	C8	117.4(5)	C26	C27	C28	126.3(5)
C7	C8	C3	120.7(5)	C27	C28	C29	118.6(5)
N1	C8	C3	110.8(5)	O3	C28	C27	125.8(5)
N1	C8	C7	128.4(5)	O3	C28	C29	115.5(5)
C10	C9	C14	122.1(6)	C1	N1	Pd1	112.6(4)
C10	C9	N2	119.0(6)	C8	N1	C1	106.4(5)
C14	C9	N2	118.9(6)	C8	N1	Pd1	140.2(4)
C9	C10	C11	118.0(7)	C2	N2	C9	122.8(5)
C9	C10	C15	121.1(6)	C17	N3	C24	107.5(5)
C11	C10	C15	120.9(7)	C17	N3	Pd1	112.9(4)
C12	C11	C10	120.8(7)	C24	N3	Pd1	139.4(4)
C13	C12	C11	120.2(7)	C26	O2	Pd1	123.6(4)
C14	C13	C12	120.7(8)	C28	O3	Pd1	124.2(4)
C9	C14	C16	120.9(6)	N3	Pd1	N1	81.1(2)
C13	C14	C9	118.2(7)	N3	Pd1	O2	92.72(18)
C13	C14	C16	120.9(7)	O2	Pd1	N1	173.73(18)
C1	C17	C18	131.5(5)	O3	Pd1	N1	92.90(18)
N3	C17	C1	117.7(5)	O3	Pd1	N3	173.76(19)
N3	C17	C18	110.8(5)	O3	Pd1	O2	93.20(17)
C19	C18	C17	102.9(5)	Cl2	C30	Cl1	111.0(16)
O1	C18	C17	126.6(5)	C30	Cl1	Cl2[1]	165.6(11)
O1	C18	C19	130.4(5)	C30	Cl2	Cl1[2]	91.1(11)
C20	C19	C18	130.7(6)				

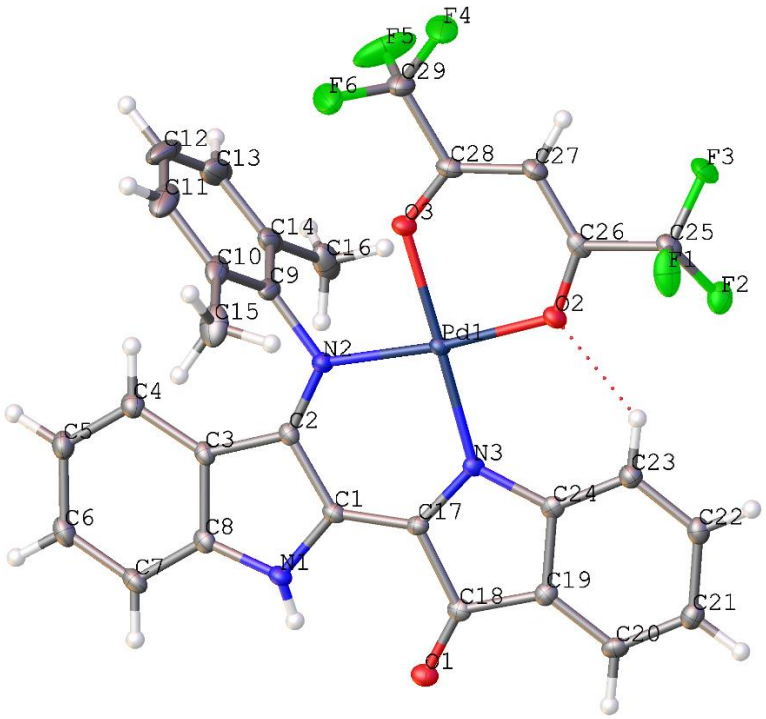

Appendix G-18 X-ray structure of **3.4**. Thermal ellipsoids are shown at the 50% probability.

Appendix G-19 Table of bond lengths (Å) for **3.4**.

C1	C2	1.439(4)	C18	O1	1.230(4)
C1	C17	1.371(4)	C19	C20	1.394(4)
C1	N1	1.390(4)	C19	C24	1.418(4)
C2	C3	1.466(4)	C20	C21	1.383(4)
C2	N2	1.319(4)	C21	C22	1.399(4)
C3	C4	1.405(4)	C22	C23	1.383(4)
C3	C8	1.419(4)	C23	C24	1.386(4)
C4	C5	1.387(4)	C24	N3	1.421(4)
C5	C6	1.402(4)	C25	C26	1.543(4)
C6	C7	1.385(4)	C25	F1	1.335(4)
C7	C8	1.392(4)	C25	F2	1.330(4)
C8	N1	1.370(4)	C25	F3	1.329(4)
C9	C10	1.403(5)	C26	C27	1.393(4)
C9	C14	1.401(5)	C26	O2	1.258(4)
C9	N2	1.444(4)	C27	C28	1.392(4)
C10	C11	1.397(5)	C28	C29	1.535(4)
C10	C15	1.498(6)	C28	O3	1.255(4)
C11	C12	1.378(7)	C29	F4	1.333(4)
C12	C13	1.369(7)	C29	F5	1.310(4)

C13	C14	1.394(5)	C29	F6	1.327(4)
C14	C16	1.496(5)	N2	Pd1	2.010(2)
C17	C18	1.503(4)	N3	Pd1	2.019(2)
C17	N3	1.363(4)	O2	Pd1	2.041(2)
C18	C19	1.452(4)	O3	Pd1	2.037(2)

Appendix G-20 Table of bond angles(°) for **3.4**.

C17	C1	C2	127.4(3)	C23	C22	C21	122.9(3)
C17	C1	N1	124.0(3)	C22	C23	C24	118.9(3)
N1	C1	C2	108.5(2)	C19	C24	N3	110.8(3)
C1	C2	C3	106.0(2)	C23	C24	C19	118.4(3)
N2	C2	C1	123.3(3)	C23	C24	N3	130.8(3)
N2	C2	C3	130.6(3)	F1	C25	C26	109.7(3)
C4	C3	C2	134.7(3)	F2	C25	C26	112.2(2)
C4	C3	C8	119.4(3)	F2	C25	F1	107.0(3)
C8	C3	C2	105.9(2)	F3	C25	C26	112.6(3)
C5	C4	C3	118.6(3)	F3	C25	F1	107.8(3)
C4	C5	C6	121.0(3)	F3	C25	F2	107.2(3)
C7	C6	C5	121.6(3)	C27	C26	C25	117.8(3)
C6	C7	C8	117.6(3)	O2	C26	C25	112.6(3)
C7	C8	C3	121.8(3)	O2	C26	C27	129.4(3)
N1	C8	C3	110.2(3)	C28	C27	C26	120.4(3)
N1	C8	C7	128.0(3)	C27	C28	C29	119.0(3)
C10	C9	N2	118.1(3)	O3	C28	C27	128.9(3)
C14	C9	C10	122.6(3)	O3	C28	C29	112.2(3)
C14	C9	N2	119.2(3)	F4	C29	C28	112.8(3)
C9	C10	C15	121.7(3)	F5	C29	C28	111.0(3)
C11	C10	C9	117.2(4)	F5	C29	F4	107.8(3)
C11	C10	C15	121.1(4)	F5	C29	F6	107.9(3)
C12	C11	C10	121.2(4)	F6	C29	C28	110.9(3)
C13	C12	C11	120.2(3)	F6	C29	F4	106.2(3)
C12	C13	C14	121.9(4)	C8	N1	C1	109.3(2)
C9	C14	C16	122.1(3)	C2	N2	C9	116.2(2)
C13	C14	C9	116.9(4)	C2	N2	Pd1	126.3(2)
C13	C14	C16	120.9(4)	C9	N2	Pd1	117.57(19)
C1	C17	C18	122.4(3)	C17	N3	C24	107.0(2)
N3	C17	C1	126.7(3)	C17	N3	Pd1	122.50(19)
N3	C17	C18	110.9(2)	C24	N3	Pd1	130.40(19)
C19	C18	C17	103.7(2)	C26	O2	Pd1	126.01(19)
O1	C18	C17	125.7(3)	C28	O3	Pd1	126.8(2)

O1	C18	C19	130.6(3)	N2	Pd1	N3	93.24(10)
C20	C19	C18	130.4(3)	N2	Pd1	O2	173.83(9)
C20	C19	C24	122.0(3)	N2	Pd1	O3	86.07(9)
C24	C19	C18	107.6(2)	N3	Pd1	O2	92.81(9)
C21	C20	C19	118.9(3)	N3	Pd1	O3	178.99(10)
C20	C21	C22	118.9(3)	O3	Pd1	O2	87.86(8)

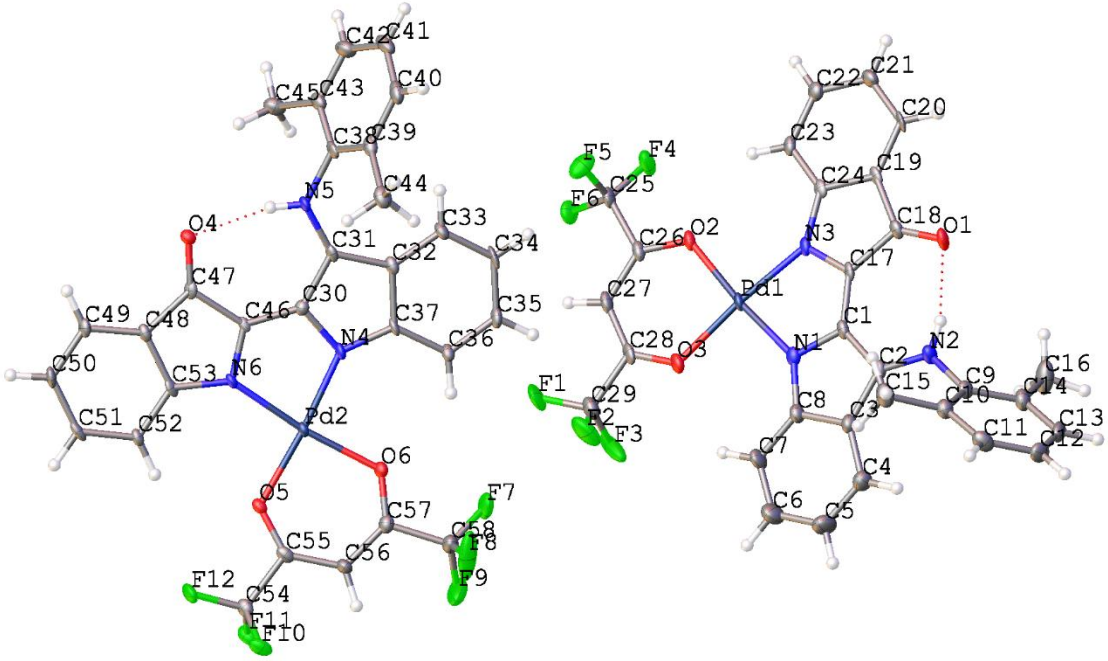

Appendix G-21 X-ray structure of **3.5**. Thermal ellipsoids are shown at the 50% probability.

Appendix G-22 Table of bond lengths (Å) for **3.5**.

C1	C2	1.453(5)	C30	C31	1.442(5)
C1	C17	1.388(5)	C30	C46	1.384(5)
C1	N1	1.373(5)	C30	N4	1.380(4)
C2	C3	1.418(6)	C31	C32	1.444(5)
C2	N2	1.348(5)	C31	N5	1.342(4)
C3	C4	1.424(5)	C32	C33	1.400(5)
C3	C8	1.430(5)	C32	C37	1.443(5)
C4	C5	1.368(6)	C33	C34	1.377(5)
C5	C6	1.413(6)	C34	C35	1.421(5)
C6	C7	1.374(6)	C35	C36	1.375(5)
C7	C8	1.400(6)	C36	C37	1.407(5)
C8	N1	1.379(5)	C37	N4	1.366(4)
C9	C10	1.399(6)	C38	C39	1.402(5)

C9	C14	1.408(5)	C38	C43	1.409(5)
C9	N2	1.437(4)	C38	N5	1.438(5)
C10	C11	1.407(5)	C39	C40	1.401(6)
C10	C15	1.506(6)	C39	C44	1.517(5)
C11	C12	1.384(6)	C40	C41	1.383(6)
C12	C13	1.392(6)	C41	C42	1.402(6)
C13	C14	1.397(5)	C42	C43	1.390(6)
C14	C16	1.514(6)	C43	C45	1.502(6)
C17	C18	1.480(5)	C46	C47	1.489(4)
C17	N3	1.355(4)	C46	N6	1.354(4)
C18	C19	1.468(5)	C47	C48	1.446(5)
C18	O1	1.238(4)	C47	O4	1.248(4)
C19	C20	1.392(5)	C48	C49	1.400(5)
C19	C24	1.417(5)	C48	C53	1.425(5)
C20	C21	1.393(5)	C49	C50	1.378(5)
C21	C22	1.392(6)	C50	C51	1.402(5)
C22	C23	1.396(5)	C51	C52	1.392(5)
C23	C24	1.399(5)	C52	C53	1.394(5)
C24	N3	1.402(5)	C53	N6	1.396(4)
C25	C26	1.540(5)	C54	C55	1.537(5)
C25	F4	1.335(5)	C54	F10	1.342(4)
C25	F5	1.339(5)	C54	F11	1.343(4)
C25	F6	1.333(4)	C54	F12	1.333(4)
C26	C27	1.394(5)	C55	C56	1.393(5)
C26	O2	1.270(4)	C55	O5	1.263(4)
C27	C28	1.398(5)	C56	C57	1.381(5)
C28	C29	1.539(6)	C57	C58	1.543(5)
C28	O3	1.257(4)	C57	O6	1.264(4)
C29	F1	1.335(5)	C58	F7	1.309(5)
C29	F2	1.319(5)	C58	F8	1.312(5)
C29	F3	1.315(5)	C58	F9	1.346(5)
N1	Pd1	1.999(3)	N4	Pd2	1.995(3)
N3	Pd1	2.011(3)	N6	Pd2	2.011(3)
O2	Pd1	2.027(2)	O5	Pd2	2.034(2)
O3	Pd1	2.021(3)	O6	Pd2	2.023(2)

Appendix G-23 Table of bond angles (°) for **3.5.**

C17	C1	C2	133.5(4)	C46	C30	C31	133.8(3)
N1	C1	C2	110.6(3)	N4	C30	C31	110.9(3)
N1	C1	C17	115.9(3)	N4	C30	C46	115.3(3)
C3	C2	C1	105.2(3)	C30	C31	C32	105.3(3)
N2	C2	C1	123.0(3)	N5	C31	C30	123.2(3)

N2	C2	C3	131.8(3)	N5	C31	C32	131.5(3)
C2	C3	C4	133.8(4)	C33	C32	C31	133.4(3)
C2	C3	C8	106.7(3)	C33	C32	C37	121.0(3)
C4	C3	C8	119.5(4)	C37	C32	C31	105.5(3)
C5	C4	C3	119.0(4)	C34	C33	C32	118.7(3)
C4	C5	C6	120.5(4)	C33	C34	C35	120.3(3)
C7	C6	C5	122.2(4)	C36	C35	C34	122.3(3)
C6	C7	C8	118.3(4)	C35	C36	C37	118.5(3)
C7	C8	C3	120.4(3)	C36	C37	C32	119.1(3)
N1	C8	C3	110.6(3)	N4	C37	C32	111.1(3)
N1	C8	C7	128.9(3)	N4	C37	C36	129.8(3)
C10	C9	C14	122.3(3)	C39	C38	C43	122.5(4)
C10	C9	N2	120.9(3)	C39	C38	N5	120.5(3)
C14	C9	N2	116.7(3)	C43	C38	N5	117.0(3)
C9	C10	C11	117.8(4)	C38	C39	C44	122.7(4)
C9	C10	C15	123.0(3)	C40	C39	C38	117.0(4)
C11	C10	C15	119.3(4)	C40	C39	C44	120.3(4)
C12	C11	C10	121.3(4)	C41	C40	C39	121.8(4)
C11	C12	C13	119.4(3)	C40	C41	C42	119.9(4)
C12	C13	C14	121.7(4)	C43	C42	C41	120.4(4)
C9	C14	C16	121.6(4)	C38	C43	C45	120.8(3)
C13	C14	C9	117.5(4)	C42	C43	C38	118.2(4)
C13	C14	C16	121.0(4)	C42	C43	C45	120.9(4)
C1	C17	C18	132.0(3)	C30	C46	C47	131.3(3)
N3	C17	C1	117.6(3)	N6	C46	C30	117.9(3)
N3	C17	C18	110.5(3)	N6	C46	C47	110.8(3)
C19	C18	C17	104.0(3)	C48	C47	C46	103.6(3)
O1	C18	C17	126.0(3)	O4	C47	C46	126.3(3)
O1	C18	C19	130.0(3)	O4	C47	C48	130.1(3)
C20	C19	C18	131.8(3)	C49	C48	C47	131.6(3)
C20	C19	C24	121.5(3)	C49	C48	C53	121.1(3)
C24	C19	C18	106.8(3)	C53	C48	C47	107.3(3)
C19	C20	C21	118.5(4)	C50	C49	C48	118.6(3)
C22	C21	C20	119.8(4)	C49	C50	C51	120.1(3)
C21	C22	C23	122.9(3)	C52	C51	C50	122.8(3)
C22	C23	C24	117.4(3)	C51	C52	C53	117.5(3)
C23	C24	C19	120.0(3)	C52	C53	C48	120.0(3)
C23	C24	N3	129.7(3)	C52	C53	N6	129.7(3)
N3	C24	C19	110.4(3)	N6	C53	C48	110.3(3)
F4	C25	C26	111.8(3)	F10	C54	C55	112.4(3)
F4	C25	F5	107.4(3)	F10	C54	F11	106.5(3)
F5	C25	C26	111.0(3)	F11	C54	C55	110.0(3)

F6	C25	C26	112.3(3)	F12	C54	C55	112.0(3)
F6	C25	F4	107.4(3)	F12	C54	F10	107.9(3)
F6	C25	F5	106.6(3)	F12	C54	F11	107.8(3)
C27	C26	C25	117.4(3)	C56	C55	C54	115.5(3)
O2	C26	C25	113.1(3)	O5	C55	C54	114.9(3)
O2	C26	C27	129.5(3)	O5	C55	C56	129.5(3)
C26	C27	C28	122.5(3)	C57	C56	C55	123.2(3)
C27	C28	C29	118.2(3)	C56	C57	C58	117.3(3)
O3	C28	C27	130.2(4)	O6	C57	C56	129.7(3)
O3	C28	C29	111.6(3)	O6	C57	C58	113.0(3)
F1	C29	C28	112.6(3)	F7	C58	C57	113.5(3)
F2	C29	C28	111.0(4)	F7	C58	F8	108.3(4)
F2	C29	F1	105.3(4)	F7	C58	F9	104.6(4)
F3	C29	C28	111.4(3)	F8	C58	C57	110.1(4)
F3	C29	F1	108.2(4)	F8	C58	F9	108.7(4)
F3	C29	F2	108.1(4)	F9	C58	C57	111.4(4)
C1	N1	C8	106.8(3)	C30	N4	Pd2	112.9(2)
C1	N1	Pd1	112.7(2)	C37	N4	C30	107.2(3)
C8	N1	Pd1	140.4(3)	C37	N4	Pd2	139.4(2)
C2	N2	C9	127.0(3)	C31	N5	C38	125.9(3)
C17	N3	C24	108.4(3)	C46	N6	C53	107.9(3)
C17	N3	Pd1	112.2(2)	C46	N6	Pd2	112.1(2)
C24	N3	Pd1	139.4(2)	C53	N6	Pd2	140.0(2)
C26	O2	Pd1	122.5(2)	C55	O5	Pd2	122.2(2)
C28	O3	Pd1	122.5(2)	C57	O6	Pd2	122.5(2)
N1	Pd1	N3	81.44(12)	N4	Pd2	N6	81.27(12)
N1	Pd1	O2	174.79(12)	N4	Pd2	O5	175.38(10)
N1	Pd1	O3	92.36(12)	N4	Pd2	O6	92.00(11)
N3	Pd1	O2	93.36(11)	N6	Pd2	O5	94.17(11)
N3	Pd1	O3	173.63(11)	N6	Pd2	O6	172.56(11)
O3	Pd1	O2	92.83(10)	O6	Pd2	O5	92.52(10)

Appendix G-24 Table of crystallographic parameters for **H4.11^{+}OTf^{-}** and **H4.12^{+} BF$_4$.**

Identification code	**H4.11^{+}OTf^{-}**	**H4.12^{+} BF$_4$**
Empirical formula	$C_{36}H_{30}F_3N_4O_5PdS$	$C_{43}H_{42}Cl_2N_4O_4Ru$
Formula weight	794.10	850.77
Temperature/K	90	90
Crystal system	monoclinic	orthorhombic
Space group	C2/c	$P2_12_12$
a/Å	25.632(3)	18.7127(12)
b/Å	17.342(2)	7.9606(5)
c/Å	17.450(2)	14.4925(9)
α/°	90	90
β/°	90.112(4)	90
γ/°	90	90
Volume/Å^3	7756.5(17)	2158.9(2)
Z	8	2
ρ_{calc}g/cm^3	1.360	1.309
μ/mm^{-1}	0.590	0.530
F(000)	3224.0	876.0
Crystal size/mm^3	0.6 × 0.11 × 0.03	0.5 × 0.4 × 0.13
Radiation	MoKα (λ = 0.71073)	MoKα (λ = 0.71073)
2Θ range for data collection/°	3.178 to 52.678	3.554 to 61.002
Index ranges	-31 ≤ h ≤ 31, -21 ≤ k ≤ 21, -20 ≤ l ≤ 21	-26 ≤ h ≤ 24, -8 ≤ k ≤ 11, -20 ≤ l ≤ 20
Reflections collected	33603	23685
Independent reflections	7883 [R_{int} = 0.0499, R_{sigma} = 0.0407]	6601 [R_{int} = 0.0308, R_{sigma} = 0.0283]
Data/restraints/parameters	7883/179/509	6601/0/249
Goodness-of-fit on F^2	1.046	1.047
Final R indexes [I>=2σ (I)]	R_1 = 0.0590, wR_2 = 0.1527	R_1 = 0.0220, wR_2 = 0.0528
Final R indexes [all data]	R_1 = 0.0753, wR_2 = 0.1670	R_1 = 0.0232, wR_2 = 0.0534
Largest diff. peak/hole / e Å^{-3}	1.58/-1.02	0.52/-0.28

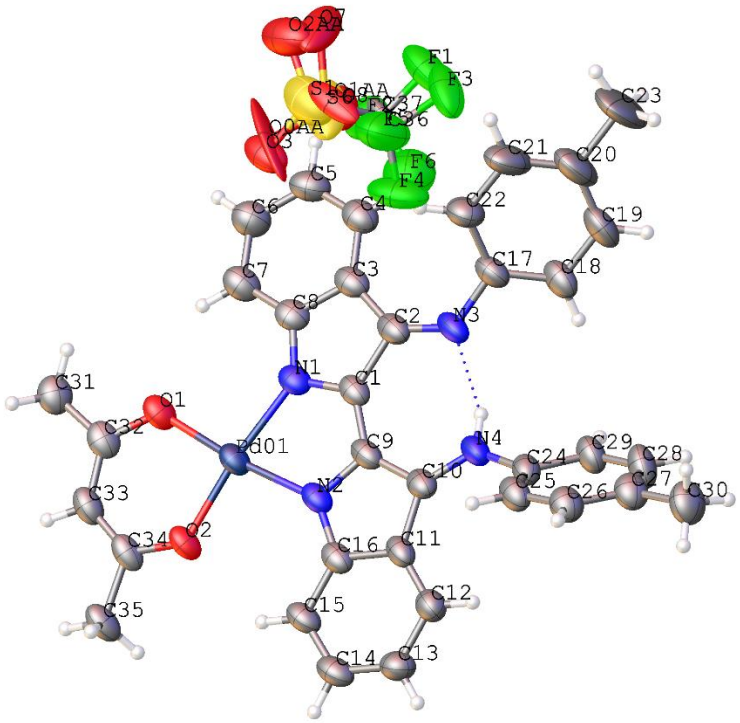

Appendix G-25 X-ray structure of **H4.11^{+}OTf**. Thermal ellipsoids are shown at 50% probability.

Appendix G-26 Table of bond lengths (Å) for **H4.11^{+}OTf**.

Pd01	O2	1.983(3)	C15	C14	1.391(7)
Pd01	O1	1.979(3)	C12	C13	1.400(7)
Pd01	N1	2.027(4)	C14	C13	1.393(7)
Pd01	N2	2.018(4)	C29	C28	1.387(8)
O2	C34	1.290(5)	C25	C26	1.382(7)
O1	C32	1.304(5)	C28	C27	1.393(8)
N1	C1	1.356(6)	C7	C6	1.387(7)
N1	C8	1.391(6)	C17	C22	1.400(7)
N4	C24	1.417(6)	C17	C18	1.400(7)
N4	C10	1.305(5)	C6	C5	1.399(7)
N2	C9	1.350(5)	C22	C21	1.403(8)
N2	C16	1.403(6)	C18	C19	1.382(7)
C1	C2	1.485(6)	C26	C27	1.392(7)
C1	C9	1.409(7)	C19	C20	1.384(10)
N3	C2	1.312(7)	C27	C30	1.508(8)
N3	C17	1.415(6)	C21	C20	1.393(10)
C3	C2	1.439(8)	C20	C23	1.529(8)
C3	C8	1.418(6)	F3	C36	1.476(9)
C3	C4	1.415(7)	F4	C36	1.270(11)

C9	C10	1.466(7)	F5	C36	1.202(12)
C32	C33	1.395(7)	S6	O7	1.633(11)
C32	C31	1.489(7)	S6	O8	1.600(12)
C11	C10	1.467(6)	S6	C36	1.596(11)
C11	C16	1.422(6)	S6	O0AA	1.343(12)
C11	C12	1.375(7)	C37	F1	1.3279
C24	C29	1.412(6)	C37	F2	1.3306
C24	C25	1.376(7)	C37	F6	1.3255
C34	C33	1.372(7)	C37	S1	1.8235
C34	C35	1.515(7)	S1	O1AA	1.4408
C8	C7	1.389(7)	S1	O2AA	1.4377
C4	C5	1.373(8)	S1	O3	1.4415
C15	C16	1.395(6)			

Appendix G-27 Table of bond angles (°) for **H4.11^{+}OTf**.

O2	Pd01	N1	173.31(15)	C15	C16	N2	127.6(4)
O2	Pd01	N2	92.97(13)	C15	C16	C11	121.8(5)
O1	Pd01	O2	93.37(13)	C11	C12	C13	119.1(5)
O1	Pd01	N1	93.26(14)	C15	C14	C13	122.3(5)
O1	Pd01	N2	173.65(13)	C14	C13	C12	120.2(5)
N2	Pd01	N1	80.40(15)	C28	C29	C24	119.0(5)
C34	O2	Pd01	123.8(3)	C24	C25	C26	120.6(4)
C32	O1	Pd01	124.4(3)	C29	C28	C27	121.9(5)
C1	N1	Pd01	112.8(3)	C6	C7	C8	118.3(5)
C1	N1	C8	108.2(4)	C22	C17	N3	122.5(5)
C8	N1	Pd01	138.8(3)	C22	C17	C18	119.9(5)
C10	N4	C24	125.9(4)	C18	C17	N3	117.4(4)
C9	N2	Pd01	113.8(3)	C7	C6	C5	120.8(5)
C9	N2	C16	108.1(4)	C17	C22	C21	118.9(6)
C16	N2	Pd01	137.8(3)	C19	C18	C17	120.1(6)
N1	C1	C2	110.0(4)	C25	C26	C27	121.5(5)
N1	C1	C9	116.8(4)	C18	C19	C20	120.7(6)
C9	C1	C2	133.2(4)	C28	C27	C30	120.9(5)
C2	N3	C17	128.0(4)	C26	C27	C28	117.6(5)
C8	C3	C2	107.2(4)	C26	C27	C30	121.4(5)
C4	C3	C2	134.2(5)	C20	C21	C22	120.7(6)
C4	C3	C8	118.5(5)	C19	C20	C21	119.5(5)
N3	C2	C1	120.5(5)	C19	C20	C23	120.4(7)
N3	C2	C3	135.2(4)	C21	C20	C23	120.0(8)
C3	C2	C1	104.3(4)	O8	S6	O7	92.3(8)
N2	C9	C1	115.9(4)	C36	S6	O7	108.9(5)

N2	C9	C10	110.7(4)	C36	S6	O8	112.6(5)
C1	C9	C10	133.4(4)	O0AA	S6	O7	112.2(11)
O1	C32	C33	124.8(5)	O0AA	S6	O8	111.2(8)
O1	C32	C31	114.7(4)	O0AA	S6	C36	117.0(11)
C33	C32	C31	120.5(4)	C4	C5	C6	121.4(5)
C16	C11	C10	105.8(4)	F3	C36	S6	112.2(8)
C12	C11	C10	134.0(4)	F4	C36	F3	112.0(8)
C12	C11	C16	119.8(4)	F4	C36	S6	108.6(7)
C29	C24	N4	116.6(4)	F5	C36	F3	103.5(8)
C25	C24	N4	123.6(4)	F5	C36	F4	101.7(9)
C25	C24	C29	119.3(5)	F5	C36	S6	118.4(8)
N4	C10	C9	121.5(4)	F1	C37	F2	107.5
N4	C10	C11	133.7(5)	F1	C37	S1	111.1
C9	C10	C11	104.8(4)	F2	C37	S1	110.7
O2	C34	C33	126.2(4)	F6	C37	F1	108.4
O2	C34	C35	114.1(5)	F6	C37	F2	107.7
C33	C34	C35	119.6(4)	F6	C37	S1	111.3
N1	C8	C3	110.4(4)	O1AA	S1	C37	103.9
C7	C8	N1	127.8(4)	O1AA	S1	O3	114.8
C7	C8	C3	121.8(4)	O2AA	S1	C37	102.9
C34	C33	C32	126.9(4)	O2AA	S1	O1AA	115.0
C5	C4	C3	119.2(5)	O2AA	S1	O3	114.8
C14	C15	C16	116.8(5)	O3	S1	C37	103.2
N2	C16	C11	110.5(4)				

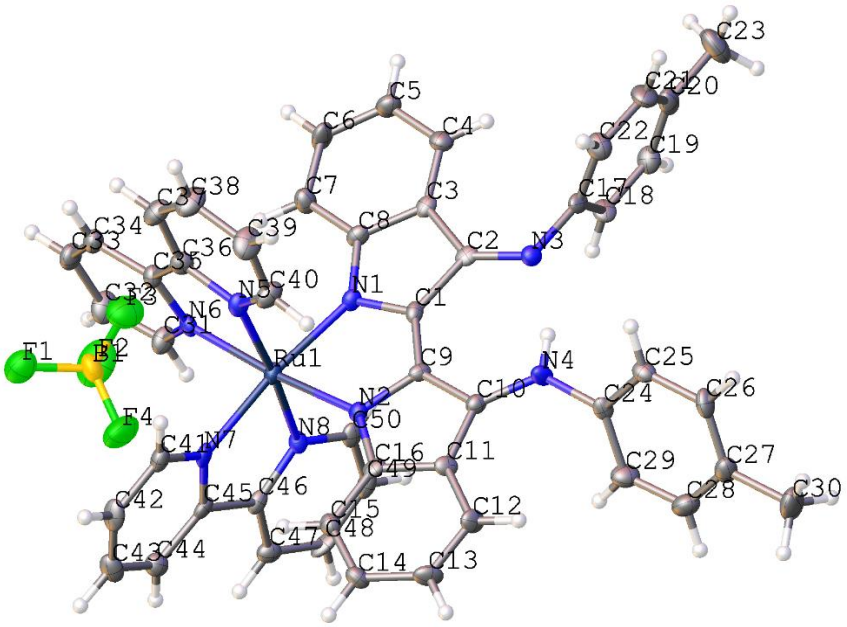

Appendix G-28 X-ray structure of **H4.12**$^{+}$. Thermal ellipsoids are shown at 50% probability.

Appendix G-29 Bond lengths (Å) for **H4.12**$^{+}$.

Ru1	N1	2.072(4)	C3	C4	1.384(6)
Ru1	N6	2.061(4)	C2	C1	1.493(6)
Ru1	N5	2.056(4)	C37	C36	1.387(7)
Ru1	N7	2.052(4)	C37	C38	1.379(7)
Ru1	N2	2.078(4)	C16	C15	1.401(6)
Ru1	N8	2.042(4)	C16	C11	1.429(7)
F1	B1	1.397(7)	C15	C14	1.375(7)
F3	B1	1.375(7)	C34	C33	1.357(7)
N1	C8	1.404(6)	C50	C49	1.383(7)
N1	C1	1.351(6)	C44	C45	1.387(7)
F4	B1	1.386(7)	C44	C43	1.363(7)
F2	B1	1.386(7)	C14	C13	1.399(7)
N6	C35	1.361(6)	C11	C12	1.415(7)
N6	C31	1.344(6)	C18	C19	1.379(7)
N5	C36	1.364(6)	C25	C26	1.397(7)
N5	C40	1.341(6)	C19	C20	1.376(7)
N7	C45	1.354(6)	C49	C48	1.379(7)
N7	C41	1.346(6)	C45	C46	1.477(7)
N3	C17	1.432(6)	C41	C42	1.376(7)
N3	C2	1.287(6)	C47	C48	1.383(7)
N2	C9	1.385(6)	C47	C46	1.380(7)
N2	C16	1.372(6)	C33	C32	1.381(7)
N8	C50	1.345(6)	C20	C21	1.370(7)
N8	C46	1.363(6)	C20	C23	1.500(7)
N4	C24	1.419(6)	C12	C13	1.366(7)
N4	C10	1.362(6)	C43	C42	1.379(7)
C17	C18	1.378(7)	C4	C5	1.384(7)
C17	C22	1.381(7)	C40	C39	1.377(7)
C8	C3	1.403(6)	C22	C21	1.396(7)
C8	C7	1.394(7)	C38	C39	1.364(7)
C24	C25	1.394(6)	C26	C27	1.371(7)
C24	C29	1.398(7)	C31	C32	1.387(7)
C10	C9	1.438(6)	C6	C5	1.380(7)
C10	C11	1.429(6)	C6	C7	1.386(7)
C9	C1	1.395(6)	C28	C29	1.378(7)
C35	C34	1.396(7)	C28	C27	1.378(7)
C35	C36	1.464(7)	C27	C30	1.523(7)
C3	C2	1.469(6)			

Appendix G-30 Bond angles (°) for **H4.12**$^{+}$.

N1	Ru1	N2	77.44(15)	N2	C16	C11	111.4(4)
N6	Ru1	N1	99.87(14)	C15	C16	C11	120.0(4)
N6	Ru1	N2	173.36(15)	C14	C15	C16	119.3(5)
N5	Ru1	N1	87.13(15)	N1	C1	C9	117.2(4)
N5	Ru1	N6	78.36(15)	N1	C1	C2	110.6(4)
N5	Ru1	N2	95.37(15)	C9	C1	C2	132.2(4)
N7	Ru1	N1	173.11(15)	C33	C34	C35	119.2(5)
N7	Ru1	N6	85.52(14)	N8	C50	C49	123.2(5)
N7	Ru1	N5	98.23(15)	C43	C44	C45	119.5(5)
N7	Ru1	N2	97.65(15)	C15	C14	C13	120.6(4)
N8	Ru1	N1	96.42(15)	C10	C11	C16	106.1(4)
N8	Ru1	N6	97.31(15)	C12	C11	C10	134.6(4)
N8	Ru1	N5	174.85(15)	C12	C11	C16	119.2(4)
N8	Ru1	N7	78.53(15)	C17	C18	C19	119.6(4)
N8	Ru1	N2	89.06(15)	C24	C25	C26	119.6(5)
C8	N1	Ru1	137.6(3)	C20	C19	C18	121.7(5)
C1	N1	Ru1	115.4(3)	N5	C36	C35	114.3(4)
C1	N1	C8	106.9(4)	N5	C36	C37	121.3(5)
C35	N6	Ru1	115.9(3)	C37	C36	C35	124.4(5)
C31	N6	Ru1	126.6(3)	C48	C49	C50	118.8(5)
C31	N6	C35	117.4(4)	N7	C45	C44	121.4(4)
C36	N5	Ru1	116.4(3)	N7	C45	C46	114.2(4)
C40	N5	Ru1	125.6(3)	C44	C45	C46	124.3(4)
C40	N5	C36	117.9(4)	N7	C41	C42	121.9(5)
C45	N7	Ru1	116.3(3)	C46	C47	C48	119.8(5)
C41	N7	Ru1	125.2(3)	C34	C33	C32	120.6(5)
C41	N7	C45	118.5(4)	C49	C48	C47	118.9(5)
C2	N3	C17	118.1(4)	C19	C20	C23	120.1(5)
C9	N2	Ru1	115.1(3)	C21	C20	C19	118.0(5)
C16	N2	Ru1	138.8(3)	C21	C20	C23	121.9(5)
C16	N2	C9	106.1(4)	N8	C46	C45	114.2(4)
C50	N8	Ru1	126.0(3)	N8	C46	C47	121.7(4)
C50	N8	C46	117.6(4)	C47	C46	C45	124.0(5)
C46	N8	Ru1	116.4(3)	C13	C12	C11	118.9(5)
C10	N4	C24	126.8(4)	C12	C13	C14	121.9(5)
C18	C17	N3	119.5(4)	C44	C43	C42	119.2(5)
C18	C17	C22	120.1(5)	C3	C4	C5	118.5(5)
C22	C17	N3	120.4(4)	N5	C40	C39	122.8(5)
C3	C8	N1	112.7(4)	C17	C22	C21	118.7(5)
C7	C8	N1	127.0(4)	C39	C38	C37	119.0(5)
C7	C8	C3	120.4(4)	C41	C42	C43	119.4(5)

C25	C24	N4	118.9(4)	C27	C26	C25	121.4(5)
C25	C24	C29	118.8(4)	N6	C31	C32	123.7(5)
C29	C24	N4	122.2(4)	C5	C6	C7	121.9(5)
N4	C10	C9	123.7(4)	C20	C21	C22	121.8(5)
N4	C10	C11	131.1(4)	C27	C28	C29	122.0(5)
C11	C10	C9	105.2(4)	C6	C5	C4	120.6(5)
N2	C9	C10	111.1(4)	C38	C39	C40	119.5(5)
N2	C9	C1	114.8(4)	C28	C29	C24	119.7(5)
C1	C9	C10	134.0(4)	C6	C7	C8	117.7(5)
N6	C35	C34	121.6(4)	C33	C32	C31	117.5(5)
N6	C35	C36	115.0(4)	C26	C27	C28	118.3(5)
C34	C35	C36	123.4(5)	C26	C27	C30	120.3(5)
C8	C3	C2	105.5(4)	C28	C27	C30	121.4(5)
C4	C3	C8	120.9(4)	F3	B1	F1	108.1(5)
C4	C3	C2	133.5(4)	F3	B1	F4	110.4(5)
N3	C2	C3	132.3(4)	F3	B1	F2	111.5(5)
N3	C2	C1	123.5(4)	F4	B1	F1	108.8(4)
C3	C2	C1	104.2(4)	F2	B1	F1	107.1(5)
C38	C37	C36	119.5(5)	F2	B1	F4	110.8(5)
N2	C16	C15	128.5(4)				

Appendix G-31 Table of crystallographic parameters for **5.3** and **H5.4**.

Identification code	**5.3**	**H5.4**
Empirical formula	$C_{36}H_{37}N_3O_6Ru$	$C_{136}H_{128}N_{12}O_{20}Ru_4$
Formula weight	708.75	2654.78
Temperature/K	90	296.15
Crystal system	triclinic	monoclinic
Space group	P-1	$P2_1/n$
a/Å	11.0090(15)	12.2288(3)
b/Å	12.2425(17)	16.6141(4)
c/Å	13.9502(19)	15.2065(4)
α/°	65.108(3)	90
β/°	73.814(4)	106.6560(10)
γ/°	86.601(4)	90
Volume/Å^3	1634.3(4)	2959.88(13)
Z	2	1
ρ_{calc}g/cm^3	1.440	1.489
μ/mm^{-1}	0.530	0.577
F(000)	732.0	1364.0
Crystal size/mm^3	0.17 × 0.11 × 0.07	0.3 × 0.16 × 0.08
Radiation	MoKα (λ = 0.71073)	MoKα (λ = 0.71073)
2Θ range for data collection/°	3.352 to 55.848	3.718 to 61.072
Index ranges	$-14 \le h \le 14$, $-16 \le k \le 16$, $-18 \le l \le 18$	$-17 \le h \le 15$, $-23 \le k \le 23$, $-21 \le l \le 21$
Reflections collected	29768	47870
Independent reflections	7787 [R_{int} = 0.0340, R_{sigma} = 0.0322]	9068 [R_{int} = 0.0398, R_{sigma} = 0.0309]
Data/restraints/parameters	7787/42/446	9068/0/398
Goodness-of-fit on F^2	1.153	1.026
Final R indexes [I>=2σ (I)]	R_1 = 0.0458, wR_2 = 0.1239	R_1 = 0.0291, wR_2 = 0.0639
Final R indexes [all data]	R_1 = 0.0532, wR_2 = 0.1283	R_1 = 0.0379, wR_2 = 0.0677
Largest diff. peak/hole / e Å^{-3}	1.61/-1.02	0.85/-0.49
Flack parameter	rh221	rh230_0m

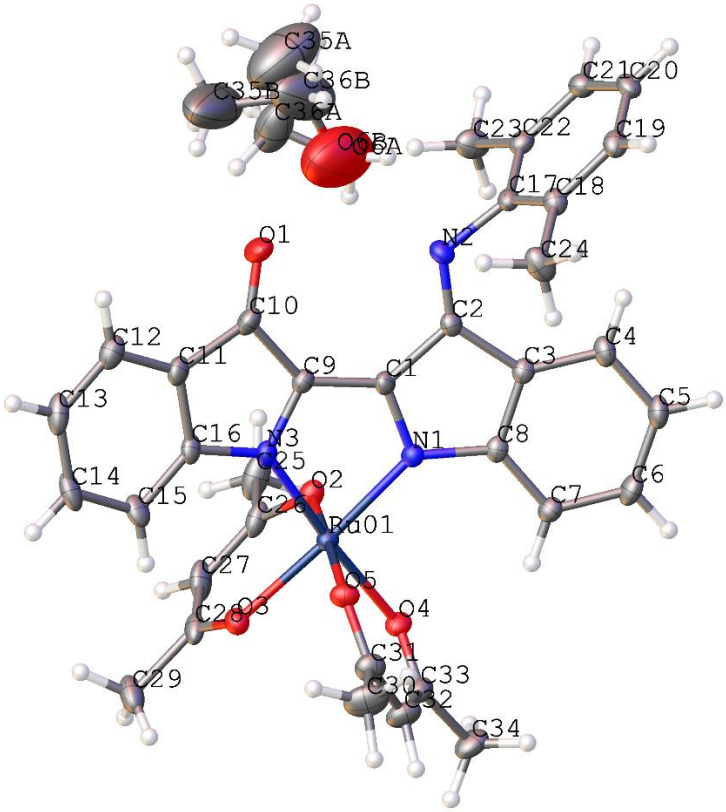

Appendix G-32 X-ray structure of **5.3·EtOH**. Thermal ellipsoids are shown at 50% probability.

Appendix G-33 Bond lengths (Å) for **5.3·EtOH**.

Ru01	O5	2.034(2)	C16	C11	1.398(5)
Ru01	O4	2.053(2)	C9	C10	1.492(5)
Ru01	O2	2.014(3)	C18	C19	1.392(5)
Ru01	O3	2.041(3)	C18	C24	1.509(5)
Ru01	N2	2.004(3)	C7	C6	1.391(5)
Ru01	N1	1.963(3)	C11	C10	1.485(5)
O5	C31	1.275(5)	C11	C12	1.386(5)
O4	C33	1.276(4)	C4	C5	1.396(5)
O2	C26	1.285(5)	C6	C5	1.388(6)
O3	C28	1.270(5)	C22	C23	1.502(5)
N2	C8	1.421(4)	C22	C21	1.392(5)
N2	C1	1.342(4)	C14	C13	1.386(6)
N3	C2	1.268(5)	C20	C19	1.385(5)
N3	C17	1.415(4)	C20	C21	1.393(5)
O1	C10	1.207(5)	C33	C34	1.506(5)
N1	C16	1.427(4)	C33	C32	1.396(6)

N1	C9	1.352(5)	C31	C32	1.396(6)
C2	C3	1.488(5)	C31	C30	1.507(5)
C2	C1	1.480(5)	C12	C13	1.392(6)
C17	C18	1.405(5)	C26	C27	1.393(6)
C17	C22	1.403(5)	C26	C25	1.506(6)
C8	C3	1.399(5)	C28	C27	1.399(6)
C8	C7	1.392(5)	C28	C29	1.512(5)
C15	C16	1.382(5)	O6A	C36A	1.4251
C15	C14	1.408(5)	C36A	C35A	1.5099
C3	C4	1.394(5)	O6B	C36B	1.4246
C1	C9	1.411(5)	C36B	C35B	1.5102

Appendix G-34 Bond angles (°) for **5.3·EtOH**.

O5	Ru01	O4	91.00(10)	C15	C16	C11	121.9(3)
O5	Ru01	O3	84.20(10)	C11	C16	N1	110.0(3)
O2	Ru01	O5	174.84(11)	N1	C9	C1	113.0(3)
O2	Ru01	O4	84.83(10)	N1	C9	C10	111.0(3)
O2	Ru01	O3	92.43(11)	C1	C9	C10	135.3(3)
O3	Ru01	O4	85.45(10)	C17	C18	C24	120.8(3)
N2	Ru01	O5	96.73(11)	C19	C18	C17	117.9(3)
N2	Ru01	O4	97.38(11)	C19	C18	C24	121.3(3)
N2	Ru01	O2	86.83(11)	C6	C7	C8	117.5(3)
N2	Ru01	O3	177.00(11)	C16	C11	C10	107.9(3)
N1	Ru01	O5	90.68(11)	C12	C11	C16	121.2(4)
N1	Ru01	O4	175.65(11)	C12	C11	C10	130.7(4)
N1	Ru01	O2	93.70(11)	O1	C10	C9	129.1(4)
N1	Ru01	O3	98.71(11)	O1	C10	C11	128.2(3)
N1	Ru01	N2	78.44(12)	C11	C10	C9	102.7(3)
C31	O5	Ru01	123.6(2)	C3	C4	C5	118.5(3)
C33	O4	Ru01	124.0(2)	C5	C6	C7	121.6(3)
C26	O2	Ru01	124.0(3)	C17	C22	C23	120.4(3)
C28	O3	Ru01	124.3(3)	C21	C22	C17	118.1(3)
C8	N2	Ru01	137.0(2)	C21	C22	C23	121.6(3)
C1	N2	Ru01	114.9(2)	C13	C14	C15	122.2(4)
C1	N2	C8	108.0(3)	C19	C20	C21	119.8(3)
C2	N3	C17	121.0(3)	C20	C19	C18	121.2(3)
C16	N1	Ru01	134.7(2)	O4	C33	C34	115.6(3)
C9	N1	Ru01	117.0(2)	O4	C33	C32	125.7(3)
C9	N1	C16	108.0(3)	C32	C33	C34	118.7(3)
N3	C2	C3	132.7(3)	C6	C5	C4	120.7(3)
N3	C2	C1	123.7(3)	O5	C31	C32	126.2(4)

C1	C2	C3	103.5(3)	O5	C31	C30	114.5(4)
C18	C17	N3	119.9(3)	C32	C31	C30	119.2(4)
C22	C17	N3	118.0(3)	C11	C12	C13	117.7(4)
C22	C17	C18	121.9(3)	O2	C26	C27	126.4(4)
C3	C8	N2	110.7(3)	O2	C26	C25	113.9(4)
C7	C8	N2	127.6(3)	C27	C26	C25	119.7(4)
C7	C8	C3	121.7(3)	O3	C28	C27	125.6(4)
C16	C15	C14	116.2(4)	O3	C28	C29	115.3(4)
C8	C3	C2	106.6(3)	C27	C28	C29	119.1(4)
C4	C3	C2	133.3(3)	C14	C13	C12	120.7(4)
C4	C3	C8	120.1(3)	C22	C21	C20	121.0(3)
N2	C1	C2	111.1(3)	C26	C27	C28	127.1(4)
N2	C1	C9	115.0(3)	C31	C32	C33	126.6(4)
C9	C1	C2	133.3(3)	O6A	C36A	C35A	107.4
C15	C16	N1	127.9(3)	O6B	C36B	C35B	107.4

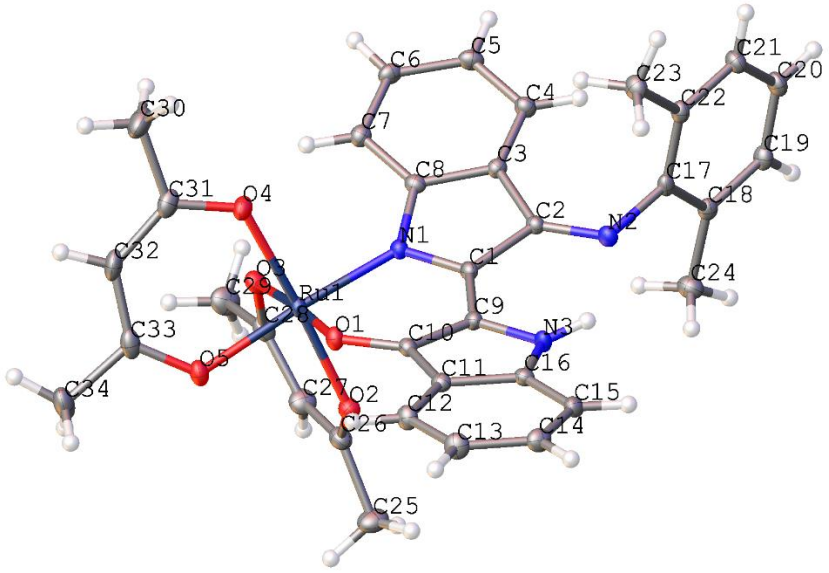

Appendix G-35 X-ray structure of **H5.4**. Thermal ellipsoids are shown at 50% probability.

Appendix G-36 Bond lengths (Å) for **H5.4**.

Ru1	O1	2.0268(11)	C19	C18	1.391(2)
Ru1	O2	2.0051(11)	C19	C20	1.387(2)
Ru1	O3	2.0131(11)	C16	C15	1.393(2)
Ru1	O4	2.0321(12)	C16	C11	1.414(2)
Ru1	O5	2.0321(11)	C3	C2	1.473(2)

Ru1	N2	1.9956(13)	C3	C4	1.395(2)
O1	C10	1.2774(18)	C7	C6	1.396(2)
O2	C26	1.2759(19)	C18	C17	1.404(2)
O3	C28	1.278(2)	C18	C24	1.507(2)
O4	C31	1.2805(19)	C21	C22	1.395(2)
O5	C33	1.280(2)	C21	C20	1.391(2)
N2	C1	1.3583(19)	C15	C14	1.387(2)
N2	C8	1.4161(19)	C11	C12	1.399(2)
N1	C9	1.390(2)	C28	C27	1.395(3)
N1	C16	1.3868(19)	C28	C29	1.511(2)
N3	C2	1.291(2)	C14	C13	1.403(2)
N3	C17	1.4337(19)	C22	C17	1.404(2)
C1	C9	1.383(2)	C22	C23	1.504(2)
C1	C2	1.484(2)	C12	C13	1.384(2)
C10	C9	1.439(2)	C26	C27	1.404(2)
C10	C11	1.444(2)	C26	C25	1.509(2)
C8	C3	1.413(2)	C33	C32	1.392(3)
C8	C7	1.389(2)	C33	C34	1.513(2)
C5	C4	1.390(2)	C31	C32	1.403(2)
C5	C6	1.397(2)	C31	C30	1.502(3)

Appendix G-37 Bond angles (°) for **H5.4**.

O1	Ru1	O4	93.72(4)	C8	C3	C2	106.03(13)
O1	Ru1	O5	89.75(4)	C4	C3	C8	120.52(14)
O2	Ru1	O1	84.35(4)	C4	C3	C2	133.41(14)
O2	Ru1	O3	94.54(5)	C8	C7	C6	117.24(15)
O2	Ru1	O4	176.32(5)	C19	C18	C17	118.20(14)
O2	Ru1	O5	85.34(5)	C19	C18	C24	120.91(14)
O3	Ru1	O1	175.63(4)	C17	C18	C24	120.84(14)
O3	Ru1	O4	87.15(5)	C20	C21	C22	121.17(15)
O3	Ru1	O5	85.94(4)	C14	C15	C16	117.58(15)
O4	Ru1	O5	91.53(5)	N3	C2	C1	122.73(14)
N2	Ru1	O1	90.82(5)	N3	C2	C3	133.08(14)
N2	Ru1	O2	90.55(5)	C3	C2	C1	104.14(12)
N2	Ru1	O3	93.42(5)	C16	C11	C10	107.08(13)
N2	Ru1	O4	92.61(5)	C12	C11	C10	132.54(14)
N2	Ru1	O5	175.77(5)	C12	C11	C16	120.38(14)
C10	O1	Ru1	121.51(9)	O3	C28	C27	126.43(15)
C26	O2	Ru1	122.75(11)	O3	C28	C29	114.38(15)
C28	O3	Ru1	122.48(11)	C27	C28	C29	119.18(15)
C31	O4	Ru1	124.10(11)	C15	C14	C13	121.74(15)

C33	O5	Ru1	124.16(11)	C21	C22	C17	118.02(14)
C1	N2	Ru1	123.12(10)	C21	C22	C23	121.19(14)
C1	N2	C8	106.78(12)	C17	C22	C23	120.78(14)
C8	N2	Ru1	130.07(10)	C5	C4	C3	118.28(15)
C16	N1	C9	108.83(13)	C19	C20	C21	119.61(15)
C2	N3	C17	117.16(13)	C13	C12	C11	118.28(15)
N2	C1	C9	122.86(14)	O2	C26	C27	126.07(16)
N2	C1	C2	111.04(13)	O2	C26	C25	114.81(15)
C9	C1	C2	125.52(14)	C27	C26	C25	119.10(15)
O1	C10	C9	126.56(14)	C18	C17	N3	119.71(14)
O1	C10	C11	127.31(14)	C22	C17	N3	118.62(13)
C9	C10	C11	106.09(13)	C22	C17	C18	121.66(14)
C3	C8	N2	111.57(13)	O5	C33	C32	125.81(16)
C7	C8	N2	127.10(14)	O5	C33	C34	114.52(16)
C7	C8	C3	121.29(14)	C32	C33	C34	119.65(16)
N1	C9	C10	108.62(13)	C7	C6	C5	121.96(15)
C1	C9	N1	124.90(14)	C12	C13	C14	120.86(15)
C1	C9	C10	125.53(14)	C28	C27	C26	127.39(16)
C4	C5	C6	120.60(15)	O4	C31	C32	126.17(16)
C20	C19	C18	121.30(14)	O4	C31	C30	114.45(16)
N1	C16	C15	129.52(14)	C32	C31	C30	119.38(15)
N1	C16	C11	109.32(13)	C33	C32	C31	126.57(16)
C15	C16	C11	121.15(14)				

Appendix G-38 Table of crystallographic parameters for **5.5** and **H5.5**$^+$.

Identification code	**5.5**	**H5.5**$^+$
Empirical formula	$C_{43}H_{42}Cl_2N_4O_4Ru$	$C_{196}H_{196}B_4F_{16}N_{16}O_{16}Ru_4$
Formula weight	850.77	3783.20
Temperature/K	90	90
Crystal system	orthorhombic	orthorhombic
Space group	$P2_12_12$	$P2_12_12_1$
a/Å	18.7127(12)	16.2862(15)
b/Å	7.9606(5)	16.3107(14)
c/Å	14.4925(9)	16.4485(13)
α/°	90	90
β/°	90	90
γ/°	90	90
Volume/Å^3	2158.9(2)	4369.4(6)
Z	2	1
ρ_{calc}g/cm^3	1.309	1.438
μ/mm^{-1}	0.530	3.468

F(000)	876.0	1952.0
Crystal size/mm^3	0.5 × 0.4 × 0.13	0.41 × 0.07 × 0.02
Radiation	MoKα (λ = 0.71073)	CuKα (λ = 1.54184)
2Θ range for data collection/°	3.554 to 61.002	7.634 to 114.026
Index ranges	-26 ≤ h ≤ 24, -8 ≤ k ≤ 11, -20 ≤ l ≤ 20	-16 ≤ h ≤ 17, -17 ≤ k ≤ 17, -17 ≤ l ≤ 17
Reflections collected	23685	21078
Independent reflections	6601 [R_{int} = 0.0308, R_{sigma} = 0.0283]	5866 [R_{int} = 0.0925, R_{sigma} = 0.0855]
Data/restraints/parameters	6601/0/249	5866/0/577
Goodness-of-fit on F^2	1.047	1.055
Final R indexes [I>=2σ (I)]	R_1 = 0.0220, wR_2 = 0.0528	R_1 = 0.0672, wR_2 = 0.1626
Final R indexes [all data]	R_1 = 0.0232, wR_2 = 0.0534	R_1 = 0.0819, wR_2 = 0.1718
Largest diff. peak/hole / e $Å^{-3}$	0.52/-0.28	1.37/-0.52
Flack parameter	-0.017(10)	-0.017(12)

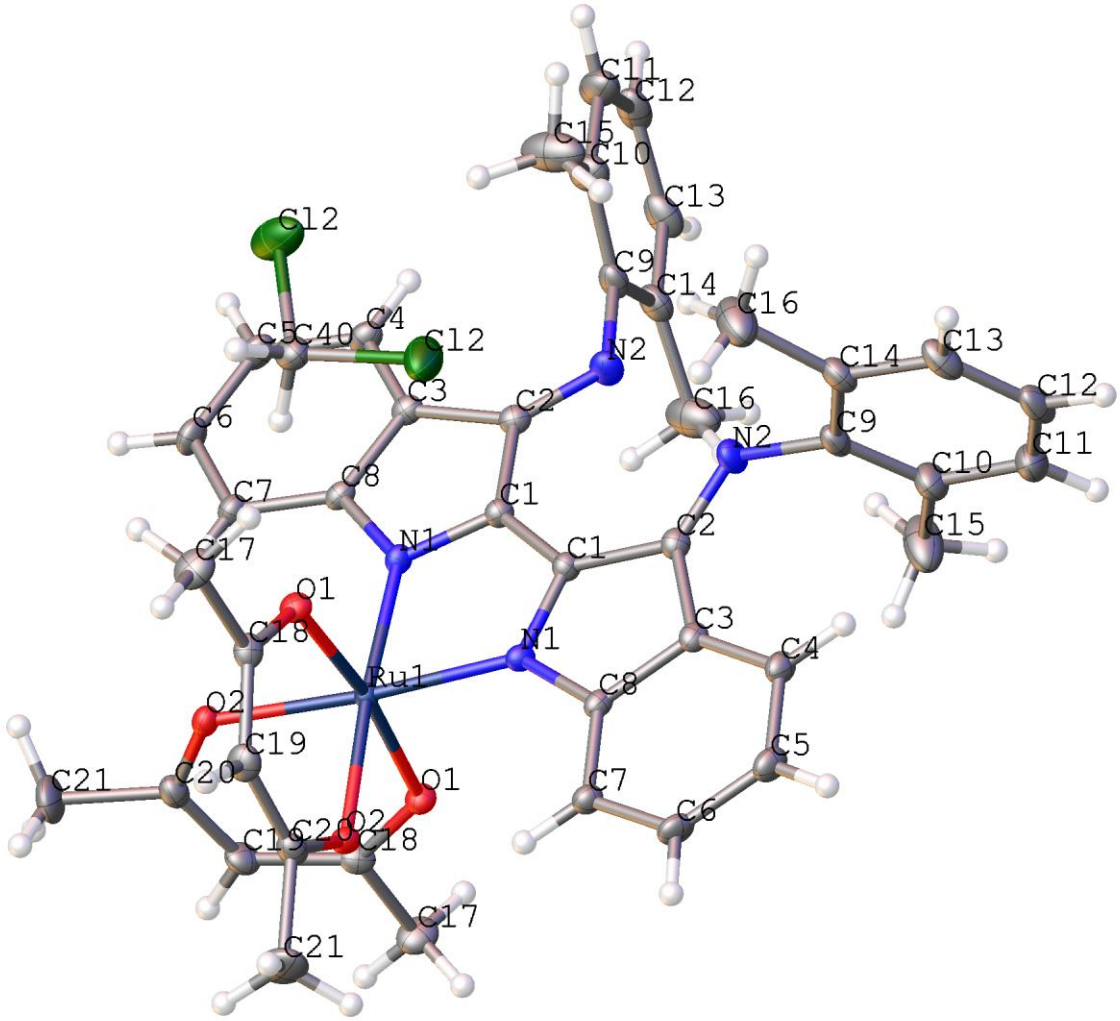

Appendix G-39 X-ray structure of **5.5**. Thermal ellipsoids are shown at 50% probability.

Appendix G-40 Bond lengths (Å) for **5.5**.

Ru1	$O2^1$	2.0555(13)	C2	C1	1.476(3)
Ru1	O2	2.0555(13)	C7	C8	1.382(3)
Ru1	$O1^1$	2.0301(13)	C7	C6	1.398(3)
Ru1	O1	2.0301(13)	C1	$C1^1$	1.413(3)
Ru1	$N1^1$	1.9982(16)	C20	C19	1.395(4)
Ru1	N1	1.9982(16)	C20	C21	1.515(3)
Cl2	C40	1.7652(16)	C9	C14	1.390(3)
O2	C20	1.272(3)	C9	C10	1.405(3)
O1	C18	1.282(2)	C13	C14	1.406(3)
N1	C1	1.351(2)	C13	C12	1.379(4)
N1	C8	1.432(2)	C40	$Cl2^2$	1.7653(16)

N2	C2	1.285(3)	C18	C17	1.507(3)
N2	C9	1.428(2)	C18	C19	1.395(3)
C5	C4	1.396(3)	C14	C16	1.499(3)
C5	C6	1.390(3)	C12	C11	1.384(4)
C3	C2	1.479(3)	C11	C10	1.400(3)
C3	C4	1.391(2)	C10	C15	1.502(3)
C3	C8	1.408(3)			

Appendix G-41 Bond angles (°) for **5.5**.

O2	Ru1	$O2^1$	83.34(7)	N1	C1	C2	111.62(15)
$O1^1$	Ru1	$O2^1$	91.28(5)	N1	C1	$C1^1$	113.72(10)
O1	Ru1	$O2^1$	82.70(5)	$C1^1$	C1	C2	134.63(10)
$O1^1$	Ru1	O2	82.70(5)	O2	C20	C19	126.23(18)
O1	Ru1	O2	91.28(5)	O2	C20	C21	114.4(2)
$O1^1$	Ru1	O1	171.96(8)	C19	C20	C21	119.4(2)
N1	Ru1	O2	175.47(6)	C3	C4	C5	118.29(19)
$N1^1$	Ru1	$O2^1$	175.47(6)	C3	C8	N1	110.67(16)
N1	Ru1	$O2^1$	99.70(5)	C7	C8	N1	127.01(17)
$N1^1$	Ru1	O2	99.70(5)	C7	C8	C3	122.31(17)
N1	Ru1	$O1^1$	93.83(6)	C14	C9	N2	118.88(19)
N1	Ru1	O1	92.44(6)	C14	C9	C10	122.39(19)
$N1^1$	Ru1	O1	93.83(6)	C10	C9	N2	118.38(19)
$N1^1$	Ru1	$O1^1$	92.44(6)	C12	C13	C14	121.1(2)
N1	Ru1	$N1^1$	77.47(9)	Cl2	C40	$Cl2^2$	112.67(15)
C20	O2	Ru1	124.47(14)	O1	C18	C17	114.32(18)
C18	O1	Ru1	124.28(12)	O1	C18	C19	126.74(18)
C1	N1	Ru1	117.49(12)	C19	C18	C17	118.93(18)
C1	N1	C8	107.09(15)	C5	C6	C7	121.31(18)
C8	N1	Ru1	135.38(13)	C9	C14	C13	117.7(2)
C2	N2	C9	119.49(17)	C9	C14	C16	120.9(2)
C6	C5	C4	121.11(18)	C13	C14	C16	121.4(2)
C4	C3	C2	133.53(18)	C13	C12	C11	119.8(2)
C4	C3	C8	119.78(17)	C20	C19	C18	126.43(18)
C8	C3	C2	106.69(15)	C12	C11	C10	121.4(2)
N2	C2	C3	132.17(18)	C9	C10	C15	120.3(2)
N2	C2	C1	123.87(17)	C11	C10	C9	117.3(2)
C1	C2	C3	103.84(15)	C11	C10	C15	122.5(2)
C8	C7	C6	117.20(19)				

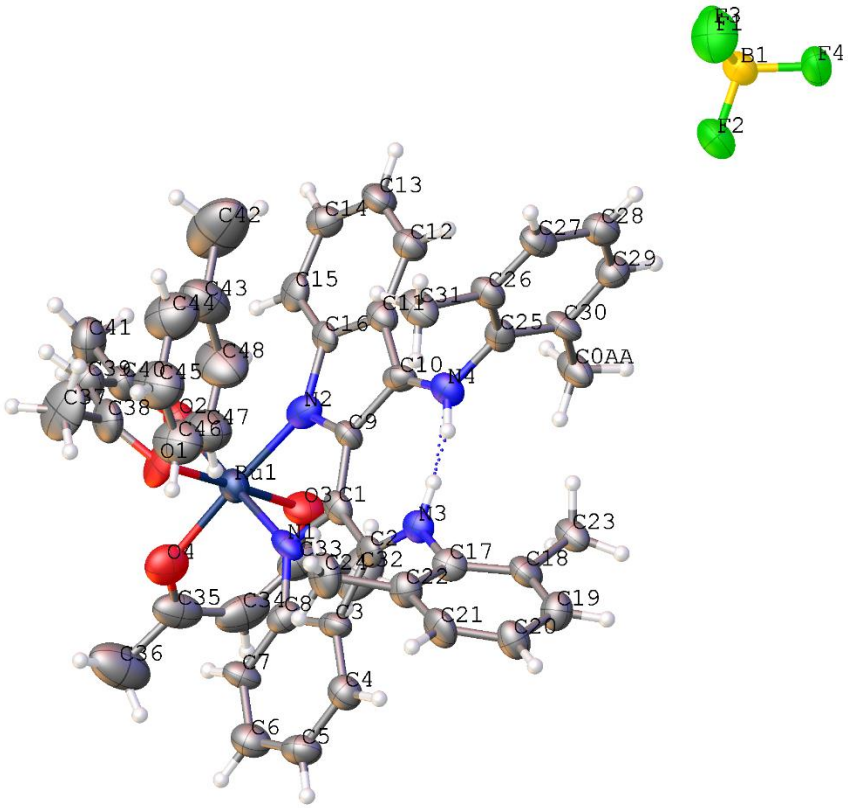

Appendix G-42 X-ray structure of **H5.5**$^{+}$. Thermal ellipsoids are shown at 50% probability.

Appendix G-43 Bond lengths (Å) for **H5.5**$^{+}$.

Ru1	O2	2.044(8)	C23	C18	1.523(18)
Ru1	O1	2.019(8)	C26	C31	1.508(19)
Ru1	N1	1.998(10)	C18	C19	1.37(2)
Ru1	N2	1.977(12)	C21	C20	1.358(19)
Ru1	O4	1.997(12)	C21	C22	1.38(2)
Ru1	O3	2.020(10)	C13	C12	1.37(2)
F4	B1	1.392(18)	C13	C14	1.39(2)
F3	B1	1.385(19)	C6	C7	1.36(2)
F2	B1	1.36(2)	C3	C8	1.392(19)
O2	C40	1.255(15)	C3	C2	1.49(2)
O1	C38	1.246(18)	C3	C4	1.395(19)
N3	C17	1.429(16)	C8	C7	1.369(19)
N3	C2	1.301(17)	C19	C20	1.417(18)
F1	B1	1.39(2)	C9	C1	1.402(18)
N1	C8	1.440(17)	C9	C10	1.454(17)
N1	C1	1.343(17)	C1	C2	1.457(18)
N2	C16	1.452(16)	C28	C29	1.39(2)

N2	C9	1.347(16)	C30	C29	1.40(2)
N4	C25	1.428(17)	C15	C14	1.40(2)
N4	C10	1.287(16)	C24	C22	1.503(19)
O4	C35	1.283(19)	C39	C40	1.398(19)
C16	C11	1.400(19)	C39	C38	1.41(2)
C16	C15	1.357(17)	C40	C41	1.49(2)
O3	C33	1.26(2)	C38	C37	1.50(2)
C25	C26	1.424(19)	C35	C34	1.43(3)
C25	C30	1.410(17)	C35	C36	1.49(3)
C27	C26	1.374(19)	C33	C34	1.40(3)
C27	C28	1.384(19)	C33	C32	1.49(2)
C17	C18	1.397(18)	C45	C44	1.37(3)
C17	C22	1.403(17)	C45	C46	1.36(3)
C5	C6	1.35(2)	C44	C43	1.40(3)
C5	C4	1.38(2)	C46	C47	1.40(3)
C11	C12	1.399(19)	C48	C43	1.41(3)
C11	C10	1.447(17)	C48	C47	1.32(3)
C0AA	C30	1.504(18)	C43	C42	1.46(3)

Appendix G-44 Bond angles (°) for **H5.5**$^{+}$.

O1	Ru1	O2	90.7(3)	C18	C19	C20	121.6(13)
O1	Ru1	O3	177.0(4)	C6	C7	C8	117.9(13)
N1	Ru1	O2	176.0(5)	N2	C9	C1	115.0(11)
N1	Ru1	O1	86.7(4)	N2	C9	C10	111.7(10)
N1	Ru1	O3	95.4(4)	C1	C9	C10	133.3(11)
N2	Ru1	O2	97.6(4)	C13	C12	C11	118.0(13)
N2	Ru1	O1	93.2(4)	N1	C1	C9	115.1(11)
N2	Ru1	N1	79.5(4)	N1	C1	C2	112.4(11)
N2	Ru1	O4	176.7(4)	C9	C1	C2	132.5(13)
N2	Ru1	O3	89.2(4)	C27	C28	C29	119.1(15)
O4	Ru1	O2	85.6(4)	N4	C10	C11	133.8(12)
O4	Ru1	O1	87.3(5)	N4	C10	C9	121.5(11)
O4	Ru1	N1	97.3(4)	C11	C10	C9	104.7(11)
O4	Ru1	O3	90.4(4)	N3	C2	C3	132.9(12)
O3	Ru1	O2	87.3(4)	N3	C2	C1	123.3(12)
C40	O2	Ru1	126.1(8)	C1	C2	C3	103.8(11)
C38	O1	Ru1	125.4(9)	C21	C20	C19	118.1(13)
C2	N3	C17	126.7(12)	C25	C30	C0AA	120.5(12)
C8	N1	Ru1	138.4(9)	C29	C30	C25	116.5(12)
C1	N1	Ru1	114.8(8)	C29	C30	C0AA	122.9(11)
C1	N1	C8	106.4(10)	C16	C15	C14	116.7(13)

C16	N2	Ru1	137.8(9)	C5	C4	C3	117.1(14)
C9	N2	Ru1	115.5(8)	C17	C22	C24	122.4(12)
C9	N2	C16	106.7(11)	C21	C22	C17	116.8(12)
C10	N4	C25	122.2(10)	C21	C22	C24	120.8(11)
C35	O4	Ru1	127.6(11)	C40	C39	C38	126.9(14)
C11	C16	N2	109.0(10)	C28	C29	C30	123.0(13)
C15	C16	N2	127.0(12)	C13	C14	C15	120.4(12)
C15	C16	C11	123.9(12)	O2	C40	C39	124.5(13)
C33	O3	Ru1	126.2(10)	O2	C40	C41	117.8(12)
C26	C25	N4	119.1(10)	C39	C40	C41	117.7(13)
C30	C25	N4	119.9(12)	O1	C38	C39	126.3(13)
C30	C25	C26	120.9(12)	O1	C38	C37	115.5(15)
C26	C27	C28	121.0(14)	C39	C38	C37	118.2(15)
C18	C17	N3	116.9(10)	O4	C35	C34	124.0(16)
C18	C17	C22	122.3(12)	O4	C35	C36	118.1(18)
C22	C17	N3	120.7(11)	C34	C35	C36	117.9(18)
C6	C5	C4	121.1(14)	O3	C33	C34	126.3(16)
C16	C11	C10	107.9(12)	O3	C33	C32	117.9(18)
C12	C11	C16	118.8(11)	C34	C33	C32	115.9(18)
C12	C11	C10	133.3(13)	F3	B1	F4	109.9(11)
C25	C26	C31	117.0(13)	F3	B1	F1	108.2(13)
C27	C26	C25	119.4(11)	F2	B1	F4	110.4(13)
C27	C26	C31	123.6(13)	F2	B1	F3	110.2(14)
C17	C18	C23	120.4(12)	F2	B1	F1	108.8(12)
C19	C18	C17	117.6(11)	F1	B1	F4	109.3(14)
C19	C18	C23	121.9(11)	C33	C34	C35	124.9(16)
C20	C21	C22	123.4(12)	C46	C45	C44	116(2)
C12	C13	C14	122.1(13)	C45	C44	C43	125(2)
C5	C6	C7	122.6(15)	C45	C46	C47	121(2)
C8	C3	C2	106.1(10)	C47	C48	C43	121(2)
C8	C3	C4	120.6(14)	C44	C43	C48	115.4(19)
C4	C3	C2	133.3(13)	C44	C43	C42	124(2)
C3	C8	N1	111.0(12)	C48	C43	C42	121(2)
C7	C8	N1	128.0(12)	C48	C47	C46	121(2)
C7	C8	C3	120.8(12)				